

**High Temperature Transformations of
Transition Metal Oxide Nanocrystals
Studied by
In-Situ Transmission Electron Microscopy**

Cover: TEM image of exfoliated MoO₂ particles and nanoflakes formed after in-situ heating of MoO₃ particles to 600 °C.

Back cover: TEM image of lath-shaped WO_x nanosheets formed by heating WO₃ nanoparticles in vacuum chamber at 900 °C.

PhD thesis, Utrecht University, the Netherlands, December 2022.

ISBN: 978-94-6469-124-5

A digital version of this thesis is available at <http://www.colloid.nl/>

Printed by: ProefschriftMaken || www.proefschriftmaken.nl

High Temperature Transformations of Transition Metal Oxide Nanocrystals Studied by In-Situ Transmission Electron Microscopy

**Transformaties van Transitie-metaaloxide
Nanokristallen op Hoge Temperatuur Bestudeerd door
Middel van In-Situ Transmissie-Elektronenmicroscopie**

(met een samenvatting in het Nederlands)

Proefschrift

ter verkrijging van de graad van doctor aan de
Universiteit Utrecht
op gezag van de
rector magnificus, prof.dr. H.R.B.M. Kummeling,
ingevolge het besluit van het college voor promoties
in het openbaar te verdedigen op

donderdag 8 december 2022 des middags te 2.15 uur

door

Xiaodan Chen

geboren op 12 mei 1990
te Xinjiang, China

Promotor:

Prof. dr. A. van Blaaderen

Copromotor:

Dr. M.A. van Huis

Beoordelingscommissie:

Prof. dr. P.E. de Jongh

Prof. dr. E.T.C. Vogt

Dr. J.E.S. van der Hoeven

Prof. dr. A. Meijerink

Prof. dr. B.J. Kooi

The research in this thesis was financially supported by the European Research Council (ERC) via the ERC Consolidator Grant NANO-INSITU (grant No. 683076).

Preface

Nanomaterials started to be a popular topic when I was a teenager. At that moment, to me as a teenager, nanomaterials meant something with fancy performance and functionalities – even though I did not understand what “nano” was and where the fancy performance came from. And of course, I had not expected I would study and do the related research in the future. In the past decades, I studied and acquired the underlying knowledge on “nano”, and performed research on nanocrystals (NCs) during my PhD years. The first Chapter will start with the topic of “nano” to introduce the difference between nanoscale materials and bulk materials. Next, the various objects of research (transition metal oxide nanoparticles) and the main research method used in this study, *in situ* transmission electron microscopy, will be described, after which the actual scientific findings will be presented. I wish you much pleasure in reading this thesis.

Utrecht, March 2022

Contents

1. Introduction.....	1
1.1 Nanoparticles: why is “nano” fancy?.....	3
1.2 Transition metal oxides.....	5
1.3 In situ TEM.....	6
1.4 Thesis Outline.....	7
1.5 References.....	9
2. Transmission Electron Microscopy.....	11
2.1 Introduction to TEM.....	13
2.2 High-resolution TEM.....	18
2.3 Elemental analysis: EDS.....	21
2.4 In-situ heating.....	22
2.5 References.....	24
3. Transformation of Co_3O_4 Nanoparticles to CoO Monitored by In-Situ TEM and Predicted Ferromagnetism at the $\text{Co}_3\text{O}_4/\text{CoO}$ Interface from First Principles.....	25
3.1 Introduction.....	27
3.2 Experimental.....	30
3.3 Computational Section.....	31
3.4 Results and Discussion.....	34
3.5 Conclusion.....	47
3.6 Acknowledgements.....	48
3.7 References.....	49
3.8 Appendix.....	51
4. Heating-induced Transformation of Anatase TiO_2 Nanorods to Rock Salt TiO Nanoparticles....	61
4.1 Introduction.....	63
4.2 Experimental.....	65
4.3 Results and Discussion.....	67
4.4 Conclusion.....	73
4.5 Acknowledgments.....	74

4.6	References	75
4.7	Appendix	78
5.	Heating-induced transformation of brookite TiO ₂ nanorods.....	83
5.1	Introduction.....	85
5.2	Experimental	85
5.3	Results and discussion	87
5.4	Conclusion	96
5.5	Acknowledgments.....	96
5.6	References	97
5.7	Appendix	99
6.	Thermal reduction and heating-induced exfoliation of MoO ₃ particles.....	103
6.1	Introduction.....	105
6.2	Experimental	108
6.3	Result and discussion.....	112
6.4	Conclusion and Outlook.....	124
6.5	Acknowledgements	126
6.6	References	127
6.7	Appendix.....	129
7.	Formation pathways of lath-shaped WO ₃ nanosheets and elemental W nanoparticles from heating of WO ₃ nanocrystals	139
7.1	Introduction.....	141
7.2	Experimental	142
7.3	Results and discussion	144
7.4	Conclusion	153
7.5	Acknowledgments.....	153
7.6	References	154
7.7	Appendix.....	157
	Summary	163
	Samenvatting.....	167

Acknowledgements.....	171
List of Publications	175
About the Author	177

1. Introduction

Nanoscience and nanotechnology are not only extensive fields of scientific research, but have also entered our daily lives as nanomaterials. The widespread applications of nanomaterials range from batteries in our smart devices to the catalysts in our cars. Despite the vast body of knowledge that has already been generated on nanoparticles and nanomaterials, much is yet unknown about their thermal and temporal stability. And the mechanisms of physical and chemical transformations of more specifically transition metal oxide nanoparticles at high temperatures still require much investigation. The elucidation of those mechanisms is the overarching aim of the PhD study described in this Thesis.

1.1 Nanoparticles: why is “nano” fancy?

It is found that with a decrease in size to a certain value at the nanoscale, particular properties of a material will most likely change. Gold is often set as an example for this phenomenon. Gold as a bulk material is a chemically inert metal with a yellowish color. However, gold nanoparticles (NPs) are chemically active, and the NPs solutions show different colors for different NP sizes, due to size-dependent surface plasmon resonance.¹ That the properties of nanomaterials differ from the corresponding bulk materials is mainly due to two reasons: surface effects and confinement effects^{2,3}.

Due to their small size, the total surface area of a collection of nanoparticles is much larger than that of bulk materials having the same volume as the combined volume of the nanoparticles. This means that there are much more atoms distributed on the surfaces which results in high total surface energies of NPs⁴. Systems always have a tendency to adopt lower energy configurations. Therefore, NPs tend to interact with each other to decrease their potential energy. This trend decreases the general stability of NPs; NPs easily become aggregated, and it can be hard to retain their nanoscale morphology. However, fortunately, this also gives NPs a high reactivity to external stimuli thereby offering ample opportunities for manipulation, and for inducing transformations to more desirable nanoscale configurations. A graphical overview of the transformations observed in this PhD study is presented in Figure 1-1.

Properties like optical, electronic, and magnetic properties may also change with decreasing size of the NPs, which results from confinement effects. The confinement effect is related to the electronic structure which is a consequence of the quantum nature of materials. The result of confinement effect varies for different materials. For example, in general metallic NPs need to be very small, typically a few nanometers, before the electronic energy levels (quantum states) start to become discrete, while for semiconductor NPs this can already take place for particles that are tens of nanometers in size.

With the combination of surface effects and confinement effects, properties of nanoparticles not only differ from the bulk materials but are also strongly size-dependent. The size dependence provides possibilities to manipulate the properties by tuning the size and morphology of the nanoparticles. This implies that nanomaterials can be fabricated for special applications by tailoring the particle sizes and shapes.

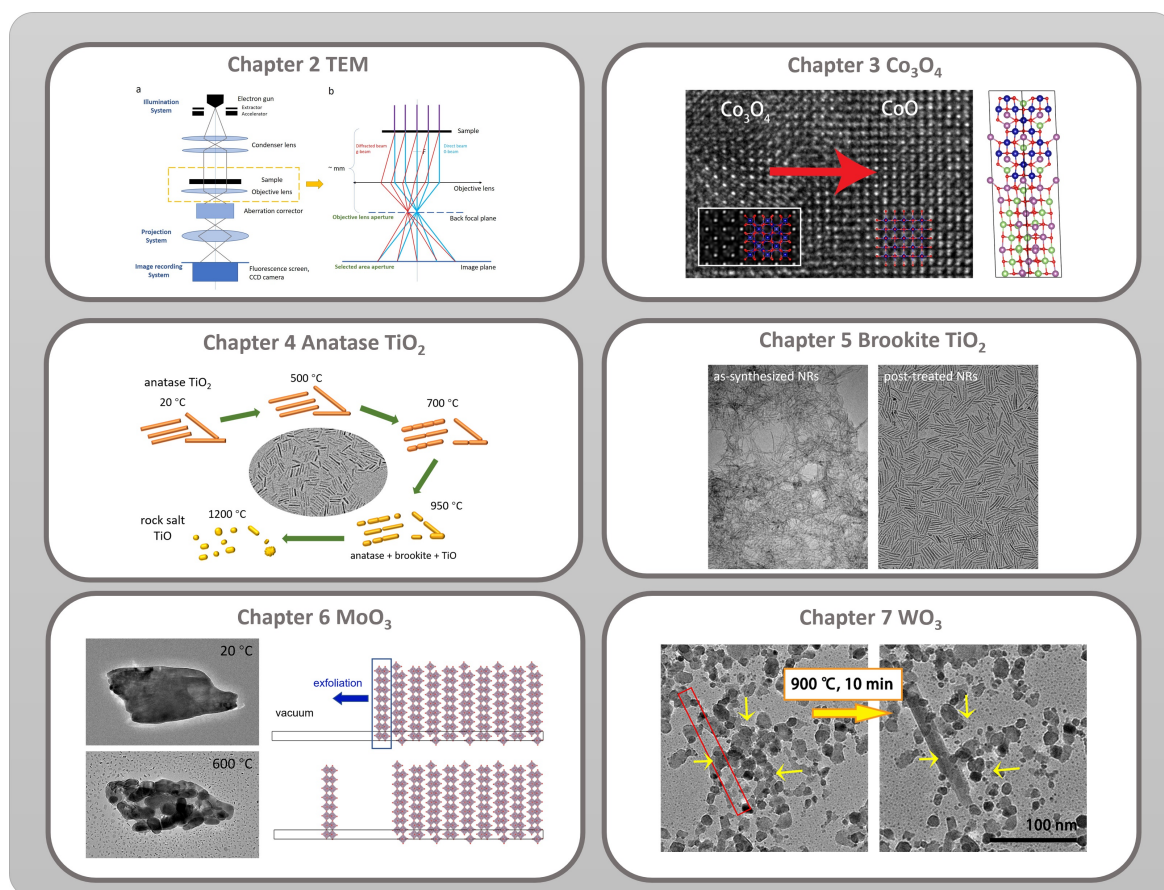


Figure 1-1 Graphical outline of the main technique used and the nanoscale transformations that were studied, that are presented in the following Chapters in this thesis.

Up to now, nanoparticles with a wide variety of shapes have been successfully synthesized. The synthesis can take place in liquid such as in sol-gel and colloid synthesis routes.⁵⁻⁷ Nanosized thin films and nanowires are often fabricated by chemical vapor deposition (CVD).⁸⁻¹⁰ Physical methods such as sputtering techniques and atomic layer deposition (ALD), sometimes used in combination with lithography techniques, can be also used to fabricate nanostructures.¹¹⁻¹³

Because of the differences between nano-sized materials and bulk materials, and the strong size dependence of nanoparticle properties, the exploration and characterization of nanomaterials with different sizes and morphologies is essential to develop further functional applications. Transmission electron microscopy (TEM) is a proper technique for this purpose, offering atomic-resolution real-space imaging enabled by the high energy of the electron beam, and offering a collection of analytical tools for chemical and physical characterization. With TEM, the morphology and crystalline structure can be easily observed, and chemical composition and oxidation states can be studied as well. The theoretical background and technique of the TEM method will be discussed in detail in Chapter 2.

1.2 Transition metal oxides

Transition metal oxides (TMOs) are a particularly interesting class of materials for academic and industrial investigations due to their exceptional and versatile physical and chemical properties. One of the most important utilizations of TMOs are as catalysts.^{14,15} TMOs nanocrystals are proven to be proper candidates for serving as oxygen evolution reaction (OER) and oxygen reduction reaction (ORR) catalysts that can be applied for energy storage and conversion¹⁶⁻¹⁹. Furthermore, TMO catalysts for the oxidation of organic chemicals can be applied in pollutants degradation^{20,21}. Besides catalytic applications, TMO nanocrystals can be also used in gas sensing^{22,23} and biomedical applications^{24,25}, such as drug delivery and permanent implant materials.

The unique properties of TMOs stem from partially occupied *d* orbitals, which leads to various valence states of the metal ions.²⁶ Consequently, TMOs often exhibit many different stoichiometries. Besides the commonly occurring trioxides, dioxides, and monoxides, TMOs with deviating stoichiometries also commonly exist, such as $\text{WO}_{2.72}$, Mo_9O_{26} , etc.²⁷⁻³⁰ Furthermore, even within the same chemical compositions, there are also polymorphs, which have the identical chemical stoichiometry but different crystal structure. For example, titanium dioxides (TiO_2) are mainly found in three phases named rutile, anatase and brookite, which will be discussed in detail in Chapter 4 and Chapter 5.

The common crystal structures of TMOs all originate from a particular 3D stacking of oxygen octahedra serving as building blocks. In TMOs, the metal ions are typically coordinated by 6 oxygen atoms, forming these octahedra. In many phases, the octahedra are distorted, and mutually connected by corner-, edge- or face-sharing. With increasing oxidation state, the most common crystal structures of binary TMOs are: rock salt for monoxides (MO), corundum (M_2O_3), rutile for dioxides (MO_2) and rhenium trioxides (MO_3). There are also Magnéli structures with stoichiometries $\text{M}_n\text{O}_{3n-1}$ that will be introduced in Chapter 6. Ternary TMOs often have a perovskite structure (ABO_3). This thesis however only focuses on binary TMO NCs.

It has been shown that the properties of bulk TMOs like their electronic structure and optical and magnetic properties are strongly correlated with temperature, pressure, chemical composition, and crystallinity.^{24,31-33} Phase diagrams show that transition metal oxides adopt various polymorphs and various oxidation states with different temperatures and pressures. When considering nanoparticles rather than bulk TMOs, the parameter space increases even further. Also the optical, conductive, and catalytic performances vary with different morphologies and crystal structures. Therefore, the study of thermal behavior and of thermal stability is very relevant to the performance of TMO nanocrystals.

One can distinguish different types of stability such as thermal, temporal, mechanical, and chemical stability of individual nanoparticles, or the stability of colloidal nanoparticle suspensions or

nanoparticle assemblies against coalescence, merging and sintering of nanoparticles.^{4,34,35} In this thesis, in particular thermal stability and heating-induced transformations of individual nanoparticles taking place under vacuum conditions are addressed. I would like to point out, however, that heating at low temperatures also provides information on temporal stability (stability in time) as room-temperature processes are accelerated at moderately elevated temperatures. That only holds, of course, as long as energy barriers corresponding to higher-temperature processes are not crossed. Furthermore, thermal stability to a certain extent also provides knowledge on chemical stability, in particular on the temperatures at which transitions to other oxidation states are to be expected in vacuum or at low partial oxygen pressures.

1.3 In situ TEM

For the investigation of nanocrystal transformations and nanoscale reactions, transmission electron microscopy is widely applied. And evidently for TMO nanoparticle studies, TEM is also frequently used. In the past decades, with the development of advanced in situ techniques, TEM is not restricted to post-treatment measurements, but also allows inspecting and monitoring the sample in real-time. This enables the observation of, amongst others, chemical reactions, phase transformations, and failure mechanisms.³⁶⁻³⁸ The in situ TEM measurements are achieved by various in situ holders (heating, liquid, gas, and biasing) or by modified TEM columns like ultra-high vacuum and environmental TEM.³⁹ To maintain the system stability and the imaging quality, the application of aberration correctors and ultra-fast imaging using highly sensitive detectors are also significant factors for successful performance of in situ TEM⁴⁰.

Although TEM is a most powerful technique for nanoscale research, there are also limitations. The high energy electron beams allow high resolution for imaging, but also bring unwanted side effects. With increasing energy of the electrons, knock-on damage is inflicted onto the sample above a certain threshold and charging effects can play a role as well. It is sometimes observed that parts of the sample fly away, melt, amorphize or crystallize with strong electron illumination. During in situ measurements, the continuous inspection to track changes brings more illumination, which can increase the beam effects. These effects are often even more pronounced for colloidal nanoparticles that are synthesized with special shapes and morphologies. Typically, ligands are covering the particle surfaces to maintain the morphology and prevent aggregation. These ligands react or degrade due to the electron beam exposure. This typically results in contamination but it can also influence the in situ observations; for instance, the bare surface of a nanoparticle (after being stripped of ligands) is more likely to interact physically or chemically, or alternatively a carbon shell around the nanoparticle is formed as a result of surfactant degradation, which may stabilize the nanoparticle so that transformations are not observed.⁴¹ Therefore, in order to monitor and control the beam effects, the

inspected areas in the following investigations have often been changed during measurements, which is feasible as the electron beam illuminates only a small portion of the sample on the TEM grid. Furthermore, ex situ experiments conducted in a vacuum chamber were performed as well, serving as a reference for the in-situ results, as will be discussed in more detail in Chapter 2.

1.4 Thesis Outline

In this thesis, several types of TMO nanocrystals were investigated using in-situ TEM. The thermal behavior and phase transformations were tracked during real-time processes. Figure 1 shows a graphical abstract of this thesis. The following Chapters of this thesis are organized as follows:

In Chapter 2, the theoretical background and techniques of transmission electron microscopy are briefly discussed. The theory of imaging, formation of diffraction patterns and of high-resolution images are explained.

In Chapter 3, the transformation of Co_3O_4 nanocrystals during vacuum annealing is shown. The Co_3O_4 nanocrystals transformed to CoO starting from a temperature of $350\text{ }^\circ\text{C}$, and were fully converted at $400\text{ }^\circ\text{C}$. The transformation progressed from the surface toward the center of particles. The energetics and magnetic properties of $\text{Co}_3\text{O}_4/\text{CoO}$ interface were calculated from first principles.

In Chapter 4 the thermal behavior of anatase TiO_2 nanorods is studied. The nanorods were stable retaining their morphology at temperatures up to $600\text{ }^\circ\text{C}$, but deformed and finally broke up into small segments after further heating. The anatase nanorods completely transformed to rock salt TiO at $1200\text{ }^\circ\text{C}$ with the brookite phase being formed in an intermediate stage.

Consecutively, in Chapter 5, the thermal evolution of brookite TiO_2 nanorods (synthesized following a different route than the anatase NRs) are also studied. Differently from anatase NRs, after annealing up to a temperature of $1200\text{ }^\circ\text{C}$, only part of the specimen transformed to TiO while an other part transformed to the rutile TiO_2 phase.

In Chapter 6, MoO_3 particles were investigated. The crystal structure of MoO_3 is quite different from the oxides mentioned above. MoO_3 has a layered structure wherein the layers are bonded by van der Waals forces rather than by chemical bonds. Consequently, the thermal behavior is very different from the other samples. The MoO_3 particles exfoliated into small flakes at $600\text{ }^\circ\text{C}$ when heated at a very fast rate ($20\text{ }^\circ\text{C/s}$), which results in images showing that the particles seem to be blown up being disintegrated, with small fragments scattered all around the primary particles. The small flakes were found to be in a MoO_2 composition.

In Chapter 7, the thermal evolution of WO_3 nanoparticles with cubic crystal structure are studied. With low concentrations of pristine NPs dropcast onto the heating chip, the samples transformed to

elemental W at 900 °C. However when high concentrations of NPs were dropcast onto the heating chip, two-dimensional nanosheets are also formed at 900 °C. The nanosheets have a lath-shape and easily fold or curl up at two of the lath sides. The nanosheets are in a WO_3 or $\text{WO}_{2.72}$ composition and are most likely formed through a solid-vapor-solid mechanism.

As a common trend, transformations to lower-valence state oxides or eventually to pure metal occurred during heating of these TMO nanoparticle systems at elevated temperatures in the microscope. From comparing these results with the outcomes of reference experiments conducted outside the microscope, we found that the (low) oxygen pressure in the vacuum of the TEM column is of importance for the temperatures at which these transformations take place. These and other findings of this PhD study have brought both scientific understanding and opportunities for future research, as described in the Summary concluding this thesis.

1.5 References

- 1 G. Mie, *Ann. Phys.*, 1908, **330**, 377–445.
- 2 C. De Mello Donegá, *Nanoparticles: Workhorses of nanoscience*, Springer-Verlag Berlin Heidelberg, 2014, vol. 9783662448.
- 3 E. Roduner, *Chem. Soc. Rev.*, 2006, **35**, 583–592.
- 4 L. Xu, H.-W. Liang, Y. Yang and S.-H. Yu, *Chem. Rev.*, 2018, **118**, 3209–3250.
- 5 S. Anu Mary Ealia and M. P. Saravanakumar, *IOP Conf. Ser. Mater. Sci. Eng.*, 2017, **263**, 032019.
- 6 L. A. Kolahalam, I. V. Kasi Viswanath, B. S. Diwakar, B. Govindh, V. Reddy and Y. L. N. Murthy, in *Materials Today: Proceedings*, Elsevier, 2019, vol. 18, pp. 2182–2190.
- 7 C. Dhand, N. Dwivedi, X. J. Loh, A. N. Jie Ying, N. K. Verma, R. W. Beuerman, R. Lakshminarayanan and S. Ramakrishna, *RSC Adv.*, 2015, 5, 105003–105037.
- 8 G. D. Nessim, *Nanoscale*, 2010, **2**, 1306–1323.
- 9 Y. M. Manawi, Ihsanullah, A. Samara, T. Al-Ansari and M. A. Atieh, *Materials (Basel)*, 2018, 11, 822.
- 10 M. Mittal, S. Sardar and A. Jana, in *Handbook of Nanomaterials for Sensing Applications*, Elsevier, 2021, pp. 119–137.
- 11 H. B. Profijt, S. E. Potts, M. C. M. van de Sanden and W. M. M. Kessels, *J. Vac. Sci. Technol. A Vacuum, Surfaces, Film.*, 2011, **29**, 050801.
- 12 H. C. M. Knoop, T. Faraz, K. Arts and W. M. M. (Erwin) Kessels, *J. Vac. Sci. Technol. A Vacuum, Surfaces, Film.*, 2019, **37**, 030902.
- 13 P. O. Oviroh, R. Akbarzadeh, D. Pan, R. A. M. Coetzee and T. C. Jen, *Sci. Technol. Adv. Mater.*, 2019, **20**, 465.
- 14 A. FUJISHIMA, X. ZHANG and D. TRYK, *Surf. Sci. Rep.*, 2008, **63**, 515–582.
- 15 M. A. Henderson, *Surf. Sci. Rep.*, 2011, **66**, 185–297.
- 16 H. Osgood, S. V. Devaguptapu, H. Xu, J. Cho and G. Wu, *Nano Today*, 2016, 11, 601–625.
- 17 J. Pan, X. L. Tian, S. Zaman, Z. Dong, H. Liu, H. S. Park and B. Y. Xia, *Batter. Supercaps*, 2019, 2, 336–347.
- 18 S. Yuan, X. Duan, J. Liu, Y. Ye, F. Lv, T. Liu, Q. Wang and X. Zhang, *Energy Storage Mater.*, 2021, **42**, 317–369.
- 19 H. Wang, K. H. L. Zhang, J. P. Hofmann, V. A. de la Peña O’Shea and F. E. Oropeza, *J. Mater. Chem. A*, 2021, 9, 19465–19488.
- 20 A. Yusuf, C. Snape, J. He, H. Xu, C. Liu, M. Zhao, G. Z. Chen, B. Tang, C. Wang, J. Wang and S. N. Behera, *Catal. Rev. - Sci. Eng.*, 2017, **59**, 189–233.
- 21 A. Akbari, M. Amini, A. Tarassoli, B. Eftekhari-Sis, N. Ghasemian and E. Jabbari, *Nano-Structures and Nano-Objects*, 2018, 14, 19–48.
- 22 J. Malallah Rzaij and A. Mohsen Abass, *J. Chem. Rev.*, 2020, **2**, 114–121.
- 23 Z. Li, Z. J. Yao, A. A. Haidry, T. Plecenik, L. J. Xie, L. C. Sun and Q. Fatima, *Int. J. Hydrogen Energy*, 2018, 43, 21114–21132.

- 24 A. Azor-Lafarga, I. Gómez-Recio, M. L. Ruiz-González and J. M. González-Calbet, *Nanomaterials*, 2021, **11**, 2073.
- 25 A. S. Agnihotri, A. Varghese and N. M, *Appl. Surf. Sci. Adv.*, 2021, **4**, 100072.
- 26 P. A. Cox, *Transition Metal Oxides: An Introduction to their Electronic Structure and Properties*, Clarendon Press, 2010.
- 27 Y. Zhang, Y. Chen, H. Liu, Y. Zhou, R. Li, M. Cai and X. Sun, *J. Phys. Chem. C*, 2009, **113**, 1746–1750.
- 28 K. Hong, M. Xie, R. Hu and H. Wu, *Appl. Phys. Lett.*, 2007, **90**, 173121.
- 29 L. Brewer and R. H. Lamoreaux, *Bull. Alloy Phase Diagrams*, 1980, **1**, 85–89.
- 30 K. Inzani, M. Nematollahi, F. Vullum-Bruer, T. Grande, T. W. Reenaas and S. M. Selbach, *Phys. Chem. Chem. Phys.*, 2017, **19**, 9232–9245.
- 31 A. Navrotsky, C. Ma, K. Lillova and N. Birkner, *Science (80-.)*, 2010, **330**, 199–201.
- 32 Y. Wang, Y. Zou, Q. Shang, X. Tan, T. Yu, X. Huang, W. Shi, Y. Xie, G. Yan and X. Wang, *Trans. Tianjin Univ.*, 2018, **24**, 326–339.
- 33 J. Pan and S. P. Jiang, *J. Colloid Interface Sci.*, 2016, **469**, 25–30.
- 34 H. Mateos and G. Palazzo, in *Colloidal Foundations of Nanoscience*, Elsevier, 2022, pp. 57–83.
- 35 F. Gambinossi, S. E. Mylon and J. K. Ferri, *Adv. Colloid Interface Sci.*, 2015, **222**, 332–349.
- 36 R. Sinclair, *MRS Bull.*, 2013, **38**, 1065–1071.
- 37 Z.-H. Xie, Z. Jiang and X. Zhang, *J. Electrochem. Soc.*, 2017, **164**, A2110–A2123.
- 38 Z. Song and Z. H. Xie, *Micron*, 2018, **112**, 69–83.
- 39 M. L. Taheri, E. A. Stach, I. Arslan, P. A. Crozier, B. C. Kabius, T. LaGrange, A. M. Minor, S. Takeda, M. Tanase, J. B. Wagner and R. Sharma, *Ultramicroscopy*, 2016, **170**, 86–95.
- 40 J. S. Kim, T. LaGrange, B. W. Reed, M. L. Taheri, M. R. Armstrong, W. E. King, N. D. Browning and G. H. Campbell, *Science (80-.)*, 2008, **321**, 1472–1475.
- 41 W. Albrecht, A. van de Glind, H. Yoshida, Y. Isozaki, A. Imhof, A. van Blaaderen, P. E. de Jongh, K. P. de Jong, J. Zečević and S. Takeda, *Ultramicroscopy*, 2018, **193**, 97–103.

2. Transmission Electron Microscopy

In this Chapter, the main experimental technique used in this PhD study is briefly introduced. Transmission Electron Microscopy (TEM) is one of the most powerful techniques for the investigation of nanostructures. By using different imaging and analysis modes, the morphology, crystalline structure, and chemical composition of nanomaterials can be observed. The discussion in this chapter is mainly based on the following references.

[I] Williams, D. B. & Carter, C. B. *Transmission Electron Microscopy: A Textbook for Materials Science* (Springer, New York, 2009)

[II] Reimer, L. & Kohl, H. *Transmission Electron Microscopy: Physics of Image Formation* (Springer, New York, 2008)

2.1 Introduction to TEM

To introduce electron microscopy, an analogy to a traditional optical microscope can be made. In an optical microscope, visible light illuminates the sample. In the simplest case of a lenses system, the image of the sample is amplified by a glass convex lens and collected by the eye or by a digital screen. The resolution is proportional to the wavelength of the photons emitted by the illumination source, and is defined as the smallest distance d between two image points that are still considered as separately distinguishable:

$$d = \frac{0.61\lambda}{\mu \sin\beta}$$

where λ is the wavelength of the light, μ is the refractive index and β is the semi-angle of collection of the magnifying lens. The wavelength range of visible light is 400-700 nm.

In the electron microscope, an electron beam is used as an illumination source. However, the relativistic wavelength of electrons is orders of magnitude smaller and can reach a picometer scale depending on the accelerating voltage applied to the electrons.¹ This allows to achieve atomic resolution, as the distance between atoms is typically $\sim 2 \text{ \AA}$ or $\sim 200 \text{ pm}$. One thing to be noted here is that, for a real electron microscope, the resolution is not only related to the wavelength of the electron beam, but is in particular limited by imperfect particle beam optics, such as the aberrations of the magnetic lenses. Furthermore, the semi-angle of collection, or aperture, is much smaller for electron microscopes in comparison to that of optical microscopes.

As electrons would be stopped in matter such as glass, electromagnetic lenses steering the electrons travelling in vacuum are applied instead of optical lenses. In scanning electron microscopy (SEM), the image is typically formed from secondary electrons that are emitted from the surface of the sample, while in transmission electron microscopy (TEM) which was typically used in this study, the electron beam fully penetrates the specimen and arrives at the viewing screen or detector at the rear side of the sample. Therefore, the specimens to be investigated by TEM are required to be sufficiently thin to ensure that the electrons can go through, i.e., are transmitted. With TEM, the result is a two-dimensional projection of the objects.

The schematic set-up of TEM is shown in Figure 2-1 (a). The electrons are extracted from the electron gun by an extraction anode, and subsequently accelerated. After the electron beam enters the column, the electron beam is transferred by a condenser lens to the specimen mainly in one of two modes: parallel or convergent. Parallel beams can form TEM images and selected area diffraction patterns (SADP) while convergent beams can be used in scanning transmission electron microscopy (STEM) and convergent-beam electron diffraction (CBED). After the electrons exit the specimen, the images

are magnified by the projection lens system and finally reach a fluorescence screen, a CCD (charge coupled device) camera, or other semiconductor-based cameras. The whole system is under vacuum conditions because the high energy electron beam can ionize gaseous impurities, which would damage the electron gun. In addition, undesired scattering of the electron beam with molecules and impurities is to be avoided as this would be detrimental to the resolution. For advanced TEM, aberration correctors are used to decrease the effect of (magnetic lens) aberrations, for improving the resolution down to even 50 or 30 picometer.²⁻⁴

As shown in Figure 2-1(b), when the electrons go through the specimens, some of the electrons do not change their direction and penetrate the specimen directly. These electrons are called the direct beam, also 0-beam. Other electrons do interact with the specimens leading to changes in their directions and/or energies, and are called scattered beams. In the case where the change of direction is caused by Bragg reflection at a crystalline atomic lattice, the beam is called a diffracted beam (g-beam). The diffracted electrons can be considered as a special case of “scattered” beams. When there is no energy loss during the electron-specimen interaction, we speak of elastic scattering, which in general provides structural information. In contrast, during inelastic scattering, the electrons lose some of their energy and bring information on elemental composition or on physical excitations.

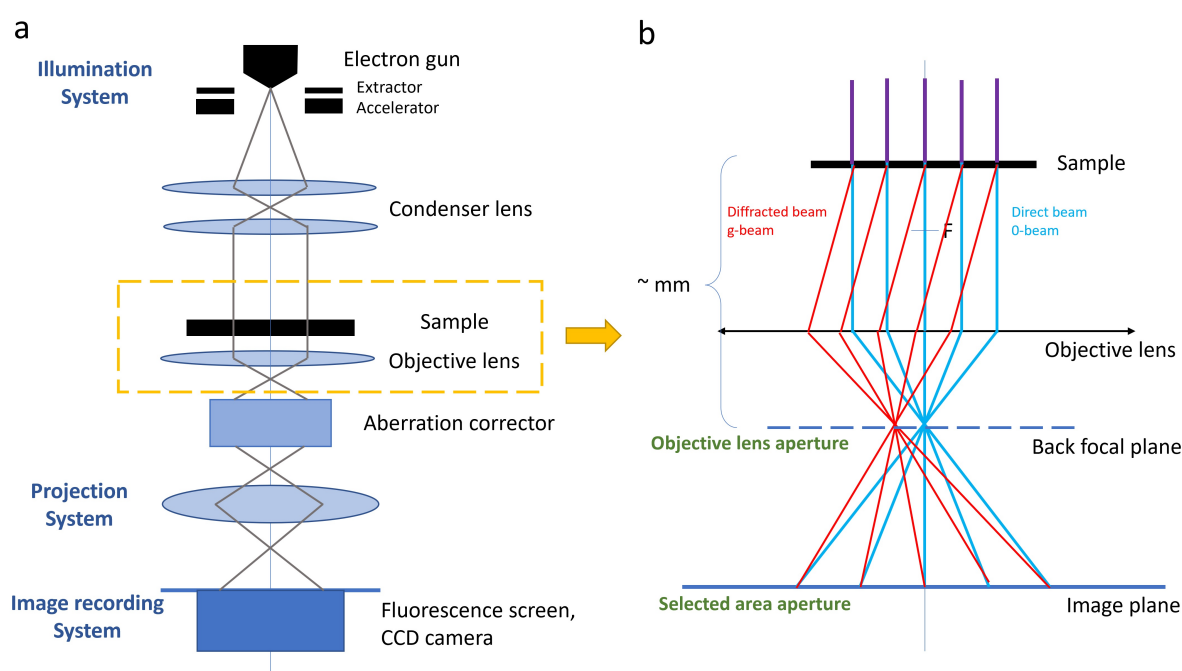


Figure 2-1 (a) The schematic illustration of TEM set-up. (b) Detailed illustration of the electron path around specimens.

Both elastic and inelastic beams penetrate the specimen and are focused at the back focal plane, and finally reach the image plane. On the image plane, the commonly known TEM images are formed. On the back focal plane, diffraction patterns are formed. Mathematically, the diffraction patterns are the

power spectra of Fourier Transforms of projections of the real space objects, giving information on the reciprocal atomic lattice. The real space images or the diffraction patterns are magnified by the projection system in TEM imaging mode and in diffraction mode, respectively.

2.1.1 Imaging mode

As mentioned above, when the image plane of the objective lens is magnified and projected on a screen, this mode is called the imaging mode. Apart from this TEM imaging mode, also the scanning TEM (STEM) imaging mode can be used. These are two complementary ways of imaging that rely on different mechanisms:

In TEM mode, the condenser lens is set to make a parallel beam illuminating the specimen. In this mode, an objective lens aperture can be applied for selecting particular beams to generate images. The image formed by the transmitted beams is called a bright-field (BF) image. And the images formed by diffracted beams are called dark-field (DF) images. During observation of NPs, the objective lens aperture can also be applied to remove the outer rim of the beam which can improve the contrast and/or the quality of the images. The images formed in TEM mode are influenced by many aspects of the specimens, such as thickness, orientation, and presence of defects. Therefore, sometimes TEM images are hard to analyze. But also due to this sensitivity, when selecting a special TEM mode, like weak-beam dark field (WBDF), defects such as dislocations can be detected more easily.

In STEM mode, a convergent beam is created by the condenser lens system and focused onto the specimen. The beam is focused to a point which can be as small as 30 picometer, and by raster scanning the specimen pixel by pixel and by detecting the scattered electrons using a ring-shaped detector above the TEM screen, images are created where the contrast is mainly determined by the atomic number of the atoms, so-called Z-contrast. By using a high-angle annular dark field (HAADF) detector, only electrons scattered to higher angles are detected, and effects of the orientation (which would generate additional diffraction contrast) can to a large extent be removed. This generates good contrast for in particular heavier atoms which have high scattering powers. Lighter atoms in samples, like C, N, and O, scatter the electrons to relatively low angles, and cannot be collected by the detector. Hence those atoms are often not visible. Since STEM images are collected point by point, the STEM mode is more sensitive to drift of the specimen. Furthermore, the convergent beam transfers more energy to the specimen per square area (locally) than a parallel beam, hence beam effects like induced contamination may be more pronounced than when imaging in TEM mode.

2.1.2 Electron diffraction

At the back focal plane, the electrons are separated to one direct beam and many diffracted beams, forming a diffraction pattern (DP). The diffraction pattern is formed by the interference of refracted electron waves from neighboring atoms and lattice planes. In the DP, the brightest and central spot is the direct beam, and other darker ones are diffracted beams. There are also electrons in the background of the DP that have undergone a phase shift in the sample (the larger the phase shift, the more out-of-center the position in the DP), but that in general are not recognizable as individual spots. By inserting a selected area aperture at the image plane of the objective lens, the information from a certain area can be selected to show the structural information of that particular area. For single crystalline materials, the DP consists of several spots arranged in a certain symmetrical pattern. For NPs, when a large number of particles lying in different crystallographic orientations are selected, the DP consists of several rings. The position of the rings or spots provides information of the lattice parameter and crystal symmetry. As mentioned above, the DP shows information in reciprocal space, therefore, the radii of the rings have a reciprocal relation with the real-space lattice spacings.

Since the DP is generated from the entire area that is illuminated by the electron beam, the information from many NPs is summed. Therefore, in the following chapters, SADPs are recorded to follow the phase transformations during heating.

2.1.3 Image formation: Contrast

Features in images can be seen due to contrast. Contrast is the relative difference in intensity between two neighboring areas. There are several contrast modes in TEM.

Mass-thickness contrast is formed due to the different mass or thickness of adjacent areas. Since the cross section for elastic scattering depends on the atomic number Z , thicker areas and areas with higher Z scatter more electrons, showing darker contrast in the bright-field images, and vice versa.

Diffraction contrast is caused by coherent elastic scattering at Bragg angles. This means that diffraction contrast depends on the crystal structure and the orientations of the crystal planes with respect to the electron beam. When the material is amorphous, there is no diffraction contrast.

Phase contrast is often the main source of contrast in high-resolution TEM images, and is formed by both direct and diffracted beams. This contrast is caused by the phase difference between the electrons in different beams, leading to interference. This contrast will be introduced in more detail in the next section.

Z-contrast: in STEM mode, the contrast mainly depends on different Z numbers of the elements in the sample, forming so-called Z -contrast. As mentioned above, with an HAADF detector, only electrons scattered to high angles (> 50 mrad) are collected.

Different types of contrast have contributions to images, but usually conditions are selected such that only one dominates. Figure 2-2 shows (S)TEM images in which different types of contrast dominate. Figure 2-2 (a) is a TEM image showing $\text{NaYF}_4@SiO_2$ core-shell particles at 700 °C. Mass-thickness contrast dominates in this image; the NaYF_4 core material (darker region) is heavier than the SiO_2 shell (brighter region). Diffraction contrast dominates in Figure 2-2 (b). For $\text{CoFe}_2\text{O}_4@Fe_xO$ core-shell particles, the core and shell materials have comparable mass density, so there is no contrast difference between the core and shell areas for most of the particles. In some of the particles, however, the core areas are darker than in other particles because the atomic lattices of these cores are in an orientation rendering a diffraction condition with the electron beam. And because the crystal structure of the core diffracts more strongly than the crystal structure of the shell, the core and shell show different contrast in these particles. Figure 2-2(c) is an HRTEM image of a Co_3O_4 nanocrystal where phase contrast dominates. The bright dots are projections of atomic columns. Figure 2-2(d) is an HAADF-STEM image of $\text{CoFe}_2\text{O}_4@Fe_xO$ core-shell particles. The carbon support appears totally dark because of the low atomic number of carbon. The core-shell structure cannot be distinguished here due to the very similar mass density of the core and the shell components of the nanoparticles.

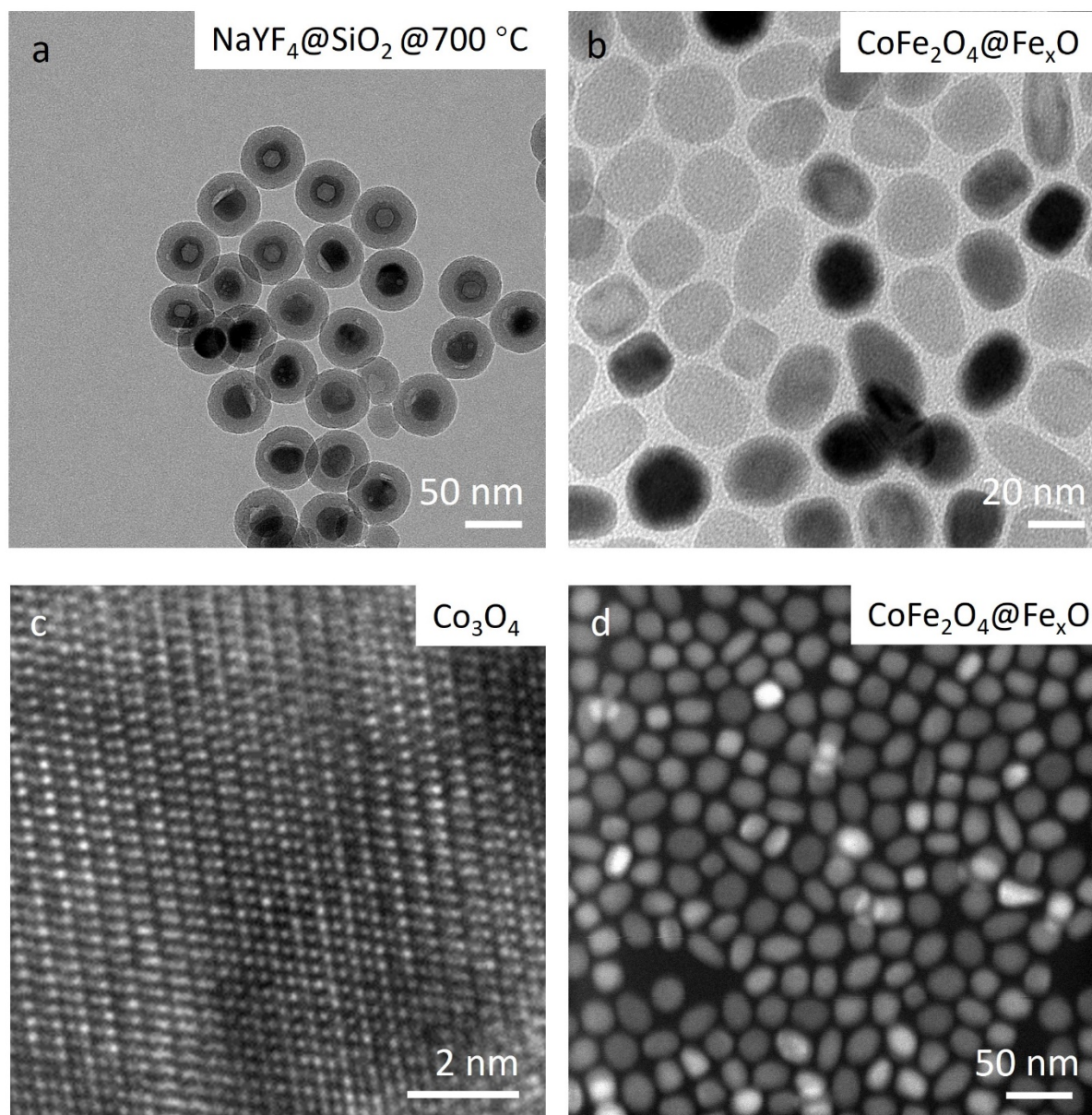


Figure 2-2. (S)TEM images showing different types of contrast. (a) NaYF₄@SiO₂ core-shell particles at 700 °C. Mass-thickness contrast dominates in this image. The NaYF₄ core material (darker region) is heavier than the SiO₂ shell (brighter region). (b) CoFe₂O₄@Fe_xO core-shell particles. Some of the particles show different brightness of the core and the shell due to diffraction contrast. (c) High resolution image of a Co₃O₄ nanocrystal. The bright dots are atomic columns; the pattern is mainly the result of phase contrast. (d) CoFe₂O₄@Fe_xO core-shell particles recorded in HAADF-STEM mode. Here Z-contrast dominates in the image.

2.2 High-resolution TEM

The high-resolution TEM mode is a commonly used technique for analyzing crystalline structure. In HR images, phase contrast dominates. The image formation process is shown in Figure 2-3.

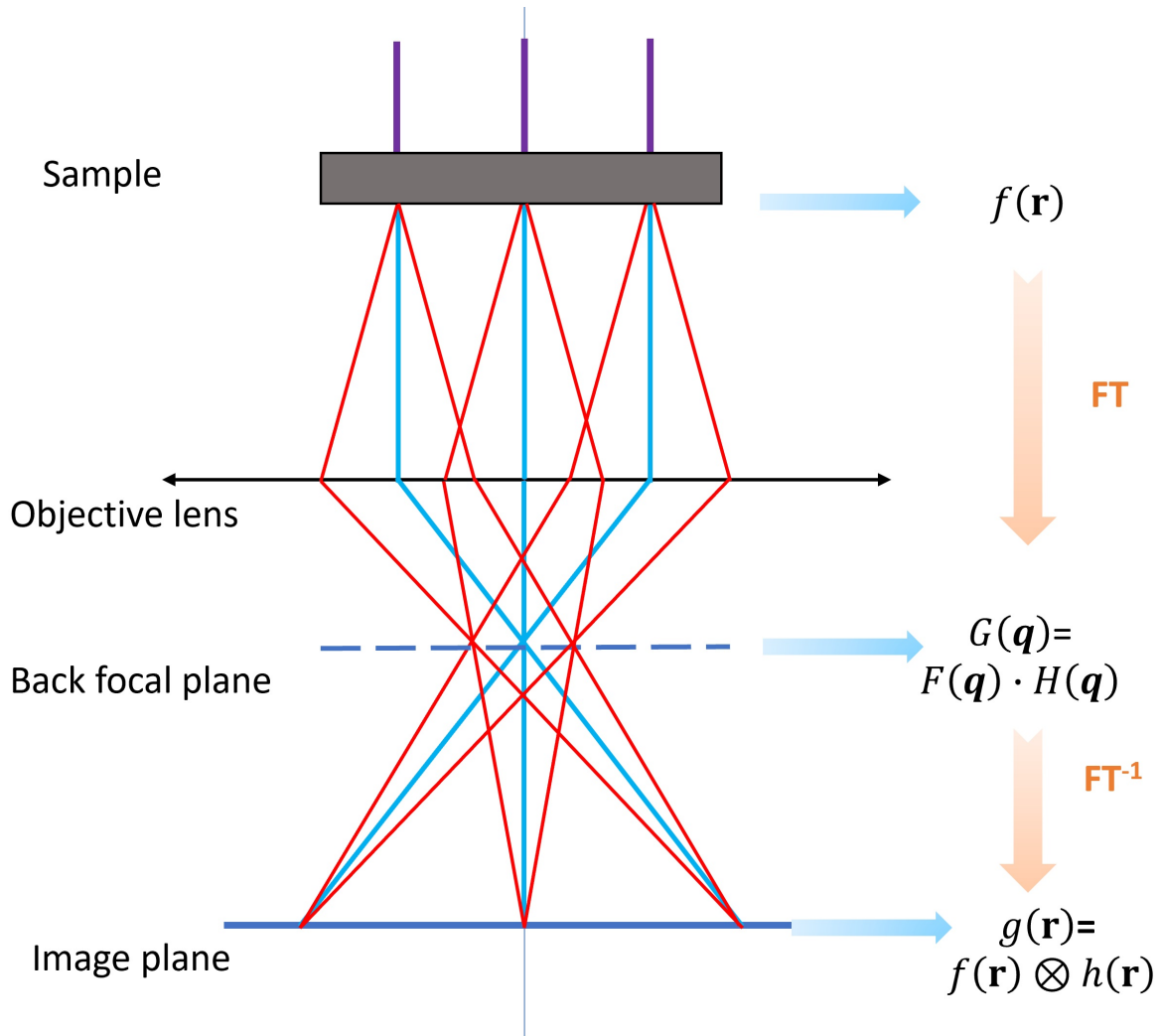


Figure 2-3 Schematic illustration of high-resolution image formation.

The electrons that impinge on the specimen, can be described as plane waves. Those electrons that interact with the electromagnetic fields inside the specimen, contribute to the overall wave function while carrying information about the specimen. During this process, the electron wave experiences a phase shift that depends on the electrostatic potential $V(\mathbf{r})$ in the specimen. The exit plane wave can be expressed as:

$$f(\mathbf{r}) = A(\mathbf{r}) \exp(-i\varphi(\mathbf{r}))$$

$$\varphi(\mathbf{r}) = \frac{\pi}{\lambda E} V(\mathbf{r})$$

In which $A(\mathbf{r})$ represents the amplitude and $\varphi(\mathbf{r})$ is the phase of the electron wave. For a very thin specimen, the amplitude equals 1 and the phase shift $\varphi(\mathbf{r}) \ll 1$, therefore the exit plane wave can be simplified to the equation below, which is called the weak phase object approximation (WPOA).

$$f(\mathbf{r}) = 1 - i\varphi(\mathbf{r})$$

For an ideal microscope, the wave on image plane $g(\mathbf{r})$ is the same as $f(\mathbf{r})$. What is detected and measured by the camera, is the intensity. The intensity on the image plane is $I = f \cdot f^* = 1$, which means that the phase shift of the wave cannot be transferred to the image, and there is no contrast.

For a real microscope, there are aberrations and other instrumental factors affecting the exit plane wave before it reaches the image plane. Therefore, the real image plane wave can be written as:

$$g(\mathbf{r}) = f(\mathbf{r}) \otimes h(\mathbf{r})$$

Where $h(\mathbf{r})$ is called the point spread function or smearing function, which is a characteristic of mainly the objective lens. The formula above means that the image is a convolution of the object with the optics of the objective lens. To get rid of the convolution operator, the formula is often expressed in reciprocal space, by applying a Fourier transformation to both sides of the equation:

$$G(\mathbf{q}) = F(\mathbf{q}) \cdot H(\mathbf{q})$$

Where $G(\mathbf{q})$, $F(\mathbf{q})$, and $H(\mathbf{q})$ are the Fourier transforms of $g(\mathbf{r})$, $f(\mathbf{r})$ and $h(\mathbf{r})$, respectively. \mathbf{q} represents the spatial frequency and has the unit of length^{-1} . $G(\mathbf{q})$ describes the diffraction pattern on back focal plane. $H(\mathbf{q})$ is called the contrast transfer function (CTF), describing how contrast is transferred from the specimen to the image in reciprocal space. $H(\mathbf{q})$ is affected by several factors and can be expressed as:

$$H(\mathbf{q}) = A(\mathbf{q})B(\mathbf{q})E(\mathbf{q})$$

where $A(\mathbf{q})$ is the aperture function and $E(\mathbf{q})$ is the envelope function, describing the effect of insertion of apertures and of the incoherent electron source, respectively. $B(\mathbf{q})$ is called the aberration function which describes the limited optics of the objective lens, and is usually expressed as

$$B(\mathbf{q}) = \exp(-2\pi i\chi(\mathbf{q}))$$

where

$$\chi(\mathbf{q}) = \frac{1}{4}C_s\lambda^3\mathbf{q}^4 + \frac{1}{2}\Delta f\lambda\mathbf{q}^2 + \dots$$

Here $\chi(\mathbf{q})$ is called the phase-distortion function or wave-aberration function. C_s is the spherical aberration and Δf is the defocus. By adjusting these two values, $\chi(\mathbf{q})$ can be controlled and consequently an extra phase shift is multiplied to each component of $G(\mathbf{q})$. Consequently, the intensity measured by the camera is not 1 anymore and the contrast can be appreciated. After calculating the intensity with $I = g \cdot g^*$ the intensity can be found as

$$I = 1 + \frac{2\pi}{\lambda E}V(\mathbf{r}) \otimes \text{Im}(h(\mathbf{r}))$$

This means that in the WPOA, only the imaginary part of $h(\mathbf{r})$ has an effect on I . In reciprocal space, $\text{Im}(H(\mathbf{q})) = A(\mathbf{q})E(\mathbf{q})\sin\chi(\mathbf{q})$, and a new function is then defined as

$$T(\mathbf{q}) = A(\mathbf{q})E(\mathbf{q})2\sin\chi(\mathbf{q})$$

where $T(\mathbf{q})$ is called the phase contrast transfer function (PCTF), sometimes also called CTF because there is no amplitude contribution. $T(\mathbf{q})$ is a characteristic of the microscope, acting as a filter in reciprocal space. The PCTF realizes the translation from phase to amplitude modulation, resulting in phase contrast.

Due to the sine component, $T(\mathbf{q})$ oscillates around 0. Every time it crosses the \mathbf{q} -axis, contrast also changes between positive and negative. Ideally, the PCTF should be more or less constant over a range of spatial frequencies, thereby providing a uniform transfer of information. By tuning the spherical aberration and defocus value, the PCTF can be adjusted and form a proper condition for imaging. The Scherzer defocus value makes a good compromise between width and value of the PCTF in the 1st band. At a defocus value equal to the Scherzer defocus, the resulting resolution can be expressed as⁵

$$D_{Sch} = 0.66 C_S^{1/4} \lambda^{3/4}$$

2.3 Elemental analysis: EDS

Besides observation of the morphology and crystalline structure, with TEM it is also possible to retrieve elemental or physical information, which is sometimes also referred to as analytical TEM.

The electrons going through the specimen have a probability of kicking out inner-shell electrons of an atom in the sample. These inner-shell electrons are then knocked out and are removed from the atom. Typically, an outer-shell electron will then jump to the vacancy in the inner-shell and occupy the position of the original electron. As a result of this transition, energy is released, and a characteristic X-ray photon is emitted. These X-rays are collected by a detector for elemental analysis. The whole process is illustrated in Figure 2-4.

The characteristic X-ray can be collected for an array of points in the sample in a line profile (1D scan). And when scanning in 2D in HAADF-STEM mode, an X-ray spectrum is collected point by point and after analysis of the X-ray spectrum at every pixel, an elemental 2D map of the various elements is generated. STEM-EDS is often the only way to confirm compositional changes taking place in nanoparticles and nanostructures, and has been frequently used as will also become clear in the following Chapters of this thesis.

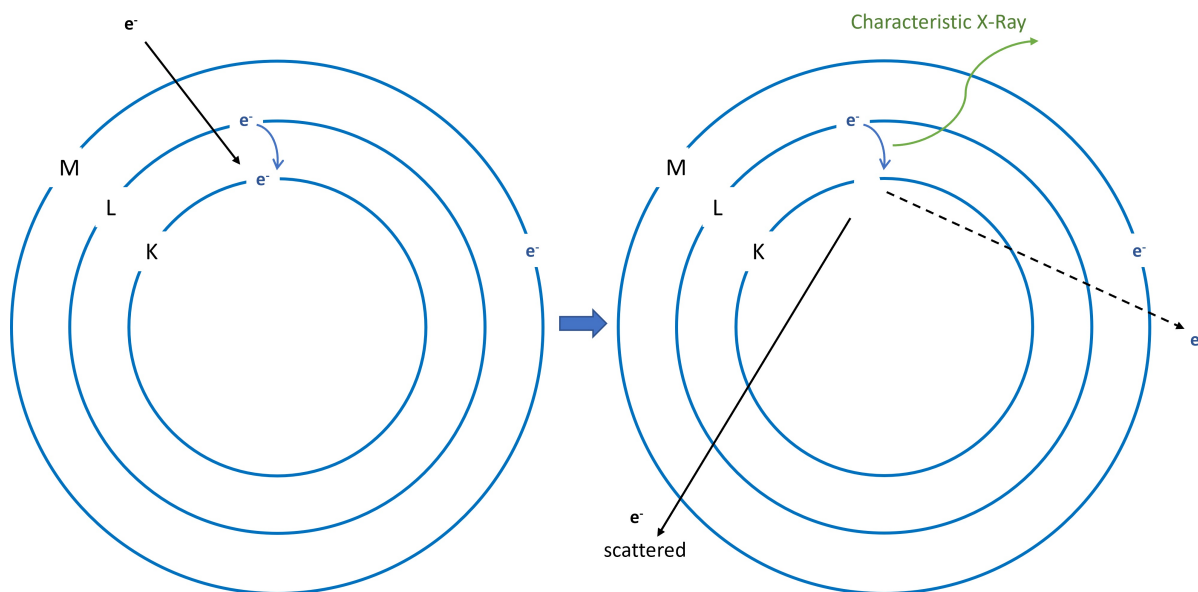


Figure 2-4 The schematic process of X-ray generation onto which EDS analysis is based. One inner-shell electron of a specimen atom is kicked out by a primary electron from the electron beam of the TEM. An electron from the outer-shell, under release of a particular energy, jumps to the inner-shell and occupies the position of the kicked-out electron. A characteristic X-ray is simultaneously released.

2.4 In-situ heating

In-situ TEM is a fast-developing field nowadays, through which the real-time evolution of specimens can be monitored. With in-situ techniques, the properties of NPs in gas, in liquid or in electromagnetic fields can be observed.⁶⁻⁹ The mechanical properties of specimens can also be investigated by applying tensile or shear stress.¹⁰ To investigate thermal behavior and phase transformations at elevated temperatures in a real time, the in-situ heating technique was developed.

The in-situ heating experiments described in this thesis are conducted with a DENSsolutions Wildfire single tilt heating holder mounted with microelectromechanical system (MEMS) chips with heating functionality (shown in Figure 2-5). MEMS-based systems are frequently used for in situ studies that apply heat stimuli to the samples. Different MEMS-based heating holders for in situ TEM investigations have been designed and fabricated in recent years.¹¹⁻¹⁴

By using DENSsolutions MEMS chips, thermal drift caused by thermal expansion of the various components of the holder can be strongly reduced due to lower power dissipation. And a resolution of 100 pm can be achieved with an aberration corrected TEM while heating at 1000 °C. NPs are dropcast on the heating chip which contains windows with Si₃N₄ support membranes of 10-15 nm thickness. The heating takes place by flowing electrical current through an embedded Pt nanowire that is wined like a planar spiral around the viewing windows. The chip is connected with the holder via 4 contact pins. The whole set up is connected to an electronics box and a computer providing accurate control

of the temperature. In the following chapters, different transition metal oxide (TMO) NPs were heated in-situ using this heating holder, enabling morphological changes and structural transformation to be recorded and investigated.

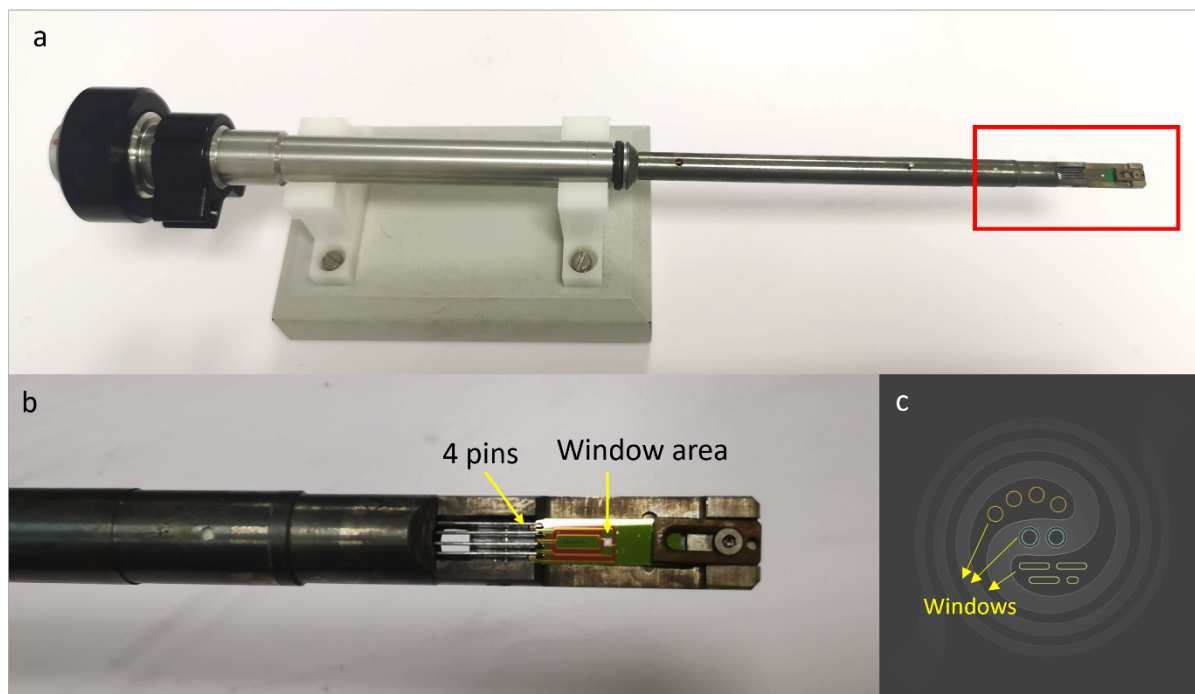


Figure 2-5 (a,b) Photos of DENSsolution Wildfire heating holder with a chip mounted. The chip was connected with holder by 4 pins. (c) Sketch of the window area of heating chip. The windows are marked, and the spiral part are Pt that provide heat to the windows.

2.5 References

- 1 D. B. Williams and C. B. Carter, in *Transmission Electron Microscopy: A Textbook for Materials Science*, Springer, Boston, MA, 2009, pp. 3–22.
- 2 B. Kabius, M. Haider, S. Uhlemann, E. Schwan, K. Urban and H. Rose, *Microsc. Microanal.*, 2001, **7**, 902–903.
- 3 B. Kabius, M. Haider, S. Uhlemann, E. Schwan, K. Urban and H. Rose, in *Journal of Electron Microscopy*, 2002, vol. 51, pp. 51–58.
- 4 B. Kabius, P. Hartel, M. Haider, H. Müller, S. Uhlemann, U. Loebau, J. Zach and H. Rose, *J. Electron Microsc.* (Tokyo), 2009, **58**, 147–155.
- 5 D. B. Williams and C. B. Carter, in *Transmission Electron Microscopy: A Textbook for Materials Science*, Springer, Boston, MA, 2009, pp. 483–509.
- 6 M. L. Taheri, E. A. Stach, I. Arslan, P. A. Crozier, B. C. Kabius, T. LaGrange, A. M. Minor, S. Takeda, M. Tanase, J. B. Wagner and R. Sharma, *Ultramicroscopy*, 2016, **170**, 86–95.
- 7 Z.-H. Xie, Z. Jiang and X. Zhang, *J. Electrochem. Soc.*, 2017, **164**, A2110–A2123.
- 8 F. Wu and N. Yao, *Nano Energy*, 2015, **13**, 735–756.
- 9 C. Zhang, K. L. Firestein, J. F. S. Fernando, D. Siriwardena, J. E. von Treifeldt and D. Golberg, *Adv. Mater.*, 2020, 32, 1904094.
- 10 H. D. Espinosa, R. A. Bernal and T. Filleter, *Small*, 2012, **8**, 3233–3252.
- 11 R. G. Spruit, J. T. van Omme, M. K. Ghatkesar and H. H. P. Garza, *J. Microelectromechanical Syst.*, 2017, **26**, 1165–1182.
- 12 M. Zhang, E. A. Olson, R. D. Twisten, J. G. Wen, L. H. Allen, I. M. Robertson and I. Petrov, *J. Mater. Res.* 2005 207, 2005, **20**, 1802–1807.
- 13 L. Mele, S. Konings, P. Dona, F. Evertz, C. Mitterbauer, P. Faber, R. Schampers and J. R. Jinschek, *Microsc. Res. Tech.*, 2016, **79**, 239–250.
- 14 L. F. Allard, W. C. Bigelow, M. Jose-Yacamán, D. P. Nackashi, J. Damiano and S. E. Mick, *Microsc. Res. Tech.*, 2009, **72**, 208–215.

3. Transformation of Co₃O₄ Nanoparticles to CoO Monitored by In-Situ TEM and Predicted Ferromagnetism at the Co₃O₄/CoO Interface from First Principles

Nanoparticles of Co₃O₄ and CoO are of paramount importance because of their chemical properties propelling their applications in catalysis and battery materials, and because of their intriguing magnetic properties. Here we elucidate the transformation of Co₃O₄ nanoparticles to CoO into nanoscale detail by in-situ heating in the transmission electron microscope (TEM), and we decipher the energetics and magnetic properties of the Co₃O₄/CoO interface from first principles calculations. The transformation was found to start at a temperature of 350 °C, and full conversion of all particles was achieved after heating to 400 °C for 10 minutes. The transformation progressed from the surface to center of the nanoparticles under the formation of dislocations, while the two phases maintained a cube-on-cube orientation relationship. Various possibilities for magnetic ordering were considered in the density functional theory (DFT) calculations and a favorable Co₃O₄/CoO {100}/{100} interface energy of 0.38 Jm⁻² is predicted for the lowest-energy ordering. Remarkably, the DFT calculations revealed a substantial net ferromagnetic moment originating from the interface between the two antiferromagnetic compounds, amounting to approximately 13.9 μB/nm². The transformation was reproduced ex-situ when heating at a temperature of 400 °C in a high vacuum chamber.

Based on:

X. Chen, H. Van Gog and M. A. Van Huis, *J. Mater. Chem. C*, 2021, **9**, 5662–5675.

3.1 Introduction

Co₃O₄ nanocrystals are materials of great importance to many applications. Cobalt oxide nanoparticles and its reduced derivatives are used as catalysts in the well-known Fischer-Tropsch process for the production of hydrocarbon fuels, but are also considered as catalysts for water splitting.¹⁻⁴ Furthermore, cobalt oxide is one of the most frequently used materials in Li-ion batteries^{5,6} powering cell phones and other electronic equipment, and is used in gas sensors⁷ as well. Understanding the reduction process and its mechanism at the nanoscale is essential for controlling the nanoparticle properties in these applications. The reduction of Co₃O₄ under different chemical and physical conditions has been extensively investigated, as will be discussed in more detail below. A two-stage reduction process has been reported by many researchers,⁸⁻¹⁰ where spinel Co₃O₄ first transforms to rock salt CoO and subsequently to elemental Co,



Elemental Co adopts the hexagonal close packed (hcp) crystal structure in the bulk phase, but adopts the face centered cubic (fcc) structure with a lattice parameter of 0.354 nm when the particle size is less than 30 nm.¹¹ The crystal structures of Co₃O₄ and CoO are both cubic and the lattice parameter of Co₃O₄ is approximately twice as large as the lattice parameter of CoO. Figure 3-1 shows their schematic structure. Co₃O₄ has the spinel crystal structure. Cobalt atoms are in the interstices of the distorted fcc lattice of oxygen atoms. Co²⁺ cations occupy tetrahedral interstitial sites and Co³⁺ cations occupy octahedral interstitial sites. In contrast, CoO has a rock salt structure with Co²⁺ cations on one of the interpenetrating fcc sublattices and O²⁻ anions on the other fcc sublattice.

The thermal stability of the Co-O system has been investigated in several ways. The thermodynamic properties of both solid and liquid phases of the Co-O system were calculated by Chen *et al.*¹² In a study employing interatomic potentials obtained by machine learning, Kong *et al.* showed that only CoO and Co₃O₄ are stable compositions in the Co-O system and that the transition between cubic CoO and Co₃O₄ is reversible.¹³ Navrotsky *et al.* calculated phase diagrams for both the bulk Co-O system and the nanoscale Co-O system, and showed that the range where the CoO phase is stable (in terms of partial oxygen pressure and temperature) is considerably narrower for 10-nm sized nanoparticles in comparison to the CoO range of stability in the bulk phase diagram.¹⁴

The reduction processes has been investigated experimentally under a H₂ atmosphere^{4,8,10,15,16} and under plasma exposure.¹⁷ Ward *et al.* observed the reduction using environmental transmission electron microscopy (ETEM) under low hydrogen pressures, and found that Co₃O₄ nanoparticles reduced to CoO predominantly at a temperature of 350 °C at a hydrogen pressure of 0.1 mbar (10 Pa), while formation of pure Co was only observed upon further heating at 450 °C at a higher hydrogen

pressure of 0.3 mbar (30 Pa).¹⁸ Bulavchenko *et al.* investigated the transformation at standard pressure ($1.0 \cdot 10^5$ Pa) using X-ray diffraction (XRD) and reported the two-stage process, but in addition also reported a one-step process where the Co_3O_4 particles could be reduced directly to metallic Co, without intermediate formation of CoO, when the samples were exposed to pure H_2 .⁹ The standard enthalpy of reduction of Co_3O_4 to CoO was reviewed and investigated experimentally by Mayer *et al.*¹⁹ A detailed high-resolution study of the nanoscale structural transformation during heating in vacuum conditions, in the absence of any reducing agents, has not yet been performed, though. The rapidly-developing in-situ transmission electron microscopy (TEM) technique now enables direct observation of phase transformations at atomic resolution,²⁰ which greatly benefits a detailed investigation of the reduction process.

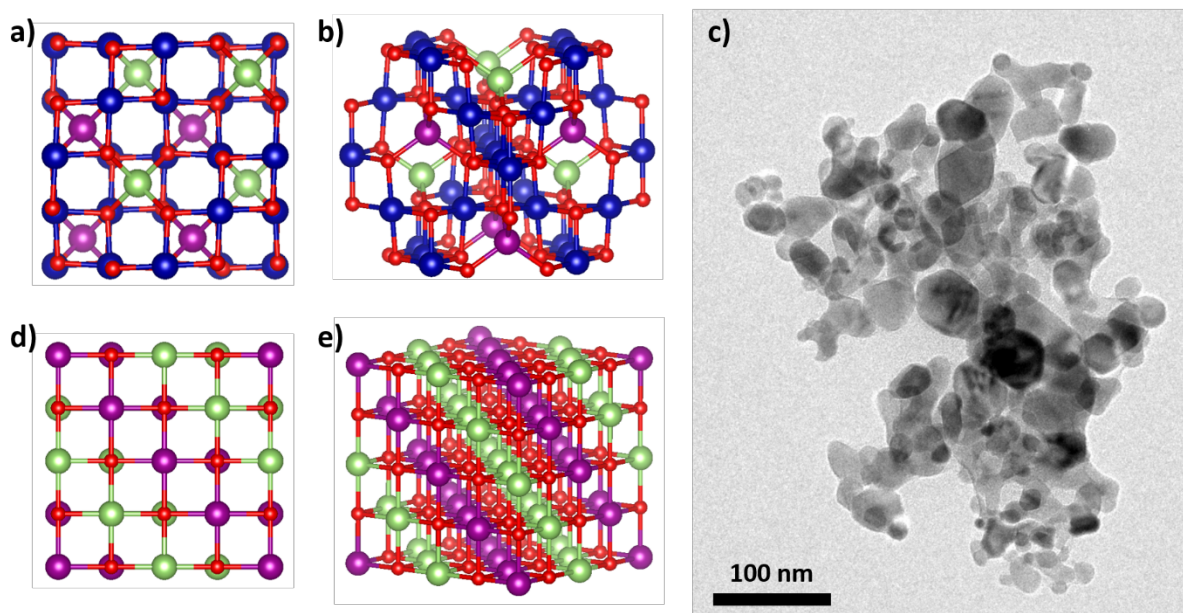


Figure 3-1 (a,b) Crystal structure of spinel Co_3O_4 with antiferromagnetic (AFM) ordering, with a [100] projection shown in (a) and a near-[110] projection shown in (b); c) Bright-field TEM overview image of the pristine Co_3O_4 nanoparticles. (d,e) Crystal structure of rock salt CoO with AFM2 ordering accommodated in a $2 \times 2 \times 2$ supercell, with a [100] projection shown in (d), and a near-[110] projection shown in (e) where the stacking of (111) spin-up Co and (111) spin-down Co atomic planes is clearly seen. Red spheres denote O atoms, and blue, green, and purple atoms denote nonmagnetic Co, spin-up Co, and spin-down Co atoms, respectively.

The Co_3O_4 and CoO phases have also been extensively studied because of their interesting electronic and magnetic structures, which have been the subject of a lively debate in the literature.^{21–25} The rock salt CoO phase undergoes a Jahn-Teller distortion at low temperature, rendering it a monoclinic phase that is still pseudo-rock salt type.²³ The magnetic ground state is antiferromagnetic (AFM), where spins of equal sign are arranged in the cubic (111) planes of Co atoms, and the spin-up/spin-down alternation is along the [111] stacking direction of these Co atomic planes. This AFM type is referred to as AFM2.²² The magnetic moment of the Co^{2+} atoms is approximately $3 \mu_B$ ^{21,22} and the Néel

temperature is $T_N=287$ K.^{21,26} The material is a semiconductor both below and above that temperature; reported values for the band gap are about 2.5–2.7 eV.^{23,27}

In the spinel-type Co₃O₄ phase the trivalent Co³⁺ ions are nonmagnetic while the Co²⁺ ions carry a magnetic moment. At low temperature Co₃O₄ phase antiferromagnetic (AFM) with the Co²⁺ ions following conventional AFM ordering with alternating magnetic moments along the cubic axes (AFM1 ordering). The experimentally determined magnetic moment of the Co²⁺ ions is 3.26 μ_B and the Néel temperature is $T_N=40$ K.²⁴ Co₃O₄ is a semiconductor, with reported values for the band gap varying from 0.74 eV (ref. ²⁵) to 1.5–2.5 eV.^{24,28}

The electronic and magnetic properties of CoO and Co₃O₄ nanoscale particles can differ dramatically from the properties discussed above for CoO and Co₃O₄ bulk compounds. That the Néel temperature of both bulk compounds is below room temperature while our experiments are performed at room temperature, does not necessarily imply that the nanoparticles under investigation in the present study will not be magnetic. In general, due to finite size effects, and surface and interface effects, the magnetization and magnetic anisotropy of nanoparticles can be much larger than the magnetization and magnetic anisotropy of their bulk counterparts, and Curie and Néel temperatures can vary by hundreds of degrees.²⁹ Typically, magnetic nanoparticles consist of only one magnetic domain, which explains their generally higher anisotropy in comparison to multi-domain bulk structures. Furthermore, below a critical size nanoparticles can become superparamagnetic, in which case the atomic magnetic moments in the nanoparticles will be continuously fluctuating when an external magnetic field is absent but respond with high levels of magnetization when an auxiliary magnetic field is applied.²⁹ The magnetic ordering temperature of a nanomaterial is generally lower than the bulk phase value, but this effect can be masked or reversed by crystallographic parameters or composition.²⁹ For CoO and Co₃O₄ nanoparticles, a reduction of the Néel temperature was observed; this reduction has been found to increase with decreasing particle size.^{30–32} At the same time, the literature on CoO and Co₃O₄ nanoparticles reports the observation of net ferromagnetism at room temperature,^{32–35} this net-ferromagnetic effect is generally attributed to surface effects. Room-temperature ferromagnetism has also been reported for Co₃O₄/CoO core/shell particles; in their case, the net-ferromagnetism was attributed to interface effects.³⁶

The experiments performed in this work established that the Co₃O₄ and CoO phases are in a cube-on-cube orientation relationship with respect to each other. We therefore employed density functional theory (DFT) calculations to investigate the {100}/{100} interface between the two phases. This particular interface orientation is observed in Co₃O₄/CoO nanocrystals in the present study, and was also described experimentally by Tung *et al.* in Co₃O₄/CoO core/shell nanocubes.³⁷ Various possible input magnetic configurations were considered for the DFT calculations. The interface energy of the lowest-energy {100}/{100} interface between the Co₃O₄ and CoO phase was calculated. We also aim

to answer the interesting question of whether the overall magnetism and the magnetic ordering changes when the two phases are brought in contact with each other.

In the present study, we first investigate the thermal reduction of Co_3O_4 to CoO nanocrystals experimentally by means of in-situ vacuum heating in the TEM. The transformation was monitored both by real-space imaging and by electron diffraction (ED) to identify the formation of new phases and their crystal structures. The reduction started at a temperature of $350\text{ }^\circ\text{C}$, and full reduction of all particles was achieved at $400\text{ }^\circ\text{C}$. During the transition, the two phases were found to be in a cube-on-cube orientation relationship. Next, the interface between Co_3O_4 and CoO is investigated by means of DFT calculations, to calculate the interface energy of the interface and to study the effect of the interface on the magnetic properties of the multiphase configuration.

3.2 Experimental

3.2.1 Sample preparation and TEM characterization

The Co_3O_4 nanocrystals (NCs) were purchased from Sigma-Aldrich and had a broad size distribution of 5–50 nm as shown in Figure 3-1(c). The Electron Diffraction (ED) and in-situ TEM investigations were conducted using a TFS TalosF200X TEM operating at 200 kV with a point-to-point resolution of approximately 1.1 \AA in bright-field TEM imaging mode. An overview TEM image of the pristine samples is shown in Figure 3-1(c). High-resolution imaging was also conducted with a double aberration corrected TFS Spectra300 TEM, operated at 300 kV and with a point-to-point resolution of 50 pm in TEM mode, on partially transformed particles to show high resolution details of the heterogeneous nanostructures. The TEM specimens were prepared by drop casting the Co_3O_4 solution onto a DENSolutions MEMS heating chip containing electron-transparent 15-nm thick SiN membranes, which we will refer to as the ‘windows’ on the chip.

3.2.2 X-Ray Diffraction (XRD)

The crystal structure of Co_3O_4 in the pristine samples was confirmed by XRD measurements (shown in Figure S 3-1). The XRD was conducted using a PW 1729 Philips diffractometer, equipped with a Co K_α X-ray source (1.79026 \AA). The Co_3O_4 powder was uniformly dispersed on an aluminum substrate for the XRD measurement.

3.2.3 In-situ TEM heating

The heating chips were subsequently mounted on a DENS Solutions single tilt heating holder. The Co_3O_4 nanocrystals were first heated from room temperature to $900\text{ }^\circ\text{C}$ with $50\text{ }^\circ\text{C}$ increments to

monitor their evolution with temperature. It was established that reduction took place at 350–400 °C. The transformation took place everywhere, also in areas on the heating chip that were not previously exposed to the electron beam. A control experiment was also performed where the NCs were heated to 400 °C and then cooled down gradually, to verify that the NCs did not transform into a structure other than CoO rock salt after cooling to room temperature, which was not the case.

3.2.4 Ex-situ heating experiments

Several ex-situ control experiments were performed. Ex-situ heating experiments were conducted in tube furnaces under air flow, N₂ flow, and under vacuum. For these experiments, the complete heating chips with the sample, prepared in the same way as for the in-situ heating experiments, were inserted in the oven. The samples heated under air and under N₂ flow were heated at a rate of 5 °C/min. The samples were kept at 400 °C for 10 minutes and allowed to cool down naturally to room temperature. The samples were also heated with the heating holder in air, and with the heating holder inserted in a high vacuum chamber (Gatan pumping station Model 655), applying the same rate as in the in-situ heating experiments. The pressure in the high vacuum chamber was approximately $1.0 \cdot 10^{-7}$ Torr. After holding the temperature at 400 °C for 10 minutes, the sample was cooled down fast to room temperature and swiftly inserted in the TEM for subsequent analysis.

3.3 Computational Section

Density functional theory calculations (DFT) were employed to study the CoO/Co₃O₄ {100}/{100} interface. First, the CoO and Co₃O₄ bulk phases were calculated separately, to obtain bulk phase reference energies and equilibrium lattice parameters, and to establish the magnetic ground state of the bulk phases. Four multiphase supercells with various magnetic orderings for the constituent bulk phase slabs were then constructed to calculate the interface energy of four different magnetic configurations. A Bader analysis³⁸ was performed to investigate if, and how, the magnetism changes when the two phases are brought into contact.

3.3.1 Computational method

The calculations were performed using the plane-wave VASP code^{39,40} employing the projector augmented wave (PAW) scheme^{41,42} and the generalized gradient approximation (GGA) with the exchange-correlation functional by Perdew, Burke and Ernzerhof (PBE).⁴³ For the bulk phases, the DFT+*U* approach⁴⁴ was considered as well. In the DFT+*U* approach, the Hubbard *U* potential has the effect of lowering the energies of the *d* electron bands and as such compensates for the deficiency of standard DFT in describing strongly correlated systems. The use of hybrid functionals such as HSE06

or PBE0 was not considered as these methods are computationally prohibitively expensive for the large interface supercells considered in this work. The energy cutoff and the density of the k -meshes were tested to ensure energy convergence well within 2 meV/atom. All calculations were performed in reciprocal space as calculations in real space were often found not to converge properly electronically. The required cutoff energy of the wave functions found from the energy convergence tests was 700 eV, which is higher than the energy cutoffs typically reported in the literature (500 to 600 eV). A cutoff energy of 980 eV was used for the augmentation functions. The electronic wave functions were sampled using the Monkhorst and Pack scheme,⁴⁵ on $6\times 6\times 6$ k -grids for both the conventional Co_3O_4 unit cell and the $2\times 2\times 2$ supercell of the conventional CoO unit cell that is required to accommodate the AFM2 magnetic ordering of the latter (see Figure 3-1(d,e)). For the interface supercells, $6\times 6\times 1$ k -grids were used.

All simulation cells were structurally optimized, relaxing atomic positions and lattice parameters, to yield lower-energy configurations. For the ionic relaxation loop, accumulative energy and atomic force convergence criteria of 10^{-5} eV and 0.01 eV/Å, respectively, were applied for the bulk phase calculations; for the interface calculations, accumulative criteria of 10^{-4} eV and 0.01 eV/Å were used. For all calculations, an energy convergence criterium of 10^{-6} eV was set for the electronic convergence loop. For the spin-polarized calculations, the initial magnitude of the magnetic moment was always set to $4 \mu_B$ for the atoms carrying a magnetic moment (*i.e.*, for all Co^{2+} atoms), and to 0 for all other atoms. The magnetic moments were not fixed but allowed to relax (to reduce in magnitude, and even to change in sign) during the electronic self-consistent calculation. The Bader analysis, performed to determine the charge distribution among the atoms and to calculate the magnetic moments on the atoms, was carried out using the approach by Henkelman *et al.*⁴⁶ All calculations are valid for a temperature of 0 K and a pressure of 0 Pa. Zero-point vibration contributions have been neglected. Non-collinear magnetism has not been considered.

3.3.2 CoO and Co_3O_4 reference phases

Most DFT calculations in the literature have been performed using the primitive cells of the cubic phases of CoO and Co_3O_4 , while Dalverny *et al.* performed calculations on the Jahn-Teller distorted monoclinic phase of CoO.²³ In the present work, we performed calculations and parameters testing on the conventional unit cells as these are more representative for the interface supercells we wish to construct. For the CoO phase, input configurations with antiferromagnetic AFM1 and AFM2, ferromagnetic (FM), and nonmagnetic (NM) magnetic orderings were considered. Here, AFM1 represents the alternation of spin-up and spin-down Co (100) planes, whereas AFM2 represents the alternation of spin-up/spin-down Co (111) atomic planes as depicted in Figure 3-1(d,e); we here follow the nomenclature by Deng *et al.*²² For the Co_3O_4 phase, AFM1 (as depicted in Figure 3-1(a,b)), FM, and NM magnetic orderings were considered as input. All configurations were calculated both

with standard DFT, *i.e.*, using the GGA-PBE exchange-correlation functional, and with DFT+*U*. In the literature reporting DFT+*U* results on CoO and Co₃O₄ phases, in general U_{eff} values between 4 and 5 eV are chosen.^{21–25} Here, for our DFT+*U* calculations, we used an identical value of $U_{\text{eff}} = 4.4$ eV for all Co atoms in the two compounds, as we wish not to distinguish between Co²⁺ and Co³⁺ when interfaces are created.

3.3.3 CoO/Co₃O₄ supercells and interface energy

Figure 3-2 shows the interface supercells with the various configurations of the magnetic orderings that were used as input for the calculations. The designation of the magnetic orderings applies to the CoO/Co₃O₄ {100}/{100} interface simulated by a supercell of which the bottom half consists of a 2×2×4 supercell of the conventional CoO unit cell and the top half consists of a 1×1×2 supercell of the conventional Co₃O₄ unit cell, adding up to a total of 240 atoms per interface supercell. Besides a fully nonmagnetic (NM/NM) and a fully ferromagnetic (FM/FM) input configuration, two antiferromagnetic input configurations were considered. In the antiferromagnetic configurations, the interface is formed by a bottom CoO slab that has either AFM1 or AFM2 ordering and a top Co₃O₄ slab that is always AFM1 ordered, which results in the AFM1/AFM1 and AFM2/AFM1 configurations depicted in Figure 3-2(c) and (3-2d,e).

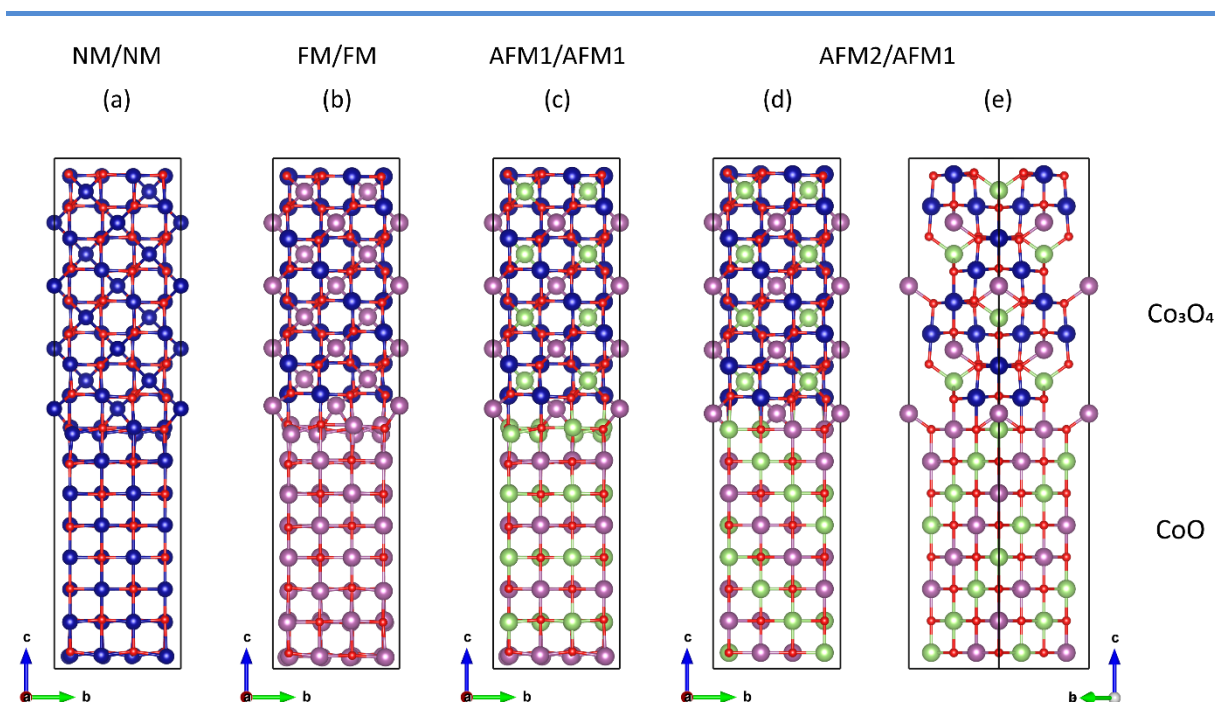


Figure 3-2 Atomic models of the interface supercells with various magnetic orderings. Panels (d) and (e) both illustrate the AFM2/AFM1 configuration, showing a [100] projection in (d) and a $[\bar{1}10]$ projection in (e). Panel (e) is included so that the AFM2 ordering in the CoO phase, *i.e.*, the antiferromagnetic ordering along the $\langle 111 \rangle$ direction, can be nicely seen. Red spheres denote O ions. Blue spheres denote nonmagnetic Co³⁺ ions. Purple and light green spheres denote spin-up Co²⁺ and spin-down Co²⁺ ions, respectively.

After full relaxation of the supercells, the interface energy γ_{int} was calculated for each of the interfaces as:

$$\gamma_{int} = \frac{E_{int}^{super} - n E_{CoO} - m E_{Co_3O_4}}{2 A_{int}} \quad (2)$$

Here, E_{int}^{super} is the energy of the interface supercell; E_{CoO} and $E_{Co_3O_4}$ are the energy of one reference unit cell of CoO and Co₃O₄, respectively; n and m are the number of CoO and Co₃O₄ unit cells in the supercell; and A_{int} is the area of the interface, calculated from the supercell lattice vectors as $A_{int} = |a \times b|$. The factor of 2 in the denominator arises from the fact that due to the periodic boundary conditions that apply to plane-wave DFT calculations, the periodic interface supercells always contain two interfaces.

3.4 Results and Discussion

3.4.1 In-situ and ex-situ TEM investigations

The in-situ heating experiments conducted on the Co₃O₄ NCs were performed as described in the Experimental section. An XRD spectrum confirming the Co₃O₄ phase of the pristine nanosamples can be found in Figure S 3-1 of the SI. First, the particles as dropcasted on the heating chip were heated from room temperature to 900 °C with increments of 50 °C. Bright-field TEM images and selected area electron diffraction (SAED) patterns were recorded at every heating step. Figure 3-3 shows TEM images of the cobalt oxide nanoparticles in two different areas at room temperature, at 400 °C, and at 800 °C. The particles agglomerated at room temperature after drying on the TEM supports. After heating at a temperature of 400 °C, the surfaces of the nanocrystals became uneven and more faceted. This indicates that particular crystallographic facets are preferentially exposed, driven by minimization of total surface energy. As the onset of faceting coincides with the transformation to CoO, which will be become clear from the SAEDs in Figure 3-4, this is possibly caused by CoO NPs having more distinct facet-dependent surface energies than Co₃O₄ NPs. In addition, stronger diffraction contrast also appeared on the particles, which we attribute to the phase transformation to CoO as also evidenced by the SAED results of Figure 3-4 and Figure S 3-2. At 800 °C, the particles coalesced and fused as is clear from the bottom-right panel in Figure 3-3, which corroborates with the results of the SAED patterns showing fewer but stronger peaks at temperatures 600 °C (Figure S 3-2 of the Appendix).

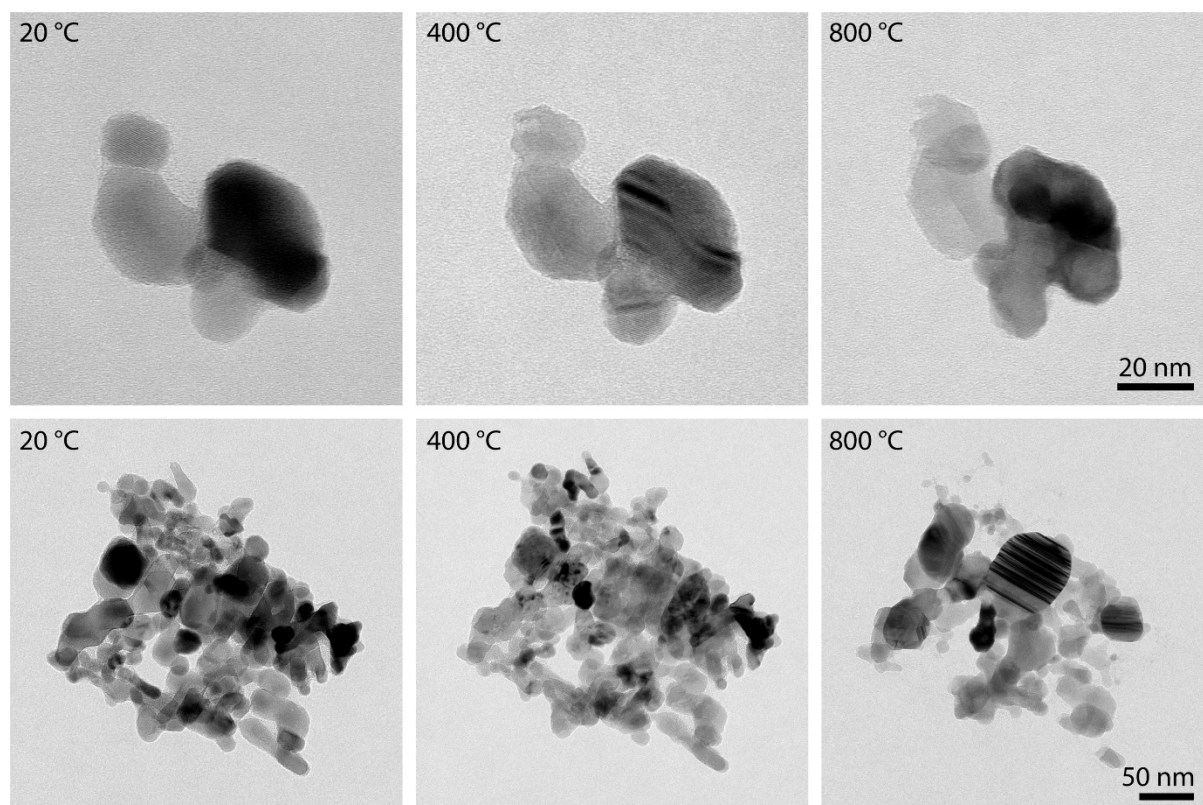


Figure 3-3 Bright-field TEM images of (initially) Co₃O₄ NPs at room temperature, at 400 °C and at 800 °C. The surfaces of the NPs become uneven at 400 °C, while diffraction contrast increases.

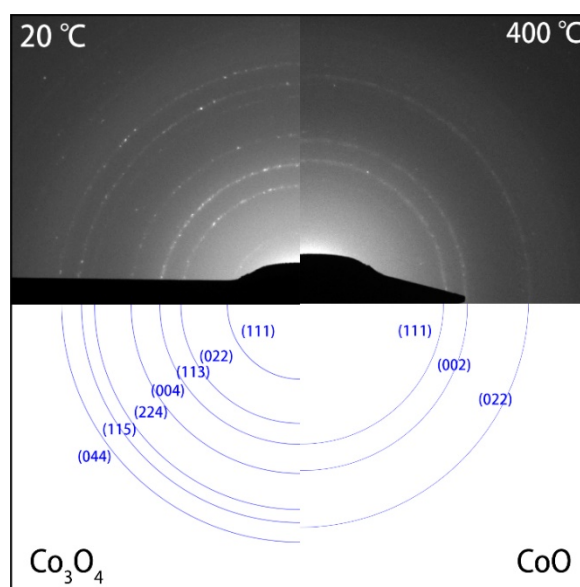


Figure 3-4 SAED patterns of Co₃O₄ NPs before heating at 20 °C (left), and after heating for 10 mins at 400 °C (right). At 20 °C, the diffraction rings in the DP corresponded to the Co₃O₄ phase. After heating at 400 °C, only three rings remained that correspond to the highly symmetric CoO phase. The rings in the experimental SAED patterns (top) are indexed in blue (bottom). Please note that the (hkl) indexing of the diffraction rings refers to reflections at {hkl} families of lattice planes. The complete DPs are shown in Figure S 3-2.

While bright-field TEM imaging provides information about changes in morphology and in size of the NCs, the SAED patterns uniquely identify the crystal structure of the NCs during the heating experiments. Figure S 3-2 of the Appendix shows the diffraction patterns (DPs) recorded during the whole heating process. At room temperature and after heating at temperatures up to 300 °C, the SAED patterns corresponded to the Co_3O_4 crystal structure. Upon annealing at 350 °C, however, the patterns started to change, and after keeping the sample at 400 °C for 10 minutes, only three rings remained that are indicative of the highly symmetric CoO phase.

In Figure 3-4, a comparison is shown between the SAED patterns at 20 °C (left) and at 400 °C (right). The rings in the DPs were indexed and found to correspond to the Co_3O_4 phase and to the CoO phase, respectively. Table S 3-2 shows the corresponding lattice spacings of the rings in both diffraction patterns. Figure S 3-3 shows the integrated DPs at 20 °C, 350 °C, 400 °C and 400 °C after 10 minutes, from which could show the transformation clearer. From 350 °C onwards, peaks corresponding Co_3O_4 started to disappear or became weaker, whereas a new peak corresponding to the (002) reflection of CoO appeared. Finally at 400 °C, only peaks corresponding to CoO were found, indicating that the transformation of the NPs was complete. Clearly, the SAED patterns show that the transformation to CoO took place from 350 °C onwards and was completed after heating to 400 °C for 10 minutes. Above 400 °C, the rings in the DPs did not change any more, indicating no further reduction. From 600 °C onwards, there are fewer spots on the rings due to coalescence and alignment of the nanocrystals, which consequently became larger and fewer in number.

Four ex-situ reference experiments were conducted for comparison with the in-situ heating experiments. Ex-situ heating was conducted in a tube oven in air (1), in a tube oven under N_2 flow (2), using the heating holder while kept in ambient air outside the TEM (3), and using the heating holder in a high vacuum chamber (4). The results are shown in Figure S 3-4. The SAED patterns after heating in the vacuum chamber clearly indicate the CoO structure, showing that the phase transformation to CoO also took place ex-situ under low pressure conditions. The SAED patterns after heating under standard pressure and under N_2 flow still show the Co_3O_4 structure, i.e., the transformation did not take place under these ex-situ conditions, which implies that the transformation from Co_3O_4 to CoO requires a very low partial oxygen pressure. The cooling processes in the microscope is typically much faster than in regular furnaces, so that high-temperature phases might be quenched to room temperature. As an additional control experiment, the NCs were also heated in-situ from 20 °C to 400 °C (transforming completely to CoO) and subsequently cooled down very slowly to verify that no other structures than CoO are formed during cooling down. The resulting SAEDs are shown in Figure S 3-5. Both diffraction patterns show a CoO rocksalt crystal structure. High resolution TEM images (shown in Figure S 3-6) also show that the particles remain in the CoO phase after heating and cooling down. Consequently, the transformation to CoO that is observed in-situ must

be caused by the combination of elevated temperature and the very low partial oxygen pressure under vacuum conditions.

The results of the ex-situ experiments conducted in air and under nitrogen flow are in good agreement with the Co-O phase diagrams that Navrotsky et al. calculated for bulk and nanoscale cobalt oxide.¹⁴ For 10 nm sized anhydrous Co₃O₄ nanoparticles, these authors predicted that the partial oxygen pressure needs to be extremely low ($(p(\text{O}_2)/1 \text{ atm}) < 10^{-20}$) for reduction to take place at a temperature of 650 K (~350 °C). Consequently, during conditions of annealing ex-situ at standard pressure either in air or under (not 100% pure) nitrogen flow, the partial oxygen pressure will not be sufficiently low for the Co₃O₄ NPs to be reduced. The transformation was observed, though, during heating in the in-situ experiments and when heating ex-situ in the high vacuum chamber. Unfortunately, the partial oxygen pressure in these high vacuum environments is not known but it will be considerably lower than the total pressure in the column of the TEM and in the vacuum chamber, which is approximately $1.0 \cdot 10^{-5}$ Pa. Therefore, the total partial pressure (with respect to atmospheric pressure) is $1.0 \cdot 10^{-10}$ and the partial oxygen pressure will be even considerably lower. The thermodynamic modelling as performed by Navrotsky et al. is only valid for systems in equilibrium, though. From a thermodynamic point of view, vacuum annealing in-situ in the TEM or in a high vacuum chamber is always an out-of-equilibrium condition as oxygen molecules are continuously removed from the system through the work done by the vacuum pumps, thereby driving the dissociation from Co₃O₄ to CoO; there is no equilibrium with any gas. For a thermodynamic assessment of the reduction reaction in equilibrium conditions, we refer to the excellent review by Mayer et al.¹⁹ and to the work of Navrotsky *et al.* who also incorporated nanosize effects.¹⁴

In Figure 3-5, high-resolution TEM (HRTEM) images of a particle at room temperature and at 350 °C are shown, revealing details of the phase transformation. In Figure 3-5(a), the particle is single crystalline being observed in a [013]-zone axis at room temperature. At 350 °C (Figure 3-5(b) and (c)), multiple smaller areas displaying a different contrast appeared on the particle, which indicates that the particle was no longer single crystalline at this temperature. The inset images show the Fast Fourier Transforms (FFTs) of the corresponding smaller areas. The FFT images in Figure 3-5 (b) and (c) show that at 350 °C the central area of this particle is still in Co₃O₄ phase while the surface area has transformed to CoO. The area marked by the green square in Figure 3-5(b) displays the CoO phase while the white area contains both Co₃O₄ and CoO phases. However, the white square area transformed to CoO after a few minutes of continued annealing (shown in Figure 3-5 (c)), which means that the relative fraction of CoO phase increased during heating., while the area marked with the yellow square in Figure 3-5 (c) was still in the Co₃O₄ phase, indicating that the transformation had not proceeded yet into the most central area of the particle. Figure 3-5 also shows that at 350 °C the spots corresponding to the (200) fringes of CoO are crystallographically aligned with the (400) fringes

of Co_3O_4 . This reveals that during the transformation, there is a cube-on-cube orientation relationship between the Co_3O_4 parent nanocrystal and the Co product nanocrystals.

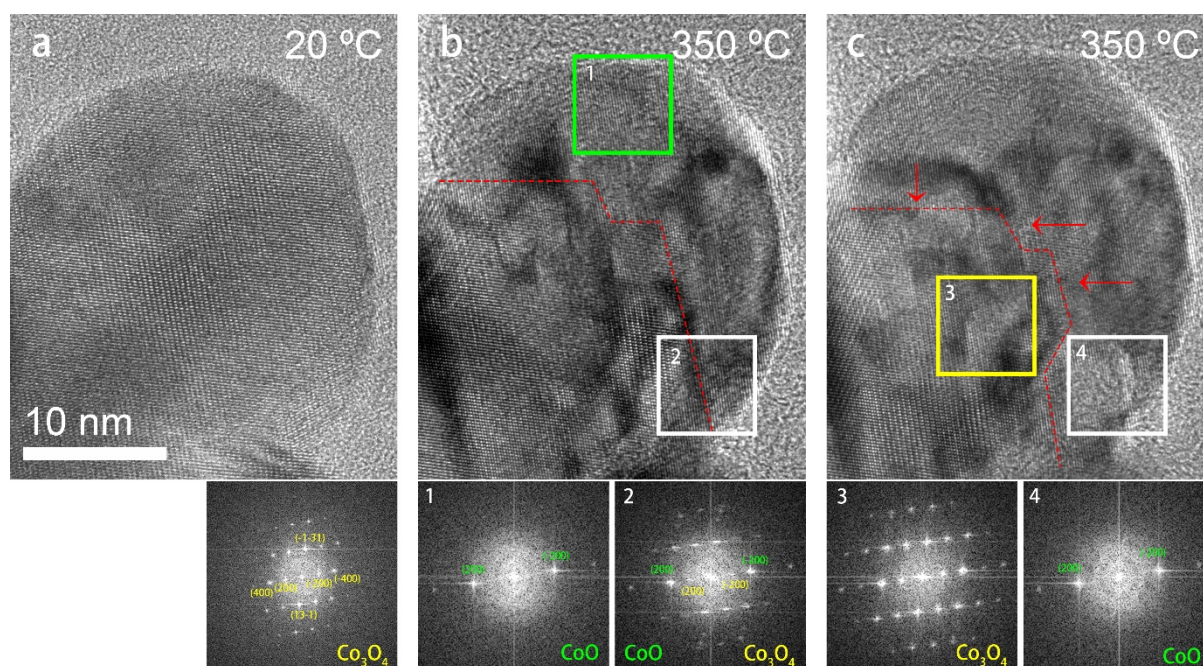


Figure 3-5 HRTEM images of a particle imaged in a $[01\bar{1}3]$ projection at a temperature of (a) $20\text{ }^\circ\text{C}$; (b) and (c) $350\text{ }^\circ\text{C}$. (c) was taken after (b) a few minutes later. The inset panels are the FFT pattern of the corresponding areas marked in the figure. The spots in FFT were indexed and showing the corresponding lattice planes. The planes written in green belong to the CoO phase and the yellow ones belong to the Co_3O_4 phase. The red dashed lines marked the interfaces between two phases. The $\text{Co}_3\text{O}_4/\text{CoO}$ interfaces moved inwards from the surface to the center of the nanoparticle.

In Figure 3-6, aberration-corrected TEM (AC-TEM) images are shown of a particle that had partially transformed to CoO, where the particle is imaged in a $[001]$ projection. The image was taken after swiftly cooling down from $400\text{ }^\circ\text{C}$ to room temperature. Figure 3-6(c) and 6(d) are FFT patterns indicating a central area (c) that is still in the Co_3O_4 phase and an area at the edge (d) that has transformed into the CoO phase, respectively. The two phases are in a cube-on-cube orientation relationship, in good agreement with the results shown in Figure 3-5. Figure 3-6 (b) shows a magnified HRTEM image of the central area of the particle (marked by the white square in panel (a)), with the Co_3O_4 phase at the left hand side and the CoO phase at the right hand side. Atomic overlays have been drawn to indicate the atomic structures. At the right hand side, the atomic columns match the CoO structure well. Very distinctively, in the Co_3O_4 part of the structure there are additional columns of atoms standing out that are generating a ‘diagonal’ pattern that is rotated 45° with respect to the cubic CoO structure. These atomic columns are the Co^{2+} ions in Co_3O_4 . The inset in Figure 3-6(b) shows a simulated image of Co_3O_4 (using QSTEM, for a thickness of 71.3 \AA and a defocus value of 10 nm) where this feature is very strong, which confirms the presence of the Co_3O_4 structure in the central areas of the partially transformed nanoparticles. Due to changes in thickness, and

possibly some mistilt, the contrast of the Co₃O₄ part in the images varies to some extent and the interfaces between both phases is not atomically sharp. This may also be caused by the fact that the TEM images are a projection of a 3D structure, while many of these particles display a core-shell structure (with a Co₃O₄ core and a CoO shell), so that in projection the central part is in fact a superposition of both phases including interfaces between them. Both {100}/{100} and {110}/{110} interfaces can be distinguished where the transition seems to be gradual. An additional HRTEM image of another particle, showing very similar features, is shown in Figure S 3-7 of the Appendix.

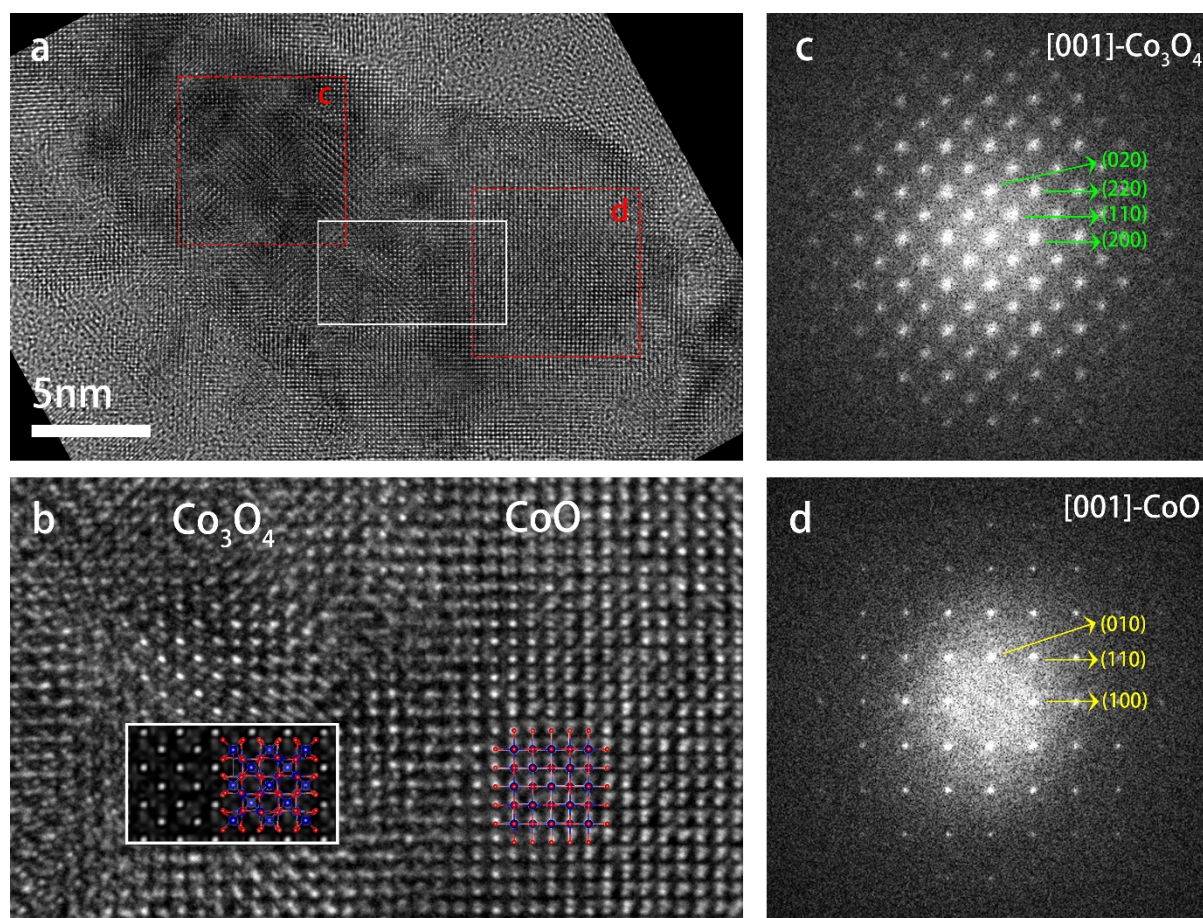


Figure 3-6 HRTEM images of a partially transformed particle. (a) Overview of the particle, the exterior and right hand side of the particle is in the CoO phase while the central part is still in Co₃O₄ phase. (b) Magnified image of the area marked by white square in (a). The inset figure is a QSTEM simulated image of Co₃O₄. Atomic overlays indicate the Co₃O₄ (left) and the CoO (right) crystal structures. (c) and (d) FFT patterns of the corresponding areas marked (a), indicating the Co₃O₄ and CoO structures, respectively.

In Figure 3-7, HRTEM images of a larger nanoparticle are shown. At room temperature, spots corresponding to Co₃O₄(220)-lattice fringes can be clearly observed in the TEM image (panel (a)) and the corresponding FFT pattern (panel (d)). After heating to 400 °C, spots corresponding to (331) lattice fringes appeared, and new pairs of spots also appeared that are very close to the Co₃O₄(440) spots, but deviating by a small tilt angle and having a slightly smaller k-spacing. These pairs of spots

correspond to the {220} lattice fringes of CoO, which implies that the surface layer of the particle was reduced to CoO, and that this layer is slightly tilted with respect to the Co_3O_4 crystal lattice at the interior of the NP. Similarly small misfits between the two phases were reported by Ward *et al.*,¹⁸ who studied reduction of Co_3O_4 nanoparticles in a chemically reducing H_2 atmosphere. Combining the result of Figure 3-5 and Figure 3-6, both phases are observed from 350 °C to 400 °C, which is in good agreement of the result of DPs. This means the transformation started from 350 °C onwards, and progressed inwards from the surface to the center of the particles until complete conversion is achieved at 400 °C.

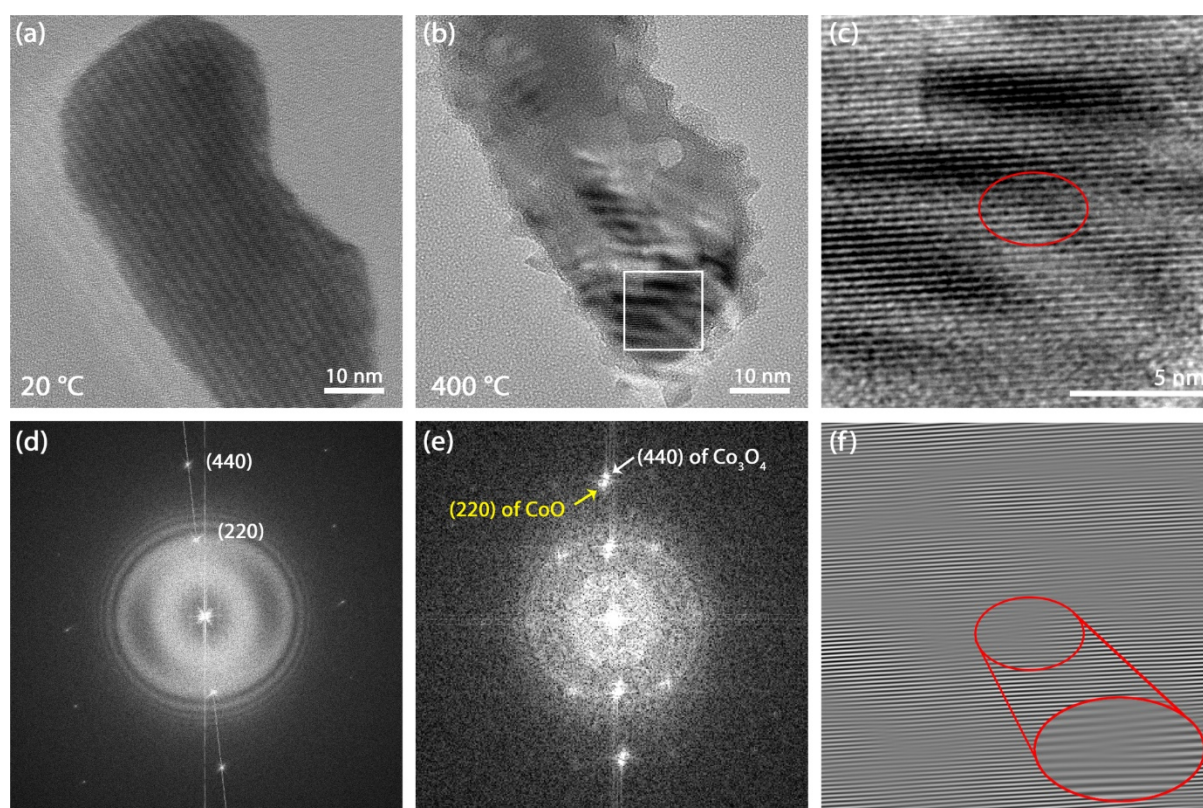


Figure 3-7 HRTEM images of a particle at (a) 20°C and (b) 400 °C. (c) Magnified image of the area marked in (b); (d) and (e) are the FFTs of (a) and (c), respectively; (f) Inverse FFT image of the (220)-spots in (e). The inset at the bottom-right shows an enlarged view of the dislocation at the center of panel (f).

A moiré pattern also appears at the bottom part of the particle, shown in Figure 3-7(b), which confirms the multi-layer structure. Figure 3-7(f) shows the inverse FFT image of a mask applied around the (220) spots of CoO in Figure 3-7(e), showing that dislocations are formed during the reduction. In Figure 3-7(b), some voids displaying bright contrast appeared on the particle, which was single crystalline at room temperature before heating. The dislocations and voids are likely formed

due to release of oxygen atoms during the reconstruction of the Co₃O₄ structure into the CoO structure. The dissociation reaction can be written as



The oxygen sublattices of Co₃O₄ and CoO are nearly identical, both being fcc sublattices and having a very commensurate lattice parameter (Figure 3-1). As 25% of the O atoms are released during reduction, the oxygen sublattice and therefore the volume of the nanoparticle itself has to reduce by about 25% (the positioning and occupation of the Co atoms in the lattices is not limiting their volume). If the shrinkage of the nanoparticle does not proceed fast enough to match the release of oxygen atoms and molecules, the formation of voids and dislocations can be expected.

3.4.2 DFT study of the CoO/Co₃O₄ interface

Density functional theory (DFT) calculations were conducted on CoO and Co₃O₄ reference bulk phase unit cells and on CoO/Co₃O₄ interface supercells, as described in the Computational Details section. To investigate the performance of the DFT (PBE) and DFT+*U* (PBE+*U*) methods considered in this study in describing the CoO and Co₃O₄ phases, the unit cells of these phases were calculated both with DFT and DFT+*U*. Table 3-1 summarizes the obtained lattice parameters and band gaps, and the relative energetic stability of the various magnetic geometries. As expected, the Hubbard *U* correction leads to increased band gap values, and even opened up band gaps for the AFM1 and FM CoO configurations, making these configurations no longer metallic and half-metallic as predicted by PBE but semiconducting instead. Surprisingly, it was found that DFT+*U* incorrectly predicts the magnetic ground state (MGS) of CoO to be AFM1 rather than AFM2. The deviation of our results from earlier DFT+*U* findings in this regard may be related to the higher (and presumably more accurate) energy cutoff used in this work, and to the fact that we performed our calculations on conventional unit cells rather than on the primitive cells. Standard DFT did predict AFM2 to be the lowest-energy phase of CoO, in agreement with experiment. Both DFT and DFT+*U* correctly predict the MGS of Co₃O₄ to be AFM1, although in these cases the ferromagnetic (FM) solution was found to be only slightly less favorable than AFM1. In a combined theoretical and experimental study by Qiao *et al.*, who investigated the electronic structure of Co₃O₄ with DFT calculations for a range of *U*_{eff} parameters for both Co²⁺ and Co³⁺ ions, it was shown that DFT+*U* leads to a severe distortion of the top of the valence band in Co₃O₄ due to strong downward bending of the band edge corresponding to Co³⁺ 3*d* orbitals,²⁵ which makes a sensible prediction of the electronic band gap cumbersome. The authors of that study found from their experiments that the fundamental band gap of Co₃O₄ is substantially lower (0.74 eV) than typically reported (1.5-2.5 eV), and concluded from their DFT calculations that standard GGA-PBE without *U* correction is best capable of describing the electronic structure of Co₃O₄.²⁵

Table 3-1 DFT results for the CoO and Co₃O₄ reference bulk phases. Calculated total energies are given relative to the calculated total energy of the energetically most favorable magnetic ordering for each compound; for this, DFT (PBE) and DFT+*U* (PBE+*U*) are considered separately. The AFM1 and AFM2 orderings of Co₃O₄ are identical due to the structure of the Co²⁺ sublattice. The lattice parameter of Co₃O₄ is divided by 2 to allow direct comparison with the lattice parameter of CoO. In the band gap column, ‘M’ stands for ‘metallic’ and ‘HM’ for ‘half-metallic’; the band gap listed for the latter is the band gap found for the spin-up electrons.

Method	Magnetism and ordering	Relative energy (meV/atom)		Lattice parameter (Å)		Band gap (eV)	
		CoO	Co ₃ O ₄	CoO	Co ₃ O ₄	CoO	Co ₃ O ₄
DFT	AFM2	0	—	4.218	4.043	0.52	—
	AFM1	113	0	4.223	4.043	M	0.31
	FM	75	4	4.247	4.046	HM: 1.08	0.16
	NM	257	95	4.101	4.014	M	M
DFT+ <i>U</i>	AFM2	345	—	4.246	4.068	1.57	—
	AFM1	0	0	4.295	4.068	0.91	2.14
	FM	435	1	4.241	4.069	2.02	2.16
	NM	857	481	4.088	4.009	M	M

In the present work we are particularly interested in a sufficiently reliable calculation of the total energies for calculating the interface energy between the two phases, and a reliable prediction of the magnetism at the interface. Considering the misidentification of the magnetic ground state for CoO and the distortion of the VB of Co₃O₄ when using DFT+*U*, there are no good reasons to choose DFT+*U* for the present study, and we performed the interface calculations using standard DFT only. For the (lowest-energy) AFM2 CoO and AFM1 Co₃O₄ phases, Table 3-2 summarizes the electric charges and magnetic moments on the Co²⁺, Co³⁺, and O²⁻ atoms, as obtained from standard DFT and Bader volume analysis. Values obtained for the magnetic moments are $\pm 2.30 \mu_B$ for the Co²⁺ ions in Co₃O₄ and $\pm 2.42 \mu_B$ for the Co²⁺ ions in CoO, in agreement with previously reported values in the literature.^{22,24}

Table 3-2 Calculated properties for the lowest-energy phases of CoO and Co₃O₄ (using GGA-PBE): magnetic ground state (MGS), lattice parameter a_0 (the lattice parameter of Co₃O₄ is divided by 2 to allow direct comparison with the lattice parameter of CoO), net magnetic moment M per unit cell, and Bader volume evaluated atomic electric charge q and magnetic moment m .

	a_0 (Å)	MGS	M (μ_B)	q (e)			m (μ_B)		
				Co ²⁺	Co ³⁺	O ²⁻	Co ²⁺	Co ³⁺	O ²⁻
CoO	4.218	AFM2	0.000	+1.31	—	-1.31	± 2.42	—	0.00
Co ₃ O ₄	4.043	AFM1	0.000	+1.33	+1.44	-1.05	± 2.30	0.00	± 0.07

Table 3-3 Results of the DFT calculations conducted on the {100}/{100} CoO/Co₃O₄ interface. The interface designation refers to the various magnetic and nonmagnetic input configurations depicted in Figure 3-2. For each interface, the total energy E_0 with respect to the energy of the lowest-energy supercell, the calculated interfacial area A_{int} , the surface energy γ_{int} according to Eq. (2), and the total net magnetic moment M of the supercell, are given. The lattice mismatch refers to the mismatch between the commensurate lattice parameters of the two separate bulk phases (Table 3-1) in the plane of the interface. All interface supercells contain the same number of atoms.

Interface	E_0 (eV)	A_{int} (Å ²)	γ_{int} (eV/Å ²)	γ_{int} (J/m ²)	M (μ _B)	mismatch (%)
AFM2/AFM1	0.00	67.84	0.024	0.38	18.9	4.2
AFM1/AFM1	3.11	63.58	0.050	0.80	6.5	4.4
FM/FM	2.76	63.87	0.047	0.75	158.9	4.8
NM/NM	26.70	62.78	0.239	3.82	0.0	2.1

Next, the four interface supercells with the magnetic ordering shown in Figure 3-2 were fully relaxed. The interface energy of the various interfaces was calculated according to Eq. (2) and using the energetically most favorable (AFM2) CoO and (AFM1) Co₃O₄ phases as obtained from the bulk phase unit cell calculations as reference phases. Table 3-3 provides the calculated interface energies and the net magnetic moments of the supercells. The precise supercells dimensions of the obtained output configurations are provided in Table S 3-1 of the Appendix.

The atomic output configurations are shown in Figure 3-8 and in Figure S 3-8 of the ESI. The atomic models are overlaid with isosurfaces of the spin-polarization density, where yellow represents excess spin-up electron density and blue represents excess spin-down electron density. Graphs with an analysis of the Bader evaluated electric charges and magnetic moments on the atoms in the interface supercells are included as well. In Figure 3-8 (a), the first notable observation is that the magnetic ordering of the AFM2/AFM1 supercell at both sides of the interface is distorted. The (bottom) CoO slab of the supercell indeed displays an AFM2 ordering, and the (top) Co₃O₄ slab an AFM1 ordering; there are, however, clearly a number of Co²⁺ atoms whose magnetic moment changed sign during relaxation (excess spin-up electron density becoming excess spin-down electron density for these atoms, and vice versa), as indicated with black circles in Figure 3-8 (a). This can easily be seen by comparing with the input magnetic ordering displayed in Figure 3-2 (d,e). Remarkably, these atoms with flipped magnetic moments are found not only close to the interface, but also quite far away (at distances of up to 4 atomic layers) from the interface.

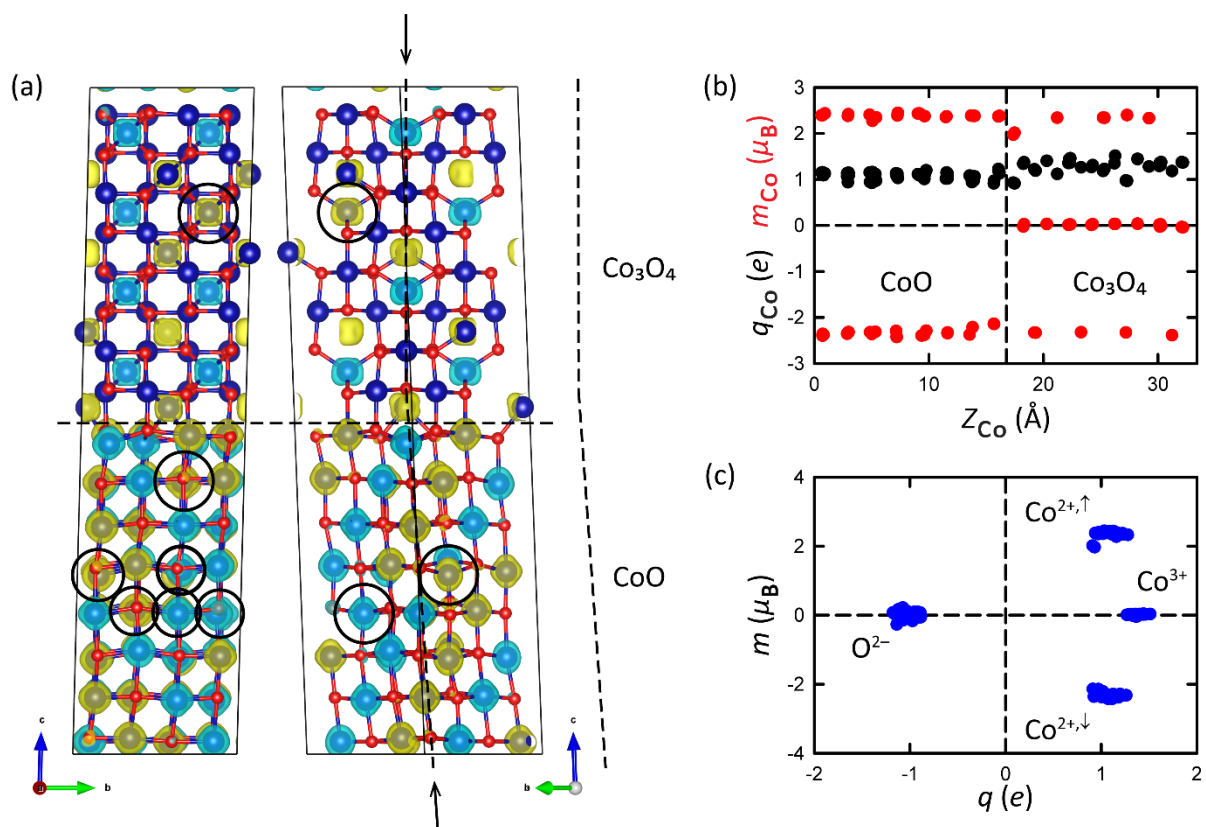


Figure 3-8 (a) Atomic output configuration of the lowest-energy CoO/Co₃O₄ interface as obtained after full relaxation of the AFM2/AFM1 supercell, shown in [100] (left) and $[\bar{1}10]$ (right) projection, with Co atoms represented in blue and O atoms in red, and a horizontal dashed line indicating the interface at $Z_{rel} \approx 1/2$. The atomic structures are overlaid with the spin-polarization density, where yellow colored isosurfaces indicate excess spin-up electron density and blue colored isosurfaces indicate excess spin-down electron density (isosurface levels are $\pm 0.24 e/\text{\AA}^3$). Black circles indicate distortions in the AFM2 and AFM1 magnetic ordering. The supercell is skewed under the influence of the AFM2 ordering in CoO; the mistilt between the crystal lattices is indicated by black arrows and also illustrated at the right-hand side of (a). (b) Charges (black dots) and magnetic moments (red dots) on the Co atoms plotted as a function of Z-coordinate (height in the supercell). The vertical dashed line indicates the interface at $Z_{rel} \approx 1/2$. (c) Correlation between the charge and magnetic moments on the Co and O atoms.

As can be seen from Table 3-3, the AFM2/AFM1 ordered input configuration resulted in the energetically most favorable interface configuration; *i.e.*, the two bulk components forming the interface, preferably follow the same magnetic ordering as the separate bulk phases. In absolute terms, the interface energy of 0.38 J/m^2 is quite favorable, in particular considering the 4.2% lattice mismatch. The NM/NM interface, with the highest total energy and an interface energy of 3.82 J/m^2 , is clearly unfavorable, despite the lower lattice mismatch of 2.1%; the higher energy difference is caused by the fact that here the structure is forced to be nonmagnetic while magnetic solutions are preferred. Figure 3-8(a) shows the atomic output configuration for the (lowest-energy) AFM2/AFM1

interface supercell. The output configurations of all interface supercells can be found in Figure S 3-8 of the ESI. The charges and magnetic moments on the Co atoms in the relaxed AFM2/AFM1 supercell are shown in Figure 3-8 (b), where they are plotted as a function of the *Z*-coordinate (height in the supercell). Figure S 3-8(d) includes the charges and magnetic moments on the O atoms. The correlation between the charges on the atoms and their magnetic moments is nicely visualized in Figure 3-8(c). Clearly, the CoO phase only contains Co²⁺ ions with either positive or negative magnetic moments, whereas the Co₃O₄ phase also contains nonmagnetic Co³⁺ ions (Figure 3-8(b)). The charges and the magnetic moments on the atoms in the supercell in general follow the same trend as the charges and magnetic moments obtained for the atoms in the CoO and Co₃O₄ bulk phase compounds (Table 3-2). As can be seen from Figure 3-8(c), the nonmagnetic Co³⁺ ions have a somewhat higher positive charge of +1.38*e* in comparison to the Co²⁺ ions, which carry an (either spin-up or spin-down) magnetic moment of ±2.34 μ_B and have Bader charges of +1.09*e* (all averaged values; the Co²⁺ atoms with upward magnetic moments actually have an averaged magnetic moment that is slightly larger, namely +2.37 μ_B, than the corresponding value for the magnetically downwardly orientated Co²⁺ atoms, which was found to be −2.31 μ_B on average). There is one Co layer (the Co layer closest to the interface at *Z*_{rel} ≈ 1/2, in the Co₃O₄ component of the supercell) where the Co²⁺ ions have slightly smaller magnetic moments and Bader charges of +1.99 μ_B and +0.92*e*. For the Co²⁺ atoms of which the magnetic moment changed sign during relaxation, slightly larger values of the magnetic moment were found, of +2.42 μ_B on average, at Bader charges of +1.05*e*.

The constituting bulk phases of the AFM2/AFM1 supercell are both AFM-type with zero net magnetic moment (Table 3-2). Remarkably, the formation of the interface leads to a substantial net ferromagnetic moment of 18.9 μ_B over the entire AFM2/AFM1 supercell (Table 3-3). The supercell as a whole is therefore ferrimagnetic. The net ferromagnetic moment that arises from the formation of the interface between the two antiferromagnetic compounds can for the largest part be retraced to the flipping of magnetic moments of Co²⁺ atoms at both sides of the interface. In total 9 ions changed the sign of their magnetic moment, 6 upwardly and 3 downwardly: in the (bottom) CoO slab, 3 Co²⁺ ions changed the sign of their magnetic moment from up to down, and 5 changed their sign from down to up; and in the (top) Co₃O₄ slab, one Co²⁺ ion changed its sign from down to up. The resulting net contribution of these atoms to the magnetization of the supercell amounts to the equivalence of 3 of their upwardly orientated atomic magnetic moments, and is accompanied by a net contribution of an equal number of (unflipped) atomic magnetic moments from the Co²⁺ sublattice, where the upwardly orientated magnetic moments of three Co²⁺ atoms due to the flipping are now no longer matched and counterbalanced by originally downwardly orientated but now flipped magnetic moments. The contribution to the net magnetic moment of the entire supercell due to the flipping of magnetic moments can therefore be estimated to be 3 × (2.42 + 2.37) = 14.4 μ_B. A smaller part (2.0 μ_B) of the magnetization of the supercell is caused by the difference in magnetic moment between the spin-up

and spin-down Co^{2+} atoms. Note that the two Co^{2+} atoms at the interface with the smaller magnetic moments will lower the magnetization (their contribution to the net magnetization of the supercell is $-0.6 \mu_{\text{B}}$). The remainder of the supercell magnetization stems from low levels of spin-polarization at the nonmagnetic O^{2-} and Co^{3+} atoms, which were found to have very small atomic magnetic moments after relaxation (of $\pm 0.08 \mu_{\text{B}}$ and $\pm 0.03 \mu_{\text{B}}$ on average and adding up to a net contribution of $2.7 \mu_{\text{B}}$ and $0.4 \mu_{\text{B}}$, respectively). Magnetic moments can change sign as a result of the exchange interaction between magnetic moments. In the present case, apparently the broken symmetry and disorder induced by the presence of the interface causes individual magnetic moments at the interface to change in sign, which consecutively causes adjacent magnetic moment to change in sign as well, eventually leading to flipped magnetic moments quite far away from the interface.

In analogy with the definition of the interface energy (Eq. (2)), the net ferromagnetization of the supercell can be expressed per unit of interfacial area as $13.9 \mu_{\text{B}}/\text{nm}^2$; the larger part of the magnetization, to a value of $10.3 \mu_{\text{B}}/\text{nm}^2$, occurs in the constituting CoO component, whereas a magnetization of $3.6 \mu_{\text{B}}/\text{nm}^2$ was found for the Co_3O_4 slab. In the literature, net ferromagnetism in antiferromagnetic nanoparticles was experimentally observed to persist even at room temperature for compounds having a bulk Néel temperature below room temperature, which has generally been attributed to surface and interface effects.^{32–36} The present calculations predict that this is indeed also the case for the CoO/ Co_3O_4 {100}/{100} interface geometry investigated here. We suggest that a follow-up study could study experimentally whether partially converted composite $\text{Co}_3\text{O}_4/\text{CoO}$ nanoparticles exhibit stronger ferromagnetism than pure Co_3O_4 NPs or pure CoO NPs.

The second notable observation that can be made from Figure 3-8(a) is that the relaxed AFM2/AFM1 supercell is clearly skewed, most likely under the influence of the directionality along $\langle 111 \rangle$ of the antiferromagnetic ordering in the CoO phase. Please note that when both phases are nonmagnetic (NM/NM), skewing of the supercell does not occur as can be seen in Figure S 3-8(a) of the ESI. (The precise dimensions of the supercells can be found in Table S 3-1.) As is indicated by arrows and illustrated schematically at the right-hand side of Figure 3-8(a), relaxation resulted in a mistilt of approximately 4° between the Z-axes of the two cubic phases. We point out that a lattice mistilt between the two phases was sometimes also observed in the experiments, as evidenced by the electron diffraction pattern of Figure 3-7(e), and by the study by Ward *et al.* who reduced Co_3O_4 in an H_2 atmosphere. In theory, the experimentally observed mistilt could be explained from the magnetic interactions between the two phases. As explained in the Introduction, magnetism is often found for nanoparticles above the Curie or Néel temperature of their corresponding bulk phases because of size effects and surface and interface effects.²⁹ In addition, there is quite a strong magnetic field present in the electron microscope with field strengths up to 2 Tesla,⁴⁷ which can easily induce magnetization. Nonetheless, we consider that, whereas the skewing and mistilt observed in the simulations is most likely related to the different directionality of the magnetic ordering of the two phases, the most

plausible explanation for the experimentally observed lattice mistilt is the formation of dislocations in the oxygen sublattice, as revealed by the real-space HRTEM observations.

3.5 Conclusion

The thermal reduction process of Co₃O₄ nanoparticles to CoO was investigated by in-situ heating in the TEM under vacuum conditions. The results show that transformation of the Co₃O₄ NPs starts at 350 °C and that the NPs are completely converted after heating at 400 °C for 10 mins. Upon heating to higher temperatures up to 900 °C, no further reduction was observed. The reaction proceeds from the surface to the center of the particle, where the parent Co₃O₄ and the product CoO nanoparticles are in a cube-on-cube orientation relationship of their crystal lattices. The CoO reduced surface layer was sometimes slightly tilted with respect to the Co₃O₄ interior, which is likely associated with the formation of dislocations as the volume of the NPs has to reduce by 25% due to oxygen release. The transformation did not take place during ex-situ heating experiments conducted in air and under nitrogen flow, however the transformation was achieved ex-situ when heating in a high vacuum chamber; vacuum conditions, equivalent to a very low partial oxygen pressure, are necessary for achieving the transformation to CoO at a temperature of 400 °C.

The energetics and magnetic structure of the interface were investigated by density functional theory (DFT) calculations predicting a favorable CoO/Co₃O₄ {100}/{100} interface energy of 0.38 Jm⁻². The antiferromagnetic orderings of the two phases at both sides of the interface, AFM2 for CoO and AFM1 for Co₃O₄, correspond to those of the lowest-energy bulk phases. It was also found, however, that the magnetic ordering is distorted as several atoms have magnetic moments with a sign that is opposite to the sign that would yield the perfect magnetic order. The distortion in the antiferromagnetic ordering takes place at the interface but also leads to flipping of magnetic moments at a considerable distance (~1 nm) from the interface, likely due to exchange coupling. The flipping in sign of the magnetic moments leads to a considerable net ferromagnetic moment of 18.9 μ_B over the entire supercell, which corresponds to a net magnetization of approximately 13.9 μ_B/nm². We suggest that verifying experimentally whether the presence of the Co₃O₄/CoO interface indeed enhances the ferromagnetism of NPs with respect to pure Co₃O₄ or pure CoO NPs, would be an interesting topic for an experimental follow-up study. Both in the experiments and in the simulations, a small mistilt between the two cubic phases was found. In the simulations, this is likely related to stress fields originating from different directionalities of the antiferromagnetic orderings in CoO and Co₃O₄. In the experiments, this is likely due to the formation of dislocations in the oxygen sublattice during the thermal reduction. In the present work we show that the formation of an interface leads to ferromagnetism in otherwise only antiferromagnetic materials. Although we demonstrate this solely for the Co₃O₄/CoO interface, this effect can be expected to take place in many other transition metal

oxide systems as well. The implication of the current findings is that it could be very beneficial to reduce transition metal oxide nanoparticles only partially, in order to boost ferromagnetism at their interfaces. This would be an interesting topic for an experimental follow-up study, as generating ferromagnetism simply by partial reduction would make these nanoparticles interesting to a much wider range of applications including magnetic recording media, sensing, and biomedical applications.⁴⁸⁻⁵⁰

3.6 Acknowledgements

This study is collaborated with Heleen van Gog. XDC performed and analyzed the in-situ and ex-situ heating experiments. HvG conceived the computational part of the study and performed and analyzed the DFT calculations. Figures of atomic structural models and spin-polarization density plots were produced using VESTA.⁵¹ We thank Bo van den Bosch, who participated in the experiments within the framework of the ‘Research Traineeship’ 2nd year Bachelor course at Utrecht University. We thank Albert Grau Carbonell and Hans Meeldijk for EM support, and Profs. Alfons van Blaaderen and Petra de Jongh for useful discussions.

3.7 References

- 1 R. Zhang, Y. C. Zhang, L. Pan, G. Q. Shen, N. Mahmood, Y. H. Ma, Y. Shi, W. Jia, L. Wang, X. Zhang, W. Xu and J. J. Zou, *ACS Catal.*, 2018, **8**, 3803–3811.
- 2 F. Song, L. Bai, A. Moysiadou, S. Lee, C. Hu, L. Liardet and X. Hu, *J. Am. Chem. Soc.*, 2018, **140**, 7748–7759.
- 3 B. Ernst, A. Bensaddik, L. Hilaire, P. Chaumette and A. Kiennemann, *Catal. Today*, 1998, **39**, 329–341.
- 4 L. J. Garces, B. Hincapie, R. Zerger and S. L. Suib, *J. Phys. Chem. C*, 2015, **119**, 5484–5490.
- 5 P. A. Connor and J. T. S. Irvine, *Electrochim. Acta*, 2002, **47**, 2885–2892.
- 6 D. Su, S. Dou and G. Wang, *Sci. Rep.*, 2015, **4**, 5767.
- 7 W. Y. Li, L. N. Xu and J. Chen, *Adv. Funct. Mater.*, 2005, **15**, 851–857.
- 8 R. Dehghan, T. W. Hansen, J. B. Wagner, A. Holmen, E. Rytter, Ø. Borg and J. C. Walmsley, *Catal. Letters*, 2011, **141**, 754–761.
- 9 O. A. Bulavchenko, S. V. Cherepanova, V. V. Malakhov, L. S. Dovlitova, A. V. Ishchenko and S. V. Tsybulya, *Kinet. Catal.*, 2009, **50**, 192–198.
- 10 D. Potoczna-Petru and L. Kępiński, *Catal. Letters*, 2001, **73**, 41–46.
- 11 O. Kitakami, H. Sato, Y. Shimada, F. Sato and M. Tanaka, *Phys. Rev. B - Condens. Matter Mater. Phys.*, 1997, **56**, 13849–13854.
- 12 M. Chen, B. Hallstedt and L. J. Gauckler, *J. Phase Equilibria*, 2003, **24**, 212–227.
- 13 F.-C. Kong, Y.-F. Li, C. Shang and Z.-P. Liu, *J. Phys. Chem. C*, 2019, **123**, 17539–17547.
- 14 A. Navrotsky, C. Ma, K. Lillova and N. Birkner, *Science (80-.)*, 2010, **330**, 199–201.
- 15 B. Tomić-Tucaković, D. Majstorović, D. Jelić and S. Mentus, *Thermochim. Acta*, 2012, **541**, 15–24.
- 16 G. Ji, S. Smart, S. K. Bhatia and J. C. Diniz da Costa, *Sep. Purif. Technol.*, 2015, **154**, 338–344.
- 17 K. C. Sabat, R. K. Paramguru, S. Pradhan and B. K. Mishra, *Plasma Chem. Plasma Process.*, 2015, **35**, 387–399.
- 18 M. R. Ward, E. D. Boyes and P. L. Gai, *ChemCatChem*, 2013, **5**, 2655–2661.
- 19 N. A. Mayer, D. M. Cupid, R. Adam, A. Reif, D. Rafaja and H. J. Seifert, *Thermochim. Acta*, 2017, **652**, 109–118.
- 20 M. A. Van Huis, N. P. Young, G. Pandraud, J. F. Creemer, D. Vanmaekelbergh, A. I. Kirkland and H. W. Zandbergen, *Adv. Mater.*, 2009, **21**, 4992–4995.
- 21 T. Archer, R. Hanafin and S. Sanvito, *Phys. Rev. B*, 2008, **78**, 14431.
- 22 H. X. Deng, J. Li, S. S. Li, J. B. Xia, A. Walsh and S. H. Wei, *Appl. Phys. Lett.*, 2010, **96**, 162508.
- 23 A. L. Dalverny, J. S. Filhol, F. Lemoigno and M. L. Doublet, *J. Phys. Chem. C*, 2010, **114**, 21750–21756.
- 24 J. Chen, X. Wu and A. Selloni, *Phys. Rev. B - Condens. Matter Mater. Phys.*, 2011, **83**, 245204.
- 25 L. Qiao, H. Y. Xiao, H. M. Meyer, J. N. Sun, C. M. Rouleau, A. A. Puzos, D. B. Geohegan, I. N. Ivanov, M. Yoon, W. J. Weber and M. D. Biegalski, *J. Mater. Chem. C*, 2013, **1**, 4628–4633.

- 26 F. B. Lewist and N. H. Saunders, *J. Phys. C Solid State Phys.*, 1973, **6**, 2525–2532.
- 27 E. Z. Kurmaev, R. G. Wilks, A. Moewes, L. D. Finkelstein, S. N. Shamin and J. Kuneš, *Phys. Rev. B*, 2008, **77**, 165127.
- 28 V. R. Shinde, S. B. Mahadik, T. P. Gujar and C. D. Lokhande, *Appl. Surf. Sci.*, 2006, **252**, 7487–7492.
- 29 Y. A. Koksharov, in *Magnetic Nanoparticles*, ed. S. P. Gubin, John Wiley & Sons, Ltd, 2009, pp. 197–254.
- 30 S. Sako, K. Ohshima, M. Sakai and S. Bandow, *Surf. Rev. Lett.*, 1996, **3**, 109–113.
- 31 L. He, C. Chen, N. Wang, W. Zhou and L. Guo, *J. Appl. Phys.*, 2007, **102**, 103911.
- 32 S. R. Gawali, A. C. Gandhi, S. S. Gaikwad, J. Pant, T. S. Chan, C. L. Cheng, Y. R. Ma and S. Y. Wu, *Sci. Rep.*, 2018, **8**, 1–12.
- 33 L. Zhang, D. Xue and C. Gao, *J. Magn. Magn. Mater.*, 2003, **267**, 111–114.
- 34 G. Yang, D. Gao, Z. Shi, Z. Zhang, J. Zhang, J. Zhang and D. Xue, *J. Phys. Chem. C*, 2010, **114**, 21989–21993.
- 35 C. Nethravathi, S. Sen, N. Ravishankar, M. Rajamathi, C. Pietzonka and B. Harbrecht, *J. Phys. Chem. B*, 2005, **109**, 11468–11472.
- 36 Z. A. Li, N. Fontañña-Troitiño, A. Kovács, S. Liébana-Viñas, M. Spasova, R. E. Dunin-Borkowski, M. Müller, D. Doennig, R. Pentcheva, M. Farle and V. Salgueiriño, *Sci. Rep.*, 2015, **5**, 1–6.
- 37 C. W. Tung, Y. Y. Hsu, Y. P. Shen, Y. Zheng, T. S. Chan, H. S. Sheu, Y. C. Cheng and H. M. Chen, *Nat. Commun.*, 2015, **6**, 8106.
- 38 R. F. W. Bader, *Atoms in Molecules: A Quantum Theory*, Oxford University Press, 1990.
- 39 G. Kresse and J. Furthmüller, *Comput. Mater. Sci.*, 1996, **6**, 15–50.
- 40 G. Kresse and J. Furthmüller, *Phys. Rev. B - Condens. Matter Mater. Phys.*, 1996, **54**, 11169–11186.
- 41 P. E. Blöchl, *Phys. Rev. B*, 1994, **50**, 17953–17979.
- 42 G. Kresse and D. Joubert, *Phys. Rev. B*, 1999, **59**, 1758–1775.
- 43 J. P. Perdew, K. Burke and M. Ernzerhof, *Phys. Rev. Lett.*, 1996, **77**, 3865–3868.
- 44 S. Dudarev and G. Botton, *Phys. Rev. B - Condens. Matter Mater. Phys.*, 1998, **57**, 1505–1509.
- 45 H. J. Monkhorst and J. D. Pack, *Phys. Rev. B*, 1976, **13**, 5188–5192.
- 46 G. Henkelman, A. Arnaldsson and H. Jónsson, *Comput. Mater. Sci.*, 2006, **36**, 354–360.
- 47 N. Shibata, Y. Kohno, A. Nakamura, S. Morishita, T. Seki, A. Kumamoto, H. Sawada, T. Matsumoto, S. D. Findlay and Y. Ikuhara, *Nat. Commun.*, 2019, **10**, 1–5.
- 48 S. Singamaneni, V. N. Bliznyuk, C. Binek and E. Y. Tsybal, *J. Mater. Chem.*, 2011, **21**, 16819–16845.
- 49 H. Lai, F. Xu and L. Wang, *J. Mater. Sci.*, 2018, **53**, 8677–8698.
- 50 Q. A. Pankhurst, J. Connolly, S. K. Jones and J. Dobson, *J. Phys. D. Appl. Phys.*, 2003, **36**, R167.
- 51 K. Momma and F. Izumi, *J. Appl. Crystallogr.*, 2011, **44**, 1272–1276.

3.8 Appendix

3.8.1 Supporting Tables

Table S 3-1 Results of the DFT calculations conducted on the {100}/{100} CoO/Co₃O₄ interface. The interface designation refers to the various magnetic and nonmagnetic input configurations displayed in Figure 3-2. Supercell dimensions and interface energies are listed, as well as the lattice mismatch between the two constituent phases in the plane of the interface. All interface supercells contain the same number of atoms.

Interface	<i>a</i>	<i>b</i>	<i>c</i>	α	β	γ	A_{int}	γ_{int}	γ_{int}	Mismatch
Co ₃ O ₄ /CoO	(Å)	(Å)	(Å)	(°)	(°)	(°)	(Å ²)	(eV/Å ²)	(J/m ²)	(%)
AFM2/AFM1	8.238	8.238	33.39	88.5	88.5	88.5	67.84	0.024	0.38	4.2
AFM1/AFM1	7.974	7.974	36.26	90.0	90.0	89.7	63.58	0.050	0.80	4.4
FM/FM	7.992	7.992	36.34	90.0	90.0	89.8	63.87	0.047	0.75	4.8
NM/NM	7.924	7.924	35.20	90.0	90.0	89.4	62.78	0.239	3.82	2.1

Table S 3-2 Lattice reflections and corresponding lattice spacings of Co₃O₄ and CoO.

Co ₃ O ₄			CoO		
No.	(h k l)	lattice spacings (Å)	No.	(h k l)	lattice spacings (Å)
1	(1 1 1)	4.67	1*	(1 1 1)	2.45
2	(0 2 2)	2.86	2*	(0 0 2)	2.12
3	(1 1 3)	2.43	3*	(0 2 2)	1.50
4	(0 0 4)	2.02			
5	(2 2 4)	1.65			
6	(1 1 5)	1.55			
7	(0 4 4)	1.42			

3.8.2 Supporting Figures

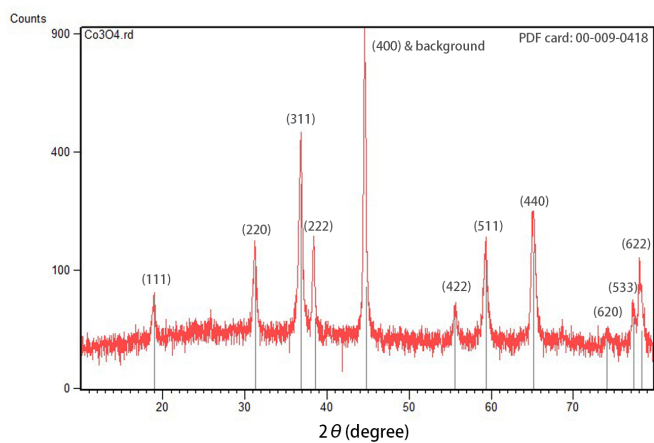


Figure S 3-1 XRD diagram of the Co_3O_4 powders.

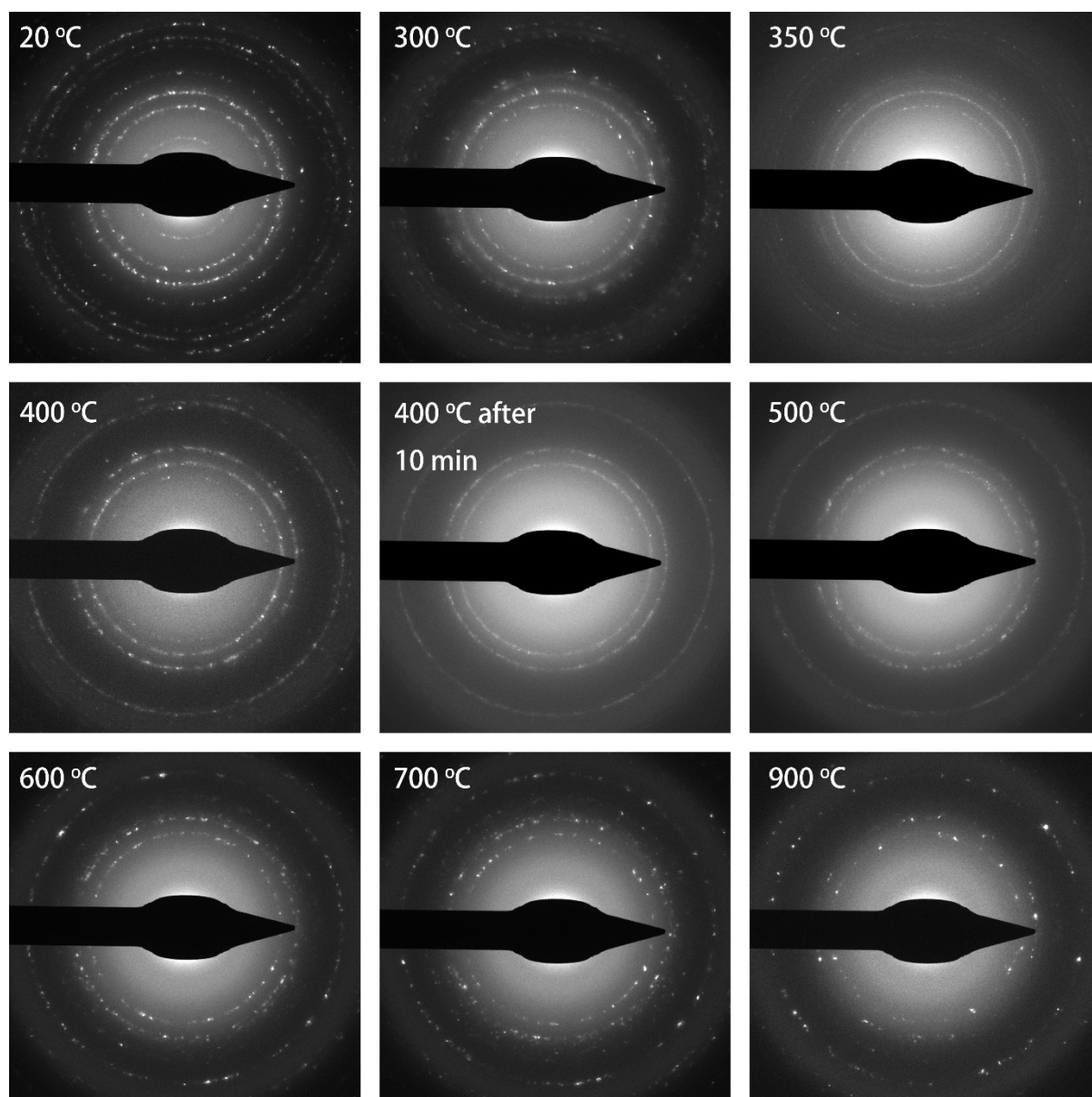


Figure S 3-2 Selected area diffraction patterns (SAED) of Co₃O₄ NPs after in situ annealing at the indicated temperatures in the temperature range from 20 °C to 900 °C. At 20 °C, the rings in the DP correspond to Co₃O₄. During annealing at 350 °C, the pattern started to change. After keeping the sample at 400 °C for 10 minutes, only three rings remained, that are indicative of the CoO phase. From 600 °C onwards, there are fewer spots on the rings due to coalescence and alignment of the nanocrystals, which consequently became fewer in number but larger. The transformation took place everywhere, also in areas that were not examined with the electron beam prior to heating, which means that the reduction is not due to electron beam exposure.

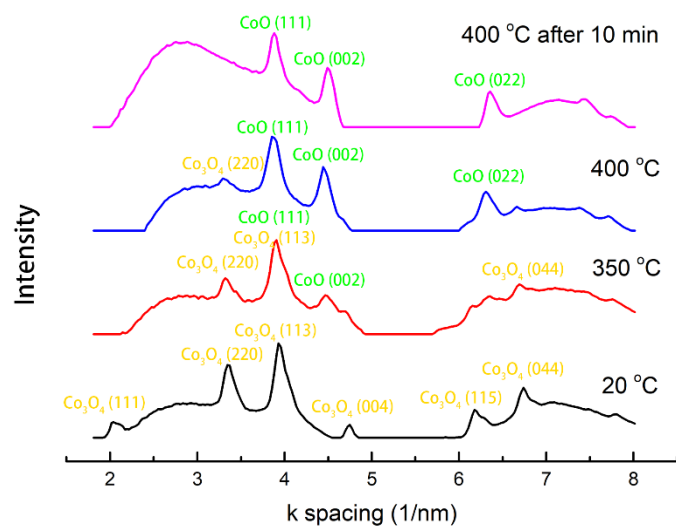


Figure S 3-3 Circularly integrated diffraction patterns obtained after heating at 20 °C, 350 °C, 400 °C, and 400 °C after 10 minutes. The corresponding lattice reflections are indicated above the peaks with Co₃O₄ reflections marked in yellow and CoO reflections marked in green. At 20 °C, all peaks corresponded to the Co₃O₄ structure. At 350 °C, the (111) peak of Co₃O₄ disappeared and the (004) reflection became very weak, while the (002) reflection of CoO appeared. This trend continued to 400 °C, and finally only three peaks corresponding to reflections of CoO remained.

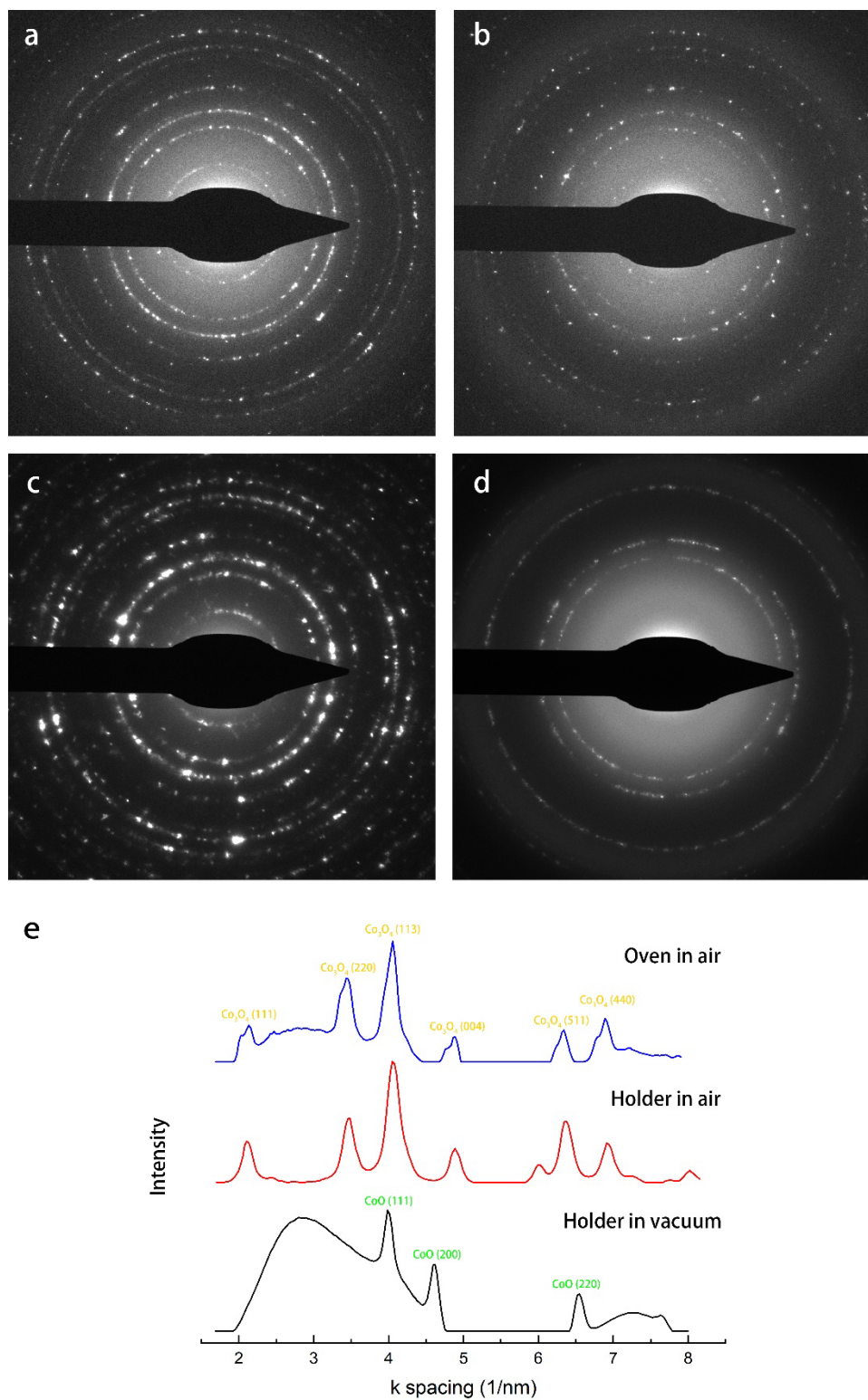


Figure S 3-4 SAED of Co₃O₄ NPs after ex-situ heating. (a) and (b) are DPs of the sample heated in the oven in air and under N₂ flow, respectively. (c) and (d) are DPs obtained after heating inside the heating holder in air and in a high vacuum chamber following the same temperature profile as in the in-situ experiments. (e) Integrated image of (a, c, d). Different intensities between panels are due to different amounts of particles in the selected areas (SA).

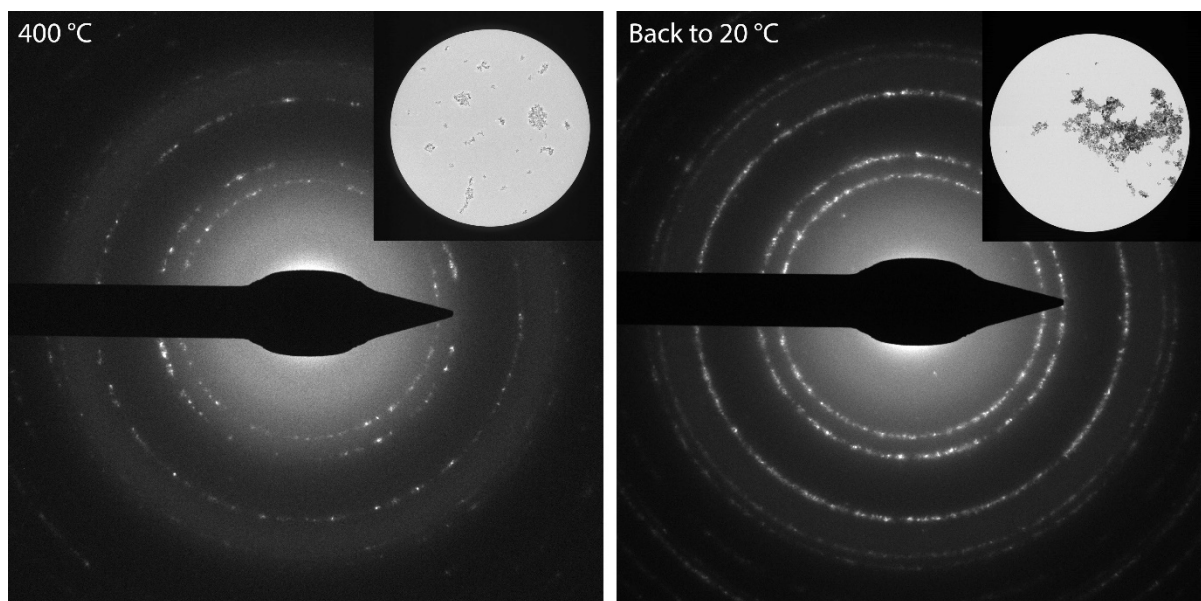


Figure S 3-5 SAED of Co_3O_4 NPs at 400 °C (left), and after cooling down to 20 °C (right). Both DPs correspond to the crystal structure of CoO. The inset images at the top-right show the selected areas which form the diffraction patterns were taken. The intensity of the DP after cooling down is higher because there are more particles in the selected area.

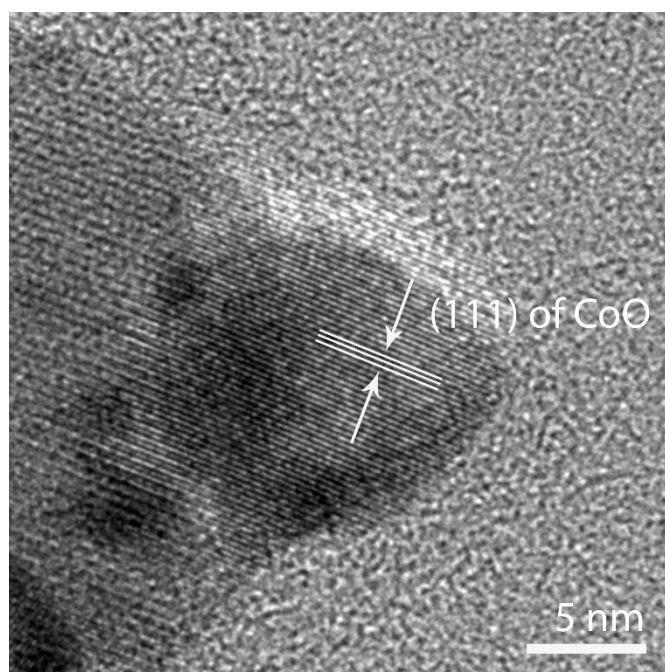


Figure S 3-6 HRTEM images after in-situ heating to 400 °C and subsequently gradually cooling down.

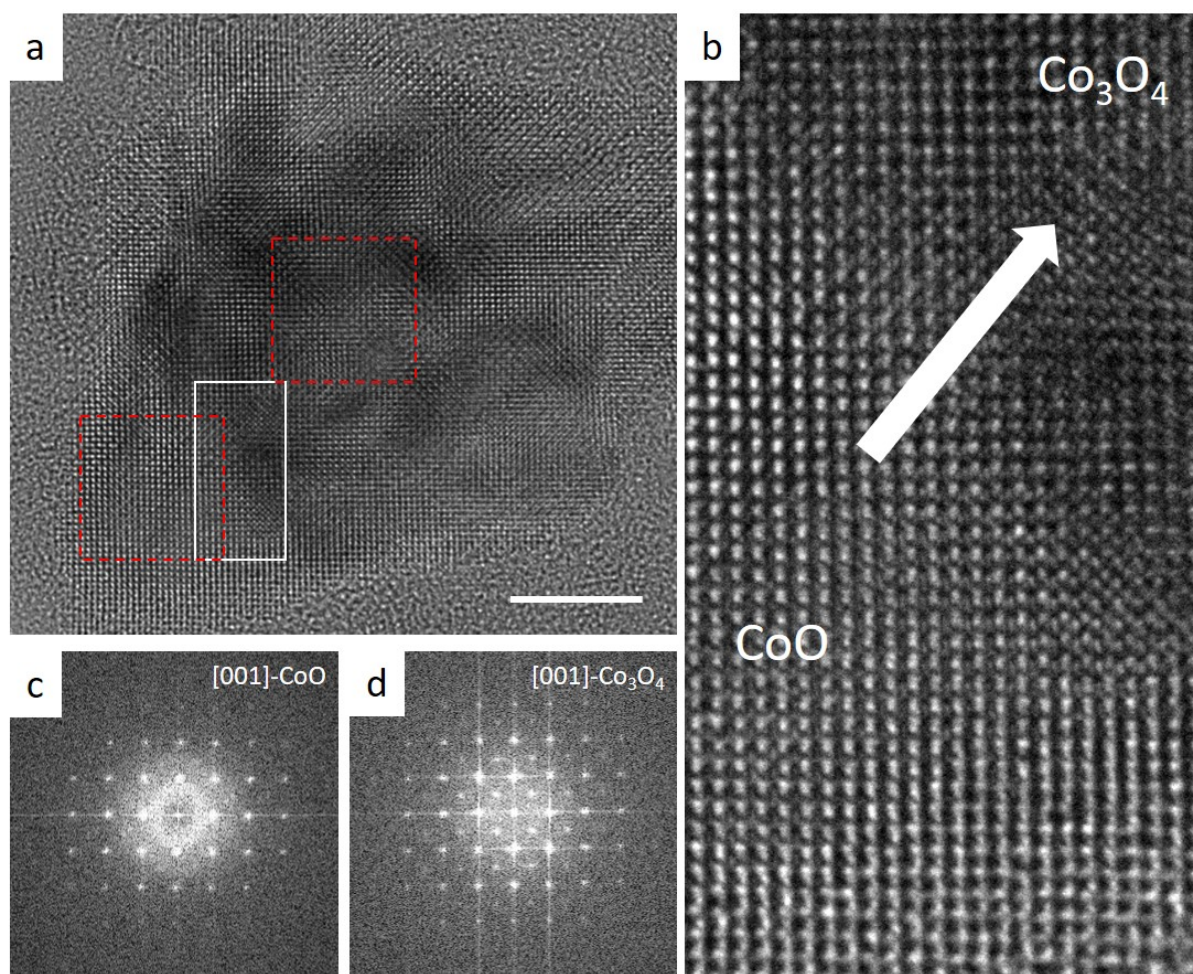


Figure S 3-7 HRTEM images of a partially transformed particle. (a) Overview of the particle, left-bottom and surface part is in CoO phase and central part is still in Co₃O₄ phase. (b) Magnified image of the area marked by white square in (a). (c) and (d) The FFT pattern of the corresponding areas marked (a), showing the CoO and Co₃O₄ structure respectively.

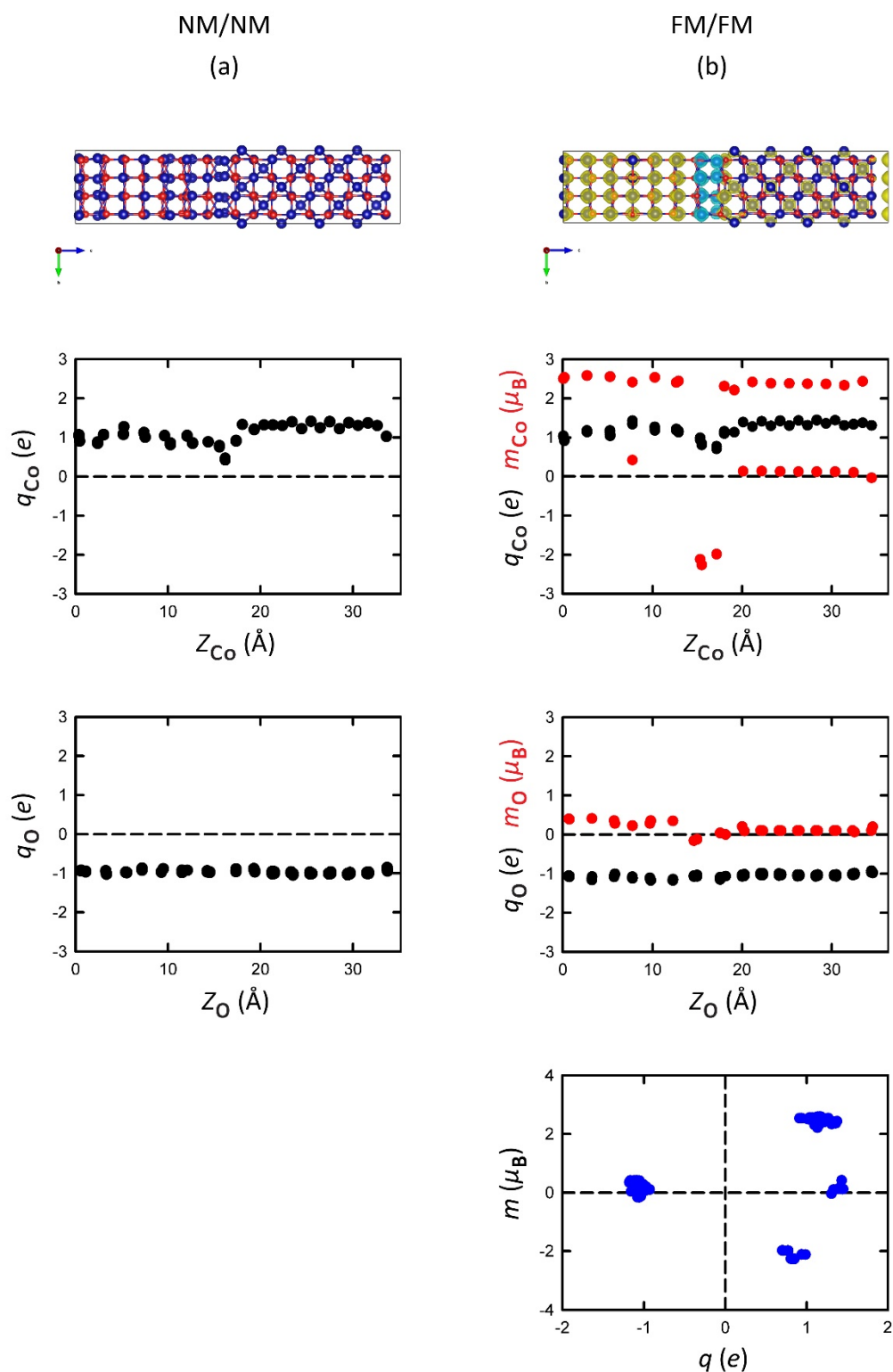


Figure S 3-8 Top: relaxed configurations of the interface supercells, with overlaid the magnetization density, with (a) the NM/NM nonmagnetic configuration and (b) the FM/FM magnetic ordering. Co atoms are depicted in blue and O atoms in red, while yellow isosurfaces indicate excess spin-up electron density and blue isosurfaces excess spin-down electron density (isosurface levels are $\pm 0.24 e/\text{Å}^3$). Middle: charges and magnetic moments on the Co and O atoms plotted as a function of Z-coordinate. Bottom: correlation between the charges and the magnetic moments on the atoms.

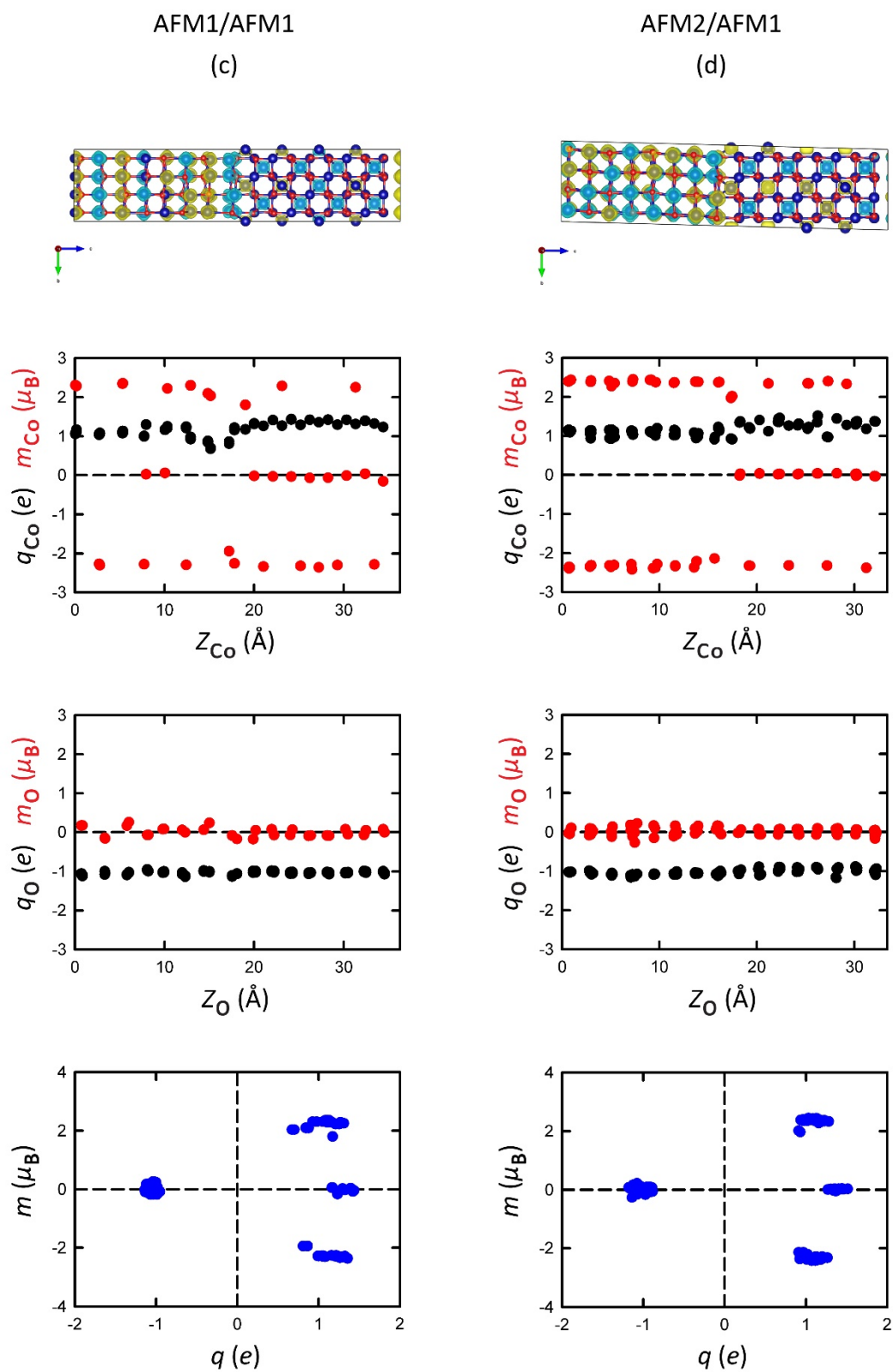


Figure S 3-8 (continued) As previous, with (c) the AFM1/AFM1 magnetic ordering and (d) the AFM2/AFM1 magnetic ordering.

4. Heating-induced Transformation of Anatase TiO₂ Nanorods to Rock Salt TiO Nanoparticles

Anatase TiO₂ nanocrystals (NCs) play a vital role in photocatalytic applications due to their high catalytic activity, and in gas-sensing applications due to their high chemical sensitivity. Here we report the transformation at elevated temperature of anatase nanorods (NRs) with a length of 25 nm into rock-salt TiO nanoparticles with an average size of 9.2±2.1 nm, investigated by means of in-situ heating in the transmission electron microscope (TEM). The nanorods were completely transformed to titanium monoxide nanocrystals after heating to a temperature of 1200 °C. We also identified an intermediate stage in the temperature range of 950 °C - 1200 °C, during which not only the anatase and rock salt phase were found, but the brookite phase. Understanding of the phase and morphology evolution at high temperatures is of essence to the functionality of the nanorods in various applications as discussed in this work. Moreover, the high-temperature transformation to titanium monoxide is of interest as rock salt TiO (γ -TiO) is known to exhibit superconducting properties. We propose the heating-induced transformation as a physical route to synthesize TiO nanocrystals of very small size.

Based on:

X. Chen, S. N. Hosseini and M. A. van Huis, *ACS Appl. Nano Mater.*, 2022, **5**, 1600–1606.

4.1 Introduction

Titanium dioxides have been studied for more than half century and the investigation of their nanostructural forms is continuously intensifying.¹⁻⁶ The interest in nanoscale TiO₂ stems from its natural abundance, non-toxicity, high stability, and advanced functional properties including in particular its very effective application as a photocatalyst.⁷⁻¹⁴ Because of the high photocatalytic performance, TiO₂ also has potential to be used as an anti-bacterial and for self-cleaning coating of high temperature process ceramics.^{11,15-20} Moreover, TiO₂ and also TiO₂ based composites are also suitable gas sensor materials in electronic devices, which are based on surface oxygen vacancy formation, selective ion absorption, or desorption mechanisms.²¹⁻²⁴

In contrast to bulk TiO₂ materials, TiO₂ nanoparticles have the advantage of high surface to volume ratio. Consequently, the nanoparticles have much higher adsorption ability than the bulk material, leading to a high reactivity in photocatalytic and gas sensing applications.²⁵ Also the morphology of the nanoscale particles is of major importance and results in different performances.⁶ It is reported that the nanorods have higher interfacial charge carrier transfer rate and density of active sites available for surface reactions in comparison to spherical particles, which is due to the even higher surface to volume ratio of the rod-like shape.²⁶ The anatase nanorods investigated in this study are also proper candidates for serving as building blocks for liquid crystals due to their shape and orientation dependent collective properties, which has been demonstrated already for brookite nanorods²⁷. The morphology, size and crystal structure of the particles are directly related to their functional properties such as catalytic and (opto)electrical properties, determining the range of applicable operation temperatures. For applications in gas sensors and antibacterial coatings, the desired operation temperatures can be very high. Consequently, the thermal behavior and temporal stability of TiO₂ nanorods are of major importance to their performance, and here we investigate the thermal evolution of anatase nanorods by in-situ heating in transmission electron microscopy (TEM).

There are three phases of TiO₂ that predominantly occur in nature: rutile, anatase and brookite. All three phases are composed of TiO₆ octahedra with different Ti-O bond lengths. Their schematic crystal structures are shown in Figure 4-1 and detailed crystallographic data are provided in Table 4-1. Rutile is the most stable phase in the bulk form, while the anatase phase is reported to have the highest photocatalytic activity.^{10,28} Many studies show the irreversible transformation from anatase or brookite to the rutile phase.²⁸⁻³³ However, the properties at the nanoscale are different. It has been shown that the anatase phase is preferred for nanoparticles.³⁴⁻³⁸ The stability and phase transformation between the polymorphs were reported to depend on several factors, such as temperature, pH³⁴, synthesis method¹⁸⁻²⁰ and presence of impurities^{39,40}. Moreover, the shape of the particles could be also manipulated during synthesis.^{18,27,41} It is also possible to enhance the adsorption properties of the

nanocrystals by exposing different facets.^{34,42} The shape of the nanocrystal is therefore important to take into consideration during investigation of the phase stability of TiO₂ nanocrystals. The transformations between different polymorphs result in changes in their chemical and physical properties, which consequently affects their functionality in applications.^{43,44}

Apart from the phase transformation between titanium dioxides, the transformation to titanium monoxides is also reported in several studies.^{45–47} Titanium monoxides have been observed in 4 different phases, of which rock salt cubic TiO (also named γ -TiO) is the stable phase at high temperature.^{48–50} It has been shown that TiO has superconducting properties.^{51–53} TiO thin films were successfully fabricated by ion bombardment induced chemical reduction, laser hydrothermal reductive ablation, and other methods.^{45,51,54} Nanopowders of TiO have been synthesized previously e.g. by ball milling, fragmentation, and other methods.^{55–58} The typical size of the nanoparticles obtained in those powders is quite large, although, in the order of ~100 nm or larger. Simon *et al.* have successfully synthesized N-doped cubic TiO nanoparticles with a size below 10 nm by laser pyrolysis.⁵⁹ In that study it was reported that apart from the N doping, carbon contamination was also introduced during the synthesis and that post-synthesis annealing was required to whiten the samples. In the present work, we have obtained pure TiO nanocrystals with a typical size of ~10 nm or smaller.

Here, we investigate the thermal evolution of anatase TiO₂ nanorods using in-situ TEM where superior resolution in the electron microscope during heating is obtained by employing MEMS technology, allowing to monitor chemical and physical transitions of nanoparticles in real-time and at the atomic scale.^{60,61} In order to avoid any influence of the electron beam on the observations, the field of view in the TEM was often changed to areas not previously exposed to the electron beam, as detailed in the Experimental section. Thermal evolution was observed to take place everywhere on the heating chip. The anatase nanorods fully transformed to rock-salt TiO at 1200 °C, with an intermediated stage appearing from 950 °C onward. At the intermediate stage, a mixture of the anatase, brookite, and rock-salt phases was found. The thermal stability of anatase nanorods is of importance for their implementation in applications. Furthermore, the transformation elucidated in this paper may serve as a route toward obtaining rock salt titanium monoxide (TiO) nanoparticles of very small size.

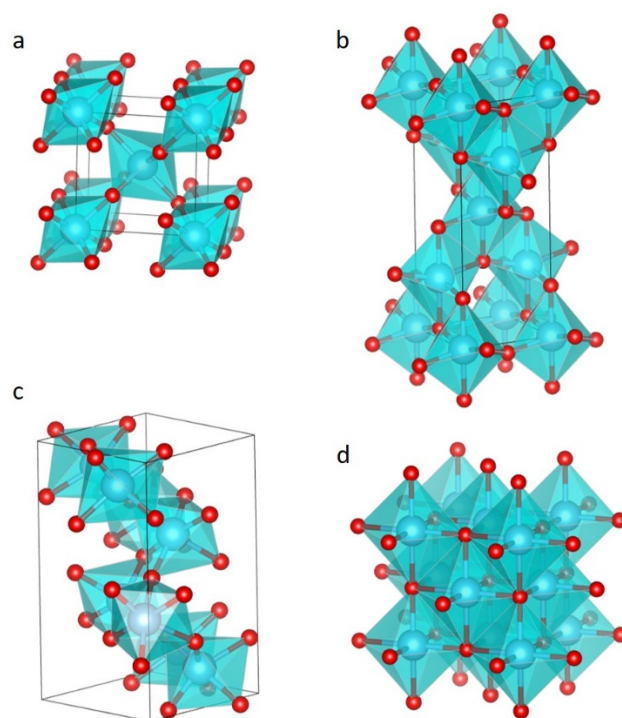


Figure 4-1 Structure of the TiO_x polymorphs: (a) rutile, (b) anatase, (c) brookite, and (d) γ -TiO (rock salt). Ti atoms are represented by blue spheres and O atoms are represented by red spheres.

Table 4-1 Structure, Space Group and Lattice Constant of Rutile, Anatase, Brookite and γ -TiO,

	Structure	Space group	Lattice parameter (Å) ^{3,44}
rutile	tetragonal	$P4_2/mnm$ (136)	$a=b=4.593$; $c=2.959$
anatase	tetragonal	$I4_1/amd$ (141)	$a=b=3.785$; $c=9.514$
brookite	orthorhombic	$Pbca$ (61)	$a=9.184$; $b=5.447$; $c=5.145$
γ -TiO	cubic	$Fm\bar{3}m$ (225)	$a=b=c=4.24$

4.2 Experimental

4.2.1 Synthesis

Titanium (IV) isopropoxide or TTIP ($\text{Ti}(\text{OCH}(\text{CH}_3)_2)_4$, 97.0%), oleic acid (OLAC, 90%), acetone, and toluene were purchased from Sigma Aldrich and used as received. All experimental procedures were carried out either in an inert atmosphere using a standard Schlenk line setup or in a glove box. The anatase titanium dioxide nanorods were synthesized following a slightly modified version of the synthesis described in the literature by Joo et al.⁶² where oleic acid (OLAC) was used as the solvent,

reagent, and ligand. In a typical synthesis, OLAC (100.0 mmol, 31.6 mL) was degassed in a 250 mL three-neck round bottom flask at 120 °C for an hour under vacuum and vigorous stirring. Then the flask was cooled down under vacuum to 40 °C, followed by switching to nitrogen and the swift addition of TTIP (34.0 mmol, 10 mL) which was prepared in the glove box in advance. The mixture was then heated up to 250 °C in 20 minutes and kept at this temperature for 2 hours. Caution should be taken as the reaction is rather violent with concomitant release of gases and foam formation expanding in the flask and should be controlled by nitrogen overflow/pressure as well as an extra needle as an outlet in a septum on one of the necks of the flask. After thermal fluctuations at high temperatures, the yellow solution gradually turned into a white-gray foam and finally a gray solution. The heating mantle was then removed after 2 hours and the flask was allowed to cool to room temperature. A size-selective precipitation process was performed on the as-synthesized TiO₂ NCs to separate TiO₂ NRs. Thus, the dispersion of the TiO₂ NCs was centrifuged at 6000 rcf (relative centrifugal force) for 10 min and then NRs precipitations were redispersed in toluene. The washing step was repeated at least two times to achieve optically clear dispersions of TiO₂ NRs. The dimension of the NRs was on average 3.6 ± 0.3 nm (diameter) and 24.6 ± 3.4 nm (length).

4.2.2 X-ray Diffraction Characterization

The crystal structure of TiO₂ NRs in pristine samples was confirmed by X-ray diffraction (XRD) measurements. XRD was performed using a Bruker-AXS D2 Phaser X-ray diffractometer with Co K α radiation ($\lambda = 1.79026$ Å) operated at 30 kV and 10 mA.

4.2.3 TEM Characterization

All in-situ TEM investigations on the anatase nanorods were conducted using a FEI TalosF200X TEM operating at 200 kV. High-resolution HAADF-STEM (high angle annular dark field scanning transmission electron microscopy) images of the rock salt TiO nanoparticles obtained after heating, were recorded with a double aberration corrected TFS Spectra 300 TEM operating at 300 kV. The specimens were prepared by drop casting the anatase TiO₂ nanorods solution onto Micro-Electro-Mechanical Systems (MEMS) heating chip. This chip was subsequently mounted on a dedicated in-situ heating TEM holder from DENSSolutions.

The TiO₂ specimens were first heated from 20 °C to 1200 °C with 100 °C increments. The heating profile is shown in Figure S 4-1 of the Appendix. The nanoscale phase transformation started around 900 °C. In a second heating experiment, the specimen was heated from 20 to 900 °C with 100 °C increments, but with smaller increments of 50 °C when raising the temperature further from 900 to

1100 °C, in order to monitor the transformations more closely.

The inspected area of the sample was changed very often to areas not previously exposed to the electron beam, in order to exclude any possible beam-induced effects. The transformations reported in this work were found to occur everywhere on the heating chip, also in areas not previously exposed to the electron beam. Furthermore, serving as a reference measurement and in order to fully exclude any electron beam effects, the samples were also heated *ex-situ* outside of the TEM. For these *ex-situ* experiments, the samples were heated with the heating holder inserted in a high vacuum chamber (Gatan pumping station Model 655), applying the same heating rate as in the *in-situ* heating experiments. The pressure in the high vacuum chamber was approximately $1.0 \cdot 10^{-3}$ - 10^{-4} Pa. After holding the temperature at 1200 °C for 15 minutes, the sample was cooled down fast to room temperature and swiftly inserted in the TEM for subsequent analysis.

4.3 Results and Discussion

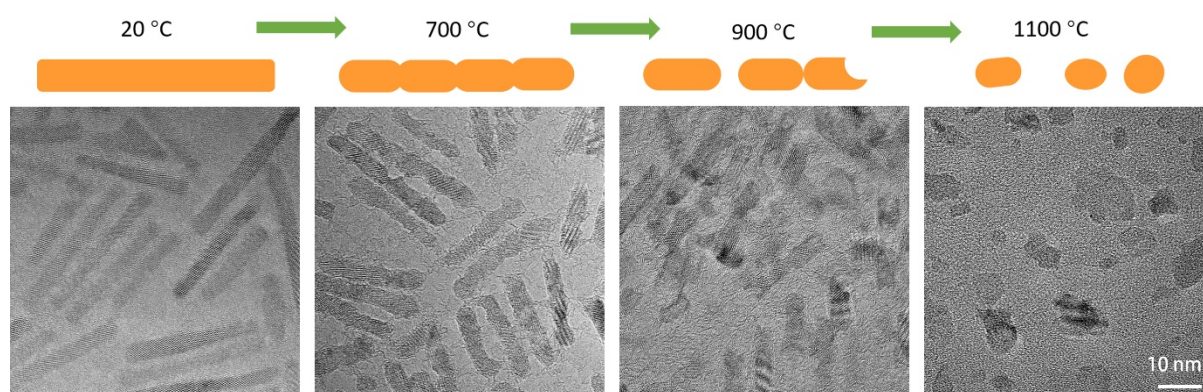


Figure 4-2 Schematic process and high-resolution TEM images of TiO_x nanocrystals during heating. At 700 °C, the surfaces of the nanorods deformed. At 900 °C, the nanorods broke up and sometimes the neighboring rods coalesced. Upon heating to 1000 °C, most nanorods transformed to smaller nanoparticles.

A TEM micrograph of the pristine as-synthesized samples is shown in the left panel of Figure 4-2. The nanorods have a length of 24.6 ± 3.4 nm and a diameter of 3.6 ± 0.3 nm. Most of the nanorods have sharp edges at room temperature. An XRD spectrum confirming the anatase phase is shown in Figure S 4-2. These anatase TiO₂ nanorods were heated from room temperature to 1200 °C following the procedure mentioned in the Experimental section. The field of view was often changed during the *in-situ* experiments to verify that the transformations took place everywhere, also in areas that had not been previously exposed to the electron beam. Figure 4-2 shows high-resolution images and schematic panels of the thermal evolution of specimens from room temperature to 1100 °C. The

morphology of the specimens changed during heating. Upon heating to 500 °C, the edges became rounded. Most likely, the oleic acid ligands degrade at this temperature resulting in destabilization of the nanorod surfaces. At 700 °C, the surfaces of the nanorods deformed more and were no longer smooth. At 900 °C, some nanorods broke up into multiple segments and were partly sublimated, while sometimes neighboring rods had coalesced. Upon heating to 1000 °C, most nanorods had transformed into smaller nanoparticles. Images with lower magnification and more temperature steps during heating are shown in Figure S 4-3.

Figure 4-3 shows the selected area diffraction patterns (SADPs) of the specimens during heating. Up to 900 °C, the diffraction pattern (DP) corresponded to that of the anatase crystal structure. When the temperature was raised to 950 °C, a few more rings appeared (marked by the yellow arcs), indicating the formation of a new structure that is neither anatase TiO₂, nor cubic TiO. The indexing of this new phase will be discussed below. With further increase in the temperature, the inner rings disappeared gradually. At 1200 °C, only three rings remained. The rings were indexed and found to correspond to the cubic γ -TiO structure. This means that the anatase TiO₂ nanorods were finally reduced to rock salt TiO. High-resolution STEM images shown in Figure 4-4 confirm the cubic TiO structure. The average size of the TiO particles is determined to be 9.2±2.1 nm (based on the measurement of the dimensions of 200 nanoparticles). A histogram of the size distribution is shown in Figure S 4-4.

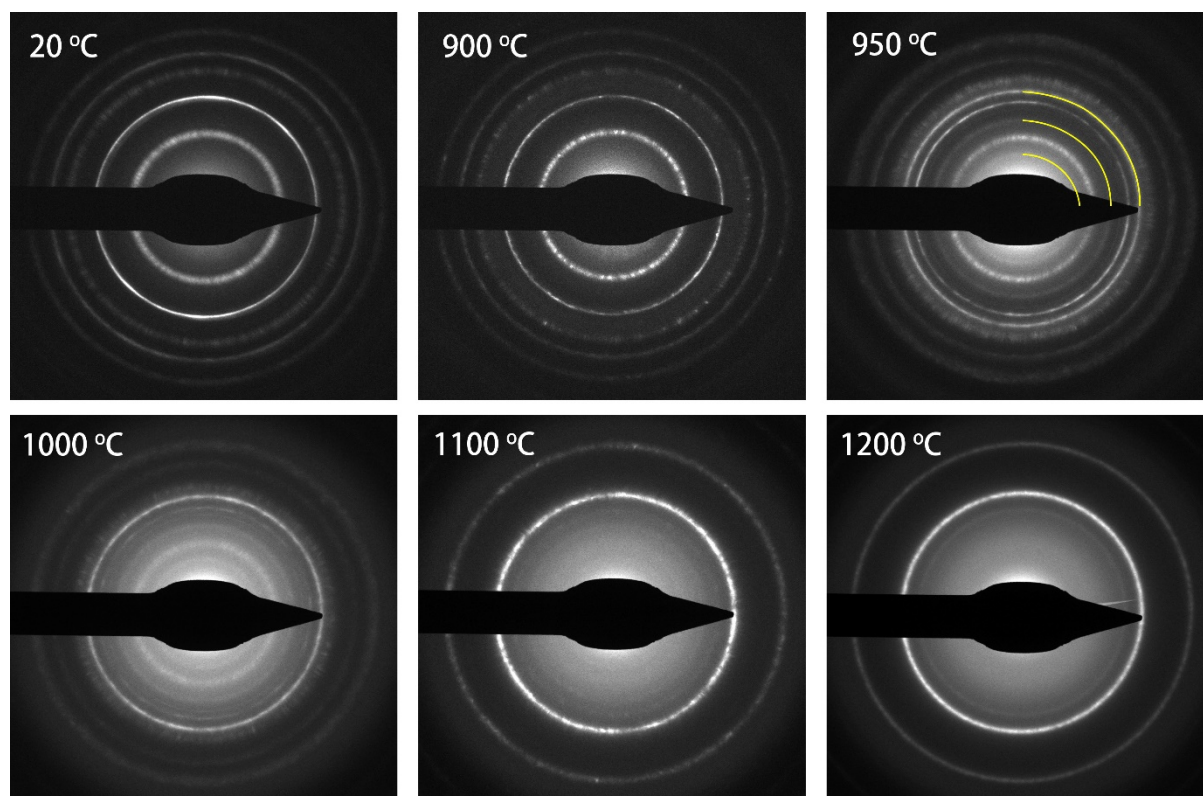


Figure 4-3 Selected area diffraction patterns (SADPs) of the titanium oxide nanorods during heating. At room temperature and up to 900 °C, the patterns correspond to the anatase crystal structure. At 950 °C, a new phase started to form as indicated by the yellow arcs. At the temperature of 1200 °C, all nanoparticles had transformed to rock salt TiO, which, because of the high symmetry of this phase, only has few rings in the SADP.

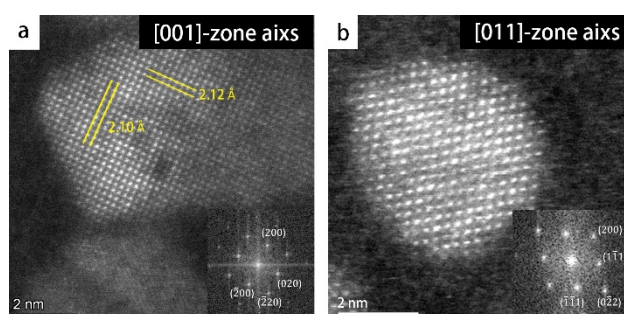


Figure 4-4 High-resolution STEM images of two γ -TiO nanocrystals recorded after heating to 1200 °C. Corresponding Fast-Fourier Transform (FFT) patterns are shown as insets, where the cubic TiO structure in (a) is oriented in the [001]-zone axis and (b) in the [011]-zone axis, respectively. The scale bar in both images indicates 2 nm.

In order to resolve the detailed phase transformation process between 950 °C and 1200 °C, the diffraction pattern (DP) at 950 °C was measured and compared with the DP at 900 °C which corresponds to the anatase structure (shown in Figure 4-5 (a)). The rings that additionally appeared at 950 °C are indicated in yellow (#1, 3, 5), and the rings corresponding to the anatase structure are

marked in red (#2, 4, 6-8). The DPs at 20 °C, 900 °C, 950 °C, 1000 °C and 1200 °C were integrated and are shown in Figure 4-5 (b).

The integrated DPs at 900 °C and 20 °C both show the anatase structure, while at 950 °C, there are 3 new peaks, marked as No. 1, 3 and 5 (corresponding to the new rings in the DP). With increasing temperature, ring No. 5 remains while the other peaks disappear gradually during further heating to a temperature of 1200 °C (also shown in Figure S 4-5). In the DP recorded at 950 °C, peak No. 1 corresponds to a lattice spacing of 4.59 Å, which is a rather big value for lattice spacing, but which corresponds very well to the (200)-reflection of the brookite phase. Moreover, ring No. 3 corresponds to a lattice spacing of 2.90 Å, corresponding to the (211)-reflection of brookite. The diffraction pattern of the specimens at 950 °C was also compared to the as-synthesized brookite nanorods at 20 °C (synthesized with the same method as the previous work²⁷). From the comparison (shown in Figure S 4-6), most of the rings in the DP of the specimen at 950 °C could be related to the corresponding rings in the DP of brookite, except for rings No. 4 and 5 while Figure 4-5 (b) shows that ring No.4 corresponds to the (004) reflection of anatase and ring No.5 corresponds to the (200) reflection of TiO. This indicates that anatase TiO₂, brookite TiO₂, and cubic TiO all existed in the temperature range between 950 °C and 1000 °C. After heating to 1100 °C and at 1200 °C, only the cubic TiO phase remained.

The nanorods remained in the anatase phase up to a temperature of 950 °C, which is different from the phase diagram shown in the paper by Murray and Wriedt⁴⁹, who reported that anatase will transform to rutile at a temperature of about 600 °C in vacuum. The difference between their and our findings can be explained by the small size of the nanorods. The research of Naicker et al.⁶³ showed that in the nanoscale range, the surface energy of anatase and brookite is smaller than that of rutile nanospheres with the same size. For nanospheres larger than 4 nm, the surface energy of brookite tends to be smaller than that of anatase. The smaller surface energy of brookite could explain the transformation of anatase in this work to brookite instead of rutile at high temperature.

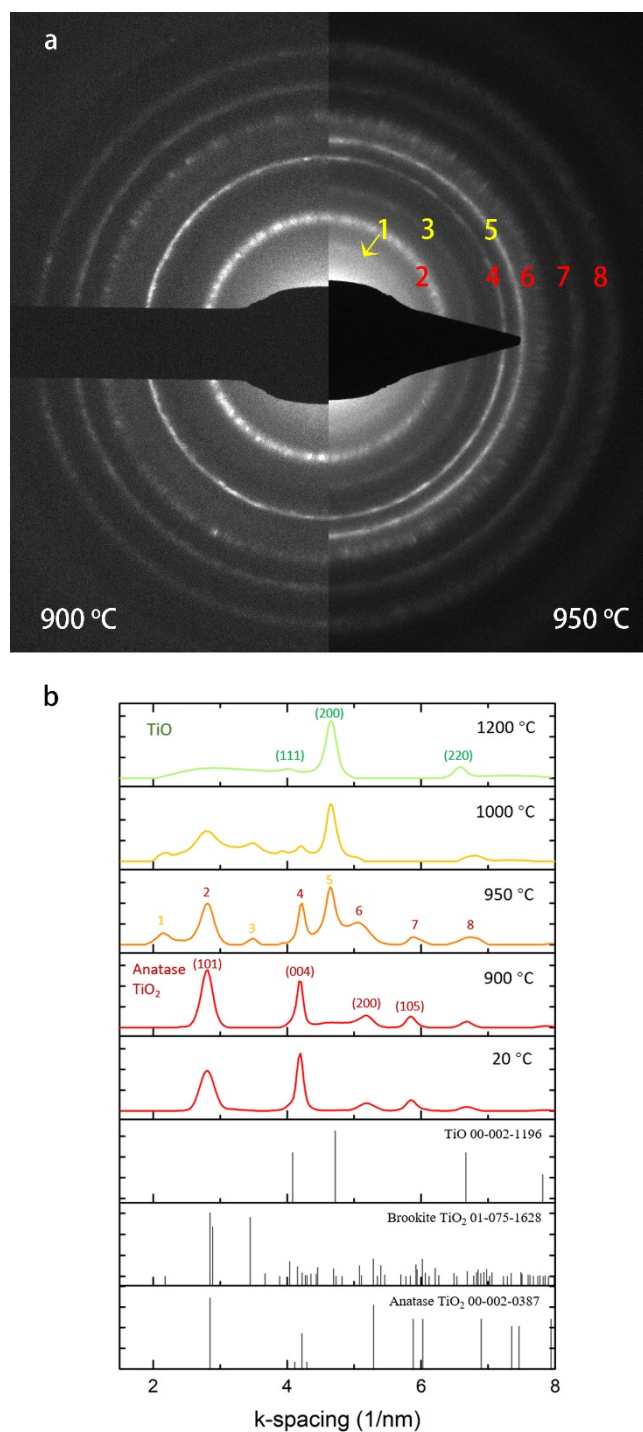


Figure 4-5 Comparison of SADPs at different temperature to show phase transformation. (a) Comparison of SADPs at 900 °C (left) and 950 °C (right) and (b) comparison of integrated DPs at 20 °C, 900 °C, 950 °C, 1000 °C and 1200 °C. The peaks at 950 °C are marked the same color as that of with the corresponding rings in the DP. The XRD reference spectra of anatase, brookite and cubic TiO are shown at the bottom.

To verify that the transformation to TiO also takes place at high concentrations of anatase NRs, a larger amount of sample was dropcast on a heating chip and heated in-situ to a temperature of

1200 °C. The result is displayed in Figure S 4-7. In particular from the SADP in panel (a) it is also clear that when a larger amount of NRs are heated, the anatase NRs fully transform to rock-salt TiO. From the TEM images in panels (b,c), it is clear that part of the material has sublimated and that some of the material has aggregated. The only difference with the heating results of the low-concentration deposited samples is that for the high-concentration deposited sample, the average TiO particle size after heating is larger than that in the experiments where only a monolayer or less of anatase nanoparticles is dropcast.

Ex-situ heating was conducted as a reference measurement and to further exclude the effect of electron illumination. NRs were heated by using the heating holder inserted in a vacuum chamber instead of in the TEM (see Experimental Section for details). After heating to 1200 °C, the sample was cooled down and moved to the microscope for electron diffraction analysis and EM characterization. The DP after ex-situ heating is shown in Figure S 4-8, in which peaks corresponding to anatase, rutile and TiO are all detected. This means that, when heating outside the microscope, the transformation to TiO is not complete. Some of the sample remained in the anatase phase and some of it transformed to rutile. The (partial) transformation to rutile can be expected under conditions of heating to high temperatures (1200 °C) while the oxygen partial pressure is not sufficiently low, as will be discussed in more detail below.

Appearance of the rutile phase upon heating of anatase or brookite nanoparticles has been reported in previous works. Koparde and Cummings⁶⁴ investigated the phase transformation between anatase and rutile by molecular dynamics (MD) simulations. Their results show that nanoparticles larger than 1.65 nm are stable as rutile. They found that when anatase was sintered with amorphous TiO₂, a brookite agglomerate was obtained. They also expressed the expectation that brookite would transform to rutile with a longer simulation time. Mao et al.⁶⁵ investigated the sintering-induced phase transformation from anatase to brookite at 1200 °C with MD, and also predicted the further transformation to rutile. All their prediction of the formation of brookite is in good agreement with our observation of brookite as the intermediate phase during the in-situ experiment. Moreover, the final transformation to rutile is in agreement with the ex-situ heating results. We mention here that the force-field molecular dynamics simulations, in general, are not suited for the simulation of chemical transitions where the valence state of the metal ions changes. That in our case a transformation to cubic TiO took place rather than further transformation to rutile, can be plausibly explained by the low-pressure experimental conditions associated with heating in the electron microscope, as discussed in our recent work on the transformation of Co₃O₄ to CoO nanoparticles.⁶¹ The temperature at which dissociation reactions take place is in general strongly dependent on the partial oxygen pressure, also when the total pressure and, therefore, the partial oxygen pressure (always expressed with respect to the standard pressure) are low.⁶⁶ In the present case, the dissociation reaction is TiO₂ (anatase) -> TiO + ½ O₂. In the vacuum inside the column of the TEM, oxygen atoms are continuously removed from the system, yielding a

very low partial oxygen pressure, thereby driving the transformation to a phase with lower oxygen content, which here is γ -TiO. When the heating took place in the vacuum chamber, the overall pressure (about 10⁻³ Pa) is not as low as that in the microscope (about 10⁻⁶ Pa). Consequently, the partial oxygen pressure (which is at most equal to the overall pressure in vacuum chambers) will be considerably lower in the TEM column than in the ex-situ vacuum chamber. The different oxygen partial pressure in the ex-situ chamber is most likely the reason that only part of the sample transformed to TiO while some of the nanoparticles transformed to rutile. Rutile is the most stable phase for TiO₂ in general, and will be eventually formed when the transformation to TiO does not fully take place.

The structural transformation to TiO will be accompanied by a drastic change in physical and chemical properties, as anatase TiO₂ is a well-known semiconductor, while rock-salt TiO is known to be metal and even a superconductor at low temperature.⁵¹⁻⁵³ It is clear that photocatalytic and gas-sensing functionalities are lost when the TiO₂ nanorods transform to rock-salt TiO, as TiO is metallic (a conductor) while both for photocatalysis and gas-sensing, a semiconductor nature of the material is required. The metallic rock-salt TiO nanoparticles may have merit as catalytic particles for other chemical reactions; however, to the best of our knowledge possible catalytic properties of nanoscale rock-salt TiO are yet to be explored.

4.4 Conclusion

In this study, anatase TiO₂ nanorods were heated from room temperature to 1200 °C. The morphology of anatase nanorods was found to be stable up to a temperature of 700 °C, after which the surface of nanorods became uneven and the shape started to deform. From 900 °C, the NRs break up into smaller nanoparticles and sometimes coalesced. Therefore, for application under high temperature conditions for either photocatalysis or gas-sensing, anatase NRs can be considered to be structurally stable and retain their functionality until 600 °C. Reduction to cubic γ -TiO was observed starting at temperatures from 950 °C. All nanoparticles had completely reduced to γ -TiO at 1200 °C. In the temperature range between 950 °C and 1000 °C, the brookite phase appeared as an intermediate phase. Then the nanocrystals exhibiting this intermediate phase completely reduced to γ -TiO after heating to 1200 °C. The size range of 9.2±2.1 nm of the rock-salt TiO nanocrystals is an order of magnitude smaller than that of TiO nanopowders and we propose the observed transformation mechanism as a physical route to the synthesis of TiO nanoparticles of very small size. The TiO nanocrystals will not have photocatalytic or gas-sensing functionalities as these particles are metallic rather than semiconducting; however, the synthesis of nanoscale rock-salt TiO opens up opportunities for future investigations of their physical and chemical properties including electronic and catalytic functionalities.

Considering the applicability of photocatalysis and gas sensor devices based on anatase NRs, we infer from our analysis of the thermal evolution that their functionality is expected to be retained at operation temperatures up to 600 °C, while above that temperature, their functionality likely degrades. As mentioned, the functionalities of rock-salt TiO NCs are yet to be explored.

4.5 Acknowledgments

This Chapter was performed with collaboration with Seyed Naveed Hosseini (nanorods synthesis). We thank Dr. Rafael Greogorio Mendes for help with the HR-STEM characterization. We thank Prof. Alfons van Blaaderen, Dr. Arnout Imhof and Dr. Patrick Baesjou for useful discussions.

Figures of atomic structural models were produced using VESTA.⁶⁷

4.6 References

- 1 C. J. Howard, T. M. Sabine and F. Dickson, *Acta Crystallogr. Sect. B*, 1991, **47**, 462–468.
- 2 E. P. Meagher and G. A. Lager, *Can. Mineral.*, 1979, **17**, 77–85.
- 3 D. T. Cromer and K. Herrington, *J. Am. Chem. Soc.*, 1955, **77**, 4708–4709.
- 4 F. De Angelis, C. Di Valentin, S. Fantacci, A. Vittadini and A. Selloni, *Chem. Rev.*, 2014, **114**, 9708–9753.
- 5 R. G. Breckenridge and W. R. Hosler, *Phys. Rev.*, 1953, **91**, 793–802.
- 6 G. Fazio, L. Ferrighi and C. Di Valentin, *J. Phys. Chem. C*, 2015, **119**, 20735–20746.
- 7 M. A. Henderson, *Surf. Sci. Rep.*, 2011, **66**, 185–297.
- 8 A. FUJISHIMA, X. ZHANG and D. TRYK, *Surf. Sci. Rep.*, 2008, **63**, 515–582.
- 9 T. L. Thompson and J. T. Yates, *Chem. Rev.*, 2006, 106, 4428–4453.
- 10 L. Kavan, M. Grätzel, S. E. Gilbert, C. Klemenz and H. J. Scheel, *J. Am. Chem. Soc.*, 1996, **118**, 6716–6723.
- 11 M. Rashidzadeh, *Int. J. Photoenergy*, 2008, **2008**, 1–4.
- 12 T. Bak, J. Nowotny, M. Rekas and C. . Sorrell, *Int. J. Hydrogen Energy*, 2002, **27**, 991–1022.
- 13 M. Grätzel, *Nature*, 2001, 414, 338–344.
- 14 O. CARP, *Prog. Solid State Chem.*, 2004, **32**, 33–177.
- 15 P. Periyat, B. Naufal and S. G. Ullattil, *Mater. Sci. Forum*, 2016, **855**, 78–93.
- 16 L. Cao, D. Chen, W. Q. Wu, J. Z. Y. Tan and R. A. Caruso, *J. Mater. Chem. A*, 2017, **5**, 3645–3654.
- 17 V. Kumaravel, S. Rhatigan, S. Mathew, J. Bartlett, M. Nolan, S. J. Hinder, P. K. Sharma, A. Singh, J. A. Byrne, J. Harrison and S. C. Pillai, *J. Phys. Chem. C*, 2019, **123**, 21083–21096.
- 18 B. M. Rao and S. C. Roy, *RSC Adv.*, 2014, **4**, 38133–38139.
- 19 S. C. Pillai, P. Periyat, R. George, D. E. McCormack, M. K. Seery, H. Hayden, J. Colreavy, D. Corr and S. J. Hinder, *J. Phys. Chem. C*, 2007, **111**, 1605–1611.
- 20 V. Etacheri, M. K. Seery, S. J. Hinder and S. C. Pillai, *Adv. Funct. Mater.*, 2011, **21**, 3744–3752.
- 21 J. Malallah Rzaij and A. Mohsen Abass, *J. Chem. Rev.*, 2020, **2**, 114–121.
- 22 B. Karunagaran, P. Uthirakumar, S. J. Chung, S. Velumani and E. K. Suh, *Mater. Charact.*, 2007, **58**, 680–684.
- 23 B. C. Sertel, N. A. Sonmez, M. D. Kaya and S. Ozcelik, *Ceram. Int.*, 2019, 45, 2917–2921.
- 24 Z. Li, Z. J. Yao, A. A. Haidry, T. Plecenik, L. J. Xie, L. C. Sun and Q. Fatima, *Int. J. Hydrogen Energy*, 2018, 43, 21114–21132.
- 25 A. S. Barnard and P. Zapol, *Phys. Rev. B*, , DOI:10.1103/PhysRevB.70.235403.
- 26 P. D. Cozzoli, A. Kornowski and H. Weller, *J. Am. Chem. Soc.*, 2003, **125**, 14539–14548.
- 27 S. N. Hosseini, A. Grau-Carbonell, A. G. Nikolaenkova, X. Xie, X. Chen, A. Imhof, A. Blaaderen and P. J. Baesjou, *Adv. Funct. Mater.*, 2020, **30**, 2005491.
- 28 D. A. H. Hanaor and C. C. Sorrell, *J. Mater. Sci.*, 2011, 46, 855–874.
- 29 W. X. Xu, S. Zhu, X. C. Fu and Q. Chen, *Appl. Surf. Sci.*, 1999, **148**, 253–262.

- 30 R. Ren, Z. Yang and L. L. Shaw, *J. Mater. Sci.*, 2000, **35**, 6015–6026.
- 31 A. A. Valeeva, I. B. Dorosheva, E. A. Kozlova, R. V. Kamalov, A. S. Vokhmintsev, D. S. Selishchev, A. A. Saraev, E. Y. Gerasimov, I. A. Weinstein and A. A. Rempel, *J. Alloys Compd.*, 2019, **796**, 293–299.
- 32 K. Li, J. Xu, W. Shi, Y. Wang and T. Peng, *J. Mater. Chem. A*, 2014, **2**, 1886–1896.
- 33 H. Kominami, M. Kohno and Y. Kera, *J. Mater. Chem.*, 2000, **10**, 1151–1156.
- 34 A. S. Barnard and L. A. Curtiss, *Nano Lett.*, 2005, **5**, 1261–1266.
- 35 H. Zhang and J. F. Banfield, *J. Mater. Res.*, 2000, **15**, 437–448.
- 36 A. A. Gribb and J. F. Banfield, *Am. Mineral.*, 1997, **82**, 717–728.
- 37 H. Zhang and J. F. Banfield, *J. Mater. Chem.*, 1998, **8**, 2073–2076.
- 38 H. Zhang and J. F. Banfield, *J. Phys. Chem. B*, 2000, **104**, 3481–3487.
- 39 K. Sohlberg, X. Nie, S. Zhuo and G. Maeng, *Int. J. Photoenergy*, , DOI:10.1155/2009/294042.
- 40 X. Bokhimi, A. Morales, E. Ortíz, T. López, R. Gómez and J. Navarrete, *J. Sol-Gel Sci. Technol.*, 2004, **29**, 31–40.
- 41 W. Hu, L. Li, G. Li, C. Tang and L. Sun, *Cryst. Growth Des.*, 2009, **9**, 3676–3682.
- 42 A. S. Barnard, P. Zapol and L. A. Curtiss, *J. Chem. Theory Comput.*, 2005, **1**, 107–116.
- 43 S. Bakardjieva, V. Stengl, L. Szatmary, J. Subrt, J. Lukac, N. Murafa, D. Niznansky, K. Cizek, J. Jirkovsky and N. Petrova, *J. Mater. Chem.*, 2006, **16**, 1709.
- 44 T. Zhu and S. P. Gao, *J. Phys. Chem. C*, 2014, **118**, 11385–11396.
- 45 B. M. Pabón, J. I. Beltrán, G. Sánchez-Santolino, I. Palacio, J. López-Sánchez, J. Rubio-Zuazo, J. M. Rojo, P. Ferrer, A. Mascaraque, M. C. Munõz, M. Varela, G. R. Castro and O. R. De La Fuente, *Nat. Commun.*, 2015, **6**, 1–6.
- 46 R. Hengerer, B. Bolliger, M. Erbudak and M. Grätzel, *Surf. Sci.*, 2000, **460**, 162–169.
- 47 A. Bouzoubaa, A. Markovits, M. Calatayud and C. Minot, *Surf. Sci.*, 2005, **583**, 107–117.
- 48 S. Amano, D. Bogdanovski, H. Yamane, M. Terauchi and R. Dronskowski, *Angew. Chemie*, 2016, **128**, 1684–1689.
- 49 J. L. Murray and H. A. Wriedt, *J. Phase Equilibria*, 1987, **8**, 148–165.
- 50 S. Bartkowski, M. Neumann, E. Z. Kurmaev, V. V. Fedorenko, S. N. Shamin, V. M. Cherkashenko, S. N. Nemnonov, A. Winiarski and D. C. Rubie, *Phys. Rev. B*, 1997, **56**, 10656–10667.
- 51 C. Zhang, F. Hao, G. Gao, X. Liu, C. Ma, Y. Lin, Y. Yin and X. Li, *npj Quantum Mater.*, 2017, **2**, 1–5.
- 52 J. K. Hulm, C. K. Jones, R. A. Hein and J. W. Gibson, *J. Low Temp. Phys.*, 1972, **7**, 291–307.
- 53 D. Wang, C. Huang, J. He, X. Che, H. Zhang and F. Huang, *ACS Omega*, 2017, **2**, 1036–1039.
- 54 J. Blazevska-Gilev, V. Jandová, J. Kupčík, Z. Bastl, J. Šubrt, P. Bezdička and J. Pola, *J. Solid State Chem.*, 2013, **197**, 337–344.
- 55 T. T. N. Nguyen and J. L. He, *Adv. Powder Technol.*, 2016, **27**, 1868–1873.
- 56 A. A. Valeeva, K. A. Petrovykh, H. Schroettner and A. A. Rempel, *Inorg. Mater.*, 2015, **51**, 1132–1137.
- 57 Y. Wei, Y. Shi, X. Zhang, D. Li, L. Zhang, C. Gong and J. Zhang, *Adv. Powder Technol.*,

-
- 2020, **31**, 3458–3464.
- 58 A. A. Valeeva, S. Z. Nazarova and A. A. Rempel, *Phys. Solid State*, 2016, **58**, 771–778.
- 59 P. Simon, B. Pignon, B. Miao, S. Coste-Leconte, Y. Leconte, S. Marguet, P. Jegou, B. Bouchet-Fabre, C. Reynaud and N. Herlin-Boime, *Chem. Mater.*, 2010, **22**, 3704–3711.
- 60 M. A. Van Huis, N. P. Young, G. Pandraud, J. F. Creemer, D. Vanmaekelbergh, A. I. Kirkland and H. W. Zandbergen, *Adv. Mater.*, 2009, **21**, 4992–4995.
- 61 X. Chen, H. Van Gog and M. A. Van Huis, *J. Mater. Chem. C*, 2021, **9**, 5662–5675.
- 62 J. Joo, S. G. Kwon, T. Yu, M. Cho, J. Lee, J. Yoon and T. Hyeon, *J. Phys. Chem. B*, 2005, **109**, 15297–15302.
- 63 P. K. Naicker, P. T. Cummings, H. Zhang and J. F. Banfield, *J. Phys. Chem. B*, 2005, **109**, 15243–15249.
- 64 V. N. Koparde and P. T. Cummings, *ACS Nano*, 2008, **2**, 1620–1624.
- 65 Q. Mao, Y. Ren, K. H. Luo and S. Li, *J. Phys. Chem. C*, 2015, **119**, 28631–28639.
- 66 A. Navrotsky, C. Ma, K. Lilova and N. Birkner, *Science (80-.)*, 2010, **330**, 199–201.
- 67 K. Momma and F. Izumi, *J. Appl. Crystallogr.*, 2011, **44**, 1272–1276.

4.7 Appendix

4.7.1 Supporting Figures

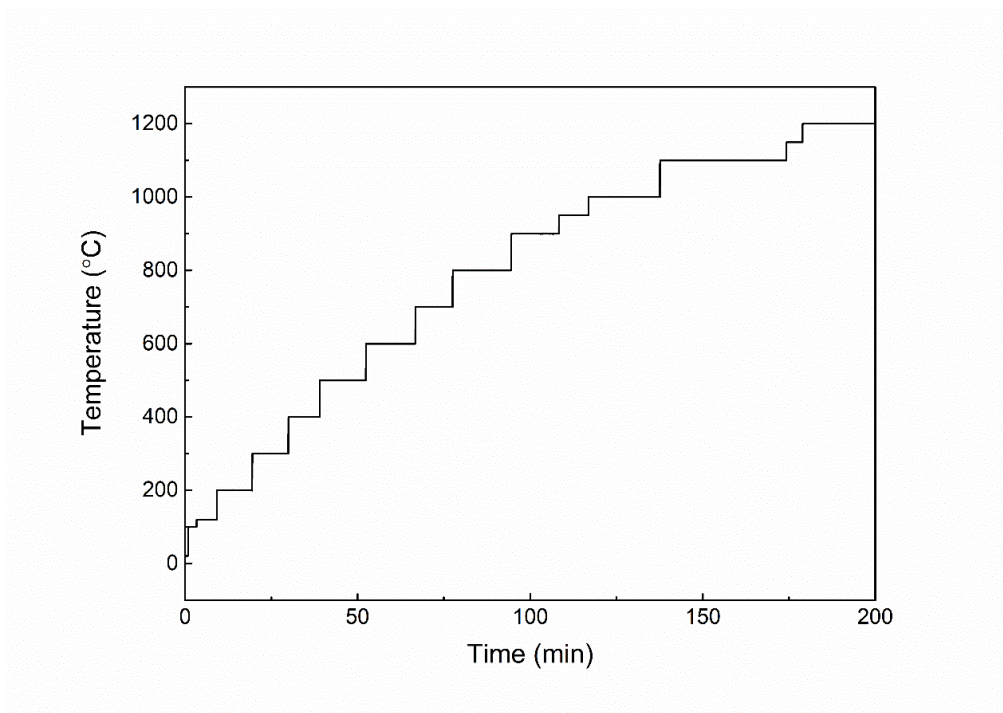


Figure S 4-1 Typical heating temperature profile of the experiments (the heating profile of one actual experiment is shown). The experiments were conducted several times, some steps may take longer time for more inspections, which does not affect the final result.

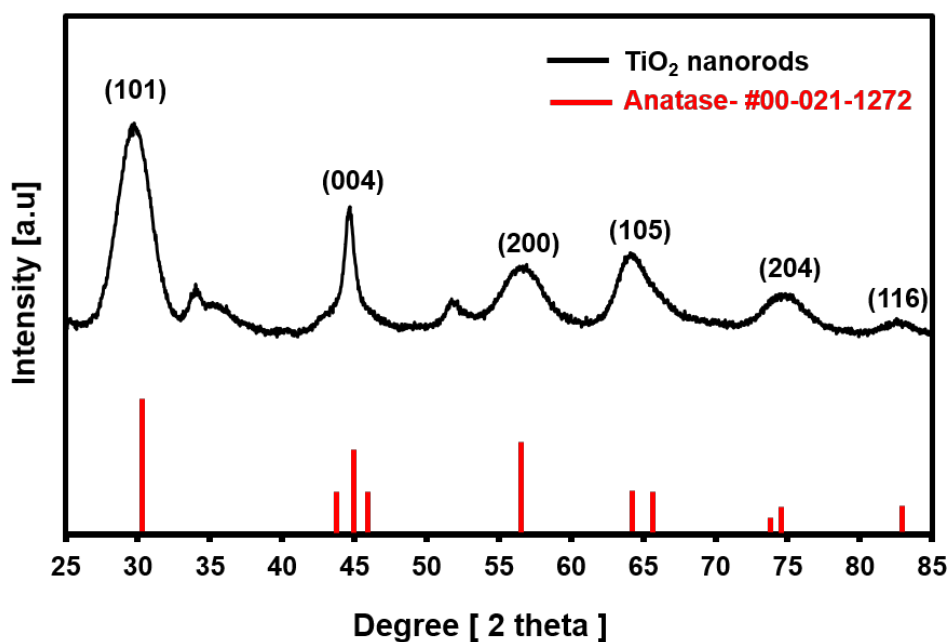


Figure S 4-2 X-ray diffraction spectrum of the as-synthesized TiO₂ NRs, confirming the anatase crystallographic phase.

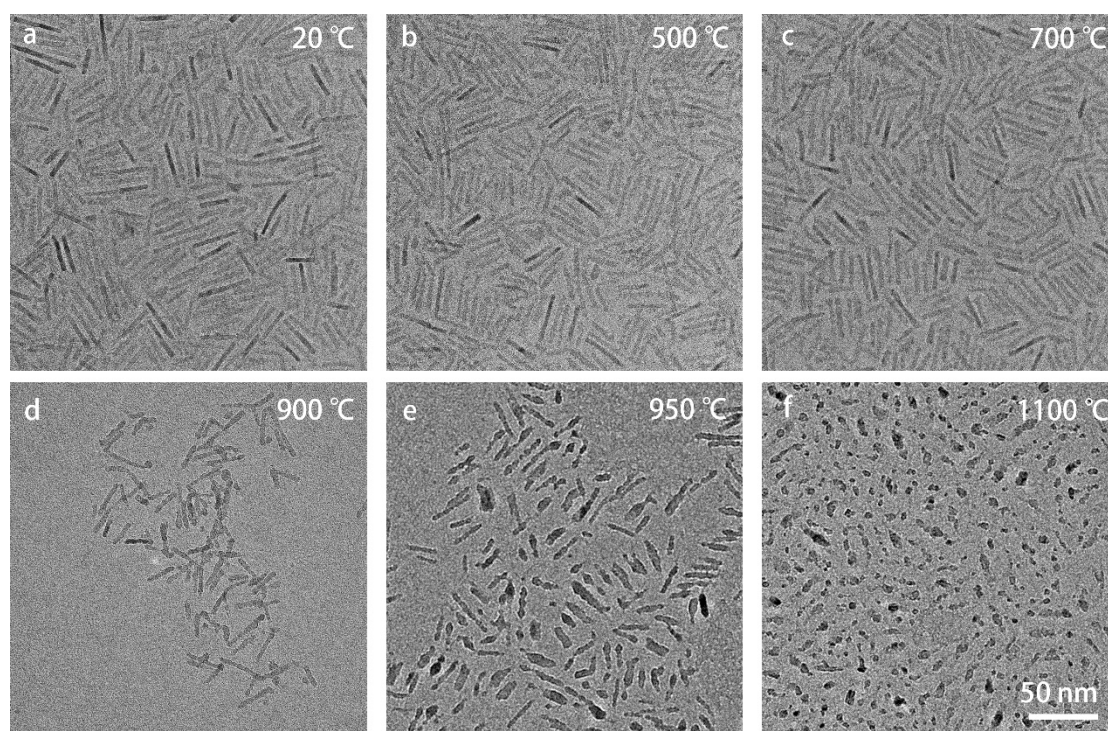


Figure S 4-3 Bright-field TEM images of TiO_x nanocrystals during heating. Some of the nanorods appear darker due to diffraction contrast. Upon heating to 500 °C, the edges became rounded. At 700 °C, the surfaces of the nanorods deformed more and are no longer sharp. At 900 °C, some nanorods broke up into multiple segments, and sometimes neighboring rods had coalesced. Upon heating to 1000 °C, most nanorods had transformed into smaller nanoparticles.

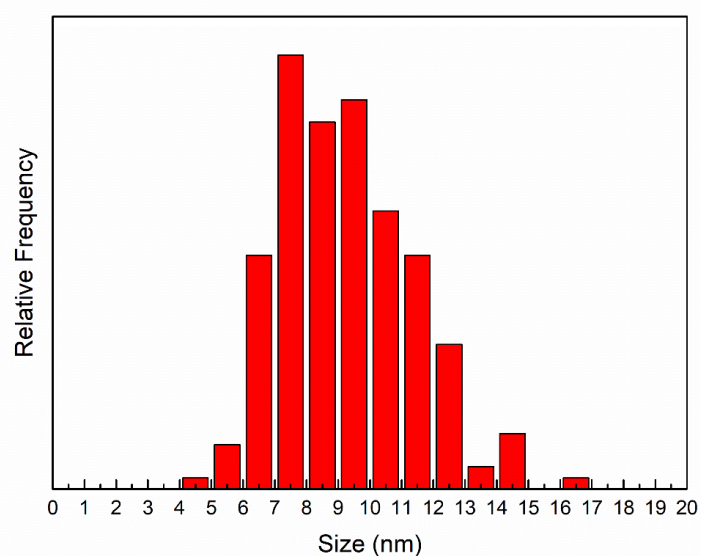


Figure S 4-4 Size distribution plot of TiO nanoparticles obtained after heating to 1200 °C, measured after cooling down to room temperature. The sizes of 200 particles are included for the statistics.

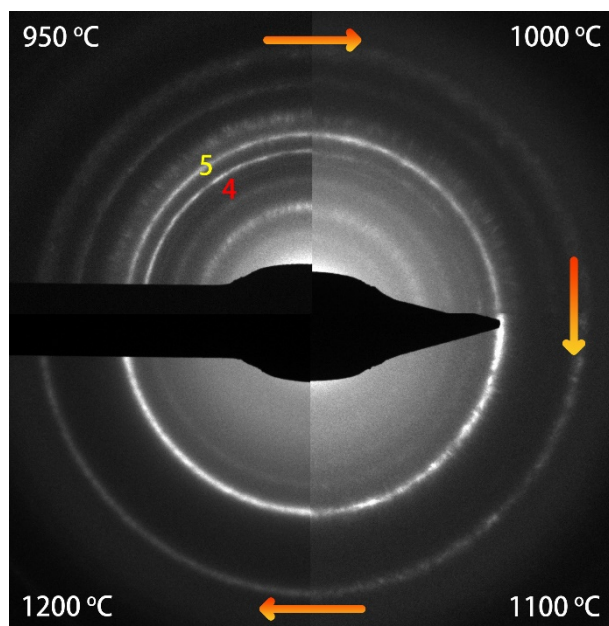


Figure S 4-5. Comparison of selected area diffraction patterns (SADPs) of TiO_x at temperatures of 950 °C (top-left), 1000 °C (top-right), 1100 °C (bottom-right), and 1200 °C (bottom-left). The rings corresponding the anatase phase (ring #4 and other inner rings) disappeared gradually, and finally only rings belonging to cubic TiO remain. Ring #5 corresponding to (200) of TiO appeared at 950 °C, and remained until 1200 °C.

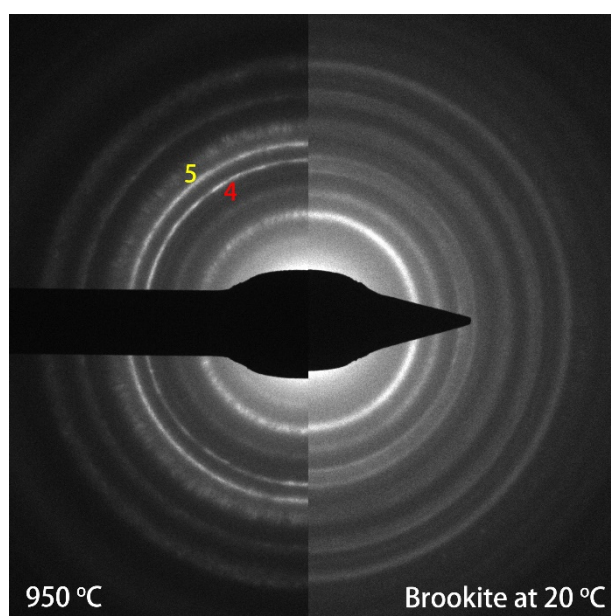


Figure S 4-6. Electron diffraction pattern (DP) of the sample annealed at 950 °C (left) and DP of pure brookite nanorods at room temperature (right). Most of the rings in both DPs are the same, except for ring No. 4 and 5 at 950 °C. Ring No. 4 corresponds to the anatase (004) reflection and ring No. 5 corresponds to the TiO (200) reflection.

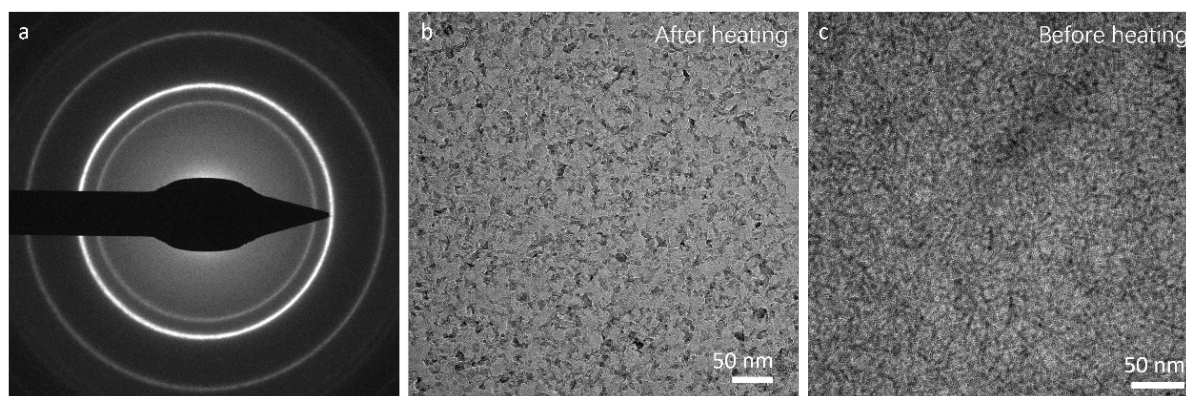


Figure S 4-7. Result of in-situ heating of very high concentration NRs to 1200 °C. (a) DP. (b) TEM image taken after heating. (c) TEM image taken at room temperature before heating. The diffraction pattern shows rock-salt TiO structure. The NRs sublimated during heating.

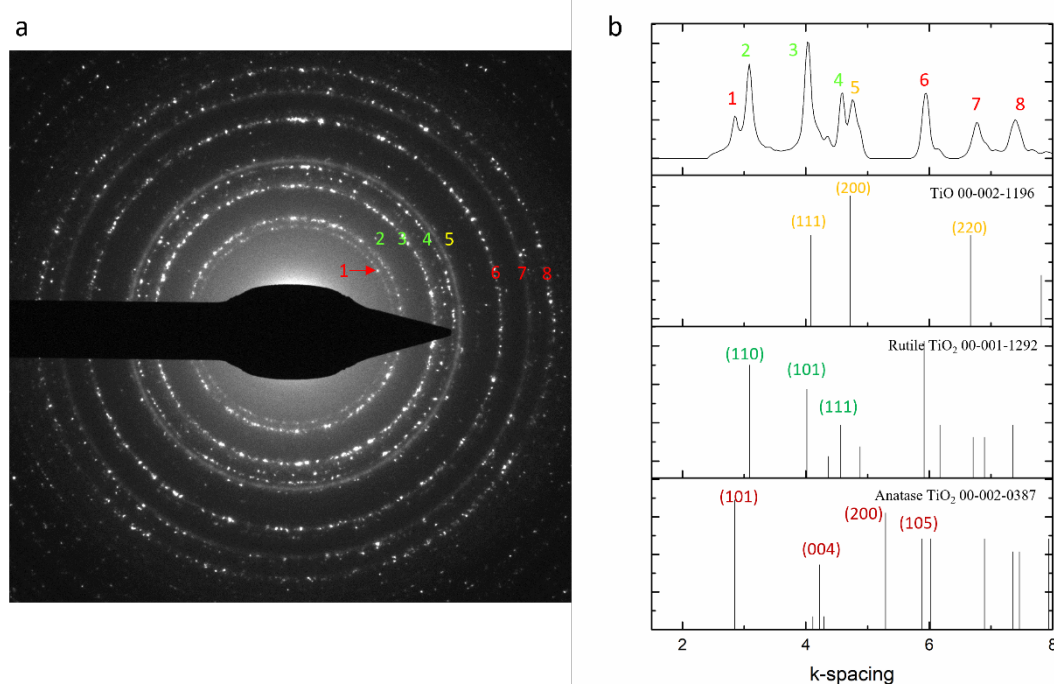


Figure S 4-8. Diffraction pattern (DP) of the sample after heating in a vacuum chamber to 1200 °C with the same heating rate as used in the electron microscope. The DP shows a mixture of anatase, rutile and cubic TiO phases. (a) The diffraction pattern; (b) integrated DP compared with the XRD spectra of anatase, rutile, and cubic TiO. The peaks in the DP are marked with different colors and correspond to lattice reflections of different phases. Ring #1 correspond to the anatase structure. Rings # 2-4 correspond to the rutile structure. Ring #5 corresponds to cubic TiO. Rings #6-8 are close to both the anatase and rutile structures.

5. Heating-induced transformation of brookite

TiO₂ nanorods

Here we report the thermal evolution of brookite nanorods (NRs) with a length of 42.2 nm and diameter of 5.1 nm. The evolution of morphologies and crystalline structures was monitored by in situ TEM. Some of the brookite NRs transformed to rutile TiO₂ or rock salt TiO, or to both, at 1100 °C. The post-treatment of the NRs was found to influence the transformations at high temperatures. For the as-synthesized NRs without post-treatment, the NRs are (nearly) in contact and have a high packing density. The processes of deformation and coalescence set in sooner and there is a tendency for the NRs to transform to rutile. For post-treated NRs, the ligand density is higher on the NRs surface. Sublimation dominated above 1000 °C, and small particles were formed. In general, most NRs retained the brookite phase at these high temperatures, while rock salt TiO was likely formed in the very smallest of nanoparticles.

5.1 Introduction

Where in the previous Chapter the thermal evolution of anatase TiO₂ nanorods and their transformation to rock salt TiO was investigated, in the present chapter an investigation into the thermal stability of brookite TiO₂ nanorods (NRs) is pursued. I refer to the previous chapter for a general introduction about titania in bulk and nanocrystalline form. As mentioned in previous Chapter, the brookite phase is one of the commonly occurring phases of TiO₂. Although brookite is usually reported to be an unstable (bulk) phase, nanostructured brookite is metastable and suitable for particular applications in photocatalysis and optoelectronics.¹⁻⁵ Brookite particles in nanoscale form have been synthesized with different shapes and sizes by many different ways⁶⁻¹³.

The thermal behavior and stability of nanoparticles are of vital importance to their performances and consequently to the corresponding applications. There are studies showing that with changing temperature, the photocatalytic activity of brookite samples changed and showed a peak performance at 500 °C.^{8,14} Many studies showed the transformation from brookite to rutile at elevated temperature, where sometimes anatase was formed in an intermediate stage. The critical temperature differs depending on shapes and sizes, as well as on heating and environmental conditions.

In this chapter, the thermal evolution of brookite NRs in vacuum is investigated. The brookite NRs are on average 42.2 nm long and have an average diameter of 5.1 nm, and have their [001] crystallographic axis along the length of the rod. The brookite NRs transformed to rutile TiO₂ or rock salt TiO, or to both, at a temperature of 1100 °C. The structural evolution is influenced by the concentration of pristine NRs dropped on the heating chips. In the areas with a high concentration, the NRs were more prone to deformation, underwent more coalescence, and were inclined to transform to rutile. At low concentrations, sublimation dominated above 1000 °C, where small particles were formed with a mixture of phases probably including the rock salt TiO phase.

5.2 Experimental

5.2.1 Synthesis

Materials and Modified Synthesis Method: Monodisperse brookite titanium dioxide (TiO₂) NRs were synthesized following a slightly modified and scaled-up version of the synthesis as described by Murray et al.^{13,15,16}

In a typical synthesis of brookite NRs, OLAC (5.0 ml), OLAM (100.0 ml), and 1-ODE (100.0 ml) were mixed in a three-neck round-bottom flask and heated at 120 °C for 1 hour. Afterward, the flask was cooled down under vacuum to 60 °C, followed by switching to nitrogen and the swift addition of

a stock solution of TiCl_4 (15.0 ml), which was prepared in the glove box and consisted of TiCl_4 (0.2 M) and OLAC (1.0 M) in 1-ODE. Then, the solution was heated to 290 °C (heating ramp of ~ 20 °C min^{-1}) and held for 30 minutes to form anatase seeds. After seed formation, based on the desired length of the final brookite NRs, various amounts of stock solution were added to the solution by employing a KDS syringe pump system at a rate of 0.25 ml/min. Here, 50.0 ml of the stock solution were injected. In the case of long brookite NRs, the concentration of the main batch, stock solution, and also the injection rate were changed. Initially, the main batch (a mixture of OLAC (1.9 ml), OLAM (51.0 ml), and 1-ODE (12.0 ml)) was degassed at 120 °C for an hour. Then, it was cooled down under vacuum to 60 °C and switched to nitrogen. In this step, (1.5 ml) from a new stock solution (consisted of TiCl_4 (0.5 M) and OLAC (1.0 M) in 1-ODE) was quickly added to the main batch and then (15.0 mL) of the same stock solution was injected dropwise by using a KDS syringe pump system over the course of 150 minutes at 290 °C. The heating mantle was then removed, and the flask was allowed to cool to room temperature. Excess ligand and unreacted precursors were removed from the crude reaction product initially by centrifugation at 6000 rcf for 10 min and then by redispersion and precipitation of the NRs using toluene and ethanol as a solvent/antisolvent pair. We chose toluene as a solvent in purification steps since it has a high refractive index which reduces the van der Waals attractions between the rods and also is a good solvent for OLAC. It has been shown that hexane has higher miscibility with oleic acid than toluene and can strip ligands off in the presence of antisolvent, while in toluene ligands prefer to remain at the surface of the NPs.¹⁷ A size-selective precipitation process was needed to improve the length monodispersity. Therefore, the NRs were dissolved in toluene and acetone was added gently to the dispersion until the mixture became turbid. The mixture was then centrifuged at 3400 rcf for 5 min to isolate the nanocrystals as a precipitate. The supernatant was discarded and the length polydispersity improved up to 10.3%. Finally, the precipitates were redispersed in toluene at the desired concentration and will be referred to as-synthesized brookite NRs.

Post-Treatment of Brookite Nanorods: As-synthesized brookite NRs dispersed in toluene were mixed with OLAC in a 1:5 volume ratio, heated at 75 °C under vacuum, degassed for 15 min, and stirred under nitrogen overnight similar to the literature reported for iron oxide nanoparticles.¹⁸ The resulting NRs were collected by precipitation with the antisolvent ethanol, centrifugation at 8000 rcf for 5 min and re-dispersion in toluene. This post-treatment procedure was repeated twice and ultimately the highly sterically stabilized brookite NRs were re-dispersed in toluene in dilute dispersions. Dispersions with the desired concentration were prepared by careful solvent evaporation.

5.2.2 TEM characterization

Bright-field TEM images and selected-area diffraction patterns (SADPs) were recorded using a TFS TalosF200X TEM operating at 200 kV. High-resolution TEM images were recorded on a TFS Titan

TEM with aberration correction for imaging and operating at 300 kV, using a DE16 direct detection camera. The specimens were prepared by drop casting the TiO₂ nanorods solution onto a DENSsolutions MEMS heating chip.

The TiO₂ specimens were first heated from 20 °C to 1100 °C with 100 °C increments. The inspected area of the sample was changed very often to areas not previously exposed to the electron beam, in order to exclude any possible beam-induced effects. The transformations reported in this work were found to occur everywhere on the heating chip, also in areas not previously exposed to the electron beam. Furthermore, in order to fully exclude any electron beam effects, the samples were also heated ex-situ outside of the TEM. For these ex-situ experiments, the samples were heated with the heating holder inserted in a high vacuum chamber (Gatan pumping station Model 655), applying the same heating rate as in the in-situ heating experiments. The pressure in the high vacuum chamber was approximately $1.0 \cdot 10^{-4}$ Pa. After holding the temperature at 1100 °C for 15 min, the sample was cooled down fast to room temperature and swiftly inserted in the TEM for subsequent analysis.

5.3 Results and discussion

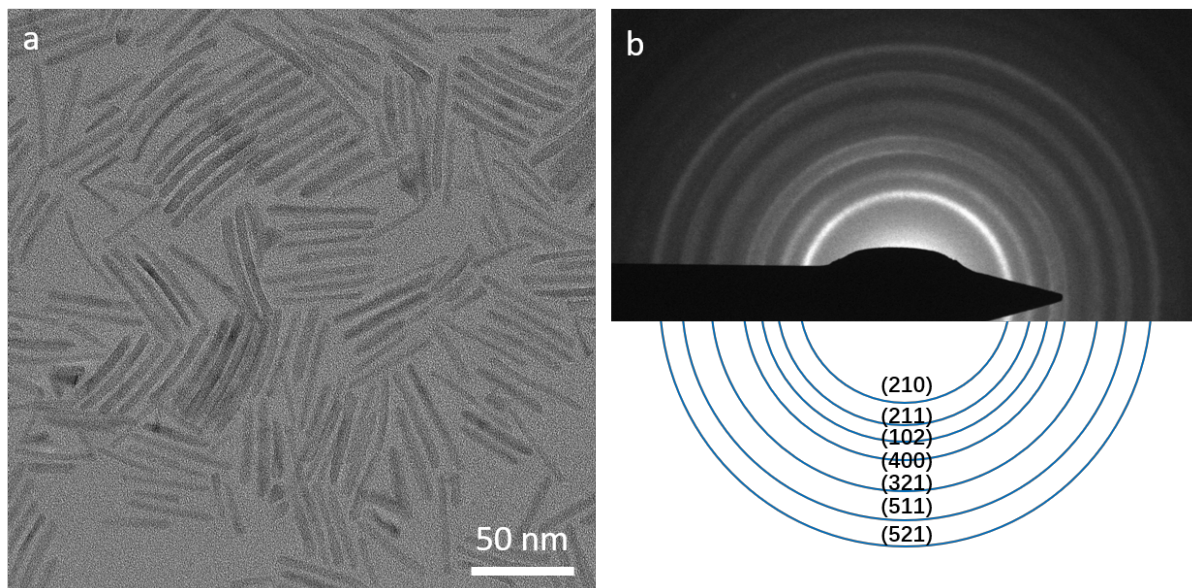


Figure 5-1 TEM images of post-treated brookite NRs at room temperature. (a) bright-field TEM image. (b) SADP with theoretical rings and corresponding lattice planes.

Brookite NRs with and without post-treatment (see Synthesis section above) were both heated and showed different behavior. In a previous study,¹³ where the NRs were not post-treated, the ligand density on the surface of the NRs was less than in the case of post-treated NRs. Due to the lower ligand density the NRs aggregated during drying, resulting in big assemblies and clusters with more

than one layer of NRs. In contrast, when the NRs were post-treated, there were less attractions between the NRs, and they spread evenly on the heating chip. As shown Figure 5-1 (a), there is only one layer NRs. The SADP at room temperature was indexed and is shown in Figure 5-1 (b). The values of indexed peaks in the DP are shown in Table S 5-1.

Figure 5-2 shows the morphological evolution of the post-treated brookite NRs during heating. The NRs here were heated from room temperature to 1100 °C with 100 °C increments. Up to 600 °C, there are not obvious changes in the shapes of the NRs. From 700 °C onward, the surface of the NRs became uneven and some of the NRs began to coalesce. At 900 °C, some NRs broke up and formed shorter rods. With increasing temperature, sublimation dominated. After keeping the sample at a temperature 1100 °C, small particles are found which resulted from (partial) sublimation and also bigger blocks formed through coalescence. Figure S 5-1 shows TEM images recorded at higher magnification. We mention here that, in panel (b) of Figure S 5-1, the NRs already have an uneven surface at 400 °C, which was not found for low magnification images of Figure 5-2. Hence we conclude that the deformation observed in Figure S 5-1 is likely due to beam effects with high intensity electron illumination; it is therefore not possible to continuously follow the whole thermal evolution in high resolution.

When the concentration of pristine NRs is so low that the NRs cannot connect to each other, sublimation took place rather than coalescence. Subsequently the NRs became thinner and shorter, as shown in Figure 5-3.

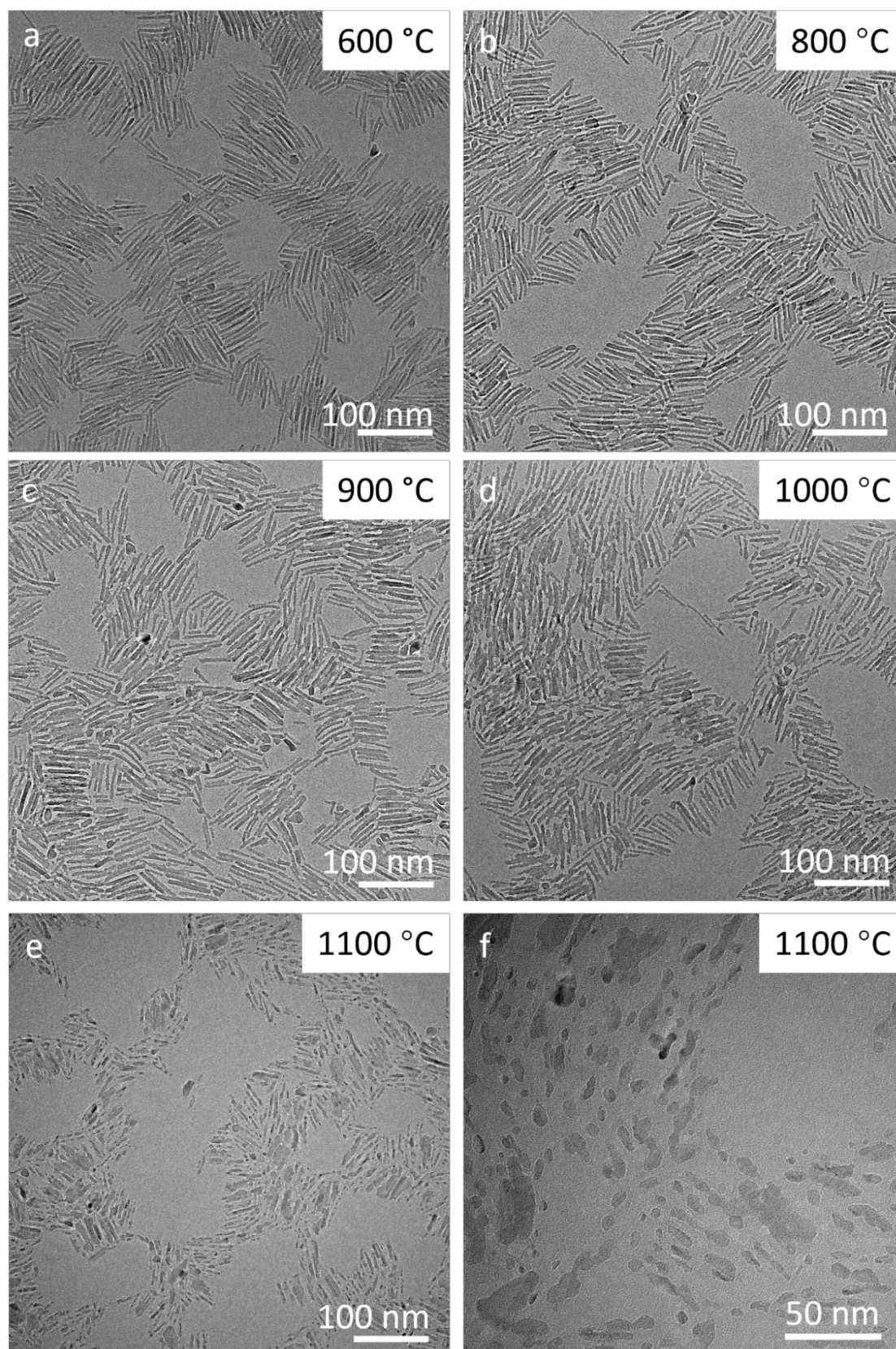


Figure 5-2 Bright-field TEM images of post-treated brookite NRs during heating recorded at the indicated temperatures. The magnification of panels (a-e) is the same. Panel (f) is at a higher magnification than the others.

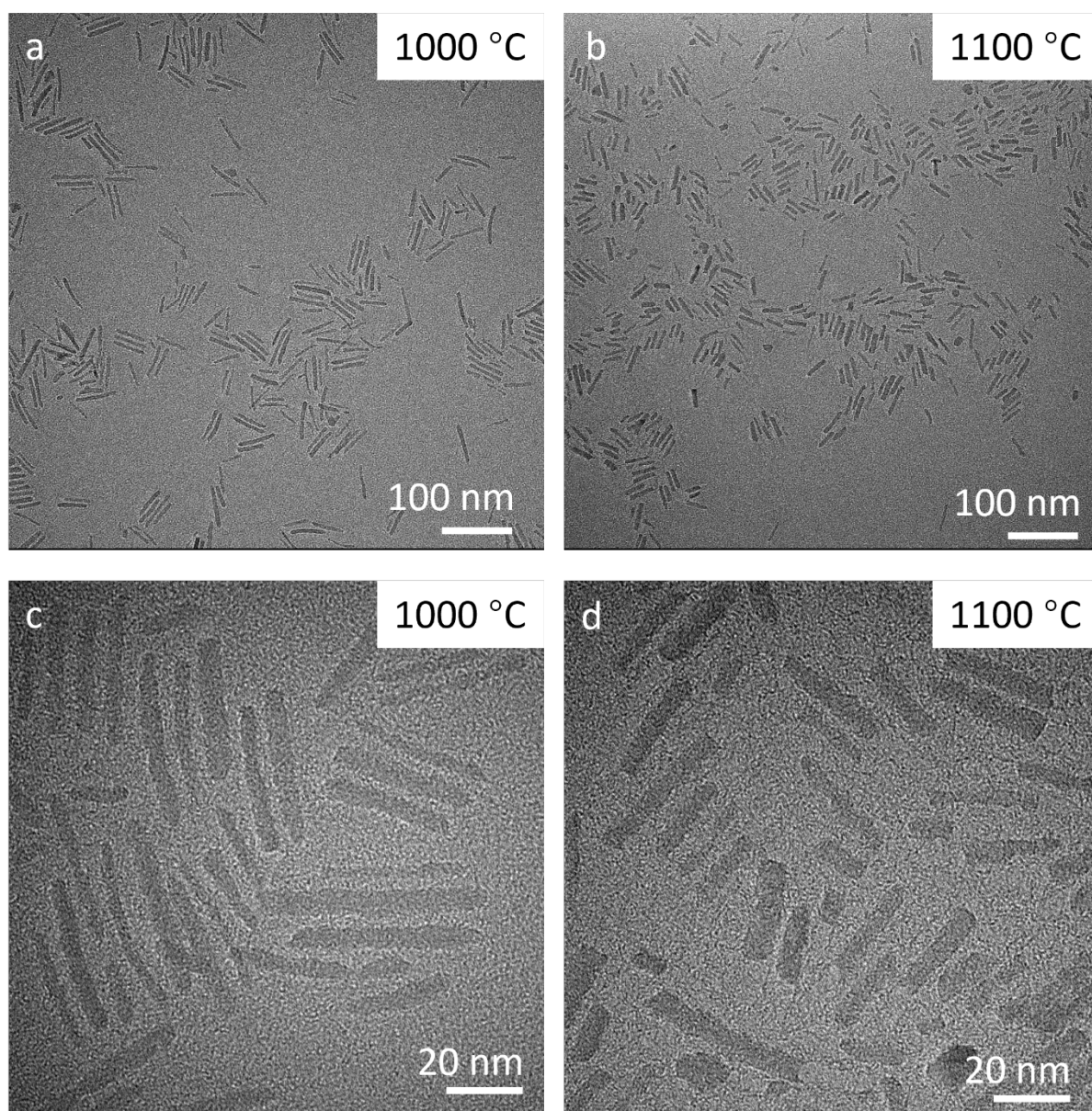


Figure 5-3 Bright-field TEM images of very low concentration brookite NRs at (a,c) 1000 °C and (b,d) 1100°C. Panels (a) and (b) show images at low magnification, panels (c) and (d) at high magnification.

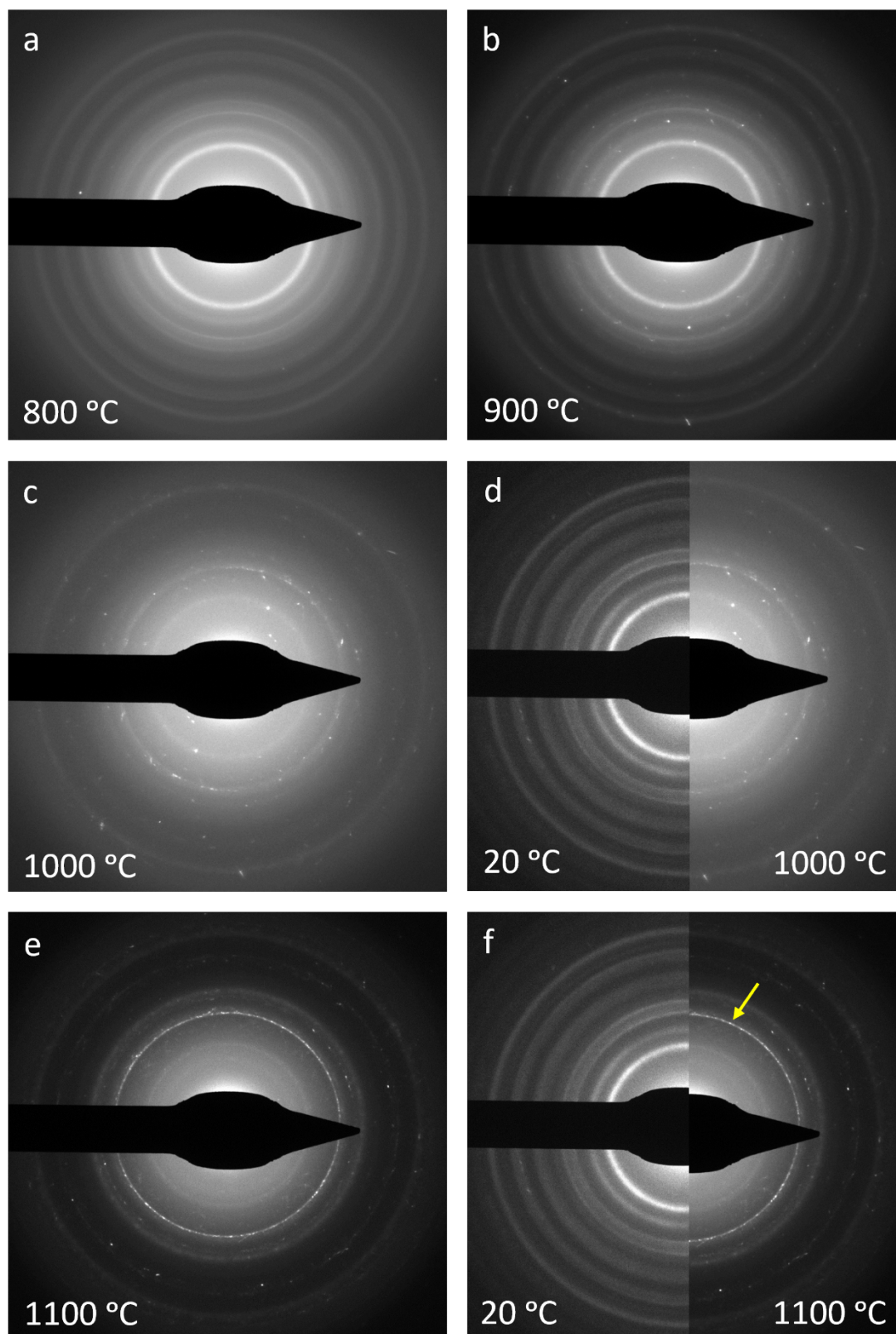


Figure 5-4 Selected area diffraction patterns (SADPs) of the post-treated brookite nanorods at (a) 800 °C, (b) 900 °C, (c) 1000 °C, (e) 1100 °C. (d) Comparison of DPs at 20 °C and at 1000 °C. (f) Comparison of DPs at 20 °C and at 1100 °C. Below 800 °C, the patterns correspond to the brookite crystal structure.

Figure 5-4 (a-c) show the SADPs from 800 °C to 1000 °C. At 800 °C, the DP still corresponds to the brookite crystal structure. At 900 °C, the rings in the DP become weaker and some bright spots are present as well. At 1000 °C, the rings are much weaker, and more spots appeared. Figure 5-4 (d) compares the DPs at 20 °C (left) and 1000 °C (right). The rings at 1000 °C correspond to the brookite phase, indicating that the brookite phase remained until 1000 °C. The bright spots appearing from 900 °C can be attributed to the coalescence of the NRs which makes reflections of some orientations stronger than average. At 1100 °C, the DP looks much different. The 1st ring corresponding to the (210)-brookite reflection became very weak, while the ring corresponding to 2.47 Å (marked by the arrow) became sharper and with an intensity much higher than that of the other rings. Brookite (102), rutile (011), and cubic TiO (111) reflections all correspond to lattice spacings very close to 2.47 Å, which makes it difficult to distinguish between these phases from the diffraction pattern. In the previous chapter, after the anatase NRs were heated in the vacuum chamber, the DP indicated a mixture of anatase TiO₂, rutile TiO₂, and rock salt TiO. Here the DP at 1100 °C was compared with the DP of the mixed phases (shown in Figure S 5-2). Rings No. 2 and 3 in correspond to the rutile peaks in the DP of ex-situ heated anatase. The 4th peak is also very close to the cubic TiO ring. Therefore, it is most probable that brookite, rutile and cubic TiO co-existed at 1100 °C. The indexed values of the DP at 1100 °C and corresponding lattice reflections are shown in Table S 5-2.

Compared to the thermal evolution of anatase NRs as described in the previous Chapter, brookite NRs are more stable at high temperature. Anatase NRs sublime more easily and form particles with a size of about 10 nm after heating to 1000 °C, while brookite NRs kept their rod-like shape. The morphological stability may one reason impeding reduction of the brookite NRs to TiO. At 1100 °C, both small particles and bigger blocks co-existed. The small particles transformed to TiO, while the bigger ones remained in the brookite phase or transformed to rutile.

The NRs without post-treatment (as-synthesized NRs) were also investigated. Figure 5-5 shows the morphology and DPs of as-synthesized NRs during heating. With aggregation, the NRs began to deform and coalesce from 600 °C onward. At 700 °C, the bigger particles are very common and apparent. Furthermore, bright spots began to appear in the DPs. At 900 °C, big blocks were formed in overlapping areas. The rings became weaker, and many more spots appeared. At 1000 °C, many NRs had transformed to bigger particles. In the DP recorded at 1000 °C, the rings were even weaker than at 900 °C, and the number of spots also decreased. The lower number of spots at 1000 °C results from a lower number of particles after coalescence.

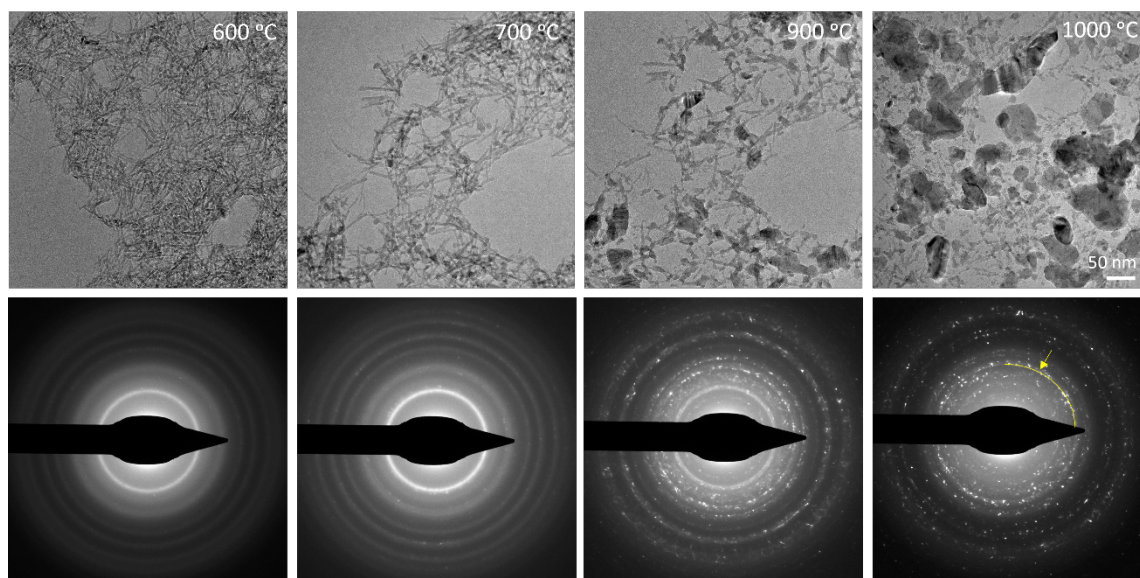


Figure 5-5 Bright-field TEM images and SADPs of as-synthesized brookite NRs during heating.

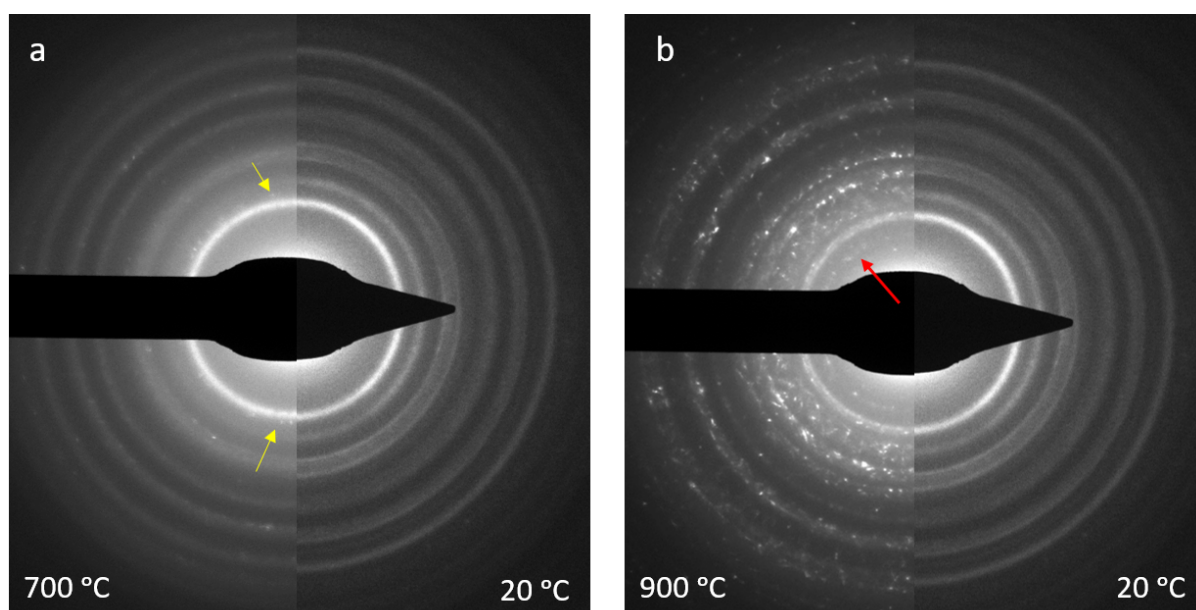


Figure 5-6 Comparison of SADPs (left-hand side) at (a) 700 °C and (b) 900 °C with the SADP at room temperature (right-hand side in both panels).

To check the crystal structural evolution, the DPs at 700 °C and 900 °C were compared with the DP recorded at room temperature (shown in Figure 5-6). At 700 °C, there are spots outside the first ring (indicated with yellow arrows). At 900 °C, more spots appeared, which do not correspond to the original rings of brookite phase, and which seem to indicate the formation of new crystal structures. However, the brookite phase has many weak lattice reflections due to its low-symmetry crystal structure. The additional reflections may have appeared because the NRs broke and coalesced, where the larger crystals are also found in other crystallographic orientations resulting in different lattice

reflections than in the case where the NRs are all lying flat on the support grid. It is difficult to exclude that a new structure formed below 1000 °C. But because all rings corresponding to brookite still remained, we conclude that most of the samples were still in the brookite phase at 900 °C. In the DP at 1000 °C shown in Figure 5-5, the first ring of brookite (corresponding to (210) lattice reflection) disappeared, and some spots remained. However, there are more spots present corresponding to 2.47 Å (marked by the yellow arc and arrow), which is similar to the findings of the low concentration condition.

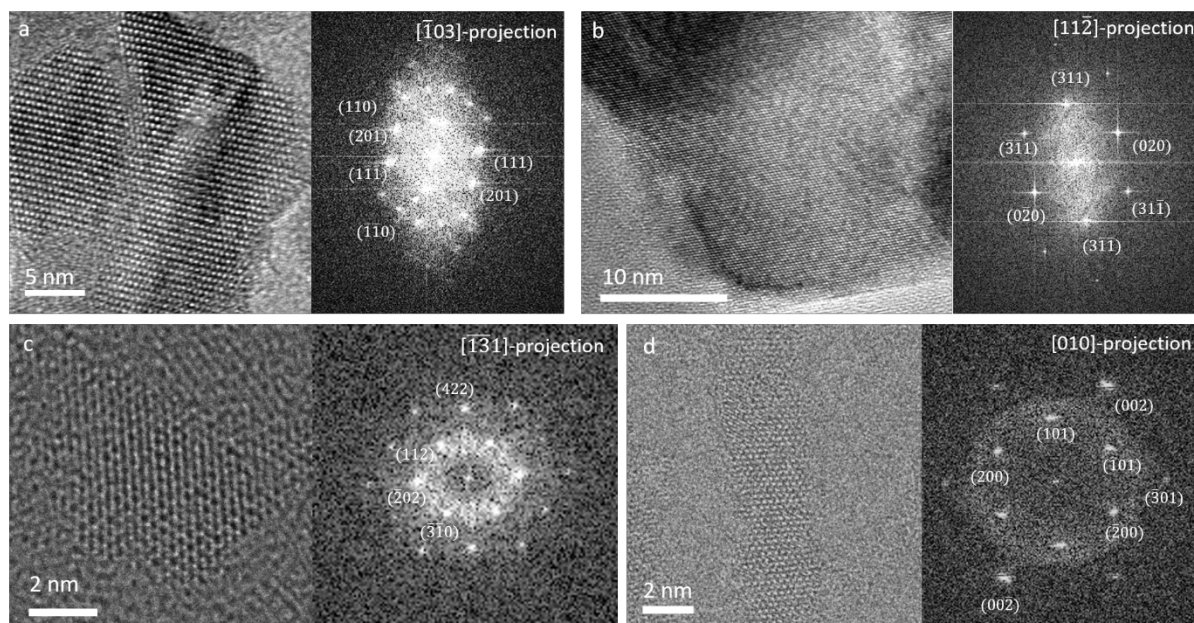


Figure 5-7 High-resolution images and corresponding FFT images taken at (a,b) 900 °C; (c) 950 °C; and (d) 700 °C. The images in (a-c) correspond to the brookite structure, while (d) show a rutile structure. The corresponding zone-axis and lattice planes are marked in the FFT images.

Figure 5-7 shows high-resolution (HR) TEM images taken at different temperatures of the as-synthesized samples. Panels (a) and (b) show images taken at 900 °C and (c) was taken at 950 °C. All the images were indexed and indicate the brookite structure in (a) $[\bar{1}03]$, (b) $[11\bar{2}]$ and (c) $[\bar{1}\bar{3}1]$ zone-axes. This confirms that the particles mostly remained in the brookite phase at temperatures above 900 °C. However, we also report one image taken at 700 °C showing a lattice corresponding to the rutile structure (shown in panel (d)), indicating that a small minority of particles transformed to rutile.

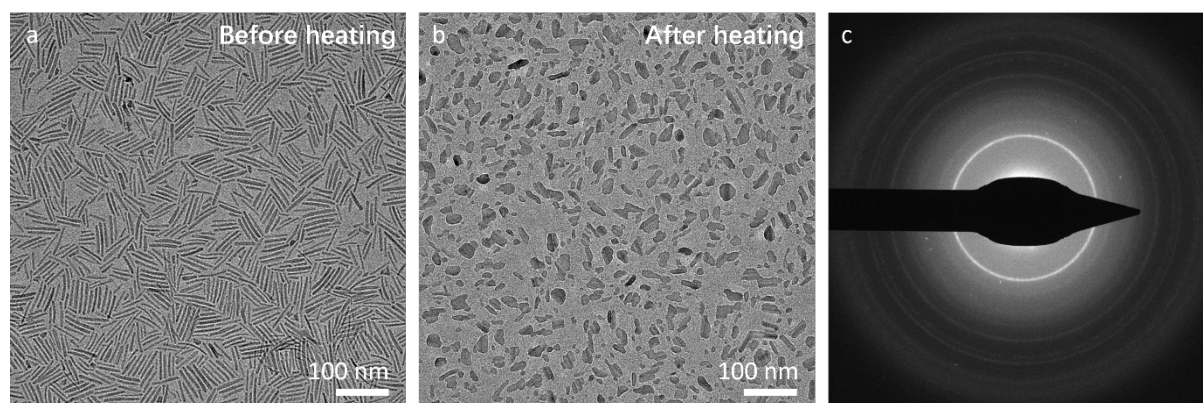


Figure 5-8 TEM images showing the results of the ex-situ heating experiments of post-treated NRs. (a, b) TEM images of the specimens before and after heating, respectively. (c) SADP after heating.

In order to completely exclude the effect of electron illumination, heating was also conducted ex-situ in a vacuum chamber by using the heating holder. The heating rate was the same as in the in-situ experiments. After keeping the temperature at 1100 °C for 15 min, the samples were cooled down to room temperature rapidly and inserted in the microscope for TEM observation. TEM images and SADP after heating are shown in Figure 5-8.

Combining the in-situ and ex-situ results, for the case where the concentration of pristine NRs is low, upon heating to 1000 °C most nanocrystals were still in the brookite structure. After keeping the sample at 1100 °C for more than 15 minutes, a phase transformation took place. The amount of particles in the brookite decreased and the final configuration likely consists of a mixture of particles in brookite, rutile, and rock salt TiO phases. For the case where the concentration of pristine NRs is very high, causing the NRs to aggregate, the NRs readily deformed and coalesced. From 700 °C onwards, some particles transformed to rutile when bigger particles were formed, and at 1100 °C, there is less of the brookite phase remaining than in the case of the post-treated, low concentration NRs.

Similar to the results from the heating of anatase NRs, the brookite NRs are also much more stable than the phase diagram showed in the research of Murray and Wriedt¹⁹, from which it can be expected that the brookite will transform to rutile at 700 °C. In many investigations^{7,20-22}, brookite samples with different shapes and sizes were heated and found to transform to rutile at temperatures ranging from 600 °C to 1000 °C, sometimes with the formation of the anatase phase as intermediate stage^{12,14}.

However, Zhang and Banfield²³⁻²⁷ found that the stabilization of TiO₂ polymorphs depends on the size of the particles. Anatase is the most stable phase below a size of 11 nm. Brookite is stable in the size range of 11-35 nm. Above 35 nm, rutile is most stable. Levchenko et al.²⁸ also reported that the energy of anatase and brookite are lower than that of rutile in small-size range. Moreover, Zhang and

Banfield²⁹ also reported that rutile nucleates primarily at interfaces between contacting particles other than at surfaces. Therefore, with high concentration pristine NRs, rutile can be formed more easily.

In our case, with increasing temperature, NRs coalesced and formed bigger particles, which benefits a transformation to rutile which is expected to make them relatively more stable. However, for most NCs that are still in the rod-like shape or for smaller particles, we find that brookite is still a favorable phase. The very small particles possibly reduced to rock salt TiO.

In comparison to the thermal evolution of anatase NRs, the brookite NRs are more stable at high temperature. The brookite NRs kept their crystalline structure or transformed to rutile, while anatase NRs reduced to TiO. Anatase NRs sublimated sooner and formed particles around 10 nm after heating to 1000 °C. Although after ex-situ heating, the NRs transformed to irregularly shaped particles, the sizes are still bigger than the rock salt TiO particles reduced from anatase NRs. Zhang and Banfield²⁹ also reported that the activation energy of rutile nucleation during anatase-to-rutile transformation increased with decreasing particle size. Anatase NRs are all smaller in size than the brookite NRs, which likely hampers the nucleation of the rutile phase.

5.4 Conclusion

The brookite NRs were heated from room temperature to 1100 °C and investigated using in-situ TEM. The evolution of morphologies and crystalline structures was monitored. Some of the brookite NRs transformed to rutile TiO₂ or rock salt TiO, or to both, at 1100 °C. The transformations observed are dependent on whether the pristine NRs have received post-treatment to induce steric hindrance, or not. For the as-synthesized NRs, the NRs are (nearly) in contact and have a high packing density. The processes of deformation and coalescence set in sooner and there is a tendency for the NRs to transform to rutile. For post-treated NRs, sublimation dominated above 1000 °C, and small particles were formed. In general, most NRs retained the brookite phase at these high temperatures, while rock salt TiO was likely formed in the very smallest of nanoparticles.

5.5 Acknowledgments

This Chapter was performed with collaboration with Seyed Naveed Hosseini (nanorods synthesis). We thank Prof. Alfons van Blaaderen, Dr. Arnout Imhof and Dr. Patrick Baesjou for useful discussions.

5.6 References

- 1 A. Di Paola, M. Bellardita and L. Palmisano, *Catalysts*, 2013, **3**, 36–73.
- 2 A. R. Sanwaria, R. Gopal, J. Jain, M. Nagar and A. Chaudhary, *J. Inorg. Organomet. Polym. Mater.*, 2020, **30**, 1393–1403.
- 3 J. Xie, X. Lü, J. Liu and H. Shu, in *Pure and Applied Chemistry*, De Gruyter, 2009, **81**, pp. 2407–2415.
- 4 M. G. Manera, A. Colombelli, R. Rella, A. Caricato, P. D. Cozzoli, M. Martino and L. Vasanelli, in *Journal of Applied Physics*, American Institute of PhysicsAIP, 2012, **112**, p. 053524.
- 5 B. Ohtani, J. ichi Handa, S. ichi Nishimoto and T. Kagiya, *Chem. Phys. Lett.*, 1985, **120**, 292–294.
- 6 Y. Wang and Y. Li, *J. Nanomater.*, 2019, **2019**, 1–7.
- 7 W. Hu, L. Li, G. Li, C. Tang and L. Sun, *Cryst. Growth Des.*, 2009, **9**, 3676–3682.
- 8 Y. Wang, Y. Zou, Q. Shang, X. Tan, T. Yu, X. Huang, W. Shi, Y. Xie, G. Yan and X. Wang, *Trans. Tianjin Univ.*, 2018, **24**, 326–339.
- 9 M. Zhao, L. Li, H. Lin, L. Yang and G. Li, *Chem. Commun.*, 2013, **49**, 7046–7048.
- 10 Q. Deng, M. Wei, X. Ding, L. Jiang, B. Ye and K. Wei, *Chem. Commun.*, 2008, 3657–3659.
- 11 H. Kominami, M. Kohno and Y. Kera, *J. Mater. Chem.*, 2000, **10**, 1151–1156.
- 12 K. Li, J. Xu, W. Shi, Y. Wang and T. Peng, *J. Mater. Chem. A*, 2014, **2**, 1886–1896.
- 13 S. N. Hosseini, A. Grau-Carbonell, A. G. Nikolaenkova, X. Xie, X. Chen, A. Imhof, A. Blaaderen and P. J. Baesjou, *Adv. Funct. Mater.*, 2020, **30**, 2005491.
- 14 S. Bakardjieva, V. Stengl, L. Szatmary, J. Subrt, J. Lukac, N. Murafa, D. Niznansky, K. Cizek, J. Jirkovsky and N. Petrova, *J. Mater. Chem.*, 2006, **16**, 1709.
- 15 T. R. Gordon, M. Cargnello, T. Paik, F. Mangolini, R. T. Weber, P. Fornasiero and C. B. Murray, *J. Am. Chem. Soc.*, 2012, **134**, 6751–6761.
- 16 M. Cargnello, T. Montini, S. Y. Smolin, J. B. Priebe, J. J. D. Jaén, V. V. T. Doan-Nguyen, I. S. McKay, J. A. Schwalbe, M. M. Pohl, T. R. Gordon, Y. Lu, J. B. Baxter, A. Brückner, P. Fornasiero and C. B. Murray, *Proc. Natl. Acad. Sci. U. S. A.*, 2016, **113**, 3966–3971.
- 17 B. Lee, K. Littrell, Y. Sha and E. V. Shevchenko, *J. Am. Chem. Soc.*, 2019, **141**, 16651–16662.
- 18 P. Wang, Q. Qiao, Y. Zhu and M. Ouyang, *J. Am. Chem. Soc.*, 2018, **140**, 9095–9098.
- 19 J. L. Murray and H. A. Wriedt, *J. Phase Equilibria*, 1987, **8**, 148–165.
- 20 J.-G. Li and T. Ishigaki, *Acta Mater.*, 2004, **52**, 5143–5150.
- 21 R. Revel, C. Perego, I. Clemencon, B. Rebours, O. Durupthy, S. Cassaigon and J.-P. Jolivet, in *Materials Research Society Symposium Proceedings*, Materials Research Society, 2008, vol. 1146, pp. 158–164.
- 22 Q. Xu, J. Zhang, Z. Feng, Y. Ma, X. Wang and C. Li, *Chem. - An Asian J.*, 2010, **5**, 2158–2161.
- 23 H. Zhang and J. F. Banfield, *J. Mater. Chem.*, 1998, **8**, 2073–2076.
- 24 A. A. Gribb and J. F. Banfield, *Am. Mineral.*, 1997, **82**, 717–728.

- 25 H. Zhang and J. F. Banfield, *J. Phys. Chem. B*, 2000, **104**, 3481–3487.
- 26 P. K. Naicker, P. T. Cummings, H. Zhang and J. F. Banfield, *J. Phys. Chem. B*, 2005, **109**, 15243–15249.
- 27 M. R. Ranade, A. Navrotsky, H. Z. Zhang, J. F. Banfield, S. H. Elder, A. Zaban, P. H. Borse, S. K. Kulkarni, G. S. Doran and H. J. Whitfield, *Proc. Natl. Acad. Sci. U. S. A.*, 2002, **99**, 6476–6481.
- 28 A. A. Levchenko, G. Li, J. Boerio-Goates, B. F. Woodfield and A. Navrotsky, *Chem. Mater.*, 2006, **18**, 6324–6332.
- 29 H. Zhang and J. F. Banfield, *J. Mater. Res.*, 2000, **15**, 437–448.

5.7 Appendix

5.7.1 Supporting Tables

Table S 5-1. Lattice reflections and corresponding measured lattice spacings of brookite NRs at room temperature.

No.	(h k l)	Measured lattice spacings (Å)
1	(210)	3.51
2	(211)	2.94
3	(102)	2.47
4	(400)	2.28
5	(321)	1.90
6	(511)	1.64
7	(521)	1.46

Table S 5-2 Measured lattice spacings and corresponding phases and lattice reflections of DP at 1100 °C shown in Figure 5-4.

No.	Measured lattice spacings (Å)	(hkl)		
		Brookite	Rutile	TiO
1	3.47	(210)	X	X
2	2.50	(102)	(011)	(111)
3	2.18	X	(111)	X
4	2.10	X	(120)	(200)
5	1.65	(511)	(221) (220)	X
6	1.46	(521)	(130)	X

5.7.2 Supporting Figures

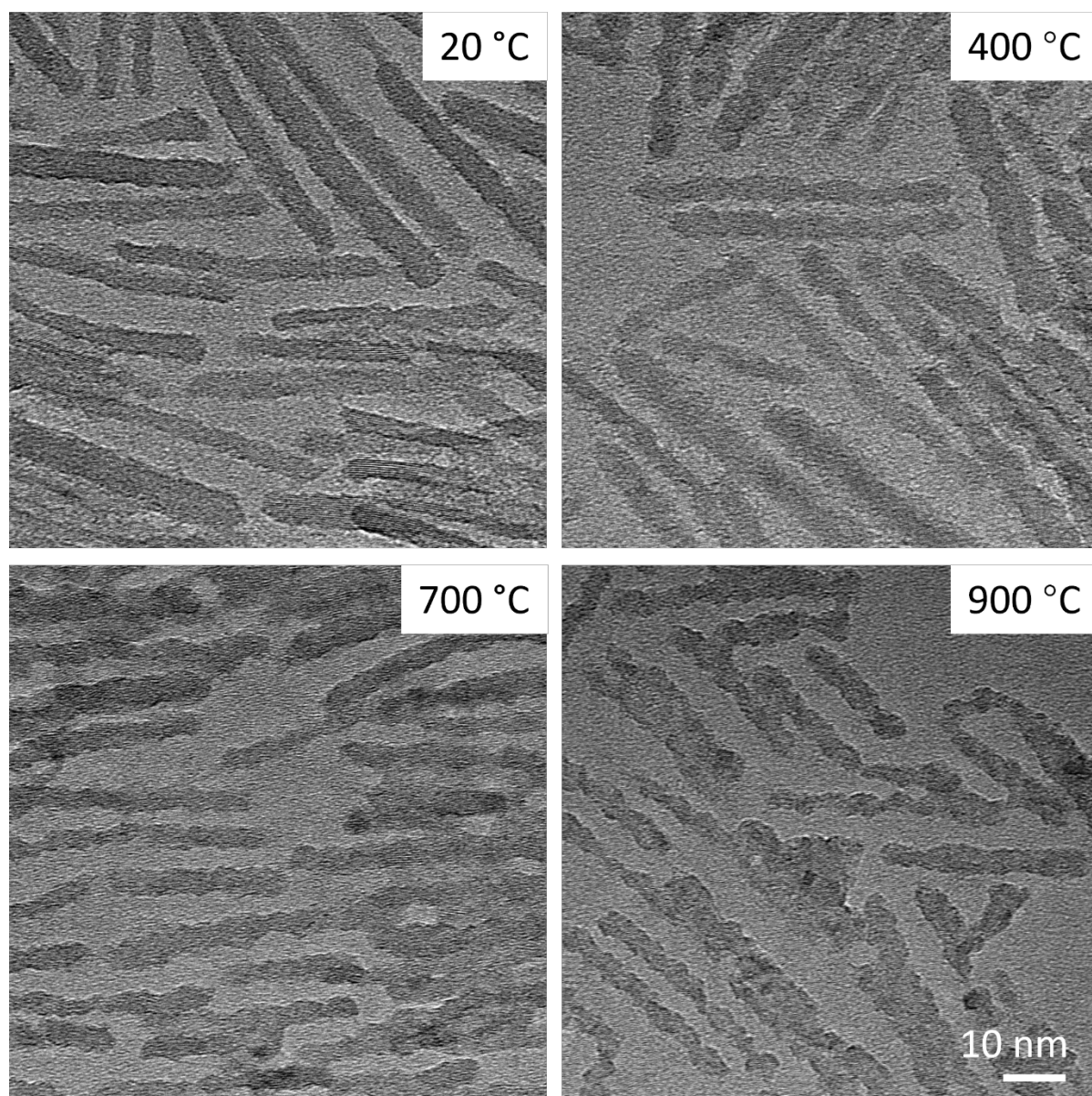


Figure S 5-1 Bright-field TEM images of low concentration brookite NRs during heating. The buckled surfaces of the particles are an indication of beam-induced effects.

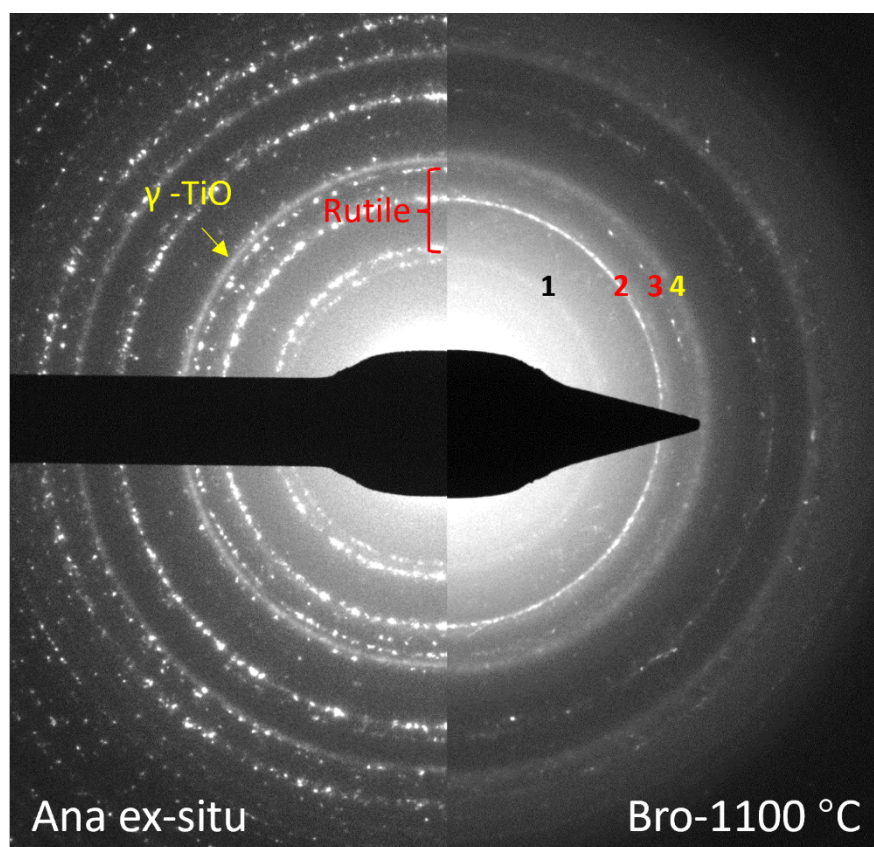


Figure S 5-2 Comparison of DPs. Left: DPs of anatase NRs after heating to 1100 °C in vacuum chamber, indicating a mixture of anatase, rutile and rock salt TiO. Right: DPs of brookite NRs at 1100 °C.

6. Thermal reduction and heating-induced exfoliation of MoO₃ particles

Nanoscale forms of molybdenum trioxide have found widespread use in optoelectronic, sensing, and battery applications. Here we investigate the thermal evolution of micrometer-sized molybdenum trioxide particles during in-situ heating in vacuum using transmission electron microscopy, and observed drastic structural and chemical changes that are strongly dependent on the heating rate. Rapid heating (flash heating) to a temperature of 600 °C resulted in massive exfoliation of the particles into MoO₂ nanoflakes that were found widely scattered around the primary particles, within a few-minutes time frame. In contrast, when heated more gently, the initially single crystal MoO₃ particles were reduced into hollow nanostructures with polycrystalline MoO₂ shells. Using density functional theory (DFT) calculations employing the DFT-D3 functional, the surface energy of MoO₃(010) was calculated to be 0.187 Jm⁻², and the activation energy for exfoliation of the van der Waals bonded MoO₃ (010) layers was calculated to be 0.478 Jm⁻². Ab initio molecular dynamics simulations show strong fluctuations in the distance between the (010) layers, where thermal vibrations lead to additional separations of up to 1.8 Å at 600 °C. The present study shows efficient pathways for the generation of either nanoflakes or hollow nanostructures with very high effective surface areas beneficial for applications.

Based on:

X. Chen, R. M. de Bore, H. Van Gog, and M. A. Van Huis, published as preprint at <https://ssrn.com/abstract=4175997>

6.1 Introduction

Molybdenum oxides are versatile materials occurring in various compositions and structural polymorphs, and have applications in many fields. They are used in, amongst others, batteries^{1,2}, electrochromic materials³, gas sensors,^{4,5} and OLEDs^{6,7}. The molybdenum trioxide (MoO₃) is a particularly interesting member of the molybdenum oxide family, as it has a layered structure and is often fabricated in planar morphologies such as thin films, 2D nanosheets, or flakes^{1,5,8}.

MoO₃ has an orthorhombic structure with layers of distorted MoO₆ octahedra. The layers are bound along the [010]-direction by van der Waals interactions. Within one layer, octahedra are corner sharing along the [100]- and [001]-directions. In contrast, molybdenum dioxide MoO₂ has a monoclinic, distorted rutile-type structure. Here the MoO₆ octahedra share edges along the [001]-direction. Also phases with intermediate compositions of MoO_{3-x} (0<x<1) have been observed. With the reduction of MoO₃ in an oxygen-deficient environment, there are many MoO_{3-x} (0<x<1) phases occurring with a ReO₃ type structure, like Mo₉O₂₆, Mo₈O₂₃ and Mo₄O₁₁. These phases are described as Magnéli series with composition Mo_nO_{3n-1}.⁹⁻¹¹ In 1969, Bursill¹² reported the thermal decomposition of MoO₃ induced by beam heating, and in years thereafter, the structures of MoO₃ and of ReO₃ types were also investigated.^{13,14} The crystal structure information and schematic structures of MoO₃, MoO₂ and Mo₄O₁₁ are listed in and displayed in Figure 6-1. Other lattice spacings of the three oxides are given in Tables S6-1-S6-3 of the Appendix.

Table 6-1. Structural details of MoO_x phases.^{11,15,16}

	MoO ₃	MoO ₂	Mo ₄ O ₁₁
Structure	orthorhombic	monoclinic	orthorhombic
Space group	Pbnm	P21/c	Pn21a
Lattice parameter (Å)	a=3.966; b=13.88; c=3.703	a=5.608; b=4.842; c=5.517	a=24.400; b=5.450; c=6.723

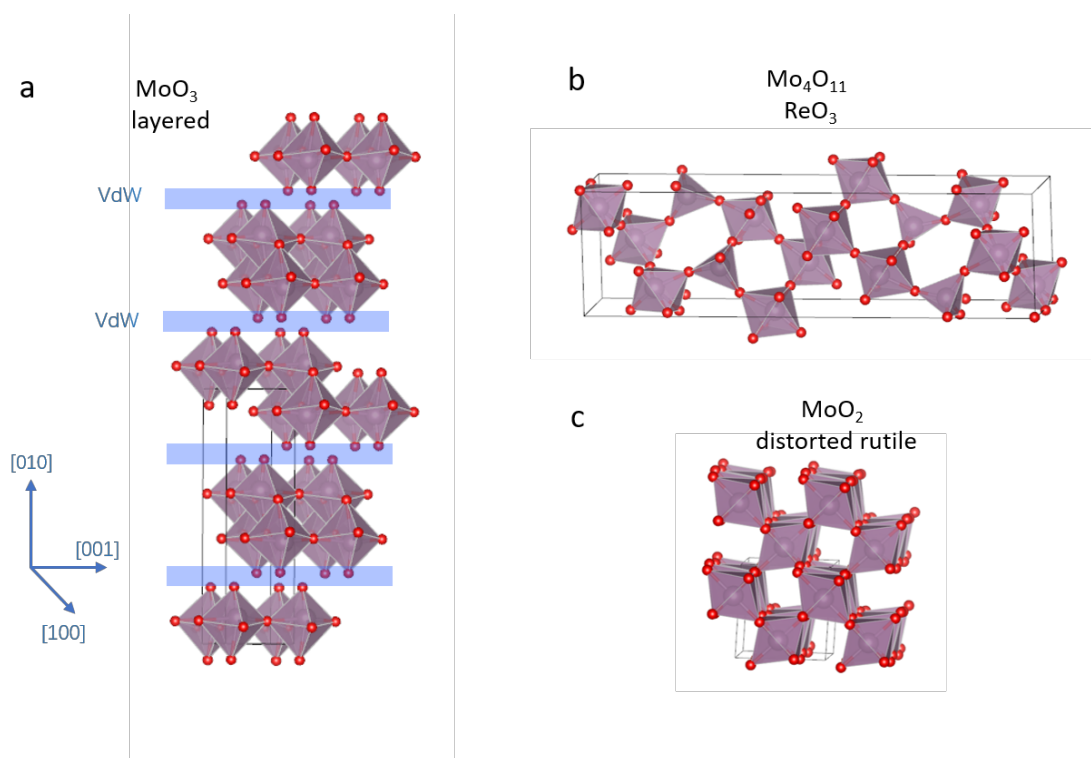


Figure 6-1. Crystal structure of (a) orthorhombic MoO₃ with van der Waals (vdW) bonded layers, (b) Mo₄O₁₁, and (c) monoclinic MoO₂. Purple spheres denote Mo atoms while red spheres denote oxygen atoms. Crystallographic details are given in Table 6-1.

The reduction process of MoO₃ to MoO₂ has been investigated in various studies.^{17–25} Mainly two types of reduction processes were reported. The first one is the one-step process, in which MoO₃ reduces directly to MoO₂ without any intermediate phases. The second one is a two-step process, in which Mo₄O₁₁ is also involved. In the reports in which Mo₄O₁₁ was observed, various mechanisms were proposed. In 1978, Burch²⁶ first found the formation of Mo₄O₁₁ during the reduction. Ressler et al.²⁷ investigated the reduction with H₂ during annealing and reported that the reduction process depended on the temperature. When the temperature was below 425 °C, the MoO₃ reduced to MoO₂ directly. Otherwise the Mo₄O₁₁ was formed in a parallel reaction. Lalik²⁸ proposed an autocatalytic comproportionation kinetics model which means that the MoO₂ first formed on the surface of MoO₃ after which it reacted with the remainder of MoO₃ and formed Mo₄O₁₁. Dang et al.²⁹ reported a consecutive mechanism in which the transformation of MoO₃ to Mo₄O₁₁, and of Mo₄O₁₁ to MoO₂ proceeded simultaneously.

In this study, the thermal behavior of MoO₃ particles was investigated. Figure 6-2 shows transmission electron microscopy (TEM) images and an electron diffraction (ED) pattern of the pristine MoO₃ particles that are the starting point of this study. These particles were heated under high vacuum conditions, serving as an oxygen-poor environment. When heated at a rapid pace a fast exfoliation of nanoflakes from the larger MoO₃ particles was observed. The resulting nanoflakes were found to be reduced to lower oxidation states. When heated gently, however, exfoliation took place slower and the particles were reduced to hollow shell structures with MoO₂ phase. Complementary to these experimental investigations, density functional theory (DFT) calculations were used to investigate the energetics of the MoO₃ nanoparticles reduction. DFT is a quantum mechanical computational method that uses the Schrödinger equation to perform calculations on molecules and crystal structures. Using DFT, the stability of the different molybdenum oxide phases is assessed and the reaction energies calculated. Furthermore, ab initio molecular dynamics (AIMD) simulations were performed to investigate the effects of thermal vibrations on the stability of the layered MoO₃ structure.

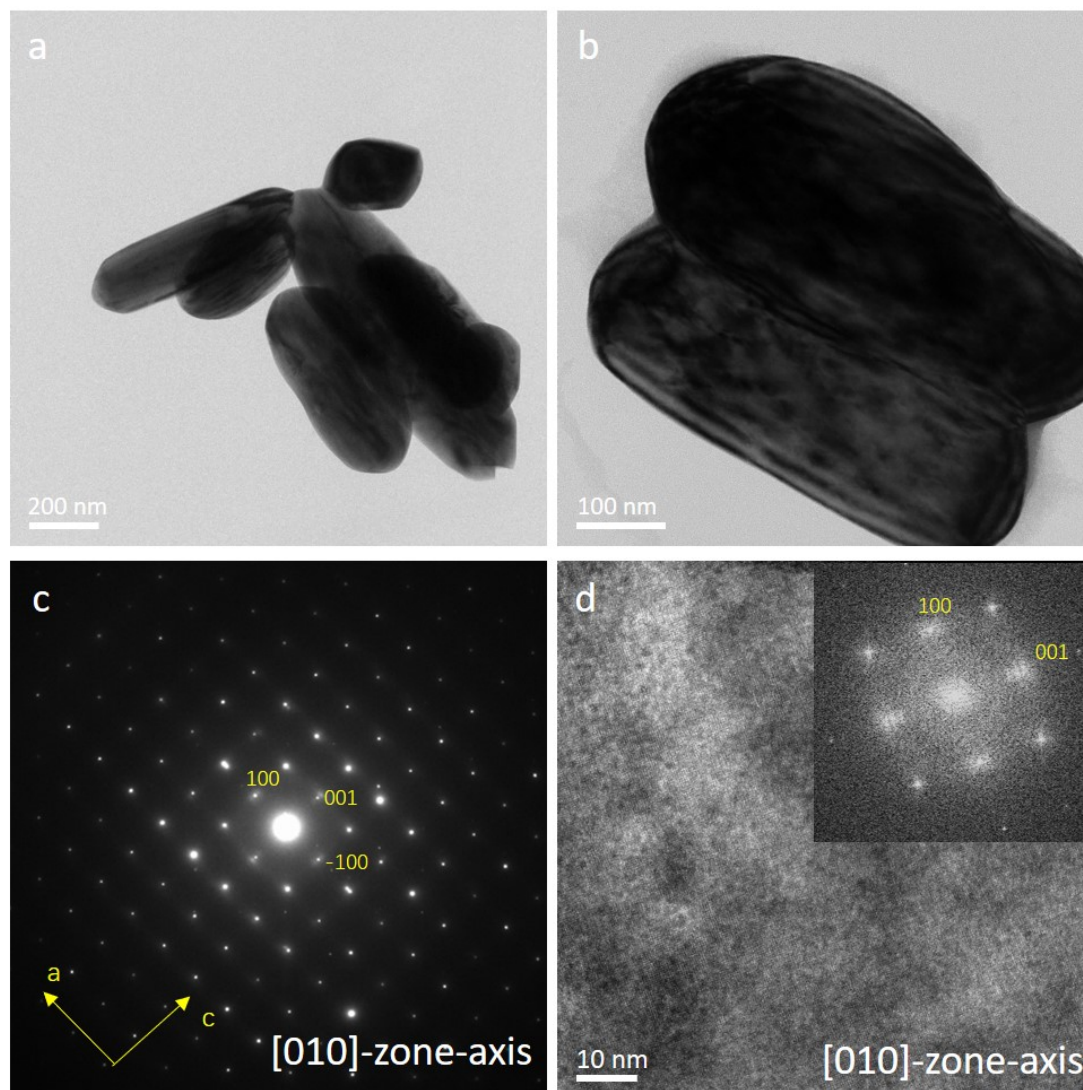


Figure 6-2 (a,b) Bright-field TEM images of MoO₃ particles at room temperature; (c) Diffraction pattern; (d) High-resolution TEM image with the FFT in the inset. (c) and (d) are both taken in the [010]-zone axis.

6.2 Experimental

6.2.1 TEM investigations

The MoO₃ particles were purchased from Sigma-Aldrich and had a broad size distribution. Most of the particles are in the size range of 200 nm – 1 μ m. All TEM investigations were conducted using a FEI TalosF200X TEM operating at 200 kV. The in-situ heating was conducted using a dedicated DENSSolutions heating holder. The specimens were prepared by drop casting the MoO₃ solution onto

a DENSSolutions MEMS heating chip with windows covered by SiN membrane for observation. The chip was then mounted on the holder. The MoO₃ specimens were first heated from 20 °C to 600 °C with 100 °C increments. Exfoliation started at 500 °C. In a second set of heating experiments, the specimens were heated from 20 °C to 400 °C with 100 °C increments, but more gently with smaller increments of 25 °C when raising the temperature further from 400 °C to 700 °C. Great care was taken to exclude any influence of the electron beam on the observations. The electron beam illuminates only a very small part of the sample area. The field of view was changed frequently to verify that in areas previously not exposed to the electron beam, the particles underwent the same thermal evolution.

6.2.2 DFT calculations

To obtain more insight into the energetics of the observed transformations, plane-wave density functional theory (DFT) calculations were conducted using the VASP code.^{30,31} The energy cutoff for the wavefunctions and the density of the k-mesh were tested on the unit cell of the MoO₃ structure in order to ascertain energy convergence within 0.5 meV/atom. The cutoff energy for the wavefunctions was set to 800 eV and the cutoff energy for the augmentation functions to 1120 eV while the k-mesh was set at 6×2×6. For MoO₂ and Mo₄O₁₁, the k-mesh was rescaled to the lattice parameters to have a similar density of the k-mesh, yielding a k-mesh of 6×8×6 for MoO₂ and a k-mesh of 2×8×6 for Mo₄O₁₁. The calculations were performed using the general gradient approximation (GGA) employing the exchange-correlation functional of Perdew, Burke and Ernzerhof (PBE)^{32,33}. To account for the van der Waals interactions in the layered MoO₃ structure as displayed in Figure 6-1, two other functionals were tested as well to find which one gives the best agreement with experimental values: the DFT-D3³⁴ functional which adds a van der Waals interaction to the GGA-PBE functional, and the optB88-vdW³⁵⁻³⁸ functional, which is a nonlocal exchange-correlation functional that accounts for dispersion interactions and is optimized for the correlation part. For each functional, the cell was relaxed with the optimal energy cutoff and k-mesh settings. The lattice parameters were compared to experimental values^{11,38} and an overview of the results is given in Table 6-2.

Table 6-2. DFT-calculated lattice parameters for MoO₃, Mo₄O₁₁, and MoO₂ for three different functionals compared to experimental values. The deviations of the calculated values from the experimental values are given in percentages.

	Functional	a (Å)	Δa (%)	b (Å)	Δb (%)	c (Å)	Δc (%)
MoO ₃	Experimental	3.962		13.856		3.698	
	GGA-PBE	3.94	0.58	15.85	14.4	3.69	0.28
	DFT-D3	3.93	0.87	14.35	3.59	3.69	0.31
	OptB88-vdW	3.91	1.25	14.07	1.57	3.71	1.09
Mo ₄ O ₁₁	Experimental	24.29		5.457		6.752	
	GGA-PBE	24.73	1.83	5.52	1.16	6.81	0.89
	DFT-D3	24.71	1.72	5.52	1.16	6.80	0.74
	OptB88-vdW	24.66	1.52	5.49	0.65	6.78	0.42
MoO ₂	Experimental	5.608		4.842		5.517	
	GGA-PBE	5.39	3.93	4.90	1.15	5.50	0.37
	DFT-D3	5.37	4.28	4.88	0.84	5.48	0.71
	OptB88-vdW	5.40	3.75	4.89	1.07	5.48	0.61

For MoO₃, the GGA-PBE functional performs poorly in predicting the b lattice parameter which is in the layer stacking direction, with a deviation from the experimental value by as much as 14%. The DFT-D3 and optB88-vdW functionals give great improvements compared to the GGA-PBE functional, deviating in this particular lattice parameter by 3.6 and 1.6%, respectively. The optB88-vdW functional predicts best the lattice parameters compared with the experimental values. For MoO₂ and Mo₄O₁₁, the best functional is again optB88-vdW, although this time the other functionals perform almost equally well. One of the goals of the DFT investigations is to calculate the activation energy for the exfoliation of MoO₃ nanosheets from larger MoO₃ particles, which requires a supercell including vacuum. As the optB88-vdW functional is known to show difficulty in electronic convergence when vacuum is present in the supercell, the DFT-D3 functional was selected as the optimal choice and will be used for all further density functional calculations in the remainder of this study.

The energies of the different molybdenum structures were calculated by fully relaxing the unit cell, both the lattice parameters and atomic coordinates, using the settings and functionals given above. The energy of the paramagnetic O₂ molecule was calculated as well, in order to compare the energies of the MoO₃, Mo₄O₁₁, and MoO₂ structures taking into account the change in chemical composition. To calculate the energy of the O₂ molecule, a spin-polarized calculation was performed with the

molecule at the center of a large cubic supercell of vacuum (with edge lengths of 25 Å), employing the DFT-D3 functional with a k-mesh of 1×1×1.

The surface energy of the (010) surface of MoO₃ was calculated by constructing a MoO₃ supercell consisting of 5 stacked unit cells of MoO₃ and a vacuum layer of 57 Å. This supercell was relaxed using the same settings as those used for the unit cell, but with the k-mesh scaled accordingly (6×1×6). The surface energy is then given by:

$$(MoO_3)_{(010)} = \frac{E(\text{supercell}) - 5 \cdot E(\text{unitcell})}{2A} \quad (1.)$$

where A is the area of the surface in the supercell. The factor of 2 account for the fact that because of the periodic boundary conditions, the supercell contains two surfaces.

Using the relaxed supercell, the activation energy required to exfoliate one layer of MoO₃ was calculated by keeping the dimensions of the supercell fixed while shifting the upper layer upwards in 10 steps, amounting to a total shift of 1.38 nm, at which point we consider the top layer to be well separated from the main slab. To evaluate the change in potential energy and a possible activation barrier associated with the exfoliation, the nudged elastic band (NEB) method of Henkelman *et al.*³⁹ was used with a spring force constant of $-5.0 \text{ eV}/\text{Å}^2$.

To gain more insight into the thermal vibrations leading to the observed exfoliation, ab initio molecular dynamics (AIMD) simulations were performed. To this end, a 192-atom simulation cell was constructed consisting of a 2×3×2 MoO₃ slab and a vacuum layer of more than 70 Å along the [010] axis of the stacking direction. Just as for the NEB calculation, for the AIMD simulations the exchange and correlation energy terms were described using the PBE functional³², and the DFT-D3 method³⁴ was applied to account for dispersion interactions. Before performing the AIMD simulations, the simulation cell was first fully relaxed at high accuracy. Because of the high computational cost, the AIMD calculations were performed at lower accuracy settings, with a cutoff energy of 400 eV for the wave functions and a cutoff energy of 560 eV for the augmentation functions, and including the Γ -point only. With a timestep of 1 fs, a 2-ps initial equilibration

consisting of a ramp-up from 0 K and a 6-ps subsequent canonical (NVT) ensemble simulation using a Nosé thermostat⁴⁰⁻⁴² was carried out at a simulation temperature of 300 K. The 300-K simulation was followed by a 2-ps ramp-up to 900 and 1100 K and continued at these temperatures for another 8 ps.

6.3 Result and discussion

6.3.1 In-situ TEM investigation of MoO₃ particles

The MoO₃ particles used in this study have a broad size distribution. The particles agglomerated after drying on the heating chip. Figure 6-2(a) and (b) show the bright-field TEM images of several particles at room temperature. Figure 6-2(c) and (d) are a selected area diffraction pattern (SADP) and a high-resolution TEM (HRTEM) image of the particle. Both DP and HR images are taken with the particle oriented along the [010]-zone axis (normal to the van der Waals bonded layers). The DP and the HR images show that the particles are single crystalline at room temperature.

The particles were first heated from room temperature to 600 °C with relatively large 100 °C increments. Figure 6-3 shows the evolution of the whole process. Below 500 °C, the morphology of particles hardly changes. At 500 °C, some small flakes appeared near the parent particles, which are likely fragments of the parent particle that detached from the main particle and were scattered away. When the temperature was raised to 600 °C, many more flakes exfoliated at a rapid pace, and it appeared as if the larger particles were blown up. The disintegration of the larger particle and scattering of the sheet-like fragments proceeded for almost 4 mins and finally the main part of the parent big particles broke up into smaller crystals.

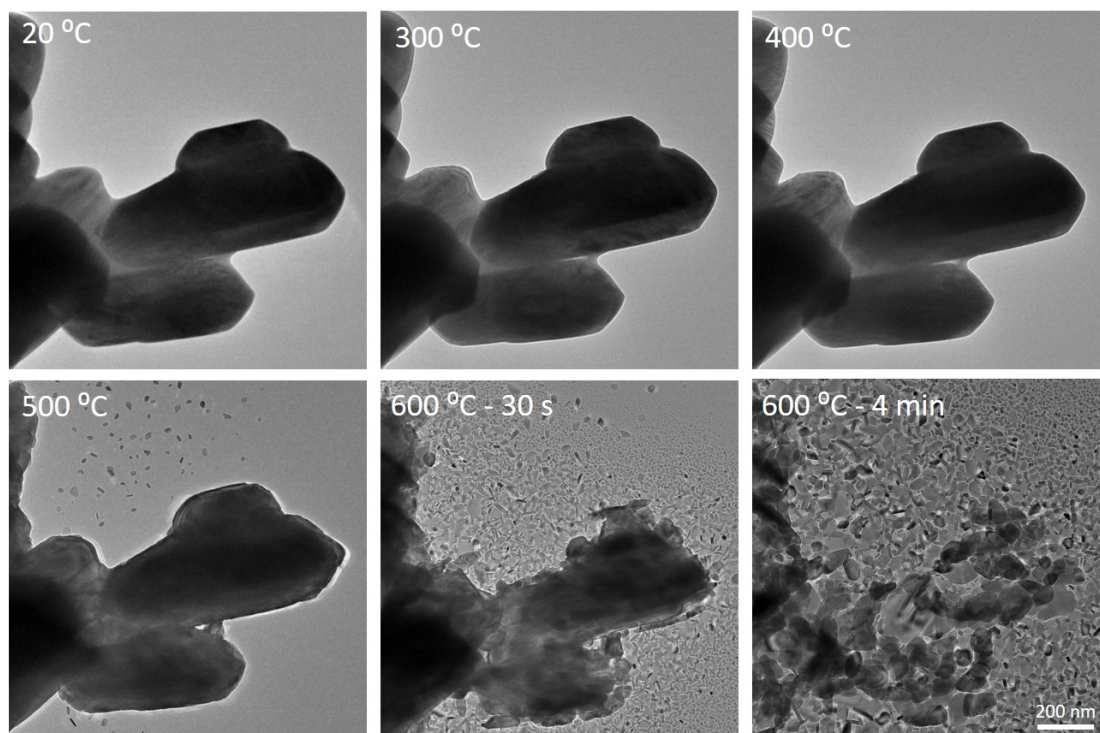


Figure 6-3 Bright-field TEM image of MoO_x particle heating from 20 °C (room temperature) to 600 °C. All images are at the same magnification.

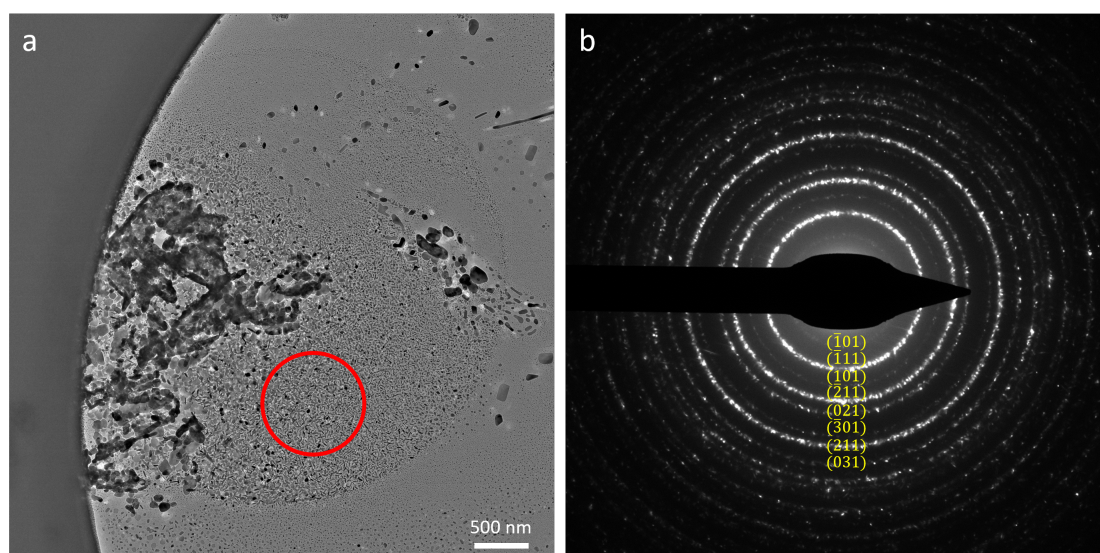


Figure 6-4 (a) Overview image after heating to 600 °C; (b) Diffraction pattern of the area marked in (a). The pattern was indexed, confirming the monoclinic MoO₂ structure.

Figure 6-4(a) shows the overview of the particles after heating to 600 °C at low magnification. Figure 6-4(b) is the diffraction pattern of the area marked in (a) with a red circle. The DP was indexed and

found to match the monoclinic MoO_2 phase. Therefore, at 600 °C, the scattered small flakes were reduced to MoO_2 .

Figure 6-5 shows another group of particles at 400 °C and 500 °C. Figure 6-5(c) is the zoomed in image of the area marked with a square in (a), in which small zones in different orientations were formed in the parent particle. Figure 6-5(d) is the diffraction pattern of the marked area in (b), which correspond to the MoO_3 structure. The yellow arrows mark the split spots, which indicates that the bigger particle had partly exfoliated along the [010]-direction, and that there are small tilts between the layers. The exfoliation along [010] is plausible, as in this direction the layers in MoO_3 are only bonded by van der Waals forces. Therefore, before the small flakes appeared near the parent particles at 500 °C, the smaller MoO_3 particles already partly exfoliated and formed several domains at 400 °C. The central area of the big particles partly exfoliated at a higher temperature of 500 °C, while the small domains at the surface completely detached and scattered away, landing on the SiN window around the original particle. Very likely, a considerable portion of these detaching fragments were lost as they were blown away into the vacuum of the TEM. Figure S 6-1 shows an SADP of a pristine particle at 500 °C in $[\bar{3}\bar{1}1]$ -zone axis. With a beam stopper, the (000) beam was blocked and more weaker peaks became visible. This confirms the formation of cracks and small domains in the bigger particles before exfoliation, as peaks corresponding to different orientations appear.

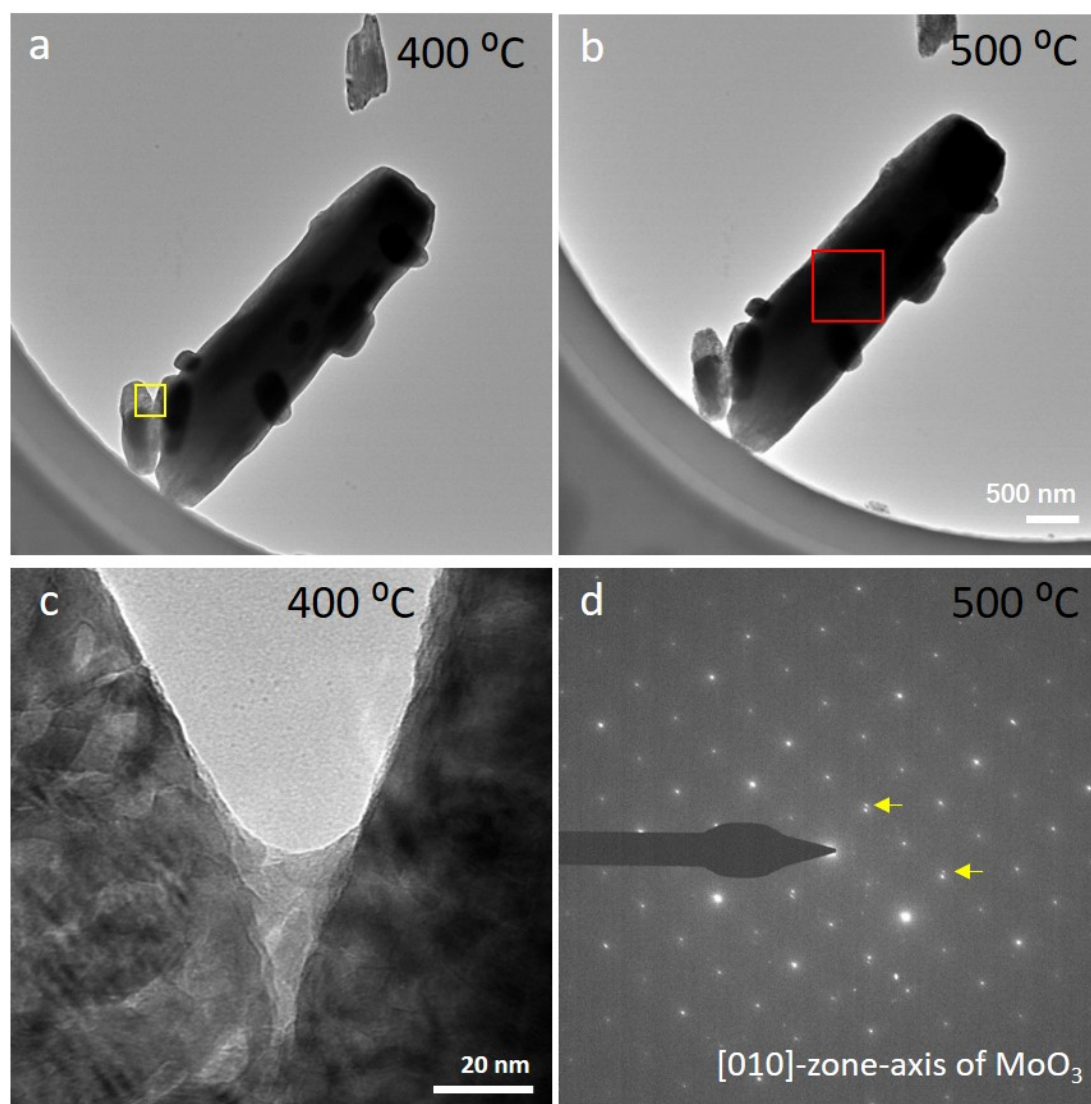


Figure 6-5 (a,b) BF-TEM images at 400 °C and 500 °C, respectively. (c) TEM image of the marked area in (a), showing the details. (d) SADP of the marked area in (b), indicating the MoO₃ structure observed in [010]-zone axis. Some of the spots in (d) split (marked by yellow arrows), indicating that the layers of MoO₃ exfoliated partly, and have a small tilt with each other.

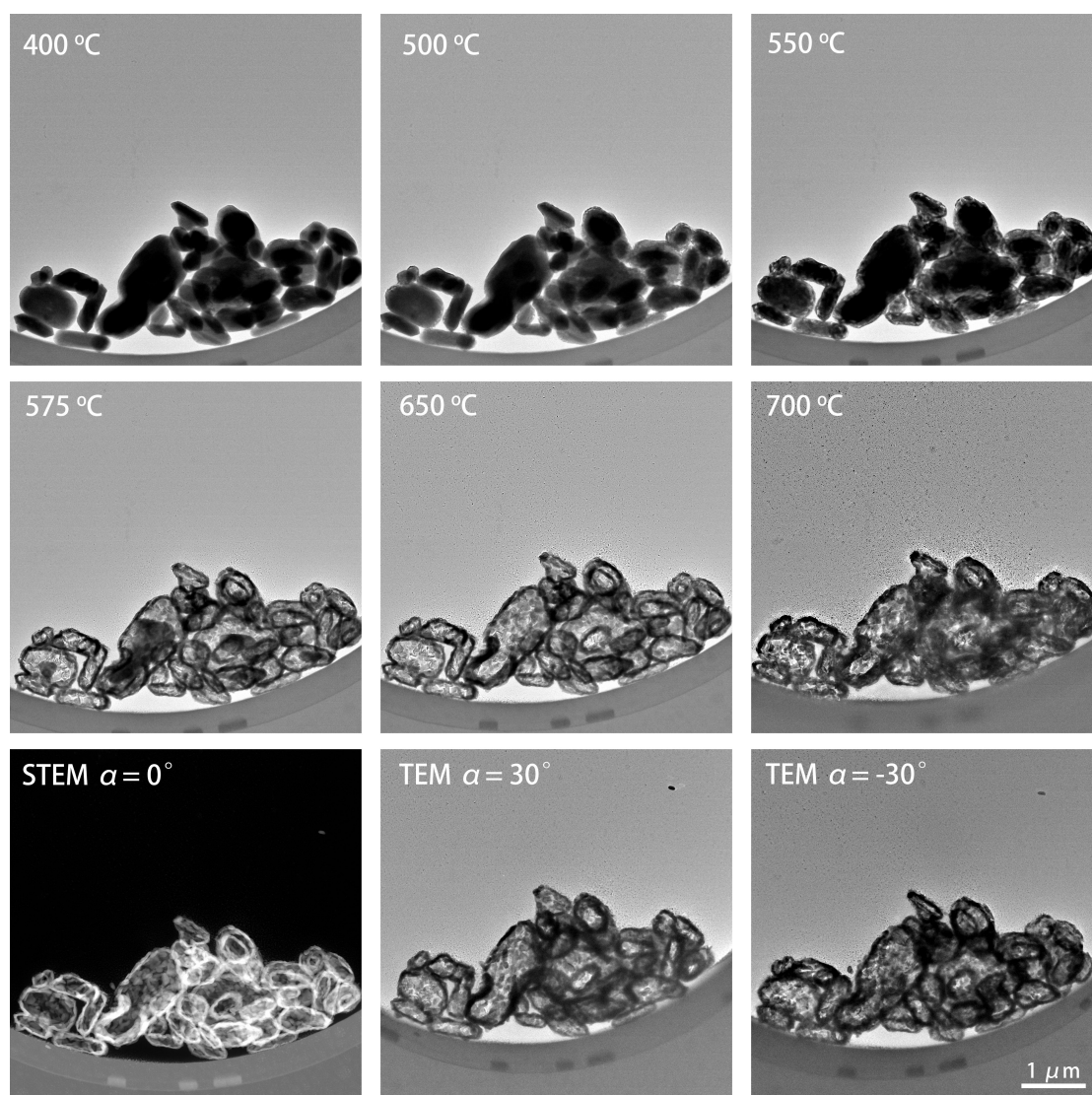


Figure 6-6 TEM images of MoO_x particles at temperatures above 400 °C. These particles were heated gently, with 25 °C increment above 400 °C. The bottom-left image is a HAADF-STEM image obtained after heating. The last two images at the bottom-right are also recorded after heating, with the sample tilted over $\pm 30^\circ$.

As the exfoliation happened extremely fast in the first heating experiment, the MoO_3 particles were also heated more gently in follow-up experiments, using smaller steps of 25 °C increments above temperatures of 400 °C. At this slower heating rate, the fast disintegration with massive exfoliation of the large particles did not happen, and there are fewer flakes formed around the parent particles (shown in Figure 6-6). After heating to 500 °C, the edges of the particles show a brighter contrast (grey) than the central area (black) because of a different projected thickness. From 575 °C onwards, however, the central areas of the particles exhibited a brighter contrast, with every particle having a

dark contour, suggesting that the particles became hollow. To avoid contributions from diffraction contrast in bright-field TEM imaging (BF-TEM), high angle annular dark field scanning transmission electron microscopy (HAADF-STEM) image was also recorded and is displayed at the bottom-left panel in Figure 6-6. In addition, BF TEM images with $\pm 30^\circ$ tilts were also taken after heating and are shown at the bottom-right panels of Figure 6-6. All these results show that the edges are thicker and heavier than the central area after heating, and that the particles have become hollow. The DP shown in Figure S 6-2 indicates that the hollow particles are also in MoO₂ phase.

To show the details of structural changes taking place during this gentle heating process, the thermal evolution of an agglomerate consisting of two smaller MoO₃ domains was followed as well and is shown in Figure S6-3. At 400 °C, fringes appeared on the cluster, especially in the right domain, which is likely from bending of the lattice and a different crystallographic orientation. At 500 °C, the edges of the particles broke into small flakes, while the central area showed vertical fringes. This proceeded further inwards at 550 °C, and finally the central area also broke up at 575 °C. But the remaining particles at the center are bigger than those at the edges. This could explain what happened to the configurations shown in Figure 6-6. The exfoliation and cracking of the lattices started from the surface of the particle. Next, domains in different orientations formed at the surface while the center was still single crystalline. This resulted in the bright contour at 550 °C. With increasing temperature, small flakes also formed in the central area at a relatively slow rate. Part of the crystals sublimated during heating, while some small flakes disappeared into the vacuum of the microscope column, while some of them accumulated at the edges when being expelled. Therefore, less flakes appeared around the parent particles, and more crystals are left at the edges of the particles.

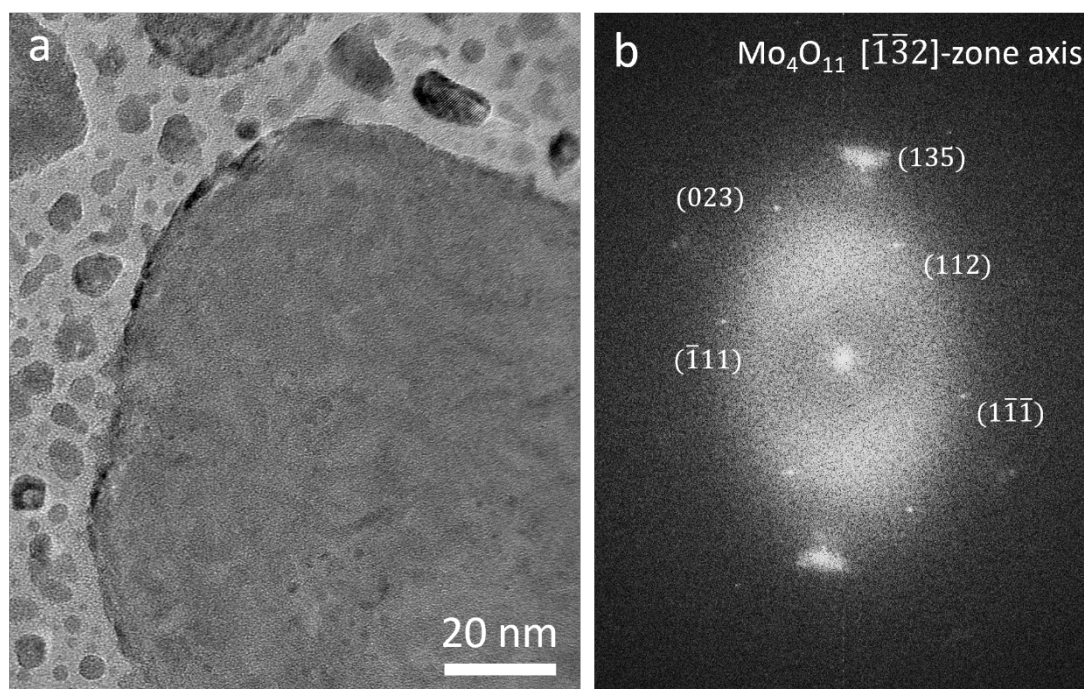


Figure 6-7 HRTEM image and corresponding FFT images of an exfoliated flake at 550 °C.

To find out whether the transformation to MoO_2 already happened below 600 °C, HRTEM images of the flakes formed below 600 °C were measured and indexed as well. Figure 6-7 shows a HRTEM image of an exfoliated flake at 550 °C. The FFT image corresponds to an $[\bar{1}\bar{3}2]$ - Mo_4O_{11} projection. Since the lattices spacings of MoO_3 and Mo_4O_{11} are very similar, the FFT image can be also indexed as $[1\bar{1}\bar{1}]$ of MoO_3 . However, the van der Waals bonded layers of MoO_3 are stacked in $[010]$ -direction, and it is therefore very unlikely that nanosheets with $[1\bar{1}\bar{1}]$ surface are formed. Therefore, the nanosheets are most likely Mo_4O_{11} . It is clear, however, that the flakes formed below 600 °C have not reduced yet to MoO_2 . Similar HR images matching the Mo_4O_{11} phase are shown in Figure S6-4. We consider it possible that the flakes exfoliate as $\text{MoO}_3(010)$ layers, after which they transform to MoO_2 phase via Mo_4O_{11} .

One remaining question is why the massive exfoliation as shown in Figure 6-3 only takes place during rapid heating. Although it is clear, also from the DFT and AIMD simulations presented below, that the weakly bound (010) layers in MoO_3 are prone to heating-induced exfoliation, we hypothesize that the strong dependence on the heating rate is due to thermal shock taking place at the nanoparticle as the temperature of the MEMS heater is swiftly increased. The fast heating rate results in an out-of-

equilibrium process involving shock-wise heat transport, likely leading to high shear stresses between the weakly bound layers, and resulting in efficient exfoliation and scattering of exfoliated flakes around the primary particles.

6.3.2 DFT calculations

To gain more insight into the relative stability and the energetics of the observed phases, density functional theory (DFT) calculations were performed by Roos M de Boer. The MoO₃, Mo₄O₁₁, and MoO₂ structures were first relaxed using the DFT-D3 functional as described in the Methods section. Also the energy of the O₂ molecule was calculated. The optimized O₂ bond length is 1.23 Å, which agrees well with the reference value of 1.21 Å.

The reduction reaction of MoO₃ to MoO₂ is given by:



and from the total energies of these three phases, it follows that there is an energy cost of 1.97 eV per MoO₃ formula unit (f.u.) that is reduced to MoO₂. In a similar way, the reduction reaction of MoO₃ to Mo₄O₁₁ is given by:



the energy cost of which is 0.31 eV/f.u. of MoO₃. The DFT calculations yield formation enthalpies valid for a temperature of 0 K and a pressure of 0 Pa. Because the heating was performed in high vacuum, we assume that the oxygen pressure is zero and that entropy can be neglected. Since there is an energy cost associated to the reduction of MoO₃, the reduction is not energetically favorable at 0 K. Because the energy cost to form Mo₄O₁₁ is lower than the cost to form MoO₂, it is expected that Mo₄O₁₁ will form before MoO₂. It is also possible to form Mo₄O₁₁ in a reaction between MoO₃ and the already formed MoO₂:



which actually results in an energy gain of 0.25 eV/f.u. of MoO₃. From the DFT calculations, it cannot be inferred whether the found Mo₄O₁₁ is formed as an intermediate, or in a side reaction. There was little evidence of Mo₄O₁₁ in the larger particles and only at 500 and 550 °C. It is therefore possible

that Mo_4O_{11} is only an intermediate phase that quickly reduces further to MoO_2 . Another possibility is that Mo_4O_{11} is formed in a side reaction, after which it also reduces to MoO_2 at higher temperatures. Because the side reaction is energetically favorable at 0 K, it is more likely that the Mo_4O_{11} will form in the side reaction.

In order to calculate the (010) surface energy, an MoO_3 supercell consisting of a 5-layer slab was also relaxed, using the same settings and functional as for the MoO_3 unit cell. The surface energy of the (010) MoO_3 surface was calculated using Equation 1. With a surface area of 14.46 \AA^2 as calculated from the lattice parameters of the relaxed MoO_3 supercell, the surface energy was calculated to be $1.17 \cdot 10^{-2} \text{ eV/ \AA}^2$, or 0.187 J/m^2 .

The energy required for the exfoliation will be at least twice the surface energy, but can also be higher when an additional energy barrier needs to be overcome. To calculate the activation energy for exfoliation of the (010) MoO_3 layers as observed during heating in the TEM, the upper (010) layer was shifted away from a thicker MoO_3 slab, and the potential energy of the supercell was calculated along that pathway using the NEB method as described in the Methods section. Figure 6-8(a) shows the configuration of the slab before shifting of the top layer, Figure 6-8(b) the configuration with a fully exfoliated top layer, and Figure 6-8(c) shows the potential energy evolution during the shift. Remarkably, apart from the difference in potential energy between the starting and final configuration there is no additional energy barrier. In other words: the activation energy is equal to the total difference in potential energy. The energy cost to remove one layer from the MoO_3 bulk is therefore 0.478 Jm^{-2} . This energy is higher than twice the (010) surface energy (as two surfaces are created). The absence of an additional activation barrier indicates that the MoO_3 layers are weakly bound.

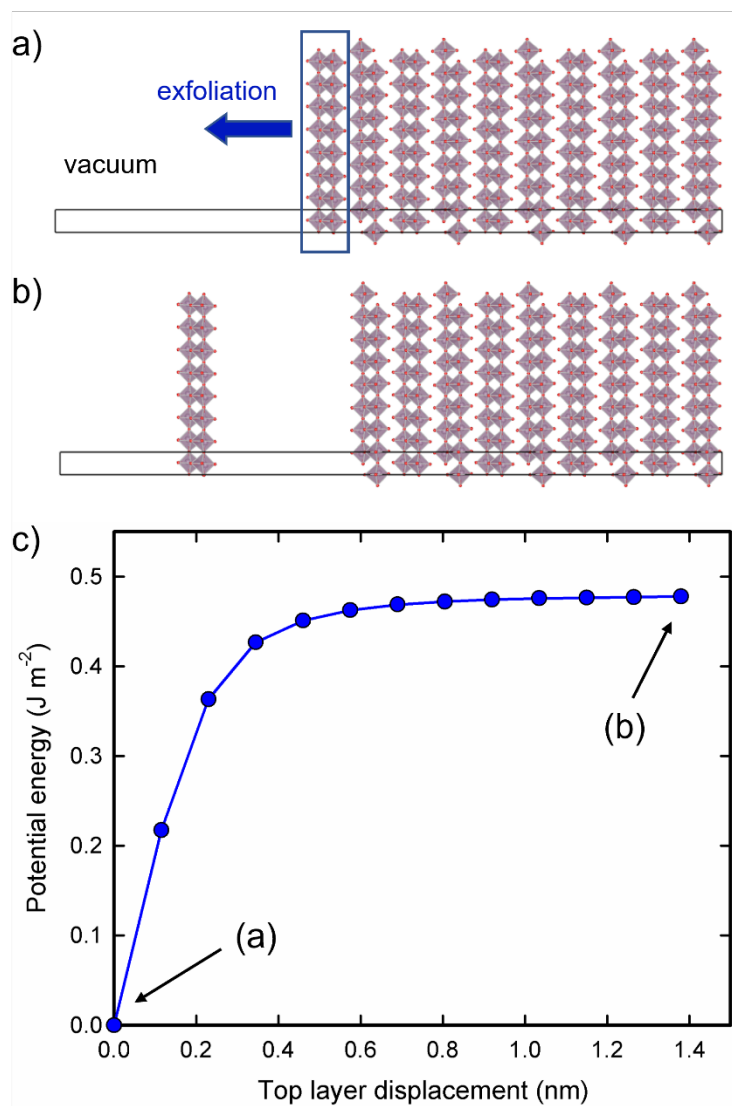


Figure 6-8. (a,b) Supercell that was used to calculate the activation energy for exfoliation, with (a) the MoO₃ supercell before exfoliation and (b) with the largest calculated shift of the top layer of 1.38 nm. Black lines indicate the boundaries of the supercell which includes a substantial vacuum layer. The periodic cell is repeated in lateral dimensions several times to display the slab-like nature of the supercell. The color coding for the atoms is the same as in Figure 1. (c) Evolution of the potential energy of MoO₃ as a function of the shift of the exfoliated top layer calculated using the nudged elastic band (NEB) method.

6.3.3 Ab initio molecular dynamics simulations

To obtain more insight into the thermal vibrations leading to exfoliation, ab initio molecular dynamics (AIMD) simulations were performed by Heleen van Gog. A 192-atom simulation cell was used consisting of a 2×3×2 MoO₃ slab and a vacuum layer of more than 70 Å along the [010] axis of the stacking direction, as described in the Methods section. In Figure 6-9 and in Figure S 6-5 in the SI, the

temperature and the separation between Mo layers are shown as observed during the AIMD simulations. Here, the separation between Mo layers is defined as the averaged perpendicular distance between the two closest Mo atomic layers of two adjacent MoO₃ bilayers (the definition of the individual separating distances d_1 , d_2 , d_3 , d_4 , and d_5 can be found illustrated in Figure S 6-5c). As can be seen, the separation between Mo layers, which was calculated to be ~ 4.17 Å at 0 K, increases at elevated temperatures.

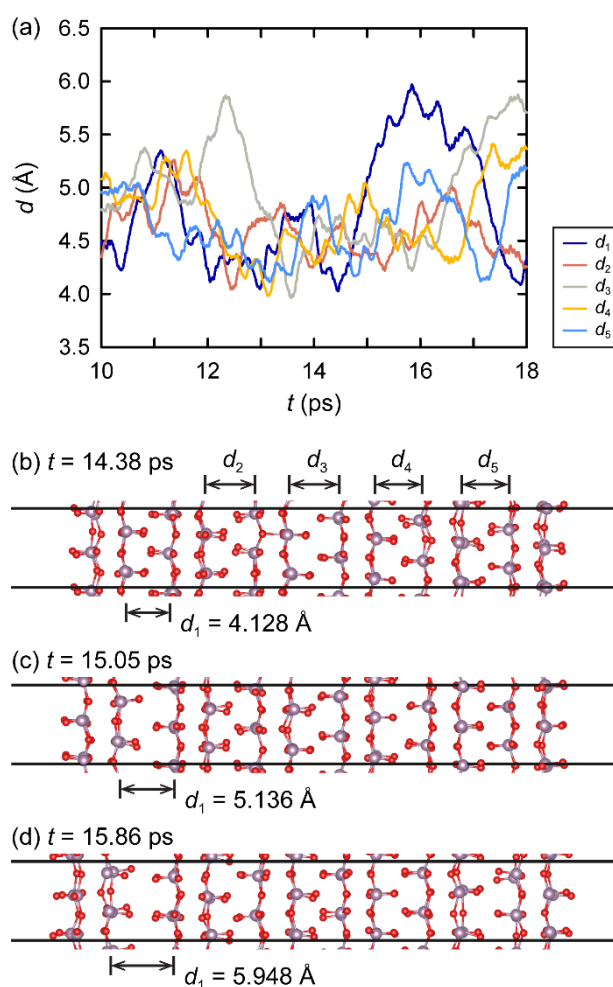


Figure 6-9 AIMD simulation of the $2 \times 3 \times 2$ MoO₃ slab at 900 K. (a) Separating distances as observed during the simulation. The definition of the distances is illustrated in panel (b). (b–d) Snapshots of three configurations leading up to the configuration in which the maximum separation occurred, showing on their left-hand side the onset of exfoliation of the outermost layer from the slab. Here, Mo and O atoms are represented by mauve and red spheres, respectively. The boundaries of the simulation cell are indicated by black solid lines.

It should be noted that for the AIMD simulations, the dimensions of the supercell are fixed. This means that during the simulations, thermal expansion of the system can only be accommodated in the stacking direction of the MoO₃ layers. At the same time, MoO₃ is known to exhibit anisotropic thermal expansion, where with increasing temperature the lattice expands considerably along the stacking direction but only a little along the [100] direction, and even slightly contracts along the [001] direction⁴⁴. To get a general idea of the effect of the fixed cell parameters and the limited time and length scale of the AIMD simulations on the observed separating distances, we compared the increase of the separation in the middle (d_3), which is the most bulk-like part of the slab, as obtained during the 300-K simulation with previous experimental results on the thermal lattice expansion of MoO₃ bulk⁴⁴. The averaged value of d_3 during the 300-K simulation was found to be 4.23 Å, which is an increase along the stacking direction of 1.4% relative to the 0-K value. Experimentally, for MoO₃ bulk, a lattice expansion of 0.9% has been indicated for this temperature range along the stacking direction, and an expansion of 0.2% and -0.04% along the other two directions⁴⁴. This indicates that the effect of the fixed cell parameters with only the possibility of expansion along the stacking direction and the limited time and length scale of the simulations on the observed values of d can be considered to be small.

The maximum separation observed during the 300-K simulation has a value of 4.88 Å, which is an increase of ~0.7 Å relative to the 0-K value. A snapshot of the configuration in which this maximum separation occurred can be found in Figure S 6-5, and shows that the simulation at 300 K, in agreement with our experimental results, does not point to the possibility of exfoliation at this temperature.

The picture is quite different for the simulations at 900 and 1100 K. The maximum separation observed during the 900-K simulation has a value of 5.97 Å (see Figure 6-9a) and involves the moving away of an outermost layer (see Figure 6-9 b–d and Video 1). This moving away clearly qualifies as the onset of exfoliation of this layer from the slab. Not only did its separating distance increase by ~1.8 Å relative to the value at 0 K; as can be seen from the configurations depicted in Figure 6-9 b–d (and see also Figure S 6-5 i and Video 1), the moving away of this layer along the stacking direction was accompanied by a shifting of the layer along the [001] direction by which the oxygen atoms alongside the formed gap started occupying positions more opposite of each other (but

only in this direction). A similar moving and shifting away was observed for the layers involved in the maximum separation occurring during the 1100-K simulation. In this case, the gap formed in the middle of the slab (see Figure S 6-5l–n), which suggests the onset of separation of the slab into two halves rather than the onset of the exfoliation of a single layer from the slab, and resulted in a maximum separating distance of 6.13 Å (see Figure S 6-5k), which is an increase of ~ 2.0 Å relative to the value at 0 K. Such an onset of separation of the slab into two halves was observed during the 900-K simulation as well (see Video 1), with a maximum value of d_3 of 5.88 Å (see Figure 6-9a), which is an increase of ~ 1.7 Å relative to the value at 0 K. The averaged value of d_3 during the 900-K simulation was found to be 4.95 Å and corresponds to an increase of 18.6% relative to the 0-K value, while in the mentioned previous experimental study on MoO₃ bulk a lattice expansion of 4.2% has been reported for the 0–900-K energy range⁴⁴. This is yet another indication that at temperatures of 900 K and higher, exfoliation and separation of single- and multi-layer MoO₃ nanosheets will very likely take place.

At the limited time-scale of the AIMD simulations presented here, full delamination was not observed. Structural features such as terrace steps at the (010) surface and edges, which are expected to serve as starting points for delamination during our experiments, were not incorporated in the simulations. Considering the quite extreme additional separation between the layers, of up to ~ 1.8 Å for the 900-K simulation, full delamination events can very well be expected to occur, however, for prolonged simulation times.

6.4 Conclusion and Outlook

In this study the thermal evolution of micrometer-sized MoO₃ particles was investigated. When heated rapidly, the particles were exfoliated and broke up into smaller flakes at around 500 °C. The HRTEM images of these flakes show a MoO₃ or Mo₄O₁₁ crystal structure. The exfoliation started from the surface and progressed into the center of the particles. Upon rapid annealing at a higher temperature of 600 °C, the exfoliation of small flakes from the pristine particles took place at a very high pace and these very thin flakes were found scattered on the substrate in a wide area around the larger particles. The SADPs of the small flakes show that these have the MoO₂ crystal structure. Therefore,

nanosheets were exfoliated from the MoO₃ particles and were reduced to MoO₂ nanosheets during thermal treatment, possibly with Mo₄O₁₁ forming as intermediate stage.

Upon gentle annealing, MoO₃ particles can be reduced to MoO₂ without high-pace disintegration, and less nanoflakes chipped off and flied away from the larger particles. Here the initial morphology is more or less retained, but in this case the initially single crystal MoO₃ micron-sized particles turned into hollow structures having a polycrystalline shell.

DFT calculations were performed to obtain insight into the energetics of the transformation. Taking into account van der Waals interactions was found to give a major improvement in the prediction of the *b* lattice parameter of bulk MoO₃, which is along the layer stacking direction. Using the DFT-D3 functional, the surface energy of MoO₃ (010) surface was calculated to be 0.187 Jm⁻² and the activation energy for exfoliation of a single MoO₃ layer was calculated to be 0.478 Jm⁻². This latter value is only slightly higher than the energy it takes to create two surfaces, which is 0.374 Jm⁻². The energy path showed that the activation energy for the exfoliation is equal to the potential energy change before and after the exfoliation, meaning that the layers in MoO₃ are weakly bound and that there is no additional activation barrier. Ab initio molecular dynamics (AIMD) simulations were also performed, and showed that thermal vibrations result in strong fluctuations of the (010) interlayer distances, where for a temperature of 900 K the additional separation between the layers can be as large as 1.8 Å (in comparison to the separation at 0 K), marking the onset of exfoliation. Both the DFT and AIMD simulations show that the (010) layers are weakly bound and prone to delamination. The reason that the exfoliation takes place experimentally only for high heating rates, is most likely due to thermal shock resulting in mechanical stresses inside the primary particles, which not only causes delamination but also scattering of the exfoliated flakes over considerable distances away from the primary particles.

Our study shows that depending on the heating rate, micron-sized MoO₃ particles can either be turned into hollow structures with polycrystalline shells, or can be nearly completely disintegrated into thin nanoflakes when heated at a very high pace at a temperature of 600 °C. The efficient production of molybdenum oxide nanosheets with a very large effective surface area may be very interesting for e.g. applications in catalysis.

6.5 Acknowledgements

This study is collaborated with Roos M de Bore and Heleen van Gog on computational part. RMdB performed the DFT calculations on the bulk phases and the surface energy calculations. RMdB and HvG performed the NEB calculation. HvG performed the AIMD simulations. The figures of atomic configurations were produced using VESTA⁴³. The video was produced using VMD⁴⁵.

6.6 References

- 1 H. Zhang, L. Gao and Y. Gong, *Electrochem. commun.*, 2015, **52**, 67–70.
- 2 A. Roy, P. K. Dutta and S. Mitra, *J. Mater. Chem. A*, 2017, **5**, 20491–20496.
- 3 M. Ranjba, F. Delalat and H. Salamati, *Appl. Surf. Sci.*, 2017, **396**, 1752–1759.
- 4 S. Bai, S. Chen, L. Chen, K. Zhang, R. Luo, D. Li and C. C. Liu, *Sensors Actuators B Chem.*, 2012, **174**, 51–58.
- 5 F. Ji, X. Ren, X. Zheng, Y. Liu, L. Pang, J. Jiang and S. (Frank) Liu, *Nanoscale*, 2016, **8**, 8696–8703.
- 6 P. S. Wang, Y. Y. Lo, W. H. Tseng, M. H. Chen and C. I. Wu, *J. Appl. Phys.*, 2013, **114**, 063710.
- 7 J. Liang, F. S. Zu, L. Ding, M. F. Xu, X. B. Shi, Z. K. Wang and L. S. Liao, *Appl. Phys. Express*, 2014, **7**, 111601.
- 8 D. Hanlon, C. Backes, T. M. Higgins, M. Hughes, A. O'Neill, P. King, N. McEvoy, G. S. Duesberg, B. Mendoza Sanchez, H. Pettersson, V. Nicolosi and J. N. Coleman, *Chem. Mater.*, 2014, **26**, 1751–1763.
- 9 M. Sato, M. Onoda and Y. Matsuda, *J. Phys. C Solid State Phys.*, 1987, **20**, 4763.
- 10 A. Magnéli, N. Hofman-Bang and P. Gjertsen, *Acta Chem. Scand.*, 1948, **2**, 501–517.
- 11 S. Åsbrink, L. Kihlberg, L. M. Jackman and D. R. Sparrow, *Acta Chem. Scand.*, 1964, **18**, 1571–1573.
- 12 L. A. Bursill, *Proc. R. Soc. London. A. Math. Phys. Sci.*, 1969, **311**, 267–290.
- 13 L. A. Bursill, *Acta Crystallogr. Sect. A*, 1972, **28**, 187–191.
- 14 L. A. Bursill, *Acta Crystallogr. Sect. A*, 1973, **29**, 28–30.
- 15 L. Brewer and R. H. Lamoreaux, *Bull. Alloy Phase Diagrams*, 1980, **1**, 85–89.
- 16 B. G. Brandt, A. C. Skapski, E. Thom, E. Stoll, G. Eriksson, R. Blinc, S. Paušak, L. Ehrenberg and J. Dumanović, *Acta Chem. Scand.*, 1967, **21**, 661–672.
- 17 W. Thöni, P. Gai and P. B. Hirsch, *J. Less-Common Met.*, 1977, **54**, 263–271.
- 18 P. A. Spevack and N. S. McIntyre, *J. Phys. Chem.*, 1992, **96**, 9029–9035.
- 19 T. Matsuda, Y. Hirata, H. Itoh, H. Sakagami and N. Takahashi, *Microporous Mesoporous Mater.*, 2001, **42**, 337–344.
- 20 D. Wang, D. S. Su and R. Schlögl, *Zeitschrift für Anorg. und Allg. Chemie*, 2004, **630**, 1007–1014.
- 21 B. Hu, L. Mai, W. Chen and F. Yang, *ACS Nano*, 2009, **3**, 478–482.
- 22 A. Borgschulte, O. Sambalova, R. Delmelle, S. Jenatsch, R. Hany and F. Nüesch, *Sci. Rep.*, 2017, **7**, 1–9.

- 23 K. Inzani, M. Nematollahi, S. M. Selbach, T. Grande and F. Vullum-Bruer, *Thin Solid Films*, 2017, **626**, 94–103.
- 24 J. Chen and Q. Wei, *Int. J. Appl. Ceram. Technol.*, 2017, **14**, 1020–1025.
- 25 S. Macis, J. Rezvani, I. Davoli, G. Cibin, B. Spataro, J. Scifo, L. Faillace and A. Marcelli, *Condens. Matter*, 2019, **4**, 1–7.
- 26 R. Burch, *J. Chem. Soc. Faraday Trans. 1 Phys. Chem. Condens. Phases*, 1978, **74**, 2982.
- 27 T. Ressler, R. E. Jentoft, J. Wienold, M. M. Günter and O. Timpe, *J. Phys. Chem. B*, 2000, **104**, 6360–6370.
- 28 E. Lalik, *Catal. Today*, 2011, **169**, 85–92.
- 29 J. Dang, G.-H. Zhang, K.-C. Chou, R. G. Reddy, Y. He and Y. Sun, *Int. J. Refract. Met. Hard Mater.*, 2013, **41**, 216–223.
- 30 G. Kresse and J. Furthmüller, *Comput. Mater. Sci.*, 1996, **6**, 15–50.
- 31 G. Kresse and J. Furthmüller, *Phys. Rev. B - Condens. Matter Mater. Phys.*, 1996, **54**, 11169–11186.
- 32 J. P. Perdew, K. Burke and M. Ernzerhof, *Phys. Rev. Lett.*, 1996, **77**, 3865–3868.
- 33 J. P. Perdew, K. Burke and M. Ernzerhof, *Phys. Rev. Lett.*, 1997, **78**, 1396–1396.
- 34 S. Grimme, J. Antony, S. Ehrlich and H. Krieg, *J. Chem. Phys.*, 2010, **132**, 154104.
- 35 G. Román-Pérez and J. M. Soler, *Phys. Rev. Lett.*, 2009, **103**, 096102.
- 36 J. Klime, D. R. Bowler and A. Michaelides, *Phys. Rev. B - Condens. Matter Mater. Phys.*, 2011, **83**, 195131.
- 37 J. Klimeš, D. R. Bowler and A. Michaelides, *J. Phys. Condens. Matter*, 2010, **22**, 022201.
- 38 H. Sitepu, B. H. O'Connor and D. Li, *J. Appl. Crystallogr.*, 2005, **38**, 158–167.
- 39 G. Henkelman, B. P. Uberuaga and H. Jónsson, *J. Chem. Phys.*, 2000, **113**, 9901–9904.
- 40 S. Nosé, *J. Chem. Phys.*, 1984, **81**, 511–519.
- 41 N. Shuichi, *Prog. Theor. Phys. Suppl.*, 1991, **103**, 1–46.
- 42 D. M. Bylander and L. Kleinman, *Phys. Rev. B*, 1992, **46**, 13756–13761.
- 43 K. Momma and F. Izumi, *J. Appl. Crystallogr.*, 2011, **44**, 1272–1276.
- 44 H. Negishi, S. Negishi, Y. Kuroiwa, N. Sato and S. Aoyagi, *Phys. Rev. B - Condens. Matter Mater. Phys.*, , DOI:10.1103/PhysRevB.69.064111.
- 45 W. Humphrey, A. Dalke and K. Schulten, *J. Mol. Graph.*, 1996, **14**, 33–38.

6.7 Appendix

6.7.1 Supporting Figures

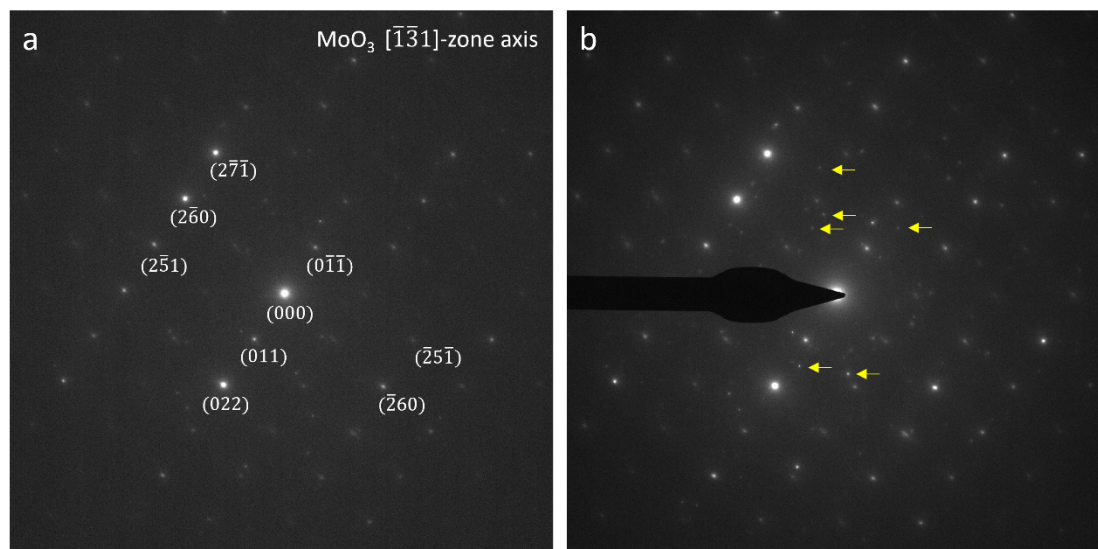


Figure S 6-1. Selected area diffraction patterns (SADPs) at 500 °C with MoO₃ in the $[\bar{1}\bar{3}1]$ -zone axis. (a) without beam stopper; (b) with beam stopper. Yellow arrows mark the new peaks appeared when using the beam stopper. These peaks corresponds to different orientations, confirming the formation of cracks and small domains before exfoliation.

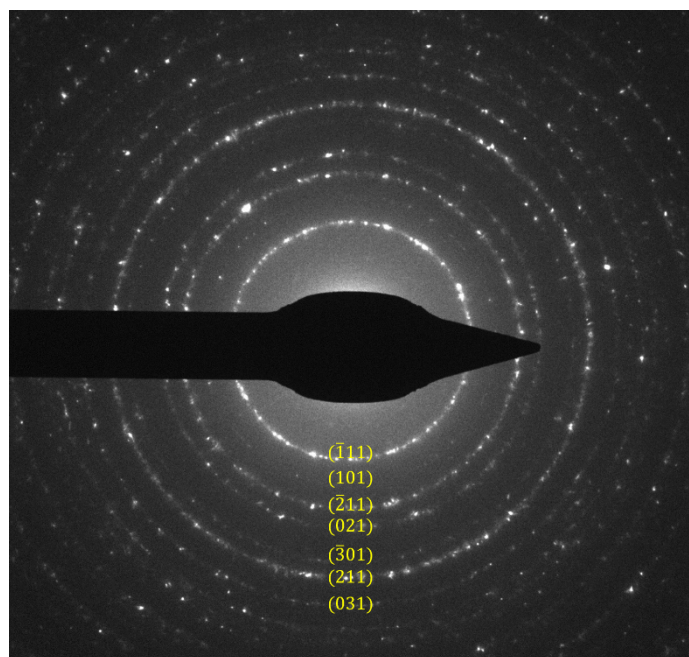


Figure S 6-2 SADP of the particles after gentle heating to 600 °C, showing MoO₂ structure.

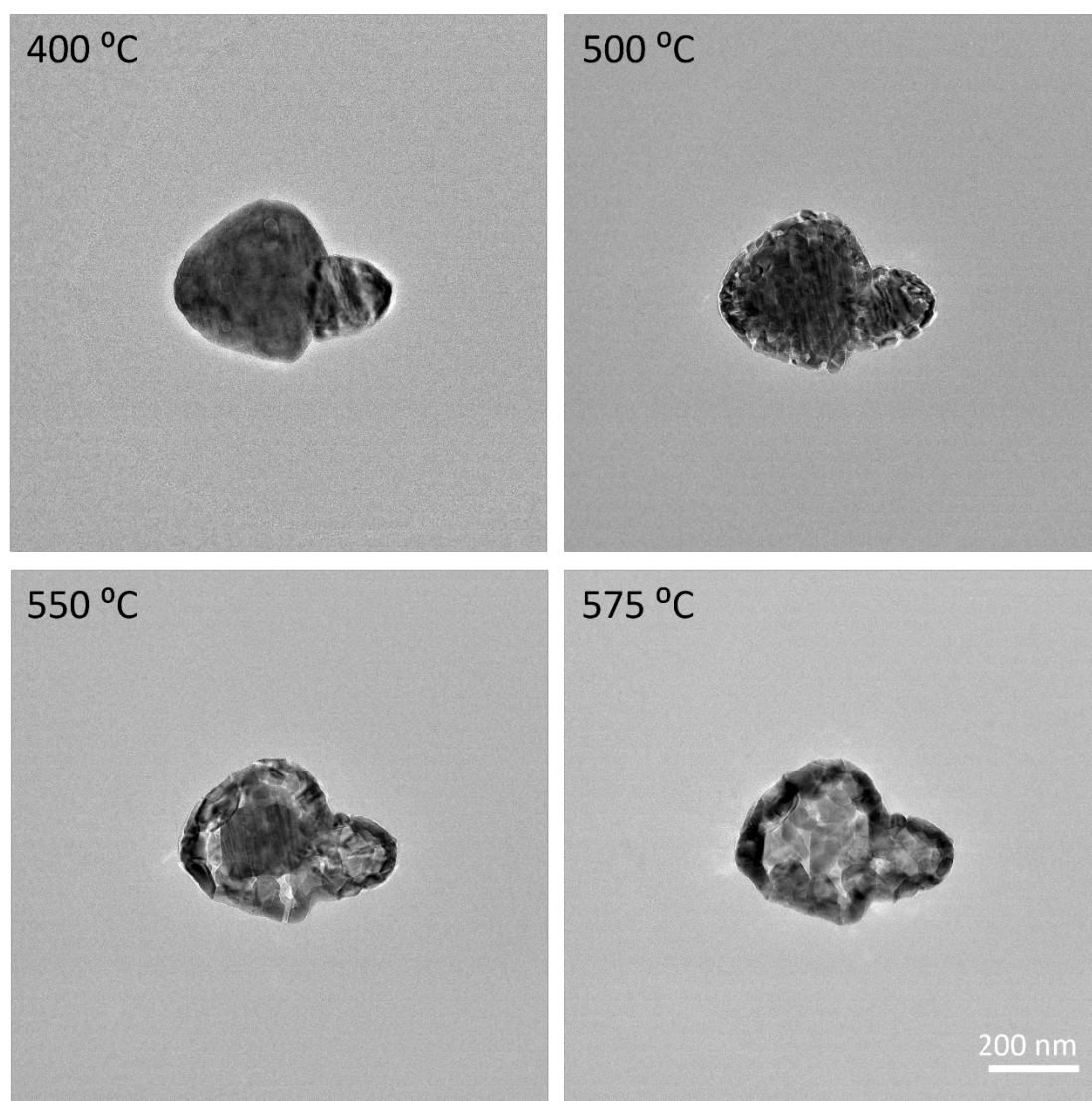


Figure S6-3. Bright-field TEM images of smaller particles heated gently with 25 °C increments to 400 °C and higher, at the indicated temperatures.

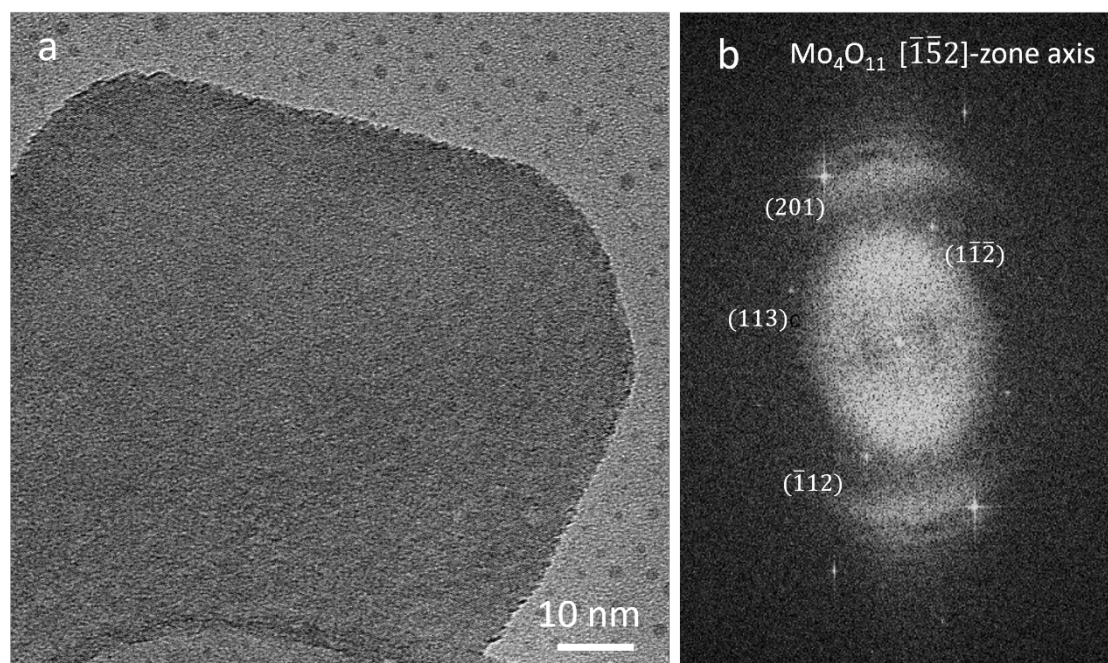


Figure S6-4. HRTEM image and corresponding FFT image of an exfoliated flake at a temperature of 500 °C. Some remaining thermal drift in the heating holder leads to a cut-off of the higher spatial frequencies in horizontal direction which is visible in the FFTs.

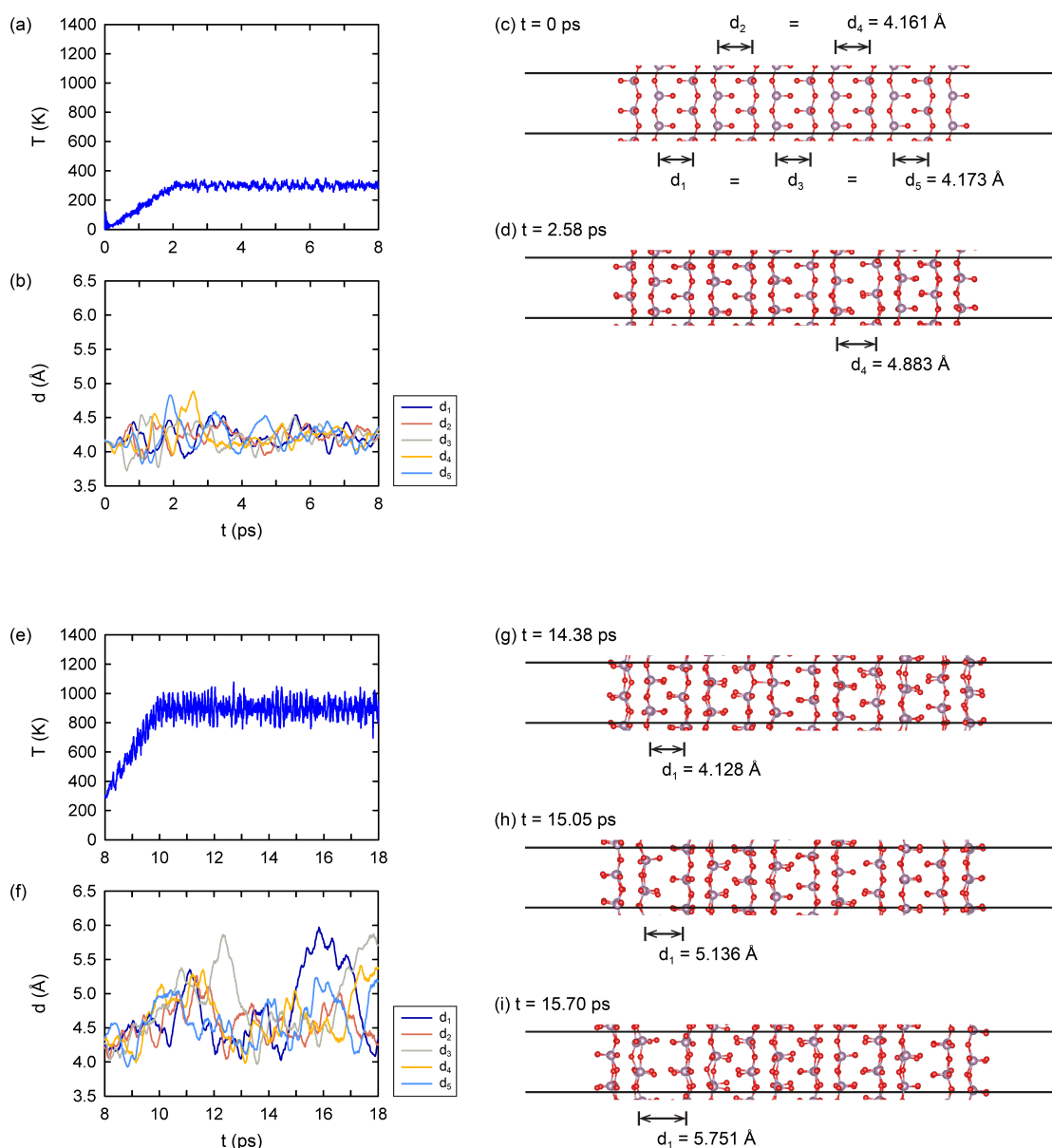


Figure S 6-5. AIMD simulation of the $2 \times 3 \times 2$ MoO₃ slab. Panels (a,b), (e,f), and (j,k) (see next page) show the temperature and the separating distances as observed during the simulations. The definition of the distances is illustrated in panel (c) showing the starting configuration corresponding to temperature of 0 K. Panel (d) shows a snapshot of the configuration in which the maximum observed separation during the 300-K simulation occurred. Panels (g–i) and (l–n) (see next page) show snapshots of three configurations leading up to the configuration in which at 900 and 1100 K the maximum separation occurred. Mauve and red spheres denote Mo and O atoms, respectively. The boundaries of the simulation cell are indicated by black solid lines.

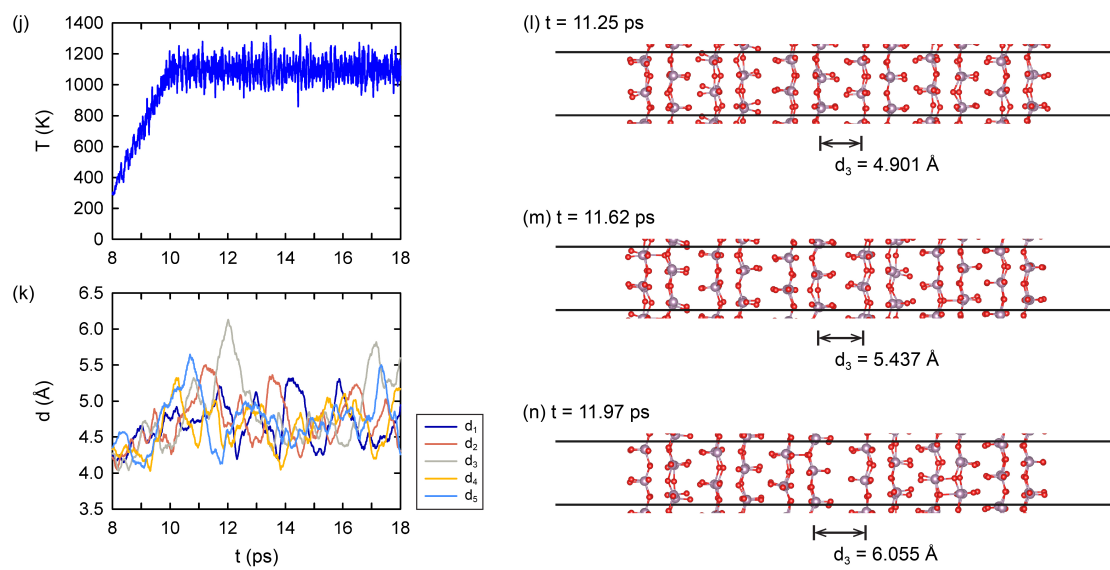


Figure S 6-5, continued. For caption, see previous page.

6.7.2 Supporting Tables

Table S 6-1 Lattice reflections of MoO₃ (JCPDS 05-0506)

No.	h	k	l	d [Å]	2Theta[deg]	I [%]
1	0	2	0	6.98000	12.672	15.0
2	1	1	0	3.82000	23.267	85.0
3	0	4	0	3.47000	25.652	20.0
4	1	2	0	3.44000	25.879	40.0
5	0	2	1	3.27000	27.250	100.0
6	1	3	0	3.01000	29.655	10.0
7	1	0	1	2.70700	33.065	40.0
8	1	1	1	2.65700	33.706	70.0
9	1	4	0	2.61300	34.291	5.0
10	0	4	1	2.52800	35.481	15.0
11	1	3	1	2.33700	38.490	30.0
12	0	6	0	2.31200	38.923	20.0
13	1	5	0	2.27700	39.546	25.0
14	1	4	1	2.13500	42.298	25.0
15	2	0	0	1.98200	45.741	40.0
16	2	1	0	1.96500	46.159	50.0
17	2	2	0	1.90700	47.649	5.0
18	0	0	2	1.85200	49.156	80.0
19	2	3	0	1.82200	50.020	35.0
20	0	2	2	1.78800	51.039	20.0
21	1	6	1	1.75400	52.102	5.0
22	0	8	0	1.73500	52.716	65.0
23	2	4	0	1.72000	53.212	5.0
24	2	2	1	1.69400	54.094	40.0
25	1	1	2	1.66600	55.080	70.0
26	1	2	2	1.63000	56.403	40.0
27	1	7	1	1.59900	57.598	20.0
28	1	3	2	1.57700	58.479	10.0
29	0	8	1	1.56900	58.806	15.0
30	2	6	0	1.50600	61.526	5.0
31	2	5	1	1.47900	62.775	30.0
32	0	6	2	1.44600	64.378	20.0
33	1	5	2	1.43500	64.931	25.0
34	2	7	0	1.40200	66.656	10.0
35	2	0	2	1.35300	69.407	35.0
36	2	1	2	1.34700	69.761	40.0
37	2	2	2	1.32800	70.907	5.0
38	0	10	1	1.30000	72.675	45.0

Table S 6-2 Lattice reflections of MoO₂ (JCPDS 32-0671)

No.	h	k	l	d [Å]	2Theta[deg]	I [%]
1	-1	0	1	4.80500	18.450	2.0
2	-1	1	1	3.42000	26.033	100.0
3	1	0	1	2.81300	31.785	4.0
4	2	0	0	2.44200	36.775	30.0
5	1	1	1	2.43700	36.853	30.0
6	-2	1	1	2.42600	37.026	70.0
7	-2	0	2	2.40300	37.393	35.0
8	2	1	0	2.18100	41.365	6.0
9	0	2	1	2.17100	41.564	2.0
10	-2	1	2	2.15600	41.867	5.0
11	-3	0	1	1.84100	49.469	11.0
12	2	1	1	1.72500	53.045	30.0
13	-2	2	0	1.72300	53.112	35.0
14	-3	1	2	1.71100	53.514	40.0
15	-2	2	2	1.70900	53.581	35.0
16	-2	1	3	1.69760	53.970	20.0
17	-3	0	3	1.60330	57.429	1.0
18	-3	1	0	1.54430	59.842	7.0
19	0	3	1	1.53600	60.198	13.0
20	0	1	3	1.52720	60.581	9.0
21	-3	2	1	1.46760	63.319	4.0
22	2	0	2	1.40570	66.458	4.0
23	-4	0	2	1.40190	66.661	20.0
24	-2	0	4	1.38450	67.611	5.0
25	3	0	1	1.35480	69.301	2.0
26	0	3	2	1.34480	69.891	1.0
27	-3	2	3	1.33810	70.293	1.0
28	-4	1	1	1.30330	72.461	5.0
29	-4	1	3	1.29120	73.250	5.0
30	-3	1	4	1.28290	73.802	1.0
31	4	0	0	1.22190	78.161	7.0
32	2	3	1	1.21750	78.498	10.0
33	1	3	2	1.21460	78.721	6.0
34	-2	3	3	1.20760	79.267	7.0
35	-2	2	4	1.20280	79.647	4.0
36	3	2	1	1.18370	81.197	2.0
37	1	2	3	1.17640	81.808	1.0
38	-3	3	0	1.14850	84.242	2.0
39	0	3	3	1.14140	84.889	4.0

Table S 6-3. Lattice reflections of Mo₄O₁₁ (JCPDS 05-0337)

No.	h	k	l	d [Å]	2Theta[deg]	I [%]
1	2	0	0	12.30000	7.181	30.0
2	3	0	1	5.19000	17.071	10.0
3	4	0	1	4.53000	19.581	25.0
4	0	1	1	4.24000	20.935	45.0
5	2	1	1	4.00000	22.206	100.0
6	5	0	1	3.95000	22.491	65.0
7	3	1	1	3.75000	23.707	95.0
8	6	0	1	3.48000	25.577	85.0
9	1	0	2	3.33000	26.750	10.0
10	6	1	0	3.26000	27.335	20.0
11	3	0	2	3.11000	28.681	15.0
12	2	1	2	2.78700	32.090	50.0
13	5	0	2	2.77100	32.280	15.0
14	0	2	0	2.72200	32.878	60.0
15	3	1	2	2.70000	33.153	45.0
16	8	1	0	2.66300	33.627	70.0
17	6	0	2	2.59300	34.563	30.0
18	2	2	1	2.47300	36.297	10.0
19	7	0	2	2.42300	37.073	12.0
20	10	1	0	2.22500	40.510	30.0
21	2	0	3	2.20700	40.855	15.0
22	6	2	1	2.14600	42.071	35.0
23	7	2	1	2.04600	44.233	10.0
24	10	0	2	1.97500	45.912	30.0
25	5	2	2	1.94100	46.764	45.0
26	6	2	2	1.87700	48.459	40.0
27	11	0	2	1.85200	49.156	35.0
28	7	2	2	1.81000	50.375	30.0
29	7	1	3	1.78400	51.161	35.0
30	1	3	1	1.75000	52.230	10.0
31	2	3	1	1.73300	52.781	10.0
32	1	2	3	1.72600	53.012	50.0
33	13	1	1	1.71600	53.345	40.0
34	11	2	1	1.66600	55.080	15.0
35	9	1	3	1.64800	55.733	70.0
36	14	1	1	1.61200	57.091	30.0
37	12	2	1	1.58300	58.236	45.0
38	7	3	1	1.56700	58.888	15.0
39	8	3	0	1.56000	59.179	20.0
40	6	0	4	1.55500	59.388	25.0

6.7.3 Supporting Movie

You can download Video1 with the following link:

https://drive.google.com/file/d/1kcULiDpK_srppMC6uapAOxiRZ-VQcxgK/view?usp=sharing

7. Formation pathways of lath-shaped WO₃ nanosheets and elemental W nanoparticles from heating of WO₃ nanocrystals

WO₃ is a versatile material occurring in many polymorphs, and is used in the nanostructured form in many applications including photocatalysis, gas sensing, and energy storage. We investigated the thermal evolution of cubic phase nanocrystals with a size range of 5-25 nm by means of in-situ heating in the transmission electron microscope (TEM), and found distinct pathways for the formation of either 2D WO₃ nanosheets or elemental W nanoparticles, depending on the concentration of initial WO₃ nanoparticles. These pristine particles were stable up to 600 °C, after which coalescence and fusion of the nanocrystals was observed. Typically, the nanocrystals transformed to faceted nanocrystals of elemental cubic W after annealing to 900 °C. However, in areas where the concentration of dropcast WO₃ nanoparticles was high, at a temperature of 900 °C considerably larger lath-shaped nanosheets (extending for hundreds of nm in length and up to 100 nm in width) were formed that are concluded to be in monoclinic WO₃ or WO_{2.7} phases. These lath-shaped 2D particles, which often curled up from their sides into folded 2D nanosheets, are most likely formed from the smaller nanoparticles through a solid-vapor-solid growth mechanism. The findings of the in-situ experiments were confirmed by ex-situ experiments performed in a high vacuum chamber.

7.1 Introduction

Tungsten trioxide is a semiconductor material with very diverse chemical and physical properties, and is consequently used in very diverse applications, including photocatalysis¹⁻⁴, gas sensing⁵⁻⁸, energy storage⁹⁻¹² and as an electrochromic^{13,14} material. WO₃ is widely applied as it is available at low cost, is abundant, and has an open tunnel-like structure which makes it permeable to gas atoms and suitable for ion transport.

The morphology and crystal structure are strongly connected to electronic properties of nanostructured WO₃¹⁴⁻¹⁶ and consequently affect their applications in catalysis and energy storage. Furthermore, gas sensors are expected to function as well in high temperature environments and therefore, an in-depth understanding of the thermal behavior and thermal stability of nanostructured WO₃ is of vital importance to assess their applicability to high-temperature applications.

There are various crystalline polymorphs of WO₃, which are based on a cubic ReO₃ structure.¹⁷ The material consists of tungsten centered oxygen octahedrons (WO₆ octahedrons) that are corner sharing and that show distortions, forming different phases with lower symmetry. Figure 7-1 shows the structure of the main 4 polymorphs with oxygen octahedrons. Corresponding crystallographic information including space groups and lattice parameters are listed in Table S1. W atoms are at the center of every octahedron. In previous studies, phase transformations between different polymorphs were observed in many cases, as a result of temperature treatment¹⁸⁻²², doping²³⁻²⁹, or mechanical treatment³⁰. The most common stable phase at room temperature is the monoclinic structure (Space group P2₁/n). With increasing temperature, the most stable phases are orthorhombic (Pbcn, ~500 °C), tetragonal (P4/ncc, 800 °C) and tetragonal (P4/nmm, 900 °C).^{17,19,20,31} Furthermore, there are metastable phases, such as hexagonal, triclinic and cubic. In an investigation by Howard *et al.*³², another monoclinic phase (P2₁/c) was observed to be formed between 760 °C to 800 °C. Ramana *et al.*¹⁸ reported that monoclinic WO₃ thin films transformed to the hexagonal phase at 500 °C. The thermal behavior of some metastable phases was also investigated.^{21,22} However, few studies have investigated the highest symmetry cubic WO₃ phases that are investigated in the present work.

Cubic WO₃ (Pm $\bar{3}$ m) is not a stable phase reported in the W-O phase diagram.¹⁷ Corà *et al.* explained

the reason of its instability as bulk material in 1996 from Hartree-Fock calculations.³³ Nanosized cubic phase WO_3 has been successfully fabricated though,^{34,35} which is commercially available, and has been used for solar cells¹⁰ and as an anode material¹¹. The emphasis in this work is to assess their thermal stability and to characterize phase transformations and morphology changes of cubic WO_3 phase nanoparticles. The nanocrystals are investigated from room temperature to 1000 °C with in-situ heating transmission electron microscopy (TEM) in order to study their structural and chemical thermal evolution in detail and in real time.³⁶ Most particles transformed to pure cubic α -W at 900 °C. At the same temperature, bigger lath-shaped WO_3 nanosheets were formed by recrystallization into a monoclinic structure. Transmission electron microscopy (TEM), selected area electron diffraction (SAED) and 2D chemical mapping by electron-dispersive X-ray spectroscopy (EDS) were employed for phase identification and to monitor structural and chemical transitions.

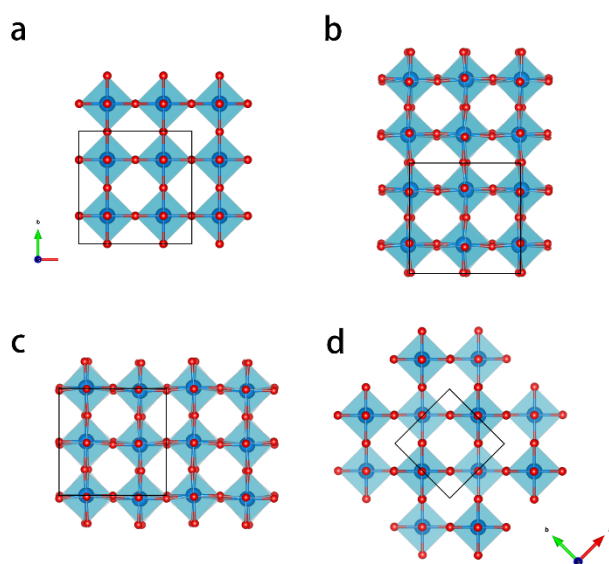


Figure 7-1 Crystal structures of the most commonly occurring WO_3 polymorphs displayed in a [001] projection. (a) cubic; (b) room temperature stable monoclinic; (c) orthorhombic; (d) tetragonal. The tetragonal phase has 45 ° tilt with respect to other phases. Crystallographic details are provided in Table S1.

7.2 Experimental

The WO_3 nanocrystals (NCs) were purchased from Sigma-Aldrich. All in-situ TEM investigations and STEM-EDS were conducted using a TFS TalosF200X TEM operating at 200 kV. The high-resolution

(HR) STEM images are taken with a double aberration corrected TFS Spectra300 TEM operating at 300 kV. The specimens were prepared by drop casting the WO₃ nanoparticles solution onto a DENSsolutions MEMS heating chip.

The heating chips were subsequently mounted on a DENS Solutions single tilt heating holder. The WO₃ nanoparticles were first heated from 20 °C to 1000 °C with 100 °C increments. The nanoscale phase transformation happened at 900 °C. In a second heating experiment, the specimen was heated from 20 °C to 800 °C with 100 °C increments, but with smaller increments of 25 °C when raising the temperature further from 800 °C to 900 °C, in order to check whether there is intermediate phase. The particles were found to be sensitive to the electron beam at elevated temperatures. Figure S 7-1 shows that the particles deformed rapidly after illumination by the electron beam for 1 min. In order to avoid such electron beam effects, the field of view was changed very often in order to always examine an area that was not previously exposed to the electron beam (the electron beam illuminates only a tiny fraction of the sample deposited area). Furthermore, in order to fully exclude any electron beam effects, the samples were also heated ex-situ outside of the TEM. For these ex-situ experiments, the samples were heated with the heating holder inserted in a high vacuum chamber (Gatan pumping station Model 655), applying the same heating rate as in the in-situ heating experiments. The pressure in the high vacuum chamber was approximately $1.0 \cdot 10^{-7}$ Torr. After holding the temperature at 900 °C for 10 minutes, the sample was cooled down fast to room temperature and swiftly inserted in the TEM for subsequent analysis.

7.3 Results and discussion

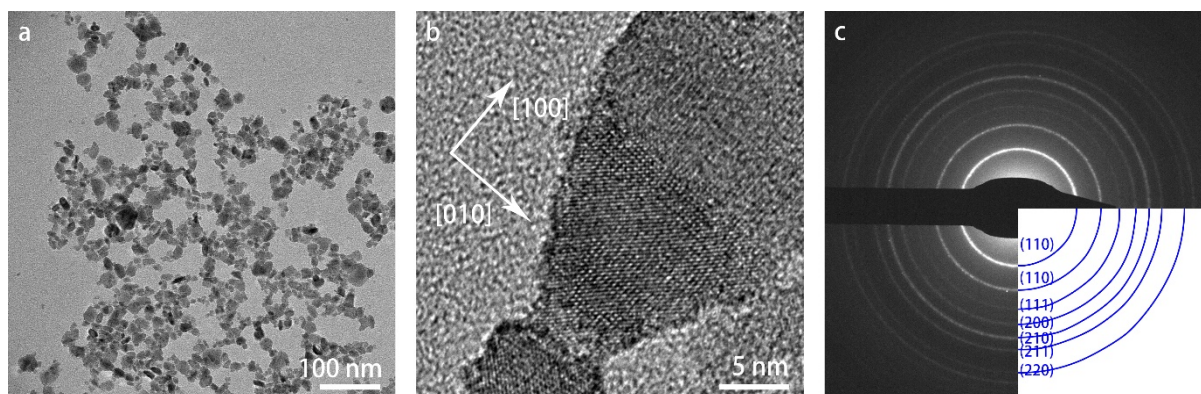


Figure 7-2 TEM images of WO_3 nanoparticles at room temperature. (a) overview image in bright-field mode; (b) High-resolution image; (c) SAED pattern with the indexing.

Figure 7-2 shows overview (a) and high-resolution (b) bright-field TEM images of the as-received WO_3 specimen at room temperature. The nanoparticles have a broad size range of 5-25 nm. Both the lattice fringes in the high-resolution TEM image in (b) and the selected-area diffraction pattern (SADP) with indexed diffraction rings in (c) confirm the cubic crystal structure.

The WO_3 nanoparticles were heated from room temperature to 1000 °C with 100 °C increments. Figure 7-3 shows bright-field TEM images of the specimen heated at different temperatures, displaying the evolution in morphology during heating. Images were taken from different areas of the heating chip in order to prevent any influence of the electron beam illumination on the observation of the thermal evolution, as explained in the Experimental section. Up to 600 °C, there is no obvious deformation of the particles yet. At 700 °C, the particles began to coalesce. At the edges of the particle clusters, some particles sublimated and left smaller dots. At 800 °C, coalescence progressed and small dots appeared commonly around the original particles. After annealing at 900 °C, the particles lost their original shape completely. In some areas, big lath-shaped particles were formed as can be seen in the bottom-right image of Figure 7-3.

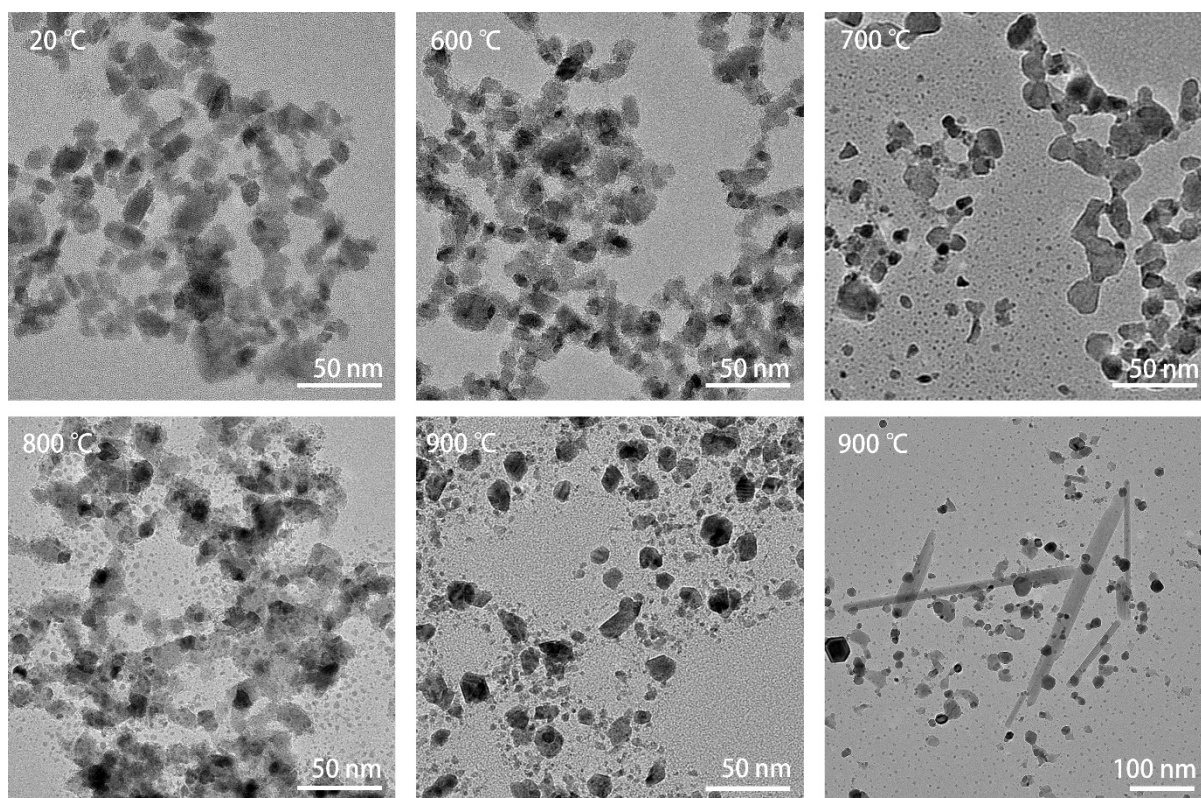


Figure 7-3. TEM images during heating from 20 °C to 900 °C in steps of 100 °C. Up to 600 °C, there is no obvious deformation of the particles yet. At 700 °C, the particles began to coalesce while some of the particles sublimated, leaving smaller dots of material. At 800 °C, coalescence continued and small dots commonly appeared around the original particles. After annealing at 900 °C, the particles lost their original shape completely. In some areas, much larger lath-shaped particles were formed as well, as can be seen in the bottom-right panel.

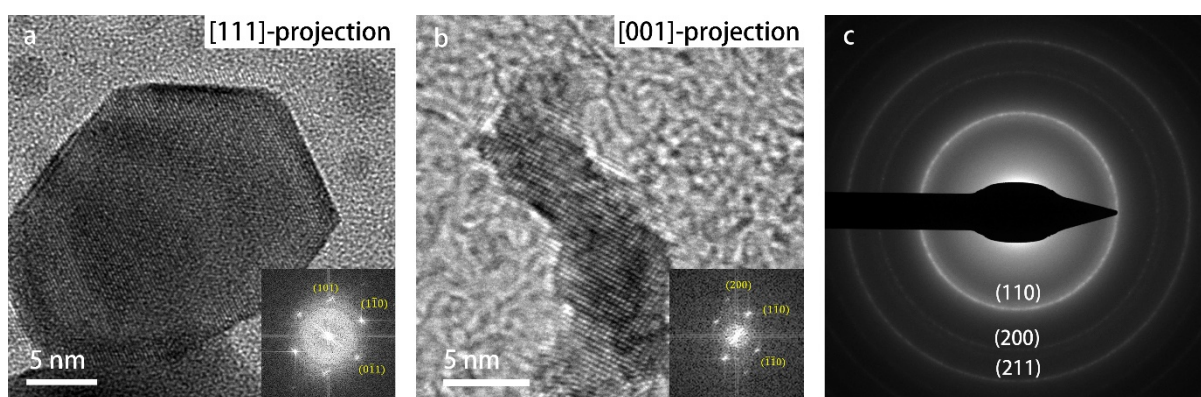


Figure 7-4 TEM images recorded at 900 °C. (a) HR-TEM image of elemental W in [111]-projection; (b) HR-TEM image of W in an [001]-projection. (c) SADP at 900 °C, with the corresponding lattice reflections indexed.

The SADPs were used for tracking and identifying the phase changes during heating. As shown in Figure S 7-2, a phase transformation took place at 900 °C. The diffraction pattern was indexed and is shown in Figure 7-4 (c), which indicated that the resulting phase is pure, body centered cubic W (α -W). High-resolution (HR) TEM images recorded along different projections of the crystal structure also confirm the cubic W structure. Therefore, the cubic WO₃ nanoparticles transformed to cubic W nanoparticles at 900 °C.

There are many other tungsten oxides with lower oxidation state and having a composition between WO₃ and pure W. The formation of other tungsten oxides like WO_{2.9}, WO_{2.72}, and WO₂ have been observed during the reduction of WO₃ by many researchers.³⁷⁻⁴² We have conducted additional experiments to check for the presence of any intermediate phases before pure W is formed. The specimens were heated to 800 °C with 100 °C increments, and subsequently from 800 °C to 900 °C with smaller, 25 °C increments. Figure S 7-3 shows the SADPs from 800 °C to 875 °C, where no other rings appeared in any of these DPs. This means that we have not observed any other intermediate phase. One noteworthy observation is that the intensity of the third ring (marked with a blue arrow) increased gradually from 825 °C (shown in Figure S 7-3(e)). This ring corresponds to both the (111) lattice reflection of WO₃ and the (110) lattice reflection of W. Therefore, cubic W is possibly already formed slightly below 900 °C.

The direct transformation to pure W, which is different from the previous studies, could be attributed to the high heating rate in our case. In the research of Fouad et al.⁴², both isothermal and non-isothermal TGA measurements were taken. During non-isothermal mode, samples were heated up to 1000 °C at 10 °C/min. Three transformation steps happened at 520-600 °C (WO_{2.7}), 600-655 °C (WO₂) and 713-875 °C (W). However, during isothermal measurement the samples are kept at constant temperature. When their powder sample was measured at 740 °C, the intermediate transformations overlapped kinetically. Only one steep step was detected in that study, corresponding to the complete reduction of WO₃ to W. In our study, the heating rate is considerably higher than 10 °C/min, implying that also here the several transformation steps are overlapping, resulting in the direct transformation to pure W. We mention here that Fouad and co-workers performed their study on WO₃ powder having initially a monoclinic crystal structure, while the present study is conducted on smaller WO₃ nanoparticles that initially have a cubic crystal structure, which explains the different

thermal evolution observed in the present investigation.

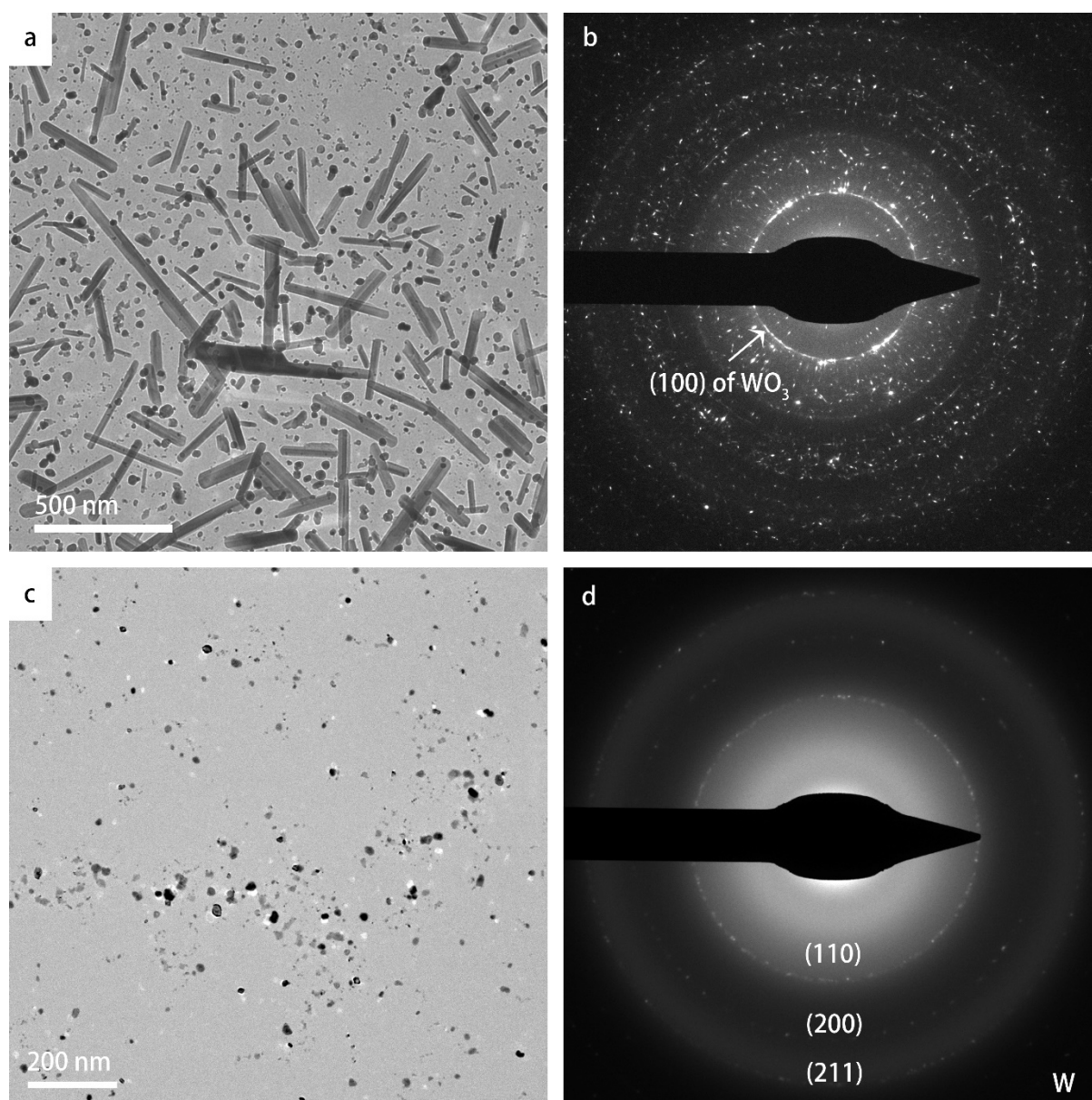


Figure 7-5 TEM images showing the results of the ex-situ heating experiments. (a,b) TEM image and corresponding DP with high concentration of dropcast specimen; (c) and (d) TEM image and DP with low concentration of dropcast specimen. Both samples were heated in a vacuum chamber by using heating holder to 900 °C with the same heating rate. After keeping the temperature at 900 °C for 10 min, the samples were cooled down to room temperature rapidly and swiftly inserted in the microscope for TEM inspection.

To rule out any possible influence of e-beam illumination to the phase transformation, ex-situ heating experiments were conducted in a vacuum chamber outside the microscope where the particles were heated to 900 °C as well, after which they were inserted in the TEM for structural characterization.

Surprisingly, in one of the experiments where a large amount of particles were dropcast onto the heating chip, many large lath-shaped particles were formed, and the DP also shows a strong peak of WO_3 . However, when less particles were dropcast onto the heating chip, lath-shaped particles were not formed and the DP only indicated a cubic W structure as shown in Figure 7-5(c,d). It seems that when the concentration of WO_3 nanoparticles is sufficiently high, lath-shaped particles can be formed, and this formation of lath-shaped particles apparently impedes the transformation to cubic W.

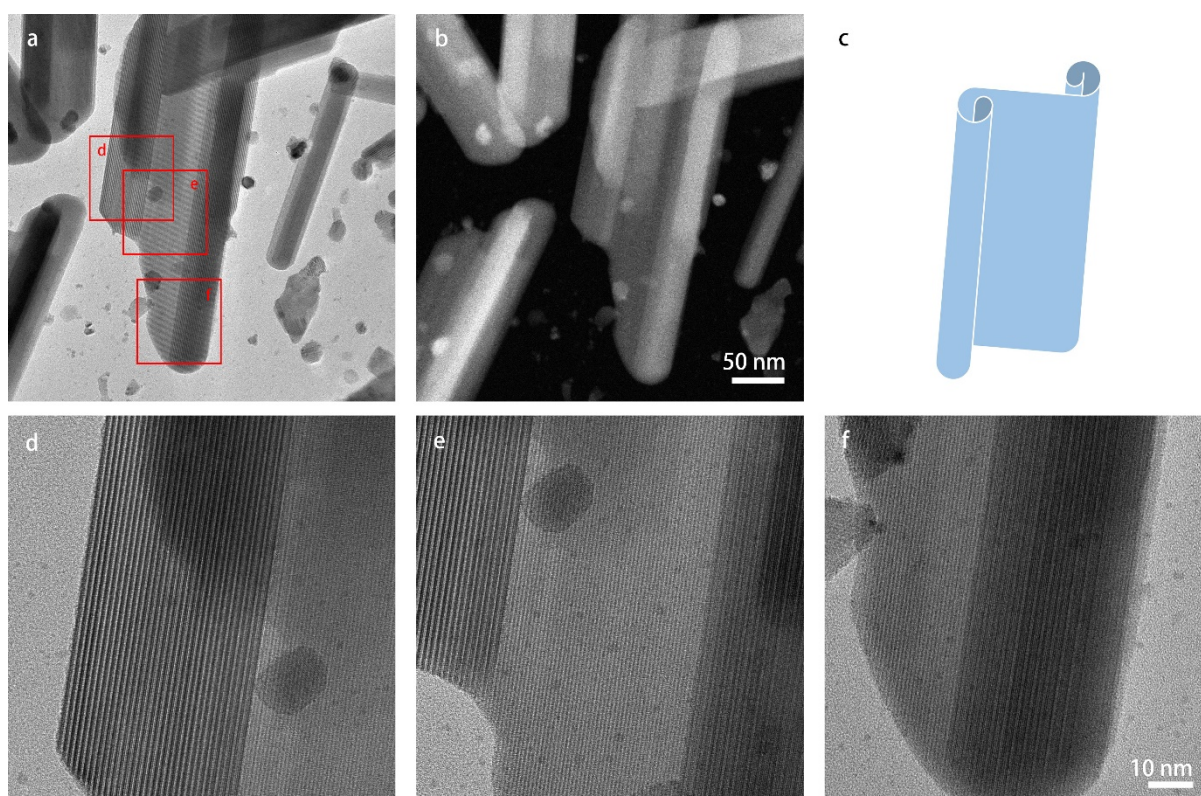


Figure 7-6. (S)TEM images of a larger lath-shaped 2D nanosheet. (a) Bright field TEM image and (b) HAADF-STEM image recorded at the same magnification; (c) model of the shape of the particle where the edges at the left-hand side and right-hand are curled up. (e)-(f) magnified TEM images of the corresponding areas indicated with red squares in panel (a). Morié patterns show multiple layers at the left-hand and right-hand edges of the particle.

In many images, the shape of the lath-shaped particles looks like a rod where the varying contrast points to curling up of the laths into cylinder-like structures. To investigate the shape of these particles further, the sample was tilted to about $\pm 30^\circ$ along the α -tilt axis. Figure S 7-4 show the images of an area projected along two tilt angles. The width of the particles changed by tilting, implying that the particles are not perfectly cylindrical. The particle shown in Figure 7-6 seems like a sheet that is folded at two sides, like the model shown in panel (c). The STEM images also show less contrast at the

center, indicating lesser thickness. Therefore, in this paper we have named the larger particles lath-shaped nanosheets.

Figure 7-6 (e-f) show magnified TEM images of the corresponding areas in panel (a). The spacings of the fringes on the two sides of the particles are much bigger than the lattice spacings. These stripe-like moiré patterns occur when two or more layers are overlapping while having different lattice spacings aligned in the same orientation. The spacing of the moiré fringes d_m formed by the different lattice spacings d_1, d_2 , can be calculated using the following equation:

$$d_{tm} = \frac{d_1}{1 - \frac{d_2}{d_1}}$$

The moiré patterns visible in Figure 7-6 (e-f) were commonly observed on the lath-shaped particles. More similar images are shown in Figure S 7-5. The moiré patterns indicate multiple layers, confirming that the two sides of the nanosheets have folded edges.

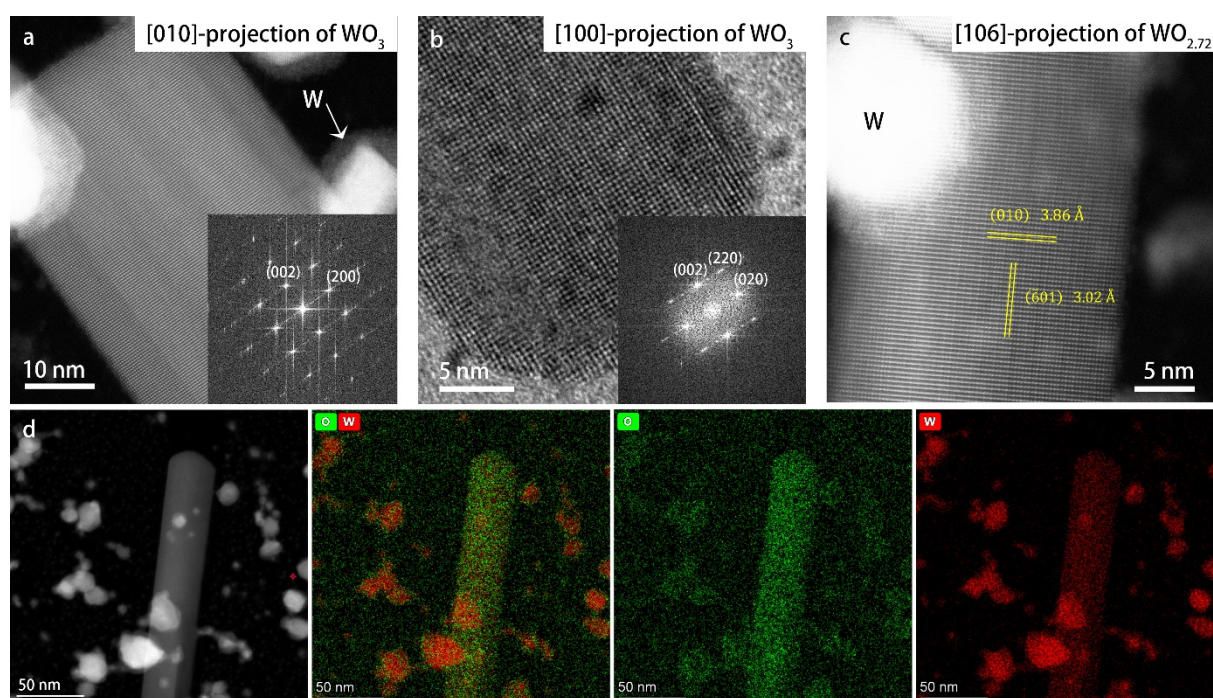


Figure 7-7. High-resolution (S)TEM images of lath-shaped particles and STEM-EDS chemical mapping results. (a) HR-STEM image; (b)(c) HR-TEM images. (d) EDS chemical mapping performed in STEM mode. The chemical maps of W (red) and O (green) are shown separately and overlapping.

Figure 7-7 shows HR images and STEM-EDS chemical mapping of the lath-shaped particles. From

the HR images, different lattice spacings are detected along the length and width of the particles, indicating that the particles are not cubic anymore. The lattice spacing along the length of the particles are about 3.85 Å, which corresponds to the (002)-plane of the $P2_1/n$ monoclinic structure. The lattice spacings in the lateral directions in panel (a) and (b) are 3.62 Å and 3.76 Å, respectively, corresponding to the (200) and (020)-spacings of the monoclinic phase. Therefore, these lath-shaped particles grow in length along the monoclinic c-axis.

In the research of Pokhrel et al.²⁰, the monoclinic nanocrystals were heated and several phase transformations were detected during heating, where elongated particles were observed between 800 and 950 °C. Their XRD results show a tetragonal phase in this temperature range. Consequently, these authors concluded that the elongated particles had the tetragonal structure. However, in our case, in the DP of the lath-shaped particles (shown as Figure 7-5(b)), there are peaks corresponding to a lattice spacing of 4.2 Å, which do not belong to the tetragonal phase. Moreover, the lath shape of the particles indicates that the growth rate along the three crystal axes is distinctly different, which agrees better with the monoclinic phase than with the tetragonal phase.

There are also HR images showing lath-shaped particles with a structure that differs from that of monoclinic WO_3 . In Figure 7-7 (c), the lattice spacing along the length of the lath-shaped particle is 3.86 Å, while the lateral lattice spacing is 3.0 Å, which does not correspond to any of the projections of monoclinic WO_3 , but which matches very well the [106] projection of $WO_{2.72}$ (space group $P2/m$). $WO_{2.72}$ also has monoclinic structure, and was often observed as intermediate phase during the reduction of WO_3 .^{37,42} Due to the presence of oxygen vacancies, the corner-sharing oxygen octahedra matrix of WO_3 is distorted and decahedra exist in the $WO_{2.72}$ structure (shown in Figure S 7-6a). The 3.86 Å lattice spacing corresponds to the (010) interplanar spacing and the lateral lattice direction is $(\bar{1}06)$. The distortion of the WO_6 octahedra decreases the symmetry of the structure and results in much more lattice planes parallel to the b-axis than in the case of the monoclinic WO_3 structure. The values of lateral lattice spacings in panel (a) and (b) also correspond to the (103) and (104) interplanar spacings of $WO_{2.72}$, respectively. This means the particles in panel (a) and (b) are also possibly $WO_{2.72}$. However, in the $[\bar{1}03]$ and $[\bar{1}04]$ projections of $WO_{2.72}$, the lattices parallel to b-axis are so condensed that the atomic columns would not be observed as sharp dots similar to those in the HR images shown in panel (a) and (b). Therefore, we consider it most likely that WO_3 and $WO_{2.72}$ lath-

shaped particles co-exist. The schematic structure of WO_{2.72} shown in different projections is shown in Figure S 7-6 and the lattice parameters of this phase are listed in Table S1. We mention here that the high vacuum environment of both the TEM and the ex-situ heating chamber is likely of importance for the formation of the WO_{2.72} phase, as a very low partial oxygen pressure affects the relative stability of phases in favor of oxygen-deficient or oxygen-depleted phases, as explained in our previous work.⁴³

Figure 7-7 (d) show the STEM-EDS chemical mapping result. The mapping area includes both lath-shaped WO₃ particles and small elemental W particles after heating. From the small particles that transformed to W, mainly an EDS signal of W was detected, proving that these particles are elemental W. In contrast, the oxygen signal on lath particle is stronger than the tungsten signal. The quantified mapping results in a W:O ratio of the lath-shaped particles of 1:3.08, which within experimental errors agrees well with the WO₃ or WO_{2.72} composition for the lath-shaped particles.

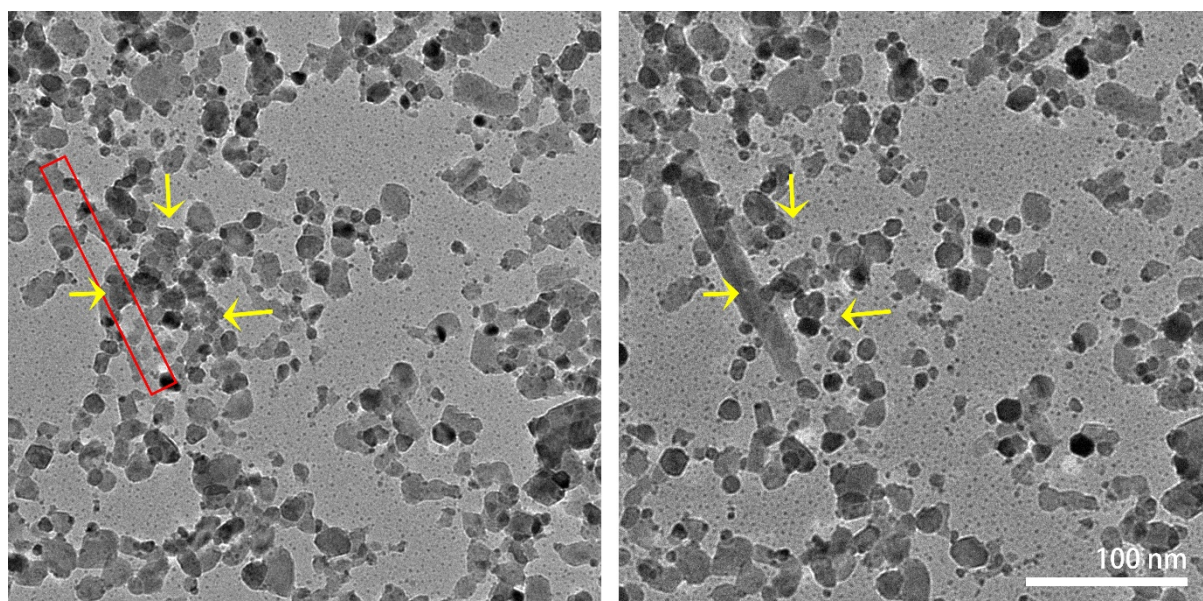


Figure 7-8. In-situ TEM images recorded before (left) and after (right) the formation of the lath-shaped particle at 900 °C. The position of the lath particle is marked with a red rectangle. Yellow arrows indicate the positions at which the WO₃ nanoparticles disappeared after the formation of lath particle.

In-situ heating experiment were repeated to track the formation of the lath-shaped particles. Figure 7-8 shows images before and after the initial formation of a lath-shaped particle at 900 °C. In the left figure, the (future) position of the lath-shaped particle is marked by a red rectangle, in which some

areas are empty before the formation. Several of the surrounding particles (marked by the yellow arrows) disappeared after the formation of the lath-shaped particle. Unfortunately, as mentioned before, the specimens are very beam-sensitive at high temperatures. Therefore, the full formation process could not be recorded.

The fabrication of 2D WO_3 nanosheets or platelets were reported with various methods, including anodization⁸, hydrothermal treatment³, mechanical exfoliation⁷, oxidation of WS_2 ⁴⁴, and colloidal chemistry methods⁴⁵. Mostly, the synthesis happened in solution involving other chemical compounds, i.e., the synthesis route there is chemical rather than physical. WO_3 and non-stoichiometric WO_{3-x} nanorods and nanowires can be fabricated with physical or chemical vapor deposition techniques⁴⁶⁻⁵⁵. Baek *et al.*⁵⁰ fabricated monoclinic WO_3 nanowires on W substrate by heating WO_3 powder under vacuum conditions. In the research of Hong *et al.*⁵², $\text{WO}_{2.72}$ nanowires were synthesized via thermal evaporation of WO_3 powder in vacuum, which is similar to the experimental conditions in our study. Zhang *et al.*⁵¹ synthesized $\text{WO}_{2.72}$ nanowires on carbon microfibers by heating a W film in an atmosphere of Ar and water, and the $\text{WO}_{2.72}$ nanowires transformed to monoclinic WO_3 after annealing at 500 °C. The growth of nanowires synthesized in these methods follows a vapor-solid mechanism, which likely also plays a role in the formation of lath-shaped particles in the current study. The vapor-solid mechanism is a common approach for forming nanostructures.⁵⁶ We hypothesize that in our case, the WO_3 nanocrystals start to sublime at temperature from 800 °C onward, and recrystallize very locally before the oxygen can disappear in the vacuum of the TEM column, corresponding to a solid-vapor-solid growth mechanism. Therefore, when a low concentration of pristine cubic phase particles are deposited on the heating chip, the sublimated O atoms are pumped out the column, resulting in cubic elemental W. From results of the ex-situ experiments displayed in Figure 7-5, it becomes clear that two distinct pathways can be selected by varying the concentration of deposited pristine particles: one pathway leading to the exclusive formation of elemental W nanoparticles, and one pathway leading to the predominant formation of 2D nanosheets of WO_{3-x} .

7.4 Conclusion

The phase transformations and morphological changes of cubic phase WO₃ nanocrystals were investigated by in-situ heating in TEM. The initial particles are stable up to 600 °C, and begin to coalesce and sublime at 700 °C. Upon heating to 900 °C, most of the particles had transformed to pure cubic tungsten. Others coalesced and formed larger lath-shaped particles in the areas where the concentration of dropcast WO₃ NPs was high. The lath-shaped particles were found to have monoclinic WO₃ and WO_{2.72} crystal structures. Sometimes the lath-shape particles curled up from the sides, like folded 2D nanosheets. As also confirmed by the ex-situ experiments, the heating of a low concentration of WO₃ nanoparticles leads to the exclusive formation of elemental W nanoparticles, while the heating of a high concentration of WO₃ nanoparticles lead to the predominant formation of lath-shaped WO_{3-x} nanosheets that are hundreds of nanometers long and up to ~100 nm wide, where the nanosheets are so thin that they are often found to curl up at their edges to form semi-cylindrical structures. The 2D character and the lath-shape of the nanosheets are the result of their monoclinic crystal structure, which results in different growth rates along the three crystal directions.

The current study has given detailed insights into the thermal stability of nanosized WO₃ particles having a cubic crystal structure. We hypothesize that the lath-shaped particles with monoclinic crystal structure are formed through a solid-vapor-solid (SVS) growth mechanism. These 2D lath-shaped structures may be of particular use as catalytic or anode materials having a high surface area. It would be interesting to explore the functional properties of these spatially more extended lath-shaped structures in future studies.

7.5 Acknowledgments

Figures of atomic structural models were produced using VESTA.⁵⁷ We thank Prof. Alfons van Blaaderen for useful discussions.

7.6 References

- 1 M. B. Tahir, M. Sagir, S. Muhammad, S. M. Siddeeg, T. Iqbal, A. M. Asiri and M. Ijaz, *Appl. Nanosci.*, 2020, **10**, 1183–1190.
- 2 Z. Yan, W. Shan, X. Shi, G. He, Z. Lian, Y. Yu, Y. Shan, J. Liu and H. He, *Catal. Today*, 2020, **355**, 408–414.
- 3 N. Li, Y. Zheng, L. Wei, H. Teng and J. Zhou, *Green Chem.*, 2017, **19**, 682–691.
- 4 W. Kong, R. Zhang, X. Zhang, L. Ji, G. Yu, T. Wang, Y. Luo, X. Shi, Y. Xu and X. Sun, *Nanoscale*, 2019, **11**, 19274–19277.
- 5 C. Cantalini, H. T. Sun, M. Faccio, M. Pelino, S. Santucci, L. Lozzi and M. Passacantando, *Sensors Actuators, B Chem.*, 1996, **31**, 81–87.
- 6 L. Wang, A. Teleki, S. E. Pratsinis and P. I. Gouma, *Chem. Mater.*, 2008, **20**, 4794–4796.
- 7 D. Wang, S. Huang, H. Li, A. Chen, P. Wang, J. Yang, X. Wang and J. Yang, *Sensors Actuators, B Chem.*, 2019, **282**, 961–971.
- 8 M. B. Rahmani, M. H. Yaacob and Y. M. Sabri, *Sensors Actuators B*, 2017, **251**, 57–64.
- 9 P. A. Shinde and S. C. Jun, *ChemSusChem*, 2020, **13**, 11–38.
- 10 T. Stubhan, N. Li, N. A. Luechinger, S. C. Halim, G. J. Matt, C. J. Brabec, T. Stubhan, N. Li, G. J. Matt, C. J. Brabec, N. A. Luechinger and S. C. Halim, *Adv. energy Mater.*, 2012, **2**, 1433–1438.
- 11 N. Li, T. Stubhan, N. A. Luechinger, S. C. Halim, G. J. Matt, T. Ameri and C. J. Brabec, *Org. Electron.*, 2012, **13**, 2479–2484.
- 12 R. Pathak, A. Gurung, H. Elbohy, K. Chen, K. M. Reza, B. Bahrami, S. Mabrouk, R. Ghimire, M. Hummel, Z. Gu, X. Wang, Y. Wu, Y. Zhou and Q. Qiao, *Nanoscale*, 2018, **10**, 15956.
- 13 O. Pyper, *Sol. Energy Mater. Sol. Cells*, 2002, **71**, 511–522.
- 14 R. Chatten, A. V. Chadwick, A. Rougier and P. J. D. Lindan, *J. Phys. Chem. B*, 2005, **109**, 3146–3156.
- 15 F. Wang, C. Di Valentin and G. Pacchioni, *J. Phys. Chem. C*, 2011, **115**, 8345–8353.
- 16 S. Z. Karazhanov, Y. Zhang, A. Mascarenhas, S. Deb and L. W. Wang, in *Solid State Ionics*, Elsevier, 2003, vol. 165, pp. 43–49.
- 17 H. A. Wriedt, *Bull. Alloy Phase Diagrams*, 1989, **10**, 368–384.
- 18 C. V. Ramana, S. Utsunomiya, R. C. Ewing, C. M. Julien and U. Becker, *J. Phys. Chem. B*, 2006, **110**, 10430–10435.
- 19 T. Vogt, P. M. Woodward and B. A. Hunter, *J. Solid State Chem.*, 1999, **144**, 209–215.
- 20 S. Pokhrel, J. Birkenstock, A. Dianat, J. Zimmermann, M. Schowalter, A. Rosenauer, L. C. Ciacchi and L. Mädler, *CrystEngComm*, 2015, **17**, 6985–6998.
- 21 I. M. Szilágyi, J. Pfeifer, C. Balázsi, A. L. Tóth, K. Varga-Josepovits, J. Madarász and G.

- Pokol, *J. Therm. Anal. Calorim.*, 2008, **94**, 499–505.
- 22 M. Righettoni, A. Tricoli and S. E. Pratsinis, *Chem. Mater.*, 2010, **22**, 3152–3157.
- 23 W. Wang, A. Janotti and C. G. Van De Walle, *J. Chem. Phys.*, 2017, **146**, 214504.
- 24 A. D. Walkingshaw, N. A. Spaldin and E. Artacho, *Phys. Rev. B - Condens. Matter Mater. Phys.*, 2004, **70**, 1–7.
- 25 Z. Wang, Y. He, M. Gu, Y. Du, S. X. Mao and C. Wang, *ACS Appl. Mater. Interfaces*, 2016, **8**, 24567–24572.
- 26 R. Clarke, *Phys. Rev. Lett.*, 1977, **39**, 1550–1553.
- 27 S. H. Lee, M. J. Seong, H. M. Cheong, E. Ozkan, E. C. Tracy and S. K. Deb, *Solid State Ionics*, 2003, **156**, 447–452.
- 28 Q. Zhong, J. R. Dahn and K. Colbow, *Phys. Rev. B*, 1992, **46**, 2554–2560.
- 29 B. W. Brown and E. Banks, *J. Am. Chem. Soc.*, 1954, **76**, 963–966.
- 30 E. Cazzanelli, C. Vinegoni, G. Mariotto, A. Kuzmin and J. Purans, *J. Solid State Chem.*, 1999, **143**, 24–32.
- 31 K. Thummavichai, N. Wang, F. Xu, G. Rance, Y. Xia and Y. Zhu, *R. Soc. Open Sci.*, , DOI:10.1098/rsos.171932.
- 32 C. J. Howard, V. Luca and K. S. Knight, *J. Phys. Condens. Matter*, 2002, **14**, 377–387.
- 33 F. Corà, A. Patel, N. M. Harrison, R. Dovesi and C. R. A. Catlow, *J. Am. Chem. Soc.*, 1996, **118**, 12174–12182.
- 34 C. Balázs, M. Farkas-Jahnke, I. Kotsis, L. Petrás and J. Pfeifer, in *Solid State Ionics*, 2001, vol. 141–142, pp. 411–416.
- 35 O. Yamaguchi, D. Tomihisa, H. Kawabata and K. Shimizu, *J. Am. Ceram. Soc.*, 1987, **70**, C-94-C-96.
- 36 M. A. Van Huis, N. P. Young, G. Pandraud, J. F. Creemer, D. Vanmaekelbergh, A. I. Kirkland and H. W. Zandbergen, *Adv. Mater.*, 2009, **21**, 4992–4995.
- 37 V. K. Sarin, *J. Mater. Sci.*, 1975, **10**, 593–598.
- 38 A. Al Mohammad, *Acta Phys. Pol. A*, 2009, **116**, 240–244.
- 39 H. Kang, Y. K. Jeong and S. T. Oh, *Int. J. Refract. Met. Hard Mater.*, 2019, **80**, 69–72.
- 40 J. S. Wang, Q. Zhao, T. Liu and W. He, *Rare Met.*, 2020, **40**, 687–692.
- 41 A. Löfberg, A. Frennet, G. Leclercq, L. Leclercq and J. M. Giraudon, *J. Catal.*, 2000, **189**, 170–183.
- 42 N. E. Fouad, K. M. E. Attyia and M. I. Zaki, *Powder Technol.*, 1993, **74**, 31–37.
- 43 X. Chen, H. Van Gog and M. A. Van Huis, *J. Mater. Chem. C*, 2021, **9**, 5662–5675.
- 44 A. Azam, J. Kim, J. Park, T. G. Novak, A. P. Tiwari, S. H. Song, B. Kim and S. Jeon, *Nano Lett.*, 2018, **18**, 5645–5651.

- 45 M. Ahmadi and M. J. F. Guinel, *Acta Mater.*, 2014, **69**, 203–209.
- 46 Y. B. Li, Y. Bando, D. Goldberg and K. Kurashima, *Chem. Phys. Lett.*, 2003, **367**, 214–218.
- 47 J. Thangala, S. Vaddiraju, R. Bogale, R. Thurman, T. Powers, B. Deb and M. K. Sunkara, *Small*, 2007, **3**, 890–896.
- 48 Y. M. Zhao, Y. H. Li, I. Ahmad, D. G. McCartney, Y. Q. Zhu and W. B. Hu, *Appl. Phys. Lett.*, 2006, **89**, 133116.
- 49 C. Y. Su, H. C. Lin, T. K. Yang and C. K. Lin, *J. Nanoparticle Res.*, 2010, **12**, 1755–1763.
- 50 Y. Baek and K. Yong, *J. Phys. Chem. C*, 2007, **111**, 1213–1218.
- 51 Y. Zhang, Y. Chen, H. Liu, Y. Zhou, R. Li, M. Cai and X. Sun, *J. Phys. Chem. C*, 2009, **113**, 1746–1750.
- 52 K. Hong, M. Xie, R. Hu and H. Wu, *Appl. Phys. Lett.*, 2007, **90**, 173121.
- 53 G. Gu, B. Zheng, W. Q. Han, S. Roth and J. Liu, *Nano Lett.*, 2002, **2**, 849–851.
- 54 Y. Z. Jin, Y. Q. Zhu, R. L. D. Whitby, N. Yao, R. Ma, P. C. P. Watts, H. W. Kroto and D. R. M. Walton, *J. Phys. Chem. B*, 2004, **108**, 15572–15577.
- 55 G. Shen, Y. Bando, D. Golberg and C. Zhou, *J. Phys. Chem. C*, 2008, **112**, 5856–5859.
- 56 Z. R. Dai, Z. W. Pan and Z. L. Wang, *Adv. Funct. Mater.*, 2003, **13**, 9–24.
- 57 K. Momma and F. Izumi, *J. Appl. Crystallogr.*, 2011, **44**, 1272–1276.

7.7 Appendix

7.7.1 Supporting Table

Table S 7-1 Structural details including lattice parameters of WO_x phases and of cubic W. The reference code specifies the JCPDS index.

Chemical formula	Reference code	Crystal system	Space group	Lattice parameters					
				a (Å)	b (Å)	c (Å)	α (°)	β (°)	γ (°)
WO ₃	00-041-0905	Cubic	Pm $\bar{3}$ m	3.71	3.71	3.71	90	90	90
WO ₃	00-043-1035	Monoclinic	P2 ₁ /n	7.30	7.54	7.69	90	90.91	90
WO ₃	01-089-4479	Orthorhombic	Pbcn	7.36	7.57	7.76	90	90	90
WO ₃	00-005-0388	Tetragonal	P4/nmm	5.25	5.25	3.91	90	90	90
WO _{2.72}	01-073-2177	Monoclinic	P2/m	18.32	3.79	14.04	90	115.2	90
W	00-001-1203	Cubic	Im $\bar{3}$ m	3.15	3.15	3.15	90	90	90

7.7.2 Supporting Figures

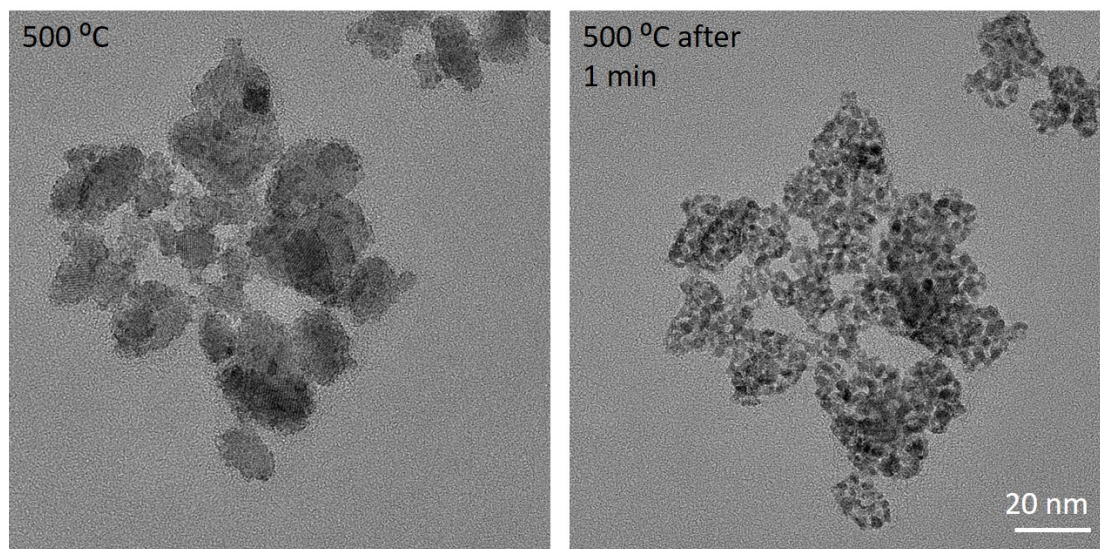


Figure S 7-1. Demonstration of the influence of a high-intensity electron beam during imaging. Bright-field TEM images of WO₃ particles at 500 °C before (left) and after (right) high-intensity illumination by the electron beam.

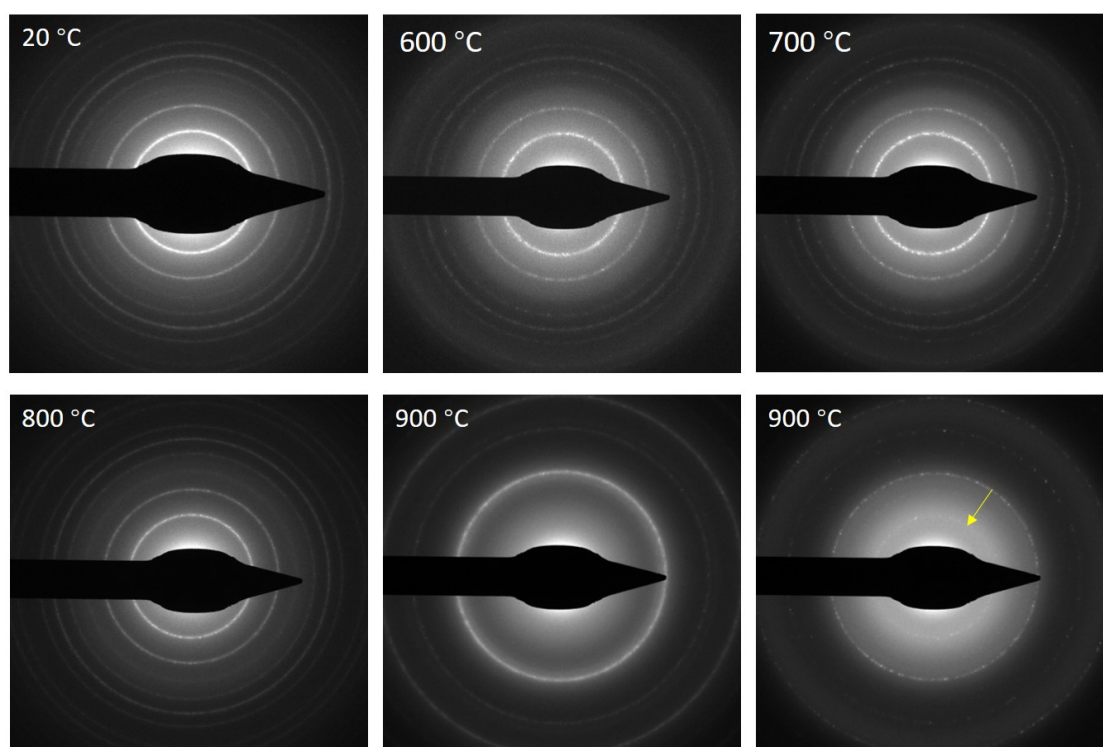


Figure S 7-2 SAEDs of WO_x nanocrystals during heating. Upon heating to 800 °C, the patterns corresponded to the cubic WO₃ crystal structure. The phase transformation to cubic W took place at 900 °C. At some areas where lath-shaped particles formed, the peaks corresponding to WO₃ (marked with yellow arrow in right-bottom image) remained at 900 °C.

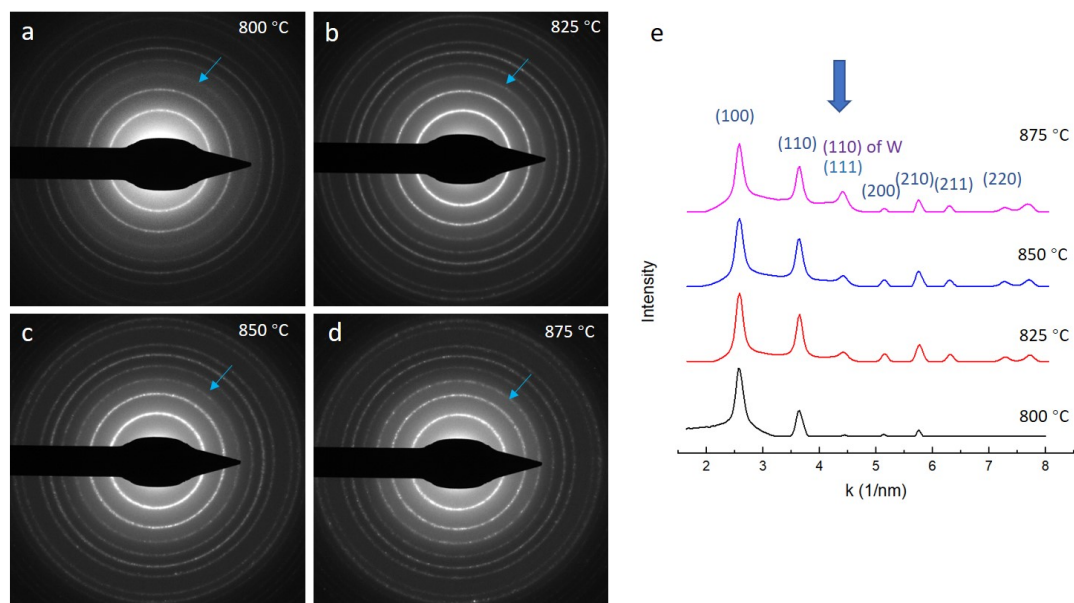


Figure S 7-3 (a)-(d) SADPs of the specimen heated from 800 °C to 875 °C. The blue arrow marks the ring corresponding to (111) reflection planes of WO₃ and the (110)-reflection of W, of which the intensity increased gradually. (e) integrated graphs of DPs in (a) to (d).

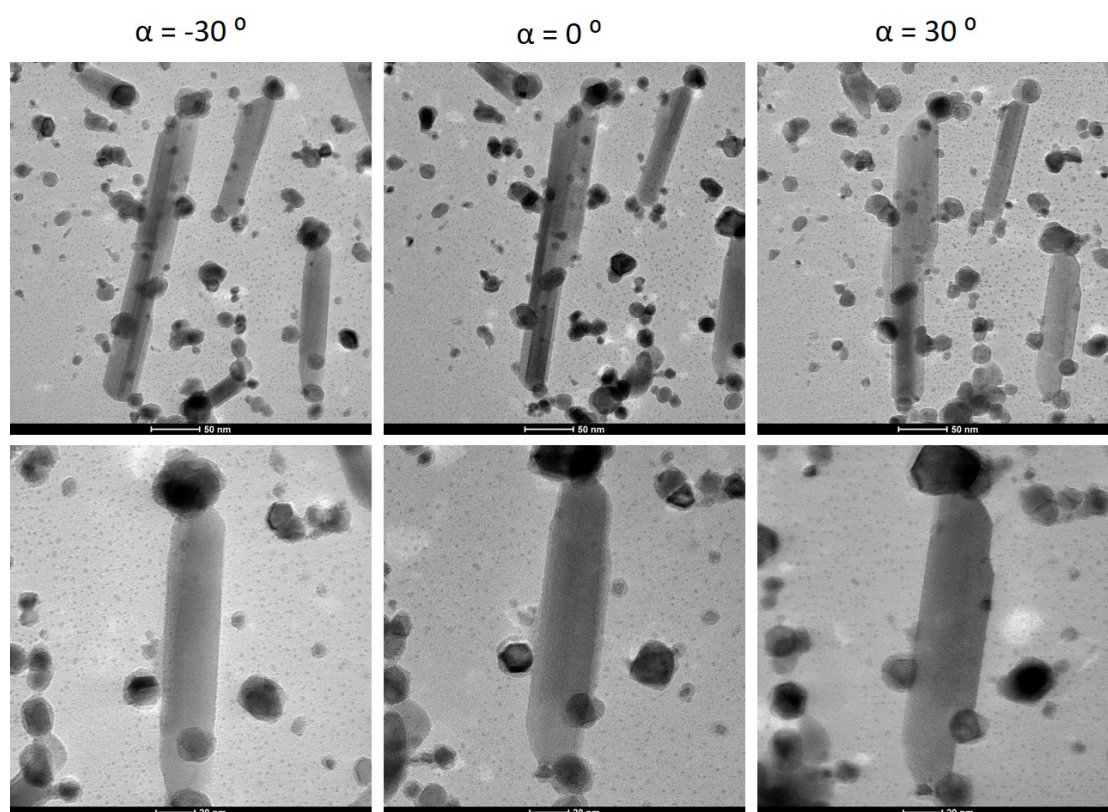


Figure S 7-4 Bright-field TEM images of lath-shaped particles tilted to angles of $\pm 30^\circ$. The widths of the particles change with tilting, which indicates that particles are curled up, but not shaped as perfect cylinders.

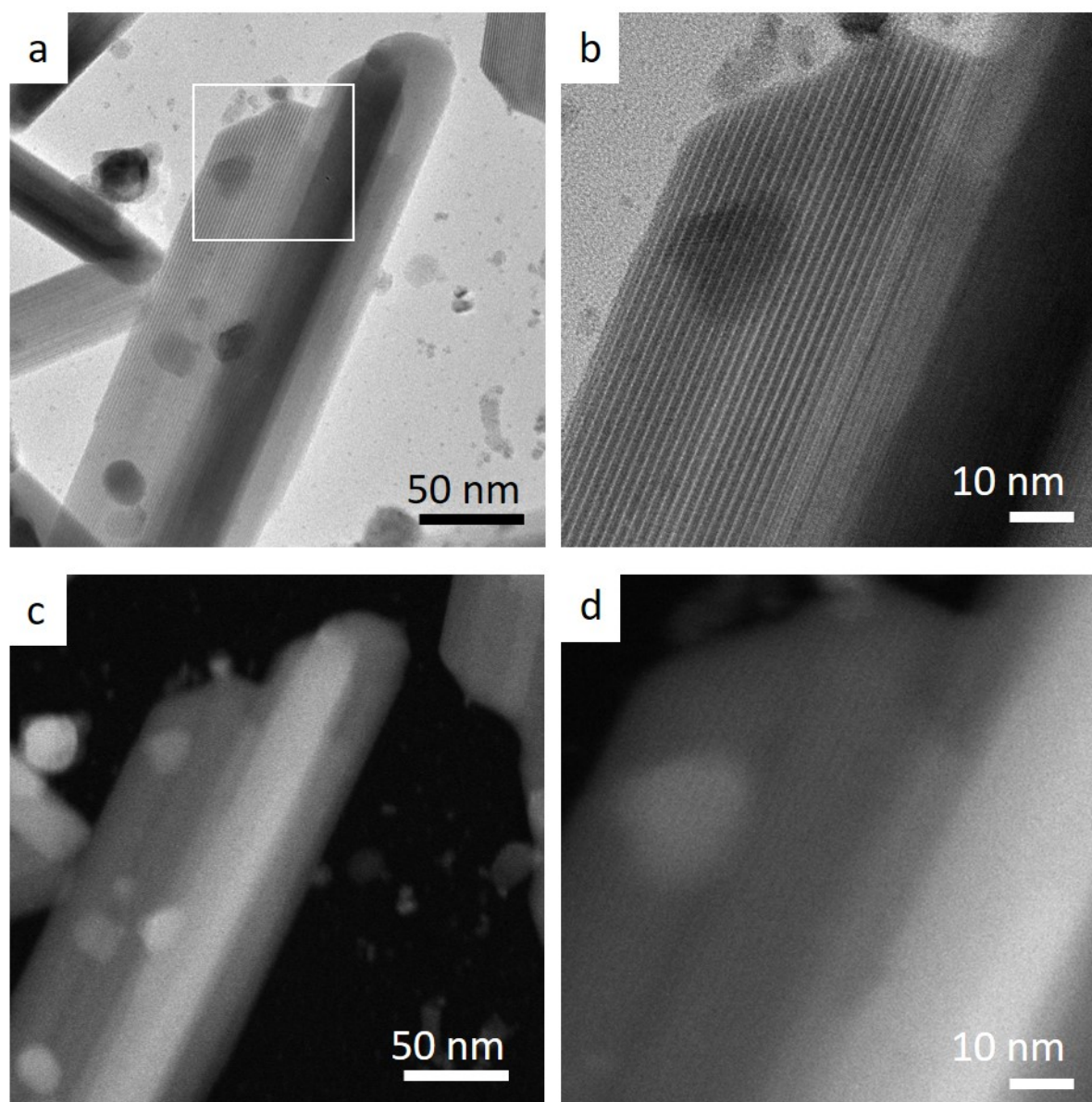


Figure S 7-5 (S)TEM images of lath particles. (a) Bright-field TEM image; (b) TEM image of the area marked with a white square in (a). Moiré patterns showing the multiple layers; (c) STEM image with the same magnification of (a); (d) STEM image with the same magnification as in (b).

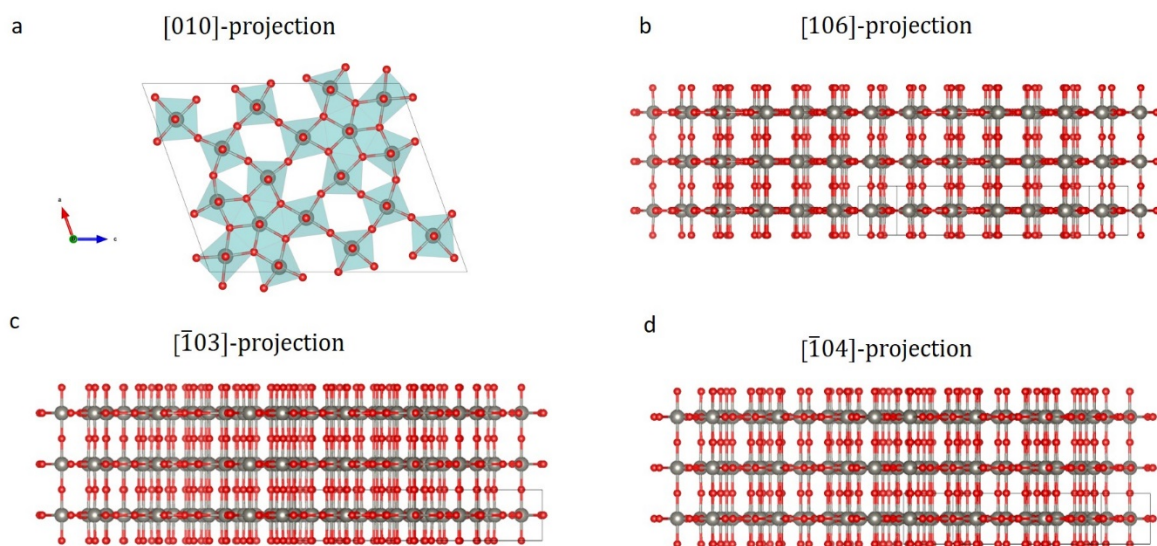


Figure S 7-6. Schematic structure of WO_{2.72} shown in different projections. (a) [010]-projection shown with polyhedral; (b) [106]-projection; (c) $[\bar{1}03]$ -projection; (d) $[\bar{1}04]$ -projection.

Summary

The scientific study described in this thesis aims to achieve understanding of the thermal behavior and thermal stability of nanostructured transition metal oxides (TMOs) by means of in-situ experimentation in the transmission electron microscope (TEM). TMO nanocrystals are proper candidate materials for catalysis, gas sensing, and biomedical applications. The properties at the nanoscale are different from those of the corresponding bulk materials due to surface effects and confinement effects. For nanoparticles, not only the intrinsic aspects like size, shape, and synthesis methods, but also environmental factors such as temperature, pressure, and chemical environment, are all related to their properties. The thermal evolution and stability of nanocrystals in different size ranges and in various shapes consequently affect their performance in applications. This study used primarily in-situ TEM, where experiments are conducted inside the electron microscope, as the main method to achieve real-time inspection of changes taking place at elevated temperatures while imaging at high spatial resolution.

In Chapter 2, the theoretical background of TEM image formation is briefly introduced. In this thesis, different TEM techniques are used to follow different aspects of the thermal evolution. Bright-field TEM images and scanning TEM (STEM) images are used for the recording of changes in morphology. Selected area diffraction patterns (SADPs) are used to follow the evolution of the crystal structure during heating. Because SADP provides average information of the crystalline structure of a collection of particles and can be recorded at lower electron beam fluxes, the use of SADPs decreases the influence of the electron beam on the thermal evolution at very high magnification. To show the details of transitions in crystal structure, high-resolution (S)TEM images are used. Moreover, energy-dispersive X-ray spectrometry (EDS) mapping is applied to show the 2D distribution of chemical elements.

From Chapter 3 to Chapter 7, several systems of TMO nanoparticles are investigated by using in-situ TEM at elevated temperatures. The TMO particles in different size ranges and with various shapes exhibited different trends in thermal evolution. The different crystalline structures also affected the transformations observed at high temperatures. The in-situ heating in this study was conducted with a dedicated heating holder, which makes it possible to elevate the temperature very swiftly. To fully exclude the influence of the electron beam on the transformations at elevated temperatures, reference experiments were often conducted in a vacuum chamber while applying the same heating profile as in the in-situ heating experiment.

In Chapter 3, the thermal evolution of Co_3O_4 nanocrystals in vacuum is shown. The Co_3O_4 nanocrystals are in a broad size range and agglomerate after being dropcast on the heating chips. The

Co₃O₄ nanocrystals transformed to CoO starting from a temperature of 350 °C and were fully converted when heated at 400 °C. The transformation progressed from the surface toward the center of the particles. Since the lattice parameter of CoO is approximately two times smaller than that of Co₃O₄ while both phases have cubic structure, the Co₃O₄ and CoO phases were found in a cube-on-cube orientation relationship. The energetics and magnetic properties of Co₃O₄/CoO interface were calculated by means of density functional theory (DFT) calculations. Co₃O₄/CoO {100}/{100} interface energy is predicted for the lowest-energy orderings to be 0.38 Jm⁻². Furthermore, the DFT calculations revealed a substantial net ferromagnetic moment originating from the interface between the two antiferromagnetic compounds.

In Chapter 4 and Chapter 5, the thermal evolution of TiO₂ nanorods in different crystallographic phases are investigated. Both types of nanorods were synthesized with OLAC ligands on the surfaces preventing the aggregation of the NRs. The thermal behavior of anatase TiO₂ nanorods is studied in Chapter 4. Anatase is known to be the most stable phase of TiO₂ at the nanoscale. The nanorods were stable and retained their morphology at temperatures up to 600 °C. Upon heating to 700 °C, the NRs deformed and finally broke up into smaller segments at a temperature of 1000 °C. When large amounts of NRs were dropcast onto the heating chips, the NRs coalesced during heating. The diffraction results show that the anatase phase completely transformed to rock-salt TiO at 1200 °C where the brookite phase was formed in an intermediate stage in the temperature range from 950 to 1000 °C. Different from the heating results obtained in the microscope, the results from ex-situ heating to 1200 °C also showed a diffraction peak corresponding to TiO, while anatase and rutile were detected as well. This indicates that the transformation to TiO is not complete, and that some of the sample transformed to rutile. The partial transformation to rutile can be expected because the oxygen partial pressure in the ex-situ vacuum chamber is not sufficiently low to achieve a full transformation to TiO.

Subsequently, in Chapter 5 the thermal evolution of brookite TiO₂ nanorods is studied as well. The as-synthesized brookite NRs can be post treated in order to increase the coverage of ligands on the nanorod surfaces. After this post-treatment, the brookite NRs were well dispersed in the solvent while the as-synthesized NRs aggregated after dropcasting. Both kinds of NRs were heated and showed a different morphology evolution at elevated temperatures. Due to aggregation, the as-synthesized NRs were more prone to deformation and underwent more coalescence. The post-treated NRs were more stable, and sublimation occurred rather than coalescence. Differently from anatase NRs, after annealing up to a temperature of 1200 °C, most of the NRs retained the brookite phase. Only part of the sample specimen transformed to TiO while another part transformed to the rutile TiO₂ phase.

In Chapter 6, MoO₃ particles in a wide size range were investigated. In contrast to the TMO nanoparticles studied in the previous three chapters, MoO₃ has a layered crystal structure wherein Mo

centered oxygen octahedra share corners in the a and c lattice directions forming layers, where the layers are bonded by van der Waals forces and stacked in the b lattice direction. Consequently, the thermal behavior is very different from that of the other samples. When the MoO_3 particles were heated at a fast rate (with 100 °C increments), the particles were exfoliated and reduced to small nanoflakes within a few seconds when heated to 600 °C. In the TEM images, it looks as if the particles were blown up being completely disintegrated. The small fragments were found scattered all around the primary particles. These small flakes were found to be in a MoO_2 composition. There are also a few flakes scattered at 500 °C which were found having a Mo_4O_{11} structure, indicating that the transformation to MoO_2 possibly occurred with formation of Mo_4O_{11} existing as an intermediate phase or formed in a side reaction. When heated at a slow heating rate (with smaller, 25 °C increments above 400 °C), the flakes were exfoliated much more slowly, and the pristine particles became hollow after this exfoliation where a polycrystalline shell of MoO_2 was formed. DFT and ab initio molecular dynamics (AIMD) calculations confirmed that the (010) layers are weakly bound, and that exfoliation is feasible due to strong thermal vibrations of the lattice at elevated temperatures.

In Chapter 7, the thermal evolution of WO_3 nanoparticles with cubic crystal structure is studied. The particles were found to be stable up to 600 °C and started to undergo coalescence and sublimation when heated at a temperature of 700 °C. With low concentrations of pristine NPs dropcast onto the heating chip, the samples transformed to pure elemental W at 900 °C. However, in the areas where high concentrations of NPs were dropcast, two-dimensional nanosheets also formed after heating to a temperature of 900 °C. The ex-situ heating experiments also confirmed the transformation to pure W and the formation of the nanosheets. The nanosheets formed in the ex-situ experiments were found to be bigger than those formed inside the microscope. The nanosheets are considerably larger than the nanoparticles from which they were formed, have a lath-shape, and are so thin that they easily fold or curl up at the two long sides of the laths. The nanosheets are in a WO_3 or $\text{WO}_{2.72}$ composition and have a monoclinic structure. We hypothesize that the formation of the 2D nanosheets most likely occurred through a solid-vapor-solid mechanism.

The common trend found for all TMO samples studied in this thesis, is that transformations to lower-valence state oxides or eventually to pure metals always occurred when heated at elevated temperatures in the electron microscope. The same transformations also occurred in the reference ex-situ experiments for most of the samples. We conclude that the (very low) partial oxygen pressure in the vacuum of the TEM column is of importance for the specific temperatures at which these transformations take place. Considering changes in nanoparticle morphology, processes of coalescence and sublimation were often observed, and were sometimes found to be dependent on the areal concentration of dropcast nanoparticles. The study described in this thesis confirms the wildly diverse behavior of nanoparticles. Phase transformations can take place at temperatures quite different from those found in the phase diagrams of bulk materials. The particle size and shape also influence

the stability of certain phases. Finally, even the type of crystal structure is of importance, with an extreme example being the massive exfoliation of nanoflakes from nanoparticles with van der Waals-bonded crystalline layers when these were subjected to a high heating rate. Some of the findings of this PhD study offer opportunities for application in the chemical and high-tech industries where TMO materials are used. However, primarily the study has brought scientific understanding on all aspects mentioned above, which is of importance to achieve full elucidation of the thermal behavior of TMO nanoparticles, thereby also serving as a reference for future research.

In follow-up studies, the characterization of the transformations could be deciphered into greater detail, for example by studying the dependence of the transition temperatures on the partial oxygen pressure, by controlling and systematically varying the partial oxygen pressure in the gas or vacuum chambers wherein the nanoparticles are heated. To this end, in addition to performing ex-situ heating experiments, performing in-situ XRD experiments or using in-situ gas cell experimentation in the TEM, would be interesting opportunities to pursue as well. Furthermore, the properties of the formed nanomaterials can be further explored. In particular, it can be investigated whether partially transformed $\text{Co}_3\text{O}_4/\text{CoO}$ nanoparticles indeed exhibit stronger net ferromagnetism as predicted by the DFT calculations, and whether rock salt TiO nanoparticles or MoO_2 nanoflakes exhibit (enhanced) catalytic activity.

Samenvatting

Het onderzoek dat wordt beschreven in dit proefschrift heeft als doel om begrip te verkrijgen van het thermische gedrag en de thermische stabiliteit van nanogestructureerde transitiemetaaloxiden (TMOs) door gebruik te maken van in-situ experimenten in de transmissie-elektronenmicroscop (TEM). TMO-nanokristallen zijn geschikte kandidaten voor gebruik in de katalyse, voor gasdetectie en voor biomedische toepassingen. De eigenschappen van materialen op nanoschaal verschillen van gelijksoortige materialen in de bulk vanwege oppervlakte-effecten en kwantumopsluiting. Niet alleen intrinsieke aspecten zoals de grootte, vorm en synthese methode zijn van belang voor de eigenschappen van nanodeeltjes, maar ook invloeden van de omgeving zoals de temperatuur, druk en chemische omgeving beïnvloeden hun eigenschappen. De thermische ontwikkeling en stabiliteit van nanokristallen in verschillende vormen en maten hebben daarom invloed op de prestaties van deze deeltjes in hun toepassingen. In dit onderzoek is voornamelijk in-situ TEM gebruikt, waarbij experimenten in de elektronenmicroscop worden uitgevoerd om in *real time* bij verhoogde temperaturen waarnemingen te kunnen doen die met hoge resolutie in beeld kunnen worden gebracht.

In hoofdstuk 2 wordt eerst kort ingegaan op de theorie achter de beeldvorming in de TEM. In dit proefschrift zijn verschillende TEM-technieken gebruikt om verschillende aspecten van thermische ontwikkelingen te bestuderen. Helderveld TEM en raster TEM (in het Engels afgekort als STEM voor scanning transmission electron microscopy) plaatjes zijn gebruikt voor het vastleggen van morfologische veranderingen. Diffractiepatronen van een geselecteerd gebied (in het Engels afgekort als SADPs voor selected area diffraction patterns) zijn gebruikt om veranderingen in kristalstructuren vast te leggen tijdens het verwarmen. Omdat SADPs informatie verstrekken over de kristallijne structuur van verzamelingen van deeltjes en ook met zwakke elektronenbundels kunnen worden vastgelegd, vermindert het gebruik van SADPs de invloed van de elektronenbundel op de thermische ontwikkelingen bij hoge vergrotingen. Om de details van transitie in kristalstructuren vast te leggen werd hoge resolutie (S)TEM gebruikt. Bovendien is er gebruik gemaakt van energiedispersieve röntgenspectroscopie (EDS) om 2D-distributies van chemische elementen weer te geven.

In hoofdstuk 3 tot en met hoofdstuk 7 worden verschillende systemen van TMO-nanodeeltjes onderzocht bij verhoogde temperaturen door gebruik te maken van in-situ TEM. De TMO-deeltjes, die verschillende vormen en maten hebben, laten verschillende trends in thermische ontwikkeling zien. De verschillende kristalstructuren beïnvloedden ook de transformaties die bij hoge temperaturen zijn waargenomen. De in-situ verhittingen in dit onderzoek zijn uitgevoerd met behulp van een speciale verwarmingshouder, die het mogelijk maakt de temperatuur rap te verhogen. Om invloeden van de elektronenbundel volledig uit te sluiten werden er vaak referentie-experimenten uitgevoerd in

een vacuümkamer, waarbij hetzelfde verwarmingsprofiel als bij de in-situ experimenten werd toegepast.

In hoofdstuk 3 wordt de thermische ontwikkeling van Co_3O_4 nanokristallen in vacuüm beschreven. De Co_3O_4 nanokristallen hebben een brede deeltjesgrootteverdeling en agglomereren nadat ze op een verhittingschip worden aangebracht. De Co_3O_4 nanokristallen transformeerden naar CoO bij temperaturen vanaf $350\text{ }^\circ\text{C}$ en waren volledig getransformeerd na verwarming bij $400\text{ }^\circ\text{C}$. De transformatie verliep vanaf het oppervlak richting het midden van de deeltjes. Omdat de roosterconstante van CoO bijna twee keer zo klein is als die van Co_3O_4 terwijl ze beide een kubische structuur hebben, werden de Co_3O_4 en CoO fasen waargenomen met een kubus-op-kubus oriëntatielatie. De energetische en magnetische eigenschappen van het $\text{Co}_3\text{O}_4/\text{CoO}$ grensvlak werden onderzocht met behulp van dichtheidsfunctionaaltheoretische (DFT) berekeningen. De $\text{Co}_3\text{O}_4/\text{CoO}$ $\{100\}/\{100\}$ grensvlakenergie voor de laagst energetische conformatie werd voorspeld 0.38 Jm^{-2} te zijn. Bovendien onthulden de DFT berekeningen een aanzienlijk netto ferromagnetisch moment afkomstig van het grensvlak tussen de twee antiferromagnetische verbindingen.

In hoofdstuk 4 en 5 wordt het onderzoek TiO_2 nanostaafjes van verschillende crystallografische fasen beschreven. Beide typen nanostaafjes werden gesynthetiseerd met OLAC-liganden op het oppervlak om aggregatie van de staafjes te voorkomen. Het thermische gedrag van anatase TiO_2 nanostaafjes wordt onderzocht in hoofdstuk 4. Anataas is de meest stabiele fase voor TiO_2 op nanoschaal. De nanostaafjes waren stabiel en behielden hun morfologie bij temperaturen tot $600\text{ }^\circ\text{C}$. Vanaf $700\text{ }^\circ\text{C}$ begonnen de staafjes te vervormen en bij $1000\text{ }^\circ\text{C}$ waren de staafjes in kleinere stukjes gebroken. Bij grote hoeveelheden nanostaafjes op de verhittingchips smolten deze samen. De elektronendiffractie liet zien dat de structuur compleet getransformeerd was van anataas naar een TiO keukenzoutstructuur bij $1200\text{ }^\circ\text{C}$, waarbij brookiet als intermediair opdook in het temperatuurverloop van 950 tot $1000\text{ }^\circ\text{C}$. Bij het ex-situ verwarmen tot $1200\text{ }^\circ\text{C}$ buiten de microscoop werd aan de hand van elektronendiffractie ook een TiO structuur vastgelegd, echter werden ook anataas en rutiel geïdentificeerd. Dit laat zien dat de transformatie naar TiO niet compleet was en dat een deel van het monster getransformeerd was naar rutiel. De gedeeltelijke transformatie naar rutiel kan verklaard worden door een partiële zuurstofdruk in de vacuümkamer die niet voldoende laag was, hetgeen een volledige transformatie naar TiO tegenaan.

In hoofdstuk 5 worden vervolgens ook de thermische ontwikkelingen van brookiet TiO_2 nanostaafjes beschouwd. De brookiet nanostaafjes werden na de synthese nabehandeld om de oppervlaktebedekking van de liganden te verhogen. Als gevolg van deze nabehandeling waren de brookiet nanostaafjes goed gedispergeerd in het oplosmiddel, terwijl de onbehandelde nanostaafjes juist aggregeerden bij het aanbrengen op een verhittingchip. Beide typen nanostaafjes werden verhit, wat verschillende morfologische ontwikkelingen opleverde bij verhoogde temperaturen. Door de aggregatie van de

onbehandelde nanostaafjes waren deze vatbaarder voor vervorming en samensmelting. De nabehandelde nanostaafjes echter waren stabiel en er trad eerder sublimatie op dan samensmelting. Anders dan de anatase nanostaafjes behielden de meeste brookiet nanostaafjes hun structuur na verwarming bij 1200 °C. Slechts een deel van de staafjes transformeerde naar TiO of rutiel TiO₂.

In hoofdstuk 6 wordt het onderzoek naar MoO₃ deeltjes van verschillende grootten beschreven. In tegenstelling tot de TMO-nanodeeltjes die in de vorige drie hoofdstukken werden beschouwd, heeft MoO₃ een gelaagde kristalstructuur. De lagen worden gevormd door zuurstof-octaëders die een centraal gepositioneerd molybdeenatoom omsluiten, en die aan de hoeken verbonden zijn in de *a* en *c* kristalrichtingen. Deze lagen zijn gebonden door Van der Waalskrachten en gestapeld in de *b* kristalrichting, waardoor het thermische gedrag heel anders is dan dat van de andere materialen in dit proefschrift. Als de MoO₃ deeltjes in rap tempo werden verhit (in stappen van 100 °C) exfolieerden en reduceerden de deeltjes binnen enkele seconden bij een temperatuur van 600 °C, wat leidde tot kleine nanovlokken. In de TEM plaatjes lijkt het alsof de deeltjes zijn geëxplodeerd en volledig zijn gedesintegreerd. De kleine fragmenten lagen overal verspreid rondom de primaire deeltjes en hadden een samenstelling die overeenkomt met MoO₂. Enkele vlokken hadden een Mo₄O₁₁ structuur bij 500 °C, wat aanduidt dat de reductie naar MoO₂ mogelijk verloopt met Mo₄O₁₁ als intermediair of dat Mo₄O₁₁ wordt gevormd in een nevenreactie. Als de MoO₃ deeltjes langzamer werden verwarmd (in kleinere stappen van 25 °C boven 400 °C), exfolieerden deze ook langzamer wat uiteindelijk leidde tot holle deeltjes bestaande uit een schil van polykristallijn MoO₂. DFT en *ab initio* moleculaire dynamica (AIMD) berekeningen bevestigen dat de (010) lagen zwak gebonden zijn en dat exfoliatie van de lagen aannemelijk is vanwege sterke thermische vibraties van het kristalrooster bij verhoogde temperaturen.

In hoofdstuk 7 wordt het onderzoek naar WO₃ nanodeeltjes met een kubische structuur beschreven. De deeltjes waren stabiel tot 600 °C en begonnen samen te smelten en te sublimeren bij een temperatuur van 700 °C. Bij lage concentraties nanodeeltjes op de verhitingschips transformeerden de deeltjes naar elementair W bij 900 °C. In de gebieden met een hoge concentratie nanodeeltjes werden echter tweedimensionale nanolagen gevormd na verwarming bij 900 °C. De ex-situ experimenten bevestigden de transformatie naar elementair W en de formatie van de nanolagen. De nanolagen die in de ex-situ experimenten werden gevormd, waren groter dan de nanolagen die in de microscoop werden gevormd. De nanolagen zijn aanzienlijk groter dan de nanodeeltjes waaruit deze zijn gevormd, hebben een uitgestrekte vorm als dat van een lat, en zijn zo dun dat ze gemakkelijk vouwen of oprollen aan de lange zijanten. De nanolagen hebben een WO₃ of WO_{2.72} samenstelling en een monokliene kristalstructuur. We vermoeden dat de 2D nanolagen door middel van een vast-damp-vast mechanisme zijn gevormd.

De algemene trend die is gevonden voor de TMO-materialen die bestudeerd zijn in dit proefschrift, is dat deze nanomaterialen altijd transformeerden naar oxides met een lagere valentietoestand, of uiteindelijk naar puur metaal, wanneer deze werden verhit in de elektronenmicroscop. Dezelfde transformaties vonden in de meeste gevallen ook plaats in de ex-situ referentie-experimenten. We concluderen dat de (zeer lage) partiële zuurstof druk in het vacuüm van de kolom van de TEM belangrijk is voor de specifieke temperatuur waarbij deze transformaties plaatsvinden. Veranderingen in de morfologie van de nanodeeltjes, alsmede samensmelting en sublimatie werden vaak waargenomen en waren soms afhankelijk van de lokale concentratie van de nanodeeltjes. Het onderzoek beschreven in dit proefschrift bevestigt het buitengewoon diverse gedrag van nanodeeltjes. Fasetransformaties kunnen plaatsvinden bij temperaturen die sterk verschillen van de temperaturen die in de fase diagrammen van de overeenkomstige bulkmaterialen worden weergegeven. De grootte en vorm van de deeltjes beïnvloedt ook de stabiliteit van bepaalde fasen. Tenslotte is zelfs het type kristalstructuur van belang, met als extreem geval het exfoliëren van nanovlokken van nanodeeltjes met Van der Waals gebonden kristallagen, wanneer deze nanodeeltjes in rap tempo worden verhit.

Sommigen van de bevindingen in dit proefschrift bieden mogelijkheden voor toepassing in de chemische en hightech-industrie waar TMO-materialen worden gebruikt. Dit onderzoek heeft echter vooral bijgedragen aan de wetenschappelijke kennis over alle bovengenoemde aspecten, hetgeen belangrijk is om tot een volledig begrip van het thermische gedrag van TMO-nanodeeltjes te komen, en kan dan ook als referentie voor toekomstig onderzoek dienen.

In vervolgstudies zou de karakterisatie van de transformaties in meer detail kunnen worden uitgezocht, bijvoorbeeld door nader te bestuderen hoe de transitie-temperaturen afhankelijk zijn van de partiële zuurstofdruk, door deze partiële zuurstofdruk in de gas- of vacuümkamers waarin de nanodeeltjes worden verhit, te controleren en systematisch te variëren. Hiervoor zou het nuttig zijn om naast het doen van ex-situ experimenten ook in-situ XRD experimenten of gas-cel TEM experimenten uit te voeren. Tenslotte kunnen de eigenschappen van de gevormde nanodeeltjes nader worden bestudeerd. In het bijzonder kan worden onderzocht of gedeeltelijk getransformeerde $\text{Co}_3\text{O}_4/\text{CoO}$ nanodeeltjes inderdaad sterker resulterend ferromagnetisme vertonen zoals voorspeld werd door de DFT berekeningen, en kan onderzocht worden of TiO nanodeeltjes en MoO_2 nanoplaatjes (verhoogde) katalytische activiteit vertonen.

Acknowledgements

It cannot be denied the whole PhD process is quite tough. Despite all the problems during research and limitations, the thesis finally came into being. Many great people gave me a great amount of help, professional advice, and encouragement. To complete a PhD program and finish the writing is not easy. Especially the long-lasting Covid lock down makes the process even harder. During these years, I experienced the periods of being stressful, lonely, and in a negative mode. It is a significant and unforgettable experience for me to spend such a long time on writing, modifying and polishing this thesis. To overcome all of those obstacles, the help and support of many people is significant. Thus, I would like to express my gratitude to all those who have helped me during these PhD years.

First of all, my deepest gratitude goes to my promotors, Prof. Dr. Alfons van Blaaderen and Dr. Marijn van Huis for their supervision and help during these years. Thanks both of you for providing this position and giving me opportunity to complete my research here. Alfons, I have benefited tremendously from your critical thinking and insightful viewpoint. Thanks for your suggestions and rigorous comments on this thesis. Marijn, Thanks for your all-along supports during not only the research, but the whole PhD years. At the beginning of my PhD years, I didn't have as much experience of scientific research as other colleagues, which make that period harder. Through your patient instruction, I finally focused on the object studied in this thesis, and obtained valuable advice on aspects ranging from frame work constructing and data collection to elaborated analysis. Also, thanks for your positive feedback and encouragement when I feel hesitate and get stuck.

Next, I would like to thank the lab technicians and administrative support staff members. Experiments are the foundation of my research. I enjoyed so much the time that spend in the lab during which I got the data that support this thesis. I would like to thank all the technicians in SCM group and EM center. Relinde, Elleka and Judith thanks for the help in OL lab. You did nice works on organizing our chemical labs and always helps me on time. Hans and Chris, thanks for all the support and teaching on microscopy. Electron Microscope is the key instrument of my research, and EM center is the second most frequently used place except my office. During these years, you are always there, keeping the microscope ready for our using and supporting me when I got problem with microscope. Hester, Marion, Mijke and Dianne, thanks for organizing all the administrative cases for me. Hester, thank you for your patience and on-time replies during my visa extension.

The ability and energy of myself is limited, without the collaborations, my thesis would be never complete. Therefore, I would like to thank my collaborators, Heleen, Naveed and Roos. Heleen, thanks for the work on DFT calculations. Yours nice work and writing make the paper more complete and fruitful. Naveed, thanks for the synthesis of the nanorods. Without your nice samples, I would not

Acknowledgement

achieve so many beautiful images in chapter 4 and 5. And thanks for your patient explanations about the synthesis, it really let me know more things. Roos, we got to know each other when you were a bachelor student, now you are finishing your master. Thanks for your work on MoO₃ calculation and the translation of the summary of this thesis. You and Jesse are the best group of the bachelor projects that I have supervised, and you kept your high quality during your bachelor and master thesis. You are always hardworking, active and enthusiastic on the scientific work, and I believe you will be a nice scientist in the future.

I would like to thank the EM group members, Xiaobin, Sina, Tom, Dnyaneshwar, Albert, Rafael and Ali. You guys are the people that I met most frequently during my PhD years. I enjoyed the discussions with all of you in our EM meetings in every two weeks.

Tom, thanks for your help during these years, especially when I just joined our group. We are officemates when I start my PhD. You introduced the people here and let me get involved in the new environment smoothly. And the help and kindness from you never stopped during the following years. Albert, thanks for your support on gas phase and Spectra measurement. You are always there when I need help. Dnyaneshwar, we are officemates from the beginning to the end of your PhD period. We shared the same office and got training together. Thanks for your accompany. Xiaobin, also my officemate, thanks for your help throughout my PhD years, even after you left Utrecht. Thanks for sharing your TEM knowledge and experience. Sina, I enjoyed the travel in Berlin with you and Nana. Ali, we didn't know each other for a long time. But you still help me a lot on TEM knowledge, thanks.

I would also thank other colleagues in SCM group. Kanako, I am happy to meet another Asian girl in our group. Anna and Jessi, thanks for your accompany during the group outing. Rama, thanks for providing the nice core-shell particles. Although I didn't make them into a chapter in this thesis, it is still an important experience of my research process, in which I also got many nice images. Da, most our conversions happened after you graduated. Thanks for the helping in research and also suggestions about the future. Now you are Prof. Wang. I wish you all the best in China.

Ruizhi, Yunhan, Chaohong and Mengwei, I feel so happy that you guys come to Netherlands and join in our group. Before you came to Netherlands, I have been the only Chinese in our group for more than one year. You are all so nice and funny person, and I enjoyed the dinners and trips with you guys. Ruizhi, you are always full of energies and good at networking. Thanks for organizing of the dinners and trips. Yunhan, you are a so nice and kind-hearted girl. I was very happy during the new year vacation of 2021 staying with you. Mengwei, the weekends we spent in Amsterdam became more interesting and unforgettable because of you.

The gratitude is the same to other members that didn't mention. SCMB is a warm and cozy group, offering a nice environment for my scientific work. Every member in SCMB contributes to this cozy

environment. I would like to thank all the member in our group, and the period in SCMB is unforgettable.

Collaborations with our neighbor groups in Debye institute are also essential to my research. I would thank the members in our neighbor groups, Atul Sontakke, Bas Salzmann and Naud van Bunningen from CMI, Savannah Turner, Nienke Visser and Min Tang from MCC. Atul and Bas, thanks for your help on the vacuum furnace heating. Naud, thanks for your help on XRD measurements. Savannah, thanks for your support on gas phase experiments and the arrangement of training. Nienke, I am happy to meet you at EM center from time to time.

I would like to thank all my Chinese friends I met in Utrecht. Firstly, I would thank the friends from CMI group, Wenjin, Weiwei, Chenghui, Yu Ting Zijun and Dechao. Chenghui and Yu Ting, thanks for your help when I moved to Zeist. Chenghui, thank you for your guide on the crystal structures and the suggestions about SADP, that helps me a lot in my following research. Weiwei, thanks for the hosting when I visit your place in Beijing.

Wenjin, my best friend in Netherlands. It is really yuafen that we meet each other in Utrecht finally. We worked in neighbor groups and moved to Zeist from UCU one after another. We met each other almost every day before 2019. After you moved to other cities, we still kept in touch and traveled together. We have many common interests and always have topic to talk. You can always comfort me when I feel down and anxious. Thanks, my friend. You are an essential component of the memories during these years.

Min and Shuang, my pretty and smart girls, it's my pleasure to be your friends. Thanks for your friendship after a long lockdown period and the left of my old friends. Min, we firstly met during the training of gas phase holder. We visited each other during the Christmas vacation of that year, and you became the first guest of my apartment. After that, you often entertained me with your tasty food and introduced Shuang to me. I enjoyed all the dinners at your place. Shuang, you are such a nice and cute girl. Thanks for the cakes. It's so lucky to be your neighborhood. Take care!

I would like to thank the supervisors of my master thesis Prof. Ute Kaiser and Dr. Haoyuan Qi and all the colleagues in Ulm. Prof. Kaiser, thank you for giving me opportunity to do my master thesis in your group, which is the beginning that I work with the TEM. I started to learn about the TEM technique and how to be a scientist at that moment. At the end of my master, you encouraged me to find a job in a new environment and wrote reference letter for me, then I can get a position in UU. Haoyuan, thanks for your supervision on my master thesis, which is a good beginning of my research life. What I learn from you is not only TEM theory and technique but also an early-stage concept of scientific research. Thanks for your patience and tolerance of my long-lasting writing period.

Moreover, I would owe my thanks to my old friends in Germany and China. When I feel depressed

Acknowledgement

and anxious, especially the writing period, you are always there, ready to listen to my complaint. Thanks for your patience to me. To be your friends, I am sort of mighty and dominant sometimes. But you guys always bear me and never show any impatience. When I feel upset and lack of energy, thanks for your encouragement and support.

Last but not the least, I would like to thank my best parents and grandparents. Thanks for the endless love and support. I am so lucky to be your child. Love you.

List of Publications

This thesis is based on the following publications:

Xiaodan Chen, H. van Gog, M. A. van Huis. Transformation of Co_3O_4 nanoparticles to CoO Monitored by: In Situ TEM and Predicted Ferromagnetism at the $\text{Co}_3\text{O}_4/\text{CoO}$ Interface from First Principles. *J. Mater. Chem. C* **2021**, 9 (17), 5662–5675. DOI: org/10.1039/d0tc05727d. **(Chapter 3)**

Xiaodan Chen, S. N. Hosseini, M. A van Huis. Heating-Induced Transformation of Anatase TiO_2 Nanorods into Rock-Salt TiO Nanoparticles: Implications for Photocatalytic and Gas-Sensing Applications. *ACS Appl. Nano Mater.* **2022**, 5 (1), 1600–1606. DOI: org/10.1021/acsnm.1c04346. **(Chapter 4)**

Xiaodan Chen, R. M. de Boer, H. van Gog, M. A. van Huis. Heating-Induced Exfoliation and Thermal Reduction of MoO_3 Particles Monitored by In-Situ Transmission Electron Microscopy. Submitted. **(Chapter 6)**

Xiaodan Chen, M. A. van Huis. Formation Pathways of Lath-shaped WO_3 Nanosheets and Elemental W Nanoparticles from Heating of WO_3 Nanocrystals Studied by In-Situ TEM. To be submitted. **(Chapter 7)**

Other publications by the author:

S. N. Hosseini, X. Chen, P. J. Baesjou, A. Imhof, A. van Blaaderen. Synthesis and Characterization of Anatase TiO_2 Nanorods: Insights from Nanorods' Formation and Self-Assembly. *Appl. Sci.* **2022**, 12 (3), 1614. DOI: org/10.3390/app12031614.

S. N. Hosseini, A. Grau-Carbonell, A. G. Nikolaenkova, X. Xie., X. Chen, A. Imhof, A. van Blaaderen, , P. J. Baesjou. Smectic Liquid Crystalline Titanium Dioxide Nanorods: Reducing Attractions by Optimizing Ligand Density. *Adv. Funct. Mater.* **2020**, 30 (52), 2005491. DOI: org/10.1002/adfm.202005491.

R. M. de Boer, X. Chen, D. Cvejn, K. Dědková, M. A. van Huis, R. G. Mendes. Nanoscale Porosity of High Surface Area Gadolinium Oxide Nanofoam Obtained with Combustion Synthesis. To be submitted.

H. Y. Qi, X. Chen, E. Benckiser, M. Wu, G. Cristiani, G. Logvenov, B. Keimer, U. Kaiser. Formation Mechanism of Ruddlesden-Popper Faults in Compressive-Strained ABO₃perovskite Superlattices. *Nanoscale* **2021**, *13* (48), 20663–20669. DOI: [org/10.1039/d1nr06830j](https://doi.org/10.1039/d1nr06830j).

H. Y. Qi, M. K. Kinyanjui, X. Chen, J. Biskupek, D. Geiger, E. Benckiser, H. U. Habermeier, B. Keimer, U. Kaiser. Control of Octahedral Rotations via Octahedral Connectivity in An Epitaxially Strained [1 u.c./4 u.c.] LaNiO₃/LaGaO₃ Superlattice. *J Mater Sci* **51**, 8168–8176 (2016). DOI: [org/10.1007/s10853-016-0092-4](https://doi.org/10.1007/s10853-016-0092-4)

About the Author

Xiaodan Chen was born on the 12th of May 1990 in Urumqi, Xinjiang, China. After finishing the high school in her home city, she started to study at Southeast University in Nanjing in 2008. In 2012, she graduated with Bachelor degree of Materials Science and Engineering, and planed to the study abroad. After one year preparation and application, she started her master program (“Advanced Materials”) in Ulm University, Germany from 2013. In 2015, she joined the Electron Microscopy Group of Materials Science for her master thesis project and started to work behind the Transmission Electron Microscope. During master project, she studied on the III-V semiconductor using TEM under supervision of Prof Ute Kaiser. After graduation of master in 2016, she applied for the PhD position at Utrecht University. In March 2017 she moved to Netherlands and started her PhD project in the Soft Condensed Matter and Biophysics group under supervision of Dr. Marijn van Huis and Prof. Alfons van Blaaderen. During her PhD, she worked on several nanocrystals by using in-situ TEM. A number of the research works have been published.